Constitutive Equations and Failure Criteria for Amorphous Polymeric Solids

by

Brian Paul Gearing

B.S. Mechanical Engineering
University of Maryland at College Park, 1996

S.M. Mechanical Engineering
Massachusetts Institute of Technology, 1999

Submitted to the Department of Mechanical Engineering
in partial fulfillment of the requirements for the degree of

Doctor of Philosophy

at the

MASSACHUSETTS INSTITUTE OF TECHNOLOGY

September 2002

Author .....
Department of Mechanical Engineering
August 9, 2002

Certified by .....
Lallit Anand
Professor of Mechanical Engineering
Thesis Supervisor

Accepted by .....
Ain A. Sonin
Chairman, Department Committee on Graduate Students

Constitutive Equations and Failure Criteria for Amorphous Polymeric Solids

by

Brian Paul Gearing

Submitted to the Department of Mechanical Engineering
on August 9, 2002, in partial fulfillment of the
requirements for the degree of
Doctor of Philosophy

Abstract

Anand & Gurtin (2002) have recently developed a continuum theory for the elastic-viscoplastic deformation of amorphous solids. Their theory is motivated by and builds on the work of Parks, Argon, Boyce, Arruda, and their co-workers (e.g. Boyce et al., 1988; Arruda & Boyce, 1993) on modeling the plastic deformation of amorphous polymers. The theory of Anand & Gurtin (2002) carefully accounts for restrictions placed on constitutive assumptions by frame-indifference and by a new mathematical definition of an amorphous material based on the notion that the constitutive relations for such materials should be invariant under all rotations of the reference configuration and, independently, all rotations of the relaxed configuration. Also, they explicitly account for the dependence of the Helmholtz free energy on the plastic deformation in a thermodynamically consistent manner, a dependence which leads directly to a backstress in the underlying flow rule. In addition to the standard kinematic and stress variables, their theory contains two internal variables: a variable $s > 0$ that represents an isotropic intermolecular resistance to plastic flow; and an unsigned variable η that represents the local free-volume.

In this thesis, we extend the work of Anand & Gurtin (2002) to model the deformation and fracture response of amorphous glassy polymers which exhibit both a ductile mechanism of fracture associated with large plastic stretches and subsequent chain scission and a brittle mode of fracture. For polymers such as polycarbonate (PC), the brittle fracture mode is characterized by a mechanism of elastic cavitational failure, which results in cleavage-type fracture similar to that observed in brittle fracture of metals. In contrast, polymers such as polymethylmethacrylate (PMMA) and polystyrene (PS) exhibit a brittle mode of fracture characterized by craze initiation, flow, and breakdown.

To model crazing, we introduce a continuum constitutive relation which contains the three ingredients of crazing – initiation, widening, and breakdown – in a suitable statistically-averaged sense. We allow for local inelastic deformation due to shear yielding in possible concurrence with that due to crazing, and introduce a craze initiation criterion based on the local maximum principal tensile stress reaching a critical

value which depends on the local mean normal stress. After crazing has initiated, our continuum model represents the transition from shear-flow to craze-flow by a change in the viscoplastic flow rule, in which the dilational inelastic deformation associated with craze-plasticity is taken to occur in the direction of the local maximum principal stress. Finally, for situations in which the local maximum tensile stress is positive, craze-breakdown and fracture is taken to occur when a local tensile plastic craze strain reaches a critical value. We apply our model to the techologically important polymer, polymethylmethacrylate. We show that the constitutive model and fracture criteria, when properly calibrated, are able to reasonably-well predict the macroscopic load-displacement curves, and local aspects of the craze-flow and fracture processes in (a) a thin plate with a circular hole under tension, and (b) notched-beams in four-point bending.

For amorphous glassy polymers which show ductile tearing and brittle cavitational fracture, as in the case of the fracture behavior of PC, we modify the model of Anand & Gurtin (2002) for large elastic volume changes to accommodate the experimental observation of the key role of the hydrostatic tension in the nucleation of internal cracks. To model fracture we introduce two simple local fracture criteria: (*i*) Brittle fracture is taken to occur when a local elastic volumetric strain reaches a failure value; (*ii*) Ductile fracture will be taken to occur when a measure of the plastic stretch of the polymer chains reaches a critical value. We show that the constitutive model and fracture criteria, when suitably calibrated, are able to *quantitatively* capture the notch-sensitive fracture response exhibited by notched-beams of polycarbonate in bending.

To further demonstrate the capabilities of the constitutive model, we study the micro-indentation behavior of PC and PMMA. Our work in this area builds upon the development of novel flexure-based apparatuses for mechanical testing at the small scale. Details of our nano- and micro-indentation apparatuses as well as a biaxial compression/shear apparatus are presented. We analyze Berkovich and conical micro-indentation and perform parametric studies with dimensional analysis to elucidate the key material parameters that determine the indentation response. Our study of the *forward problem* in indentation motivates a framework for the *reverse problem* in indentation of amorphous glassy polymers. We show that an applicaton of our proposed reverse approach is able to reasonably-well predict the macroscopic stress-strain behavior of polystyrene (PS) in simple compression.

Thesis Supervisor: Lallit Anand
Title: Professor of Mechanical Engineering

Acknowledgments

First and foremost, I would like to express my sincere gratitude to Professor Lallit Anand for his support and guidance over the last six years. His demand of impeccable standards and fastidiousness for detail will continue to inspire me. I would also like to thank Professor Mary Boyce, Professor Mark Spearing, and Professor Subra Suresh for serving on my thesis committee.

Many thanks to Ray Hardin, Una Sheehan, Leslie Regan, and Joan Kravit for their support, which always far exceeded administrative details.

I would like to thank my research partners over the past years. To Sauri Gudlavalleti for our resonance in developing the small scale testing machines; I look forward to our future collaboration. To Cheng Su for his meticulous work on the polycarbonate beam bending experiments.

Infinite thanks to the Mechanics and Materials family here at MIT. To Nici Ames, Jeremy Levitan, Matt Busche, Chief Bass, Tom Arsenlis, Dora Tzianetopoulou, Rajdeep Sharma, Mats Danielsson, Ethan Parsons, Franco Capaldi, Cheng Su, Yujie Wei, Jin Yi, Yu Qiao, Hang Qi, Nuo Sheng, and Yin Yuan. Cheers to our future friendships.

To Prakash Thamburaja – thank you for being both a best friend as well as esteemed colleague. While I will miss our great times in Boston, I shall look forward to our friendship around the globe. May you always continue to be blessed by great karma.

Finally, I would like to thank my family for always supporting me through my academic endeavors and for always being there for me. My special thanks to Rose Zitelli for all of the prayers and support!

This research was supported by the Singapore-MIT Alliance and the DuPont-MIT Alliance.

Contents

List of Figures

List of Tables

Chapter 1

Introduction

Anand & Gurtin (2002) have recently developed a continuum theory for the elastic-viscoplastic deformation of amorphous solids. Their theory is motivated by and builds on the work of Parks, Argon, Boyce, Arruda, and their co-workers (e.g. Boyce et al., 1988; Arruda & Boyce, 1993) on modeling the plastic deformation of amorphous polymers. The theory of Anand & Gurtin (2002) carefully accounts for restrictions placed on constitutive assumptions by frame-indifference and by a new mathematical definition of an amorphous material based on the notion that the constitutive relations for such materials should be invariant under all rotations of the reference configuration and, independently, all rotations of the relaxed configuration. Also, they explicitly account for the dependence of the Helmholtz free energy on the plastic deformation in a thermodynamically consistent manner, a dependence which leads directly to a backstress in the underlying flow rule. In addition to the standard kinematic and stress variables, their theory contains two internal variables: a variable $s > 0$ that represents an isotropic intermolecular resistance to plastic flow; and an unsigned variable η that represents the local free-volume.[1]

In this thesis, we extend the work of Anand & Gurtin (2002) to model the deformation and fracture response of amorphous polymeric solids which exhibit both a

[1]It is commonly believed that the evolution of the local free-volume is the major reason for the highly non-linear stress-strain behavior of glassy materials which precedes the yield-peak and gives rise to the post-yield strain-softening.

ductile mechanism of fracture associated with large plastic stretches and subsequent chain scission and a brittle mode of fracture which depends upon the class of polymer under consideration. For polymers such as polycarbonate (PC), the brittle fracture mode is characterized by a cavitational mechanism,[2] which results in a cleavage-type of fracture similar to that observed in brittle fracture of metals. In contrast, polymers such as polymethylmethacrylate (PMMA) and polystyrene (PS) are well-known to craze at room temperature in the absent of solvents.

To model crazing in amorphous polymeric solids, we introduce a continuum constitutive relation which contains the three ingredients of crazing – initiation, widening, and breakdown – in a suitable statistically-averaged sense. We allow for local inelastic deformation due to shear yielding in possible concurrence with that due to crazing, and introduce a craze initiation criterion based on the local maximum principal tensile stress reaching a critical value which depends on the local mean normal stress. After crazing has initiated, our continuum model represents the transition from shear-flow to craze-flow by a change in the viscoplastic flow rule, in which the dilational inelastic deformation associated with craze-plasticity is taken to occur in the direction of the local maximum principal stress. Finally, for situations in which the local maximum tensile stress is positive, craze-breakdown and fracture is taken to occur when a local tensile plastic craze strain reaches a critical value. We have calibrated the constitutive parameters in our model for PMMA under normal dry conditions. We show that our model, when suitably calibrated and implemented, is able to reasonably-well predict the macroscopic load-displacement curves, and local aspects of the craze-flow and fracture processes in (a) a thin plate with a circular hole under tension, and (b) notched beams in four-point bending.

For amorphous polymeric solids which exhibit ductile tearing and brittle cavitational fracture, similar to the fracture behavior of PC, we modify the model of Anand & Gurtin (2002) to account for large elastic volume changes to accommodate the experimental observation of the key role of the hydrostatic tension in the nucleation of internal cracks. To model the fracture we introduce two simple local fracture:

[2]Polycarbonate is known to exhibit surface crazing in the present of solvents.

(*i*) Brittle fracture is taken to occur when a local elastic volumetric strain reaches a failure value; (*ii*) Ductile fracture will be taken to occur when a measure of the plastic stretch of the polymer chains reaches a critical value. We show that our theory, when suitably implemented and calibrated, is able to *quantitatively* predict the experimentally-observed ductile failure response of blunt-notched beams, as well as the competition between the brittle and ductile mechanisms in more sharply-notched beams of polycarbonate in bending.

Our fracture experiments on PC and PMMA are concerned with applications when specimens dimensions are on the order of mm and loads are in the range of kN. As a final application for this thesis, we consider experimentation and constitutive modeling when dimensions of the specimens are on the order of nm to μm with forces in the μN to N range. We present novel flexure-based apparatuses for mechanical testing at the small scale. As an application for our newly developed experimental capabilities, we investigate the forward problem in indentation of amorphous polymeric solids, with specific application to PC and PMMA. After demonstrating the applicability of the constitutive model for predicting the indent morphologies and load-displacement, or P-h curves, we elucidate through a parametric study and dimensional analysis the key material parameters that determine the indentation response. The results of our study of the forward approach, parametric studies, and dimensional analysis motivate a framework for the reverse problem in indentation of amorphous polymeric solids. We propose a first attempt at the reverse approach by extracting material parameters for polystyrene (PS) from Berkovich indentation experiments and comparing the predicted stress-strain curves against the experimental results in simple compression under monotonic loading and loading with an imposed strain-rate jump. The predicted stress-strain responses are found to be in reasonable accord with the macroscopic stress-strain curves for PS.

The plan of the thesis is as follows. In Chapter 2, we present our constitutive model for the deformation and fracture response of glassy polymers due to shear-yielding and crazing. We demonstrate the determination of material parameters for PMMA and show our predictions of the deformation and fracture response of thin plates with

circular windows and notched-beams in four-point bending. Chapter 3 presents the constitutive equations proposed to model the deformation and fracture response of materials undergoing elastic cavitational failure. The model is utilized to capture the notch-sensitive fracture behavior of PC observed in four-point bending experiments on blunt and sharp-notched beams. Chapter 4 details our study of the forward and reverse problem in indentation of amorphous polymeric solids, which draws upon the experimental capabilities for mechanical testing at the small scale. The novel testing apparatuses – flexure-based designs for a microindenter, nanoindenter, and biaxial compression/shear apparatus – are presented in the Appendices. We note that each chapter has been composed as separate papers to allow for self-contained reading, therefore some redundancy in the presentation exists.

Chapter 2

Deformation and fracture due to shear-yielding and crazing

2.1 Introduction

Under stress states where the maximum principal stress is compressive, amorphous glassy polymers typically show extensive plastic deformation by a "shear yielding" mechanism which involves profuse densely-packed microscopic shear bands; the material shows substantial ductility, and eventual fracture occurs at large stretches by a chain-scission mechanism. In contrast, under stress states where the maximum principal stress is tensile, glassy polymers may at first show a little (or no) macroscopic inelastic deformation due to shear yielding, but then the mechanism of inelastic deformation switches to "crazing". An individual craze is a thin plate-like microscopic region in the material with a microstructure distinguished by a dense array of fibrils (interspersed with elongated voids) which span the boundaries of the individual crazes. The plate boundaries of the crazes are typically oriented perpendicular to the maximum principal stress direction, and the dominant inelastic deformation occurs by craze widening in the local maximum principal stress direction. Macroscopically, however, the material shows little ductility, and the nominally brittle fracture occurs by craze breakdown, crack-formation and crack-growth to failure. In most high molecular weight, flexible chain glassy polymers, such as polystyrene (PS) and polymethyl-

methacrylate (PMMA),[1] fracture under stress states where the maximum principal stress is tensile, is preceded by this craze initiation, widening, and breakdown process (cf., e.g., Kambour, 1973; Kramer, 1983).

A significant advance in modeling the plastic deformation of amorphous polymers by shear-yielding has been made by Parks, Argon, Boyce, Arruda, and their co-workers (e.g. Park et al., 1985; Boyce et al., 1988; Arruda & Boyce, 1993), and by Wu & Van der Giessen (1993); more recently, Anand & Gurtin (2002) have reformulated the theory within a rigorous thermodynamic framework. In contrast, although the phenomenon of crazing has been widely studied over the past four decades, and considerable understanding of the micro-mechanisms of crazing and cracking in amorphous polymers has been developed (cf., e.g., Kambour, 1973; Amdres, 1973; Argon & Hannoosh, 1977; Kramer, 1983; Narisawa & Yee, 1993; Donald, 1997.), *the incorporation of this understanding into an engineering tool for the quantitative prediction of the deformation and fracture response of glassy polymers is just beginning to emerge* (e.g., Estevez et al., 2000; Tijssens et al., 2000a; Tijssens et al., 2000b; Socrate et al., 2001).

Most studies on fracture of glassy polymers are based on the standard framework of linear elastic fracture mechanics (e.g. Kinloch & Young, 1983; Williams, 1984). However, as noted by Estevez et al. (2000), this approach ignores the process of initiation, widening and breakdown of crazes, and cannot be used when shear yielding of the material may be occurring at other locations in the body, especially when there are no initial sharp cracks in the body. Classical fracture mechanics cannot deal with crack nucleation, and the numerical simulation of crack propagation has also been a challenge for this classical theory. The recent work of Van der Giessen and co-workers (Estevez et al., 2000; Tijssens et al., 2000a; Tijssens et al., 2000b) and Socrate et al. (2001) is based on "cohesive surface" modeling of craze initiation, growth and breakdown.[2] Cohesive surface modeling of fracture started more than 40 years ago with

[1] But not polycarbonate, which does not craze under normal circumstances in the absence of solvents.

[2] Socrate et al. (2001) do not consider the breakdown stage which leads to final fracture.

the work of Barenblatt (1959) and Dugdale (1960). In recent years, cohesive surface models have been widely used to numerically simulate fracture initiation and growth by the finite-element method (e.g., Xu & Needleman, 1994; Camacho & Ortiz, 1996). Typically, a set of cohesive surfaces are introduced in the finite element discretization by the use of special interface elements which obey a non-linear interface traction-separation constitutive relation which provides a phenomenological description for the complex microscopic processes that lead to the formation of new traction-free crack faces. The loss of cohesion, and thus crack nucleation and extension occurs by the progressive decay of interface tractions. The interface traction-separation relation usually includes a cohesive strength and cohesive work-to-fracture. Once the local strength and work-to-fracture criteria across an interface are met, decohesion occurs naturally across the interface, and traction-free cracks form and propagate along element boundaries. An important characteristic of this methodology for modeling fracture initiation and propagation is that macroscopic fracture criteria, based on elastic or elastic-plastic analyses, such as $K_I = K_{IC}$ or $J_I = J_{IC}$, are not needed, because material strength and toughness, and crack nucleation and propagation are all characterized by the local traction-separation relation and the cohesive surface methodology.[3] Of special note is that the interface constitutive model used by Van der Giessen and co-workers (Estevez et al., 2000; Tijssens et al., 2000a; Tijssens et al., 2000b) is an *elastic-viscoplastic traction-separation relation* which accounts for the three separate stages of craze initiation, widening, and breakdown. While Van der Giessen and co-workers have produced informative *two-dimensional* parametric numerical studies on craze initiation, crack formation and crack growth around circu-

[3]There are still at least two key issues that need to be addressed in the cohesive surface modeling of fracture: (a) While it is relatively straightforward to construct a traction-separation relation for normal separation across an interface to model mode I conditions, elastic-plastic traction-separation relations for combined opening and sliding, together with the experimental methods needed to determine the parameters that might enter such coupled interface constitutive relations, are not well-developed, even for two-dimensional problems, and this issue is expected to be substantially more complicated in three dimensions. (b) The cohesive interface approach numerically restrains the orientation of crack nucleation and propagation. Once a finite element mesh is chosen, the crack can only nucleate and grow along the element boundaries. In the case of crazing, the initial element boundaries may not be aligned perpendicular to the evolving local maximum principal stress direction.

lar holes in plates under far-field tension, and in cracked plates under mode I loading conditions, much work remains to be done to correlate their parametric studies with actual experimental results, and to develop a truly predictive numerical capability for engineering design.

The purpose of the present chapter is to *present an alternative approach to modeling the competition between shear-yielding and crazing, and to develop the framework of an engineering tool for the quantitative prediction of the deformation and fracture response of glassy polymers.* Instead of attempting to represent each individual craze with an interface element, we will use a continuum constitutive relation which contains the three ingredients of crazing — initiation, widening, and breakdown — in a suitable statistically-averaged sense. Our model shall not account for the typical fine microstructural details of crazing; instead, for the continuum level of interest here, the inelastic deformation due to crazing will be defined as an average over a microstructural representative volume element that contains enough plate-like craze regions to result in an acceptably smooth process at the macroscopic level (prior to fracture). We will allow for local inleastic deformation due to shear yielding in possible concurrence with that due to crazing, and introduce a simple craze initiation criterion based on the local maximum principal tensile stress reaching a critical value which depends on the local mean normal stress. After crazing has initiated, our continuum model will represent the transition from shear-flow to craze-flow by a change in the viscoplastic flow rule, in which the dilational inelastic deformation associated with craze-plasticity will be taken to occur in the direction of the local maximum principal stress.[4] Finally, in order to model fracture we shall adopt a simple rule: for situations in which the local maximum tensile stress is positive, fracture will be taken to occur when a local tensile plastic craze strain reaches a critical value.

We have implemented our constitutive model in the finite-element computer program ABAQUS/Explicit (ABAQUS, 2001) by writing a user material subroutine.

[4]By incorporating such a constitutive model which allows for a local switch in the flow rule from shear-flow to craze-flow, we avoid *a priori* assumptions concerning the orientation and location of interface elements for crazing, assumptions which are inherent in the cohesive interface approach.

This finite-element program permits the modeling of failure, when user-specified critical values of certain parameters are reached, by an element-removal technique. By employing an appropriately dense (but computationally efficient) finite element mesh, we shall show that it is possible to predict, with reasonable quantitative accuracy, the major features of the macroscopic deformation and fracture behavior of components made from glassy polymers which craze.

In particular, we shall demonstrate that our model, when suitably implemented and calibrated against a suite of experiments to determine the constitutive parameters in the model for PMMA, is able to reasonably-well predict the macroscopic load-displacement curves, and local aspects of the craze-flow and fracture processes in (a) a thin plate with a circular hole under tension, and (b) notched beams in four-point bending, made from this important glassy polymer.

The plan of the chapter is as follows. In Section 2.2 we develop our constitutive model. In Section 2.3 we describe our experiments to calibrate the material parameters in the model for PMMA; we limit our study to experiments performed under normal dry conditions. In Section 2.4 we verify the predictive capabilities of our constitutive model and computational procedures for the deformation and fracture response of notched components made from PMMA. We close in Section 2.5 with some final remarks.

2.2 Constitutive equations for plastic deformation. Fracture criteria

In this section we begin by summarizing the constitutive model for plastic deformation of amorphous polymeric materials by the shear-yielding mechanism (Anand & Gurtin, 2002). The (isothermal) model is based on the mutliplicative decomposition, $\mathbf{F} = \mathbf{F}^e\mathbf{F}^p$, of the deformation gradient $\mathbf{F}$ into elastic and plastic parts, $\mathbf{F}^e$ and $\mathbf{F}^p$ (Kroner, 1960; Lee, 1969).[5] The theory also contains two internal variables: a variable $s > 0$

[5] *Notation*: ∇ and Div denote the gradient and divergence with respect to the material point $\mathbf{X}$ in the *reference configuration*; grad and div denote these operators with respect to the point

that represents an isotropic intermolecular resistance to plastic flow; and an unsigned variable η that represents the local free-volume.[6] Then, in terms of the variables

ψ,		Helmholtz free energy per unit volume of the relaxed configuration,
$\mathbf{T}$,	$\mathbf{T} = \mathbf{T}^\top$,	Cauchy stress,
$\mathbf{F}$,	$\det \mathbf{F} > 0$,	deformation gradient,
$\mathbf{F}^p$,	$\det \mathbf{F}^p = 1$,	plastic part of the deformation gradient,
s,	$s > 0$,	isotropic resistance to plastic flow,
η,		free-volume,

and the definitions

$\mathbf{F}^e = \mathbf{F}\mathbf{F}^{p-1}$, $\det \mathbf{F}^e > 0$,	elastic deformation gradient,
$\mathbf{C}^e = \mathbf{F}^{e\top}\mathbf{F}^e$,	elastic right Cauchy-Green strain,
$\mathbf{E}^e = \frac{1}{2}(\mathbf{C}^e - \mathbf{1})$,	elastic strain,
$\mathbf{T}^e = \mathbf{R}^{e\top}\mathbf{T}\mathbf{R}^e$,	stress conjugate to the elastic strain $\mathbf{E}^e$,
$\sigma = \frac{1}{3}\mathrm{tr}\mathbf{T}$,	mean normal stress,
$\mathbf{T}_0^e = \mathbf{T}^e - \sigma\mathbf{1}$,	deviatoric stress,
$\mathbf{B}^p = \mathbf{F}^p\mathbf{F}^{p\top}$,	left Cauchy-Green tensor corresponding to $\mathbf{F}^p$,
$\mathbf{B}_0^p = \mathbf{B}^p - \frac{1}{3}(\mathrm{tr}\mathbf{B}^p)\mathbf{1}$,	deviatoric part of $\mathbf{B}^p$,
$\lambda^p = \frac{1}{\sqrt{3}}\sqrt{\mathrm{tr}\mathbf{B}^p}$,	effective plastic stretch,
$\mathbf{D}^p = \mathrm{sym}(\dot{\mathbf{F}}^p\mathbf{F}^{p-1})$, $\mathrm{tr}\mathbf{D}^p = 0$,	plastic stretching,

the constitutive equations, *under the approximative assumption of small elastic stretches*, are:

$\mathbf{x} = \mathbf{y}(\mathbf{X}, t)$ in the deformed configuration, where $\mathbf{y}(\mathbf{X}, t)$ is the motion; a superposed dot denotes the material time-derivative. Throughout, we write $\mathbf{F}^{e-1} = (\mathbf{F}^e)^{-1}$, $\mathbf{F}^{p-\top} = (\mathbf{F}^p)^{-\top}$, etc. We write sym$\mathbf{A}$, skw$\mathbf{A}$, respectively, for the symmetric, and skew parts of a tensor $\mathbf{A}$. Also, the inner product of tensors $\mathbf{A}$ and $\mathbf{B}$ is denoted by $\mathbf{A} \cdot \mathbf{B}$, and the magnitude of $\mathbf{A}$ by $|\mathbf{A}| = \sqrt{\mathbf{A} \cdot \mathbf{A}}$.

[6] It is commonly believed that the evolution of the local free-volume is the major reason for the highly non-linear stress-strain behavior of glassy materials, which precedes the yield-peak and gives rise to the post-yield strain-softening.

1. **Free Energy**:

The Helmholtz free energy is taken in the noninteractive form

$$\psi = \psi^e(\mathbf{E}^e) + \psi^p(\lambda^p), \tag{2.1}$$

where ψ^e is an elastic free energy, and ψ^p a plastic free energy. The elastic free energy is taken in the standard form for small elastic stretches

$$\psi^e = G|\mathbf{E}_0^e|^2 + \frac{1}{2}K|\mathrm{tr}\mathbf{E}^e|^2, \tag{2.2}$$

where G and K are the elastic shear and bulk moduli, respectively. In amorphous polymeric materials the major part of ψ^p arises from an "entropic" contribution, and motivated by statistical mechanics models of rubber elasticity,[7] is taken in the specific form

$$\psi^p = \mu_R \lambda_L^2 \left[\left(\frac{\lambda^p}{\lambda_L} \right) x + \ln \left(\frac{x}{\sinh x} \right) - \left(\frac{1}{\lambda_L} \right) y - \ln \left(\frac{y}{\sinh y} \right) \right], \tag{2.3}$$

$$x = \mathcal{L}^{-1} \left(\frac{\lambda^p}{\lambda_L} \right), \qquad y = \mathcal{L}^{-1} \left(\frac{1}{\lambda_L} \right), \tag{2.4}$$

where $\mathcal{L}^{-1}$ is the inverse[8] of the Langevin function $\mathcal{L}(\cdots) = \coth(\cdots) - (\cdots)^{-1}$. This functional form for ψ^p involves two material parameters: μ_R, called the rubbery modulus, and λ_L, called the network locking stretch.

2. **Equation for the stress**:

$$\mathbf{T}^e = \frac{\partial \psi^e}{\partial \mathbf{E}^e} = 2G\mathbf{E}_0^e + K(\mathrm{tr}\mathbf{E}^e)\mathbf{1}. \tag{2.5}$$

[7] Cf., Treloar, 1975; Arruda & Boyce, 1993; Anand, 1996.

[8] To evaluate $x = \mathcal{L}^{-1}(y)$ for a given y in the range $0 < y < 1$, we numerically solve the non-linear equation $f(x) = \mathcal{L}(x) - y = 0$ for x. For numerically intensive calculations we approximate the Langevin-inverse by the first 26 terms of its Taylor series expansion; see Appendix A.

3. **Equation for back stress:**[9]

$$\mathbf{S}_{\text{back}} = 2\text{sym}_0\left(\frac{\partial\psi^p}{\partial\mathbf{B}^p}\,\mathbf{B}^p\right) = \mu\mathbf{B}_0^p, \quad \text{with} \tag{2.6}$$

$$\mu = \frac{1}{3\lambda^p}\frac{\partial\psi^p}{\partial\lambda^p} = \mu_R\left(\frac{\lambda_L}{3\lambda^p}\right)\mathcal{L}^{-1}\left(\frac{\lambda^p}{\lambda_L}\right). \tag{2.7}$$

The back stress modulus $\mu \to \infty$ as $\lambda^p \to \lambda_L$, since $\mathcal{L}^{-1}(z) \to \infty$ as $z \to 1$.

4. **Flow rule**:

The evolution equation for $\mathbf{F}^p$ is

$$\dot{\mathbf{F}}^p = \mathbf{D}^p\mathbf{F}^p, \qquad \mathbf{F}^p(\mathbf{X}, 0) = \mathbf{1}, \tag{2.8}$$

with $\mathbf{D}^p$ given by the flow rule

$$\mathbf{D}^p = \nu^p\left(\frac{\mathbf{T}_0^e - \mathbf{S}_{\text{back}}}{2\bar{\tau}}\right), \qquad \nu^p = \nu_0\left(\frac{\bar{\tau}}{s - \alpha\sigma}\right)^{\frac{1}{m}}, \quad 0 < m \leq 1, \tag{2.9}$$

where

$$\bar{\tau} = \frac{1}{\sqrt{2}}\,|\mathbf{T}_0^e - \mathbf{S}_{\text{back}}|, \quad \text{and} \quad \nu^p = \sqrt{2}\,|\mathbf{D}^p|, \tag{2.10}$$

are an equivalent shear stress and equivalent plastic shear strain-rate, respectively. Here, ν_0 is a reference plastic shear strain-rate, α a pressure sensitivity parameter, and m a strain-rate sensitivity parameter. The limit $m \to 0$ renders (4.4) rate-independent, while $m = 1$ renders (4.4) linearly viscous. The equivalent plastic shear strain, γ^p, is defined by $\gamma^p = \int \nu^p\, dt > 0$.

5. **Evolution equations for the internal variables s and η**:

The evolution of s and η is taken to be governed by the coupled differential

[9] Also see Arruda & Boyce, 1993.

equations[10]

$$\left.\begin{aligned} \dot{s} &= h_0 \left(1 - \frac{s}{\tilde{s}(\eta)}\right) \nu^p, \qquad s(\mathbf{X}, 0) = s_0, \\ \dot{\eta} &= g_0 \left(\frac{s}{s_{\text{cv}}} - 1\right) \nu^p, \qquad \eta(\mathbf{X}, 0) = 0, \end{aligned}\right\} \tag{2.11}$$

with

$$\tilde{s}(\eta) = s_{\text{cv}}[1 + b(\eta_{\text{cv}} - \eta)], \tag{2.12}$$

where $\{h_0, g_0, s_0, s_{\text{cv}}, b, \eta_{\text{cv}}\}$ are additional material parameters. Here $\tilde{s} = \tilde{s}(\eta)$ is a saturation value of s: $\dot{s}$ is positive for $s < \tilde{s}$ and negative for $s > \tilde{s}$. By definition ν^p is nonnegative. Assuming that $\nu^p > 0$, all solutions to the pair of evolution equations satisfy

$$s \to s_{\text{cv}} \quad \text{and} \quad \eta \to \eta_{\text{cv}} \quad \text{as} \quad t \to \infty.$$

We restrict attention to the initial conditions $s = s_0$ with

$$s_0 \leq s \leq s_{\text{cv}}(1 + b\eta_{\text{cv}}).$$

Also, as is tacit from $(3.11)_2$, the free-volume is measured from the value $\eta = 0$ in the virgin state of the material, and thus η at any other time represents a change in the free-volume from the initial state. Figure F-1 shows the evolution of s, $\tilde{s}$ and η with γ^p. We shall say that the flow has become "fully-developed" when $\eta \to \eta_{\text{cv}}$ and $s \to s_{\text{cv}}$.

[10] We expect that $\tilde{s}$ (and perhaps h_0 and g_0) may, in general, depend on ν^p, but currently there is insufficient experimental evidence to warrant such a refinement.

2.2.1 Modification of the constitutive equations for craze initiation, flow, and breakdown

The overall inelastic deformation due to craze initiation and growth is always inhomogeneous at the microstructural length scales associated with crazing. We emphasize that our model shall not account for the typical fine microstructural details of crazing. The spatially continuous fields that define our theory are to be considered as averages meant to apply at length scales which are large compared to those associated with the fine structure of the crazes and their distribution in a representative volume element. That is, for the continuum level of interest here, the inelastic deformation due to crazing will be defined as an average over a microstructural representative volume element (the material neighborhood of a continuum material point $\mathbf{X}$) that contains enough plate-like craze regions to result in an acceptably smooth process.

What constitutes an appropriate model for craze initiation is probably the least well-agreed-upon ingredient of the overall modeling of crazing in the literature. Argon and coworkers (e.g., Argon & Hannoosh, 1977; Argon et al., 1977) have emphasized that stress-based criteria governing initiation are hard to determine with precision from experiments because of the importance of imperfections in controlling the local stress states and the sites of craze initiation. In tension-torsion, stress-controlled experiments on thin-walled tubular specimens with controlled micro-roughness, these authors observed that at stress levels where the equivalent shear stress, $\bar{\tau} = \sqrt{\mathbf{T}_0 \cdot \mathbf{T}_0}$, and mean normal stress, σ, were below ≈ 0.5 of the yield strength Y of the material (due to shear-yielding), there was a time delay between the application of stress, and the first appearance of crazing. Their experiments showed that the delay time for craze initiation decreases with increasing values of equivalent shear stress or mean normal stress, and becomes negligible at stress levels greater than ≈ 0.5 of the yield strength of the material. Under these circumstances, craze-initiation may be considered an instantaneous event when a suitable local critical stress state is reached. Since we are concerned with the competition between shear-yielding and crazing, and eventually craze-breakdown and fracture, which typically occurs at stress levels higher

than ≈ 0.5 of the yield strength, *we will ignore considerations of incubation times, and adopt a simple time-independent stress-based criterion for craze initiation.* In this time-independent limit, Argon & Hannoosh (1977) have suggested that under situations in which the local mean normal stress is positive, $\sigma > 0$, crazes initiate when the local equivalent shear stress reaches a mean normal stress-dependent critical value (their equation (22)):

$$\bar{\tau} = \bar{\tau}_{cr}(\sigma) > 0, \qquad \text{with} \qquad \bar{\tau}_{cr}(\sigma) = \frac{A\,Y}{C + 3\sigma/2YQ}. \tag{2.13}$$

Here $Q = 0.0133$ is a fixed factor controlling the dependence $\bar{\tau}_{cr}$ on the mean normal stress σ, and (A, C) are temperature-dependent material constants. Although, Argon and co-workers have suggested (2.13) as the time-independent limiting form of their detailed micro-mechanical time-dependent model,[11] this criterion does not reveal that at an instant when crazes might be considered to have initiated in a *macroscopic sense*, they are typically oriented perpendicular to the maximum principal tensile stress direction.

The earliest stress-based craze initiation criterion is due to Sternstein and co-workers (e.g., Sternstein & Ongchin, 1969; Sternstein & Meyers, 1973). Based on biaxial plane-stress ($\sigma_3 = 0$) experiments on PMMA plates with circular holes, they postulated that the critical condition for craze nucleation is when a "stress bias" σ_B reaches a critical value

$$\sigma_B = \frac{A}{\sigma} + B, \tag{2.14}$$

where A and B are temperature-dependent material parameters. Under plane stress

[11] They modeled craze-initiation by postulating: (i) the formation of microcavities by the arrest of intense localized plastic flow at a molecular scale, with the rate at which such microcavities form depending on the local equivalent shear stress; (ii) the growth of these microcavities by plastic expansion into spongy craze nuclei, with the rate at which the microcavities grow depending on the local equivalent shear stress and the mean normal stress; (iii) the subsequent growth of the spongy craze nucleus by a meniscus instability mechanism, to initiate a macroscopic craze. Based on this micro-mechanical model they developed an expression which provides an estimate for the time to initiate a craze under a given stress state.

conditions with $\sigma_3 = 0$, they defined the stress bias by $\sigma_B = |\sigma_1 - \sigma_2|$. This quantity is the difference between the maximum and intermediate principal stresses when σ_1 and σ_2 are positive; however, it becomes the difference between the maximum and the minimum principal stress when either σ_1 or σ_2 is compressive. Thus, as noted by Oxborough & Bowden (1973), the physical interpretation of σ_B is unclear, nor is it clear how to evaluate σ_B for a general triaxial stress state. A further difficulty with this criterion is that while $|\sigma_1 - \sigma_2|$ represents an in-plane shear stress intensity, the crazes actually nucleate and grow in the direction of the maximum principal tensile stress. Noting this difficulty, Oxborough & Bowden (1973), based on their own experiments on PS, found that their experimental data for craze initiation was better fit to a criterion in which the maximum principal tensile strain ϵ_1 reaches a critical value which depends on the mean normal stress σ:

$$\epsilon_1 = \epsilon_{1,cr}(\sigma) > 0, \qquad \text{with} \qquad \epsilon_{1,cr} = \frac{X'}{\sigma} + Y', \tag{2.15}$$

where X' and Y' are temperature-dependent parameters. Since $\epsilon_1 = \{\sigma_1 - \nu(\sigma_2 + \sigma_3)\}/E$ for an isotropic elastic material, with (E, ν) the usual Young's modulus and Poisson's ratio, this criterion may be written as

$$\sigma_1 - \nu(\sigma_2 + \sigma_3) = \frac{X}{\sigma} + Y, \tag{2.16}$$

where $X = E\,X'$ and $Y = E\,Y'$. For plane stress this equation is very similar to the criterion (2.14) proposed by Sternstein & Ongchin (1969).

The craze initiation criterion (2.16) of Oxborough & Bowden may be further rearranged as a criterion in stress space, wherein craze initiation may be taken to occur when the maximum principal stress σ_1 reaches a critical value which depends on the mean normal stress σ:

$$\sigma_1 = \sigma_{1,cr}(\sigma) > 0, \qquad \text{with} \qquad \sigma_{1,cr}(\sigma) = c_1 + \frac{c_2}{\sigma} + c_3\,\sigma, \tag{2.17}$$

where $c_1 = Y/(1+\nu)$, $c_2 = X/(1+\nu)$, and $c_3 = 3\,\nu/(1+\nu)$.

Based on this brief review of the literature, in this paper we shall assume that crazing in a representative volume element (the material neighborhood of a continuum material point $\mathbf{X}$) can *initiate* provided the following two conditions are met:

(C1) the maximum principal stress and the mean normal stress are positive

$$\sigma_1 > 0, \qquad \sigma = \frac{1}{3}(\sigma_1 + \sigma_2 + \sigma_3) > 0; \tag{2.18}$$

and

(C2) the maximum principal stress σ_1 reaches a mean normal stress-dependent critical value

$$\sigma_1 = \sigma_{1,cr}(\sigma) > 0. \tag{2.19}$$

To be specific, following Oxborough & Bowden (1973), we shall assume that

$$\sigma_{1,cr}(\sigma) = c_1 + \frac{c_2}{\sigma} + c_3\,\sigma, \tag{2.20}$$

with c_i temperature-dependent positive constants for a given material.

After crazing has initiated and has become fully-developed, the average macroscopic plastic flow becomes oriented in the direction of the maximum principal stress. The dominant inelastic deformation associated with fully-developed craze plasticity occurs by widening of the crazes in the direction of the maximum principal stress. Following Argon (1999), the macroscopic averaged tensile plastic strain rate ξ^p may be kinematically related to the lateral translation of a given volume fraction of active craze borders as depicted schematically in Figure F-2, which shows active planar crazes separated by an average spacing h, thickening at an average rate $\dot{\delta}$, such that $\xi^p = \dot{\delta}/h$.

In our continuum model we will represent the transition from shear-flow to craze-flow by a change in the flow rule. To do this we use a switching parameter χ having

values

$$\chi = \begin{cases} 1 & \text{if conditions C1 and C2 are met,} \\ 0 & \text{otherwise.} \end{cases} \tag{2.21}$$

Once the craze initiation conditions C1 and C2 have been met, the craze-flow will be taken to continue as long as the maximum principal stress is positive. Accordingly, we set

$$\mathbf{D}^p = \begin{cases} \nu^p \left(\dfrac{\mathbf{T}_0^e - \mathbf{S}_{\text{back}}}{2\bar{\tau}} \right), \qquad \nu^p = \nu_0 \left(\dfrac{\bar{\tau}}{s - \alpha\sigma} \right)^{\frac{1}{m}}, & \text{if } \chi = 0 \\ \\ \xi^p \, \hat{\mathbf{e}}_1 \otimes \hat{\mathbf{e}}_1, \qquad \xi^p = \xi_0 \left\{ \dfrac{\sigma_1}{s_{\text{craze}}} \right\}^{\frac{1}{m}}, & \text{if } \chi = 1 \text{ and } \sigma_1 > 0. \end{cases} \tag{2.22}$$

Here, ξ_0 is a reference craze strain rate, and s_{craze} is the resistance to craze-flow, which we take to be a constant. Also, m is the strain-rate sensitivity parameter for craze-flow, which is taken to be the same as that for shear-flow. We call

$$\epsilon^p = \int \xi^p \, dt \tag{2.23}$$

the *craze-strain.*

Finally, in order to model craze-breakdown and fracture, we adopt the simple rule that for situations in which $\sigma_1 > 0$, craze-breakdown occurs when the local craze-strain ϵ^p reaches a failure value ϵ_f^p:

$$\epsilon^p \leq \epsilon_f^p. \tag{2.24}$$

On the other hand, for situations when $\sigma_1 \leq 0$, ductile fracture due to molecular chain-scission will be taken to initiate when the effective plastic stretch, λ^p, reaches

a critical value λ_f^p:

$$\lambda^p \leq \lambda_f^p. \tag{2.25}$$

We have implemented our constitutive model in the finite-element computer program ABAQUS/Explicit (ABAQUS, 2001) by writing a user material subroutine. This finite-element program permits the modeling of failure, by an element-removal technique. To avoid numerical instabilities, once either of the two fracture criteria are met, the corresponding material resistances are not instantly set to zero, but rapidly decreased to zero within a few increments.

2.3 Estimation of material parameters for PMMA

All experiments were conducted on specimens which were annealed at the glass transition temperature of the material, $T_g = 105°C$, for 2 hours, and then furnace-cooled to room temperature in approximately 15 hours. The results reported here were for experiments conducted under isothermal conditions at room temperature.

A representative true stress-true strain curve obtained from a simple compression experiment[12] conducted at a constant true strain rate of -0.001/s is shown in Fig. F-3. The general features of the stress-strain curve are quite similar to those observed for PC (see Fig. F-32). In an analogous manner to our pre-peak studies on PC, we have investigated the pre-peak nonlinear stress-strain response of PMMA by conducting plane strain tension experiments in which the strains are measured using a sensitive extensometer. As anticipated, an initial experiment showed brittle fracture prior to reaching a peak value, however a pre-peak non-linear response was observed. Using the maximum load determined from our diagnostic experiment, five additional experiments were performed to stress levels below the value necessary to cause fracture and subsequently unloaded. The results shown in Fig. F-4 indicate a clear trend of increasing residual strain upon unloading from increasing stress levels in the non-

[12]The data has been corrected to account for compliance contributions from the loading system.

linear pre-peak regime. The residual strains upon unloading were found to recover a negligible amount over a period of one hour. Consistent with our approach for PC, we neglect this small recovery at zero loads, and consider the measured residual strains after unloading as *plastic* strains. Thus, unloading from the initial approximately linear region produces essentially no residual plastic strains and the response is considered to be "elastic", whereas unloading from any stress level above the stress at which the stress-strain curve deviates from initial linearity, produces residual plastic strains, and the response is considered to be "plastic".

With this as background, we discuss the calibration procedures to determine the material parameters for our consititutive model, and also the failure values of the craze-strain and the effective plastic stretch. Recall that the material parameters that need to be determined are

1. The elastic shear and bulk moduli (G, K) in the elastic part of the free energy.

2. The parameters (μ_R, λ_L) in the plastic part of the free energy.

3. The parameters $\{\nu_0, m, \alpha, h_0, g_0, s_{cv}, b, \eta_{cv}, s_0\}$ in the flow rule and the evolution equations for (s, η) for shear-flow.

4. The parameters $\{c_1, c_2, c_3\}$ in the craze initiation criterion, and the parameters $\{\xi_0, s_{\text{craze}}, m\}$ in the function for craze-flow.

5. The parameters $\{\epsilon_f^p, \lambda_f^p\}$ in the failure criteria.

The values of elastic moduli (G, K) are determined by measuring the Young's modulus E and Poisson's ratio ν of the material in a compression experiment and using standard conversion relations of isotropic elasticity to obtain the elastic shear and bulk moduli. The parameters $\{\nu_0, m\}$ are estimated by conducting a strain rate jump experiment in simple compression. The pressure sensitivity parameter α is estimated from compression experiments under superposed hydrostatic pressure reported in the literature. The remaining parameters $\{h_0, g_0, s_{cv}, b, \eta_{cv}, s_0\}$ and (μ_R, λ_L) for shear-flow may be estimated by fitting a stress-strain curve in compression to large strains.

Values for the craze initiation parameters, $\{c_1, c_2, c_3\}$, are estimated from three sets of experiments: (a) smooth-bar tension tests, (b) notched-bar tension tests, and (c) tests on compact tension specimens (CTS) which contain the standard notch geometry, but are not fatigue pre-cracked. These three sets of experiments are chosen to provide a reasonably large range of positive mean normal stresses, σ, at craze initiation.

For the craze flow parameters, $\{\xi_0, s_{\text{craze}}, m\}$, the strain-rate sensitivity m is taken to be the same as that for shear-flow; the parameter s_{craze} which represents the craze-matter resistance to stretching is estimated from the stress levels observed in the simple compression experiment at large values of compression. The parameter ξ_0 is chosen to ensure continuity of the magnitude of the plastic stretching $|\mathbf{D}^p|$ at the transition from shear-flow to craze-flow, this gives

$$\xi_0 = \left(\frac{\nu_0}{\sqrt{2}}\right)\left\{\left(\frac{s_{\text{craze}}}{(s^* - \alpha\sigma^*)}\right)\left(\frac{\bar{\tau}^*}{\sigma_1^*}\right)\right\}^{\frac{1}{m}}, \tag{2.26}$$

where a quantity with a superscript $(*)$ denotes the value of the quantity at the instant $\chi = 1$ when the change in the flow rule is triggered. The craze-breakdown parameter ϵ_f^p is estimated from the experiments on the notched compact-tension specimens.

Finally, since crazing is suppressed in plane strain compression, the parameter λ_f^p for ductile failure is obtained by fitting a load-displacement curve obtained from a specimen which has been loaded to failure initiation in a plane strain compression experiment.

Using a value of $\alpha = 0.204$ (Rabinowitz et al., 1970), a value of $\nu_0 = 0.0017\,\text{s}^{-1}$ and a strain rate-sensitivity parameter $m = 0.043$ obtained from the strain rate jump experiment shown in Fig. F-5, the parameters $\{G, K, \mu_R, \lambda_L, h_0, g_0, s_{cv}, b, \eta_{cv}, s_0\}$ were estimated[13] by fitting the stress-strain curve for PMMA in simple compression, Fig. F-3. The fit was performed by judiciously adjusting the values of these parameters in finite element simulations of a simple compression experiment (assuming homogeneous deformation) using a single ABAQUS/C3D8R element. After a few attempts,

[13] A guideline for the calibration procedure is given in Appendix B.

a reasonable fit was obtained, and the resulting stress-strain curve is shown in Fig. F-3. The list of parameters obtained using this heuristic calibration procedure are:[14]

$G = 1.17$ GPa	$K = 3.04$ GPa	$\mu_R = 7.70$ MPa	$\lambda_L = 1.51$
$\nu_o = 0.0017\ \text{s}^{-1}$	$m = 0.043$	$\alpha = 0.204$	
$s_o = 37.8$ MPa	$s_{cv} = 43.7$ MPa	$h_o = 1.30$ GPa	
$b = 790$	$g_o = 7.5 \cdot 10^{-3}$	$\eta_{cv} = 0.00025.$	

Material parameters for craze-initiation, craze-flow, and craze-breakdown are estimated from suitable experiments and corresponding numerical simulations using the following three-step process:

Step 1. First, the values for the craze-initiation parameters, $\{c_1, c_2, c_3\}$, are estimated from three sets of experiments and corresponding numerical simulations: (a) Simple tension tests on smooth-bar specimens, which have an initial gauge section 6.35 mm in diameter and 25.4 mm in length, performed under displacement control at 0.0125 mm/s. (b) Notched-bar tension tests on 12.7 mm diameter cylindrical specimens with a notch of root-radius 0.90 mm, depth 3.18 mm, and width 1.80 mm. An extensometer was used to measure the local relative displacement across the notch faces as the specimen was extended at a rate of 0.0125 mm/s. (c) Tests on ASTM standard compact tension specimens (CTS) which contain a 60° notch, but are *not fatigue pre-cracked.* The compact tension specimens were tested at a displacement rate of 0.0125 mm/s. These three sets of experiments were chosen to provide a reasonably large range of positive mean normal stresses, σ, at craze initiation. In our study, which is intended for *engineering applications*, we did not attempt to specially polish our specimens, but *used as-machined surfaces.*[15]

To check the repeatability of the response of the smooth-bar tension specimens, four identical specimens were tested. A representative load-displacement curve is shown in Fig. F-6; for this specimen, fracture occurs abruptly at a displacement of 1.64 mm. The measured displacements at fracture between the four experiments

[14]This list, although not unique, is adequate for present purposes.

[15]Typical surface roughness values for our specimens, resulting from the machining procedures used, are on the order of 1 to 10 μm.

varied by less than 8%. All the smooth-bar specimens failed in the gauge section, some at multiple locations, and the fracture surface was always perpendicular to the tension direction. *The PMMA tension specimens show nonlinearity prior to failure. This indicates that the material has undergone some shear-yielding prior to craze-flow and fracture.*

The repeatability of the response of the notched-bar tension experiments was investigated by conducting four experiments on nominally identical specimens. A representative experimental load-displacement curve is shown in Fig. F-7; for this specimen, fracture is seen to abruptly occur at a displacement of only 0.078 mm. The displacement at fracture varied by less than 7% between the four specimens that were tested.

A representative load-displacement response from the compact tension experiments is shown in Fig. F-8. The repeatability of the peak load between the four specimens was found to be within 2%. In these specimens, crazing initiated at the notch root, and subsequently a front of a *craze process zone* propagated in a *stable manner* into the specimen. The initiation of crazing occurs at a displacement of approximately 0.47 mm, and the load asymptotically falls to about zero load after a displacement of 1.2 mm.

To numerically model the smooth-bar tension and the notched-bar tension experiments, one-half of the respective specimens were meshed with 390 ABAQUS/CAX4R axisymmetric elements, and to model the CTS experiment, one half of the specimen was meshed using 5278 plane strain ABAQUS/CPE4R, with a very fine mesh density in the vicinity of the specimen mid-plane. The mesh design for the compact tension specimen is shown in Fig. F-9a, with a detail of the fine mesh employed at the notch-root shown in Fig. F-9b. To estimate the craze initiation parameters, the shear-flow parameters for PMMA were used in the numerical simulations, but *craze flow and craze breakdown were numerically suppressed.* These numerical simulations provide estimates of $\sigma_{1,cr}$ and σ at craze-initiation, which is taken to occur just prior to the peak loads observed in the experiments. The values estimated for smooth-bar tension are $\sigma_{1,cr} = 76.0\,\text{MPa}$, at $\sigma = 25.3\,\text{MPa}$; for notched-bar tension $\sigma_{1,cr} = 68.9\,\text{MPa}$ at

$\sigma = 32.8\,\text{MPa}$; and for the compact tension specimen $\sigma_{1,cr} = 65.2\,\text{MPa}$ at $\sigma = 44.9$ MPa. The three data points are plotted in Fig. F-10; estimated error bars associated with each data point are also given. The parameters $\{c_1, c_2, c_3\}$ are estimated by fitting Eq. 2.20 to this experimental data. The curve-fit using

$$c_1 = 45.60\,\text{MPa}, \quad c_2 = 785.56\,\text{MPa}^2, \qquad c_3 = 0,$$

is also shown in Fig. F-10. We caution that the values of craze-initiation parameters are expected to be quite sensitive to the quality of the machined surfaces, and also to the grade of the material from which the specimens are made. We also recognize that three data points are perhaps not quite enough to unambiguously specify the non-linear dependence of $\sigma_{1,cr}$ on σ. However, the trend of a decreasing value of $\sigma_{1,cr}$, with an increasing value of the mean normal stress σ, is clearly revealed by the data. Information from more complete experimental programs, as it becomes available, can easily be incorporated into our constitutive framework and numerical capability for modeling crazing.

Step 2. Recall that we have assumed that the strain rate sensitivity parameter for craze widening is taken to be the same as that for shear flow, $m = 0.043$, and that the reference craze strain rate ξ_0 is set by enforcing the continuity of the plastic stretching in switching from shear-flow to craze-flow, equation (2.26). The craze-flow resistance parameter s_{craze} is estimated from the stress levels observed in a simple compression experiment at a large value of compression. From Fig. F-3 we estimate that

$$s_{\text{craze}} = 200\,\text{MPa}.$$

Step 3. The craze-breakdown parameter, ϵ_f^p, is estimated by repeating the numerical calculations for the three sets of experiments, using both the shear-flow and the craze initiation and craze flow parameters estimated above, and adjusting the value of ϵ_f^p to match the failure portion of the load-displacement curves. Since craze-breakdown and fracture occur rather abruptly in the smooth-bar and notched-bar tension exper-

iments, the value of ϵ_f^p is best estimated from the notched compact-tension specimens because of the stable crack propagation observed in these experiments. A value of

$$\epsilon_f^p = 0.005$$

provides the best calibration to the load-displacement curves from the compact tension specimens.[16]

Using the material parameters for shear-flow, together with those for craze initiation, flow and break-down estimated above, Fig. F-11 shows the measured and numerically calculated load-displacement curves for a smooth-bar tension experiment. The load-displacement response is well captured by the model. *Note that the initial break in the numerical load-displacement curve is because of the onset of shear-flow, which precedes the craze-flow and fracture in PMMA.* Contour plots of the maximum principal stress σ_1, and the mean normal stress σ at a location just prior to peak load, are shown in Fig. F-12a and Fig. F-12b, respectively. Once the craze-breakdown conditions are met, the numerical simulation shows fracture at multiple locations, as indicated in the "failed" mesh of Fig. F-12c. This numerical result is consistent with the experimental observation that smooth-bar tension specimens fracture at multiple locations in the gauge section.

Fig. F-13 shows the measured and numerically-calculated load-displacement curves for a notched-bar tension experiment. Contour plots of σ_1 and σ at locations 1 and 2 on the numerical curve of Fig. F-13 are shown in Fig. F-14 and Fig. F-15, respectively. The contours in Fig. F-14 indicate that crazing initiates at the notch-root. Fig. F-15 shows that the craze front and the crack due to craze-breakdown propagate into

[16]In a remarkable set of experiments on specimens with near perfect surfaces and no trapped foreign particles (made from fibers drawn from individual polystyrene pellets), Argon & Hannoosh (1977) found that their PS specimens showed macroscopic inelastic deformation with a ductility of 5-8% (their Fig. 6). The macroscopic inelastic deformation was a result of extensive closely-spaced crazes ($\approx 10\,\mu$m apart) which produced whitening of the gauge section. Post-mortem microscopic examination revealed that the crazes were $\approx 0.5\,\mu$m wide. Based on a craze-width at craze-fracture of $\approx 0.5\,\mu$m, and a craze spacing of $\approx 10\,\mu$m, one obtains a macroscopic craze strain of $\approx 5\%$, as observed by Argon & Hannoosh (1977). The smaller value of $\epsilon_f^p = 0.5\,\%$ observed in our experiments is directly attributable to the imperfections and surface roughness effects in our macroscopic less well-controlled experiments.

the specimen in a direction perpendicular to the applied tensile load on the notched specimen.

Fig. F-16 shows the measured and numerically-calculated load-displacement curves for an experiment on a compact tension specimen. Contour plots of σ_1, σ, and ϵ^p at locations 1 and 2 on the numerical curve of Fig. F-16 are shown in Fig. F-17 and Fig. F-18, respectively. The contours in Fig. F-17 indicate that crazing initiates at the notch-root, and those in Fig. F-18 show that the craze front and the crack due to craze-breakdown propagate into the specimen in a direction perpendicular to the applied tensile load on the notched compact tension specimen. Note that fracture (as modeled by the element-removal technique) is confined to the elements adjacent to the symmetry plane of the simulation, and the contours of the craze strain ϵ^p in Fig. F-18c show that, while the elements adjacent to the traction-free crack face have suffered some craze-flow, they have not failed due to craze-breakdown.

Finally, in order to obtain the material parameter λ_f^p for ductile fracture, results from a plane strain compression experiment were utilized. In such an experiment crazing and craze fracture are inhibited, but ductile fracture in the material can still occur by the chain-scission mechanism at large values of λ^p. The full specimen geometry of 11.88 mm by 12.83 mm with a specimen thickness of 4.6 mm is modeled using a fine mesh of 3900 ABAQUS/CPE4R plane strain elements. The compression platens are modeled using rigid surfaces, and a coefficient of friction of 0.08 is assumed to model the interface friction between the lubricated PMMA and tool steel surfaces. The measured and calculated load-displacement curves[17] are shown in Fig. F-19; the point of ductile fracture initiation is also indicated. A contour plot of λ^p at ductile fracture initiation is shown in Fig. F-19b; this yields a value of

$$\lambda_f^p = 1.390,$$

for the initiation of ductile fracture.

[17]The experimental load-displacement curve has been corrected for machine and punch/die compliances.

2.4 Investigation of predictive capabilities of the model

In this section we investigate the accuracy of the numerical predictions from our calibrated model for PMMA. We study the deformation and fracture of three prototypical notched components: (a) a thin plate with a circular hole loaded in tension; and (b) blunt and a sharp-notched beams loaded in four point bending.

2.4.1 Tension of a thin plate with a circular hole

The specimen geometry for this experiment is shown in Fig. F-20a. The full three-dimensional geometry is modeled using 26,084 ABAQUS/C3D8R elements; a detail of the fine mesh in the vicinity of the hole is shown in Fig. F-20b. Fig. F-21 shows that the numerically-predicted load-displacement curve is in very good agreement with the one that was experimentally-measured. *Note that the load-displacement curve is non-linear, once again showing evidence of some shear-flow prior to crazing.* The specimen fractured at a displacement of about 1.4 mm into multiple pieces, and showed extensive crack-branching prior to final failure, Fig. F-22a.[18] A corresponding image from the numerical simulation is shown in Fig. F-22b.

Fig. F-23 and Fig. F-24 show contour plots of σ_1 and σ, respectively, at three instances keyed to the numerical load-displacement curve in Fig. F-21. At location 1, Fig. F-23a and Fig. F-24a, the stress distribution shows that a maximum value of $\sigma_1 = 74.7\,\text{MPa}$ and $\sigma = 26.8\,\text{MPa}$ occur at opposite edges of the hole. Since at $\sigma = 26.8$ MPa, the critical value of σ_1 is $\sigma_{1,cr} = 74.9$ MPa, the stress state at location 1 is just before that necessary to satisfy the craze-initiation criterion. By location 2, Fig. F-23b and Fig. F-24b, craze flow and fracture have occurred at opposite edges of the hole, as indicated by the removed elements.[19] At this location, the fracture

[18] Four different experiments were conducted, and the overall response from the different experiments was very similar, with the displacements at which fracture occurred varying by less than 4%.

[19] Recall that we are using an element removal technique to model fracture propagation.

process is seen to be symmetric about the window. However, by location 3, Fig. F-23c and Fig. F-24c, the cracks have branched away from the centerline of the specimen; this occurs because of small local numerical perturbations.

The numerical simulation nicely captures the major features observed in the physical experiment: (a) the non-linear load-displacement curve, (b) the process of crack initiation and propagation with crack-branching, and (c) fracture into multiple pieces.

2.4.2 Notched-beam bending

Four-point bending experiments were conducted on the specimen geometries used for PC testing shown in Fig. F-48. As indicated in the figure, specimens with a blunt notch of a root radius of 4.76 mm and specimens with a sharp notch of a root radius of 1.98 mm radius were tested. A specimen width of 50 mm was chosen so as to approximate plane strain conditions at the notch root. A four-point bending fixture was utilized with the specimen centerline coincident with the centerline of the fixture. The experiments were performed by displacing the center rollers relative to the outer rollers at a constant displacement rate of 2 mm/min. All rollers were constrained during the experiments to ensure that they did not rotate.

Bending of the blunt-notched beam

The load-displacement response for the blunt-notched specimen is shown in Fig. F-25; the experimental response of two specimens was repeatable to within 5%. The load-displacement curve is linear until a displacement of approximately 3.5 mm, at which point the curve deviates slightly from linearity. Failure occurs abruptly at a displacement of 3.6 mm. Fracture appears to initiate at the apex of the notch-root and the crack propagates along the specimen centerline. As well, a small ligament of material is seen at the top edge of the beam, which results from deflection of the craze front as it propagates into the compressive stress field at this location. Throughout most of the fractured specimen cross-section, evidence of fibrils was observed. The macroscopic observation is that the structure fails in a brittle manner as evidenced by the attainment of small plastic stretches prior to failure, and after initiation, the

crack propagates through the specimen cross-section in an unstable manner.

To simulate bending of the blunt-notched beam, the mesh shown in Fig F-51 is employed. The load-displacement curve from the numerical simulation is compared against the experimental response in Fig. F-25, where we note that the experimental response has been corrected for an estimated compliance of 0.57 mm/kN resulting from the loading system. The overall characteristics of the load-displacement curve and final failure are considerably well predicted by the constitutive model and the brittle fracture criterion. Granted that variations in the calibration experiments are on the order of 7 to 8%, the model prediction of the experimental load-displacement response is reasonable. We discuss errors associated with the beam bending experiments in the next section.

Four displacement levels of interest are marked on the numerical load-displacement curve shown in Fig. F-25. In Fig. F-26 and Fig. F-27 we show contour plots of the maximum principal stress σ_1 and the mean normal stress σ corresponding to these displacement levels:

- At location 1, Fig. F-26a and Fig. F-27a, the maximum positive values of σ_1 and σ are concentrated at the notch-root. The initiation criterion for craze-flow has not yet been satisfied.

- At location 2, Fig. F-26b and Fig. F-27b, the maximum value of σ is 32.6 MPa and since the maximum value of σ_1 at the notch-root just exceeds the critical value of $\frac{A}{\sigma} + B = 69.0$ MPa corresponding to σ, craze-flow initiates at the notch-root.

- At location 3, Fig. F-26c and Fig. F-27c, brittle fracture initiates at the notch-root since the maximum value of $\epsilon^p = \epsilon_f^p$. As indicated in the figures, an element at the notch-root which has failed due to the brittle mechanism has been removed from the mesh. Note as well that the craze-initiation criterion is met at locations ahead of the notch-root, and this local condition drives craze-flow into the beam along the specimen centerline, which is consistent with our experimental observations of the post-mortem specimen.

- By location 4, Fig. F-26d and Fig. F-27d, additional elements have undergone craze-flow and have subsequently failed due to the brittle fracture mechanism. At this location, the crack has propagated well into the specimen and the load has decreased significantly.

Bending of the sharp-notched beam

Fig. F-28 shows the load-displacement response when the sharp-notched beam is subjected to bending under the same loading conditions as were used for the blunt-notched beam. The experimental response of two specimens was repeatable to within 4%. The load-displacement response of the sharp-notched specimen is similar to that of the blunt-notched experiment, however there is no noticeable deviation from linearity of the load-displacement curve. The material fails abruptly at a displacement of 3.4 mm. The fracture surface and post-mortem specimen geometry are similar to that observed for the blunt-notched beam, where it was again observed that fracture occurs along the specimen centerline. The macroscopic observation is once again that the structure fails in a brittle manner, and after initiation, the crack propagates through the specimen cross-section in an unstable manner.

To simulate bending of the sharp-notched beam, the mesh shown in Fig F-56 is used. The load-displacement curve from the numerical simulation is compared against the experimental response in Fig. F-28. The numerically-predicted response is shown in Fig. F-28; the numerical curve under-predicts the load at fracture by about 20%. The reasons for this under-prediction are not known, but the fact that the actual loads are higher, indicates that crazing in the four-point notch-bend experiment initiates at higher levels of σ_1 and σ than those predicted by our curve fit for craze-initiation in PMMA, shown in Fig. F-10. We attribute the major reason for this discrepancy to the sensitivity of the craze-initiation criterion to various statistical effects such as material variability and surface finish that we have not fully-explored in our work.

In Fig. F-29 we show the experimental points for the initiation of craze-flow compared to the craze initiation line determined from our calibration experiments. The experimental points were found by conducting the beam bending simulations with craze-flow and fracture suppressed in the model. As can be seen from Fig. F-29, with

recourse to the scatter associated with each experiment, the model prediction of the initiation of craze-flow and subsequent brittle fracture is reasonable for the blunt and sharp-notched beam bending experiments.

The numerically predicted craze-flow and brittle fracture processes are quite similar to that observed for the case of the blunt-notched beam. For brevity, we show in Fig. F-30 the contours of σ_1 and σ at initiation of craze-flow followed by contours of σ_1 and σ once the crack has propagated along the specimen centerline and well into the beam. As can be seen from Fig. F-30a, the mean normal stress is concentrated at the notch root and reaches a maximum value of 33.4 MPa. The corresponding maximum principal stress attains a value of 68.8 MPa; this location corresponds to incipient craze-flow. Similarly to the blunt-notched beam results, craze-flow initiates at the notch-root and propagates into the beam along the specimen centerline, resulting in the failed mesh geometry shown in Fig. F-30b. Thus, similar to the case of the blunt-notched beam, in the sharp-notched beam the failure initiates due to the brittle fracture condition being satisfied at the notch root once craze-flow initiates, and the subsequent propagation of the crack occurs as the craze front propagates into the beam.

2.5 Concluding remarks

Most previous models for fracture of glassy polymers have been based on the standard framework of linear elastic fracture mechanics. This approach ignores the important details of the process of crazing in flexible chain glassy polymers, and it cannot be used when shear-yielding of the material may be occurring at other locations in the body, especially when there are no initial sharp cracks in the body. Although the phenomenon of crazing has been widely studied over the past four decades, and considerable understanding of the micro-mechanisms of crazing and cracking in amorphous polymers has been developed, the incorporation of this understanding into an engineering tool for the quantitative prediction of the deformation and fracture response of glassy polymers is just beginning to emerge. Of particular note is the recent work of

Van der Giessen and co-workers (Estevez et al., 2000; Tijssens et al., 2000a; Tijssens et al., 2000b), based on "cohesive surface" modeling of crazing. These authors used an elastic-viscoplastic traction-separation relation which accounts for the three separate stages of craze initiation, widening, and breakdown. While they have produced informative two-dimensional numerical simulations, much work remains to be done to correlate their parametric studies with actual experimental results. Here, instead of attempting to represent each individual craze with an interface element, we have developed a continuum-level model which contains the three ingredients of crazing — initiation, widening, and breakdown — in a suitable statistically-averaged sense. We have allowed for local inleastic deformation due to shear yielding in possible concurrence with that due to crazing, and introduced a craze initiation criterion based on the local maximum principal tensile stress reaching a critical value which depends on the local mean normal stress. After crazing has initiated, our continuum model represents the transition from shear-flow to craze-flow by a change in the viscoplastic flow rule, in which the dilational inelastic deformation associated with craze-plasticity is taken to occur in the direction of the local maximum principal stress. Finally, for situations in which the local maximum tensile stress is positive, craze-breakdown and fracture is taken to occur when a local tensile plastic craze strain reaches a critical value. We have implemented our constitutive model in a finite-element computer program. We have calibrated the constitutive parameters in our model for PMMA, and shown that our model, when suitably calibrated and implemented, is able to reasonably-well predict the macroscopic load-displacement curves, and local aspects of the craze-flow and fracture processes in two prototypical notched components made from this material.

In summary, we have attempted to develop the framework of an engineering tool for the quantitative prediction of the deformation and fracture response of glassy polymers. The results presented here represent a first step towards this goal. Much additional work needs to be performed for this framework to be more-fully fleshed out, and to be truly predictive. Some issues that need special further attention are (i) *Craze initiation*: The central ingredient in the continuum model for crazing is

the craze initiation criterion. It is well known that because of the importance of imperfections in controlling the local stress states and the sites of craze initiation, stress-based criteria for craze initiation are hard to determine with precision from experiments. Thus, much work needs to be done to elucidate the statistical aspects of craze intiation (and also craze breakdown). (ii) *Effects of strain rate, temperature and the environment*: The present research needs to be extended by conducting additional experiments at various strain-rates and temperatures. Further, we have limited our attention to normal dry conditions. It is well known that crazing is very sensitive to the environment, the effects of which need to be appropriately accounted for.

Chapter 3

Notch-sensitive fracture of polycarbonate

3.1 Introduction

Engineering thermoplastics such as polycarbonate which exhibit significant ductility, as evidenced by large strains to failure in smooth-bar tension or compression experiments, have been found to be significantly notch-sensitive, in that they exhibit a brittle mode of failure in notched specimens which generate a state of sufficiently large hydrostatic tension ahead of the notch (e.g. Ishikawa et al., 1977; Zuber, 1985; Nimmer & Woods, 1992; Narisawa & Yee, 1993). Experimental observations on notched specimens of polycarbonate tested in monotonic bending at moderately slow rates at room temperature show that (a) if the notch has a reasonably large root radius, then failure is initiated by ductile tearing at the notch root, while (b) if the notch has a relatively small root radius, then the failure initiates in the form of a crack-like feature *at the tip of the plastic zone surrounding the notch*, in the region of high hydrostatic tension (e.g., see Fig. 6 of Ishikawa et al., 1977; also see Figs. 15-5 and 15-61 of Narisawa & Yee, 1993). These crack-like features have been called *internal crazes* by Narisawa and his colleagues (e.g., Ishikawa et al., 1977; Narisawa & Yee,

1993)[1]. However, it is unclear whether the internal crack-like features observed at sharp notch-roots in polycarbonate exhibit the characteristic microstructural morphology in which the faces of the crack-like features are bridged by highly-oriented fibrils, as is typical for crazes in polymeric materials. Accordingly, here we refrain from calling these internal crack-like features crazes, and simply associate the initiation of such features at sharp notch-roots to be the outcome of internal cavitation in the material.

Many experiments indicate that a hydrostatic tension plays a key role in the nucleation of such an internal crack, and a critical value of the hydrostatic tension, σ_c, has been suggested as a suitable criterion for the nucleation of internal cracks (e.g. Ishikawa et al., 1977; Nimmer & Woods, 1992). For example, Narisawa and his colleagues have estimated σ_c for slow-cooled polycarbonate to be approximately 87-89 MPa; to obtain such an estimate they used classical slip-line field analysis, coupled with a measurement of the craze location below the notch-tip in three-point bending experiments[2]. A similar estimate of $\sigma_c \approx$ 90-100 MPa for polycarbonate has been obtained by Nimmer & Woods (1992); they performed a finite element analysis, using a non-hardening J_2-flow theory of plasticity, of a three-point bending experiment to determine the hydrostatic stress field at the instant when the corresponding physical experiment showed a load drop due to the initiation of an internal crack.

The purpose of this chapter is to develop a constitutive model and failure criteria which can capture the competition between the ductile mechanism of inelastic deformation by "shear-yielding" and the eventual ductile tearing, typically observed in amorphous thermoplastic materials under states of low triaxial tension, and the brit-

[1]They use this terminology to distinguish the internal crazes from *surface crazes*. Surface crazing is a complex phenomenon which is time and temperature-dependent, and the initiation of surface crazes is strongly affected by the environment, especially the presence of organic liquids. In contrast, the occurrence of internal crazes is due primarily to mechanical conditions, and the environment plays little or no role in their initiation and growth. However, unlike surface crazes which exhibit a microstructural morphology in which the craze faces are bridged by highly-oriented fibrils (c.f., Fig. 15-6 of Narisawa & Yee, 1993), post-mortem examination (e.g., Zuber, 1985) of the faces of the crack-like features of internal crazes observed in polycarbonate shows them to be relatively smooth and featureless, similar to cleavage facets in metallic materials.

[2]Estimates of σ_c for initiation of internal cracks in other amorphous glassy polymers are given in Table 15-1 of Narisawa & Yee, 1993.

tle internal cracking phenomenon that is observed in states of high triaxial tension. A significant advance in modeling the plastic deformation of amorphous polymers by "shear-yielding" has been made by Parks, Argon, Boyce, Arruda, and their co-workers (e.g. Parks et al., 1985; Boyce et al., 1988; Arruda & Boyce, 1993), and by Wu & Van der Geissen (1993). More recently, Anand & Gurtin (2002) have reformulated the theory within a rigorous thermodynamic framework, and introduced an internal-state variable in the theory to represent the local free-volume in the material to capture the highly non-linear stress-strain behavior that precedes the yield-peak and gives rise to post-yield strain-softening. We shall build on this model for plastic deformation of glassy polymers developed by the aforementioned authors. In particular, we shall extend the model to *allow for large local elastic volumetric changes*, and as a first attempt to model fracture in such materials we will introduce two simple local fracture criteria: (a) Brittle fracture will be taken to have occurred when a local elastic volumetric strain has reached a critical value. (b) Ductile fracture will be taken to have occurred when a local measure of plastic deformation, *an effective plastic stretch*, has reached a critical value. We shall show that the constitutive model and failure criteria, when suitably calibrated, are able to *quantitatively* predict the ductile failure response of blunt-notched beams, as well as the competition between the ductile and brittle mechanisms in more sharply-notched beams of polycarbonate in bending.

The plan of this chapter is as follows. In Section 3.2 we summarize our constitutive model and introduce local fracture criteria. In Section 3.3 we describe our experiments to calibrate the material parameters in the model. In Section 3.4 we compare our numerical predictions for (*i*) the deformation response of PC in simple and plane strain compression and (*ii*) both the deformation and failure response of a "blunt"-notched specimen geometry and a "sharp"-notched specimen geometry of polycarbonate under four-point bending. We close in Section 3.5 with some final remarks.

3.2 Constitutive equations for plastic deformation. Fracture criteria

In this section we begin by summarizing the constitutive model for plastic deformation of amorphous polymeric materials by the shear-yielding mechanism (Anand & Gurtin, 2002). The (isothermal) model is based on the mutliplicative decomposition, $\mathbf{F} = \mathbf{F}^e\mathbf{F}^p$, of the deformation gradient $\mathbf{F}$ into elastic and plastic parts, $\mathbf{F}^e$ and $\mathbf{F}^p$ (Kroner, 1960; Lee, 1969).[3] The theory also contains two internal variables: a variable $s > 0$ that represents an isotropic intermolecular resistance to plastic flow; and an unsigned variable η that represents the local free-volume.[4] Then, in terms of the variables

ψ,		Helmholtz free energy per unit volume of the relaxed configuration,
$\mathbf{T}$,	$\mathbf{T} = \mathbf{T}^\top$,	Cauchy stress,
$\mathbf{F}$,	$\det \mathbf{F} > 0$,	deformation gradient,
$\mathbf{F}^p$,	$\det \mathbf{F}^p = 1$,	plastic part of the deformation gradient,
s,	$s > 0$,	isotropic resistance to plastic flow,
η,		free-volume,

and the definitions

[3] *Notation*: ∇ and Div denote the gradient and divergence with respect to the material point $\mathbf{X}$ in the *reference configuration*; grad and div denote these operators with respect to the point $\mathbf{x} = \mathbf{y}(\mathbf{X}, t)$ in the deformed configuration, where $\mathbf{y}(\mathbf{X}, t)$ is the motion; a superposed dot denotes the material time-derivative. Throughout, we write $\mathbf{F}^{e-1} = (\mathbf{F}^e)^{-1}$, $\mathbf{F}^{p-\top} = (\mathbf{F}^p)^{-\top}$, etc. We write sym$\mathbf{A}$, skw$\mathbf{A}$, respectively, for the symmetric, and skew parts of a tensor $\mathbf{A}$. Also, the inner product of tensors $\mathbf{A}$ and $\mathbf{B}$ is denoted by $\mathbf{A} \cdot \mathbf{B}$, and the magnitude of $\mathbf{A}$ by $|\mathbf{A}| = \sqrt{\mathbf{A} \cdot \mathbf{A}}$.

[4] It is commonly believed that the evolution of the local free-volume is the major reason for the highly non-linear stress-strain behavior of glassy materials, which precedes the yield-peak and gives rise to the post-yield strain-softening.

$\mathbf{F}^e = \mathbf{F}\mathbf{F}^{p-1},\ \det \mathbf{F}^e > 0,$	elastic deformation gradient,
$\mathbf{C}^e = \mathbf{F}^{e\top}\mathbf{F}^e,$	elastic right Cauchy-Green strain,
$\mathbf{E}^e = \frac{1}{2}(\mathbf{C}^e - \mathbf{1}),$	elastic strain,
$\mathbf{T}^e = \mathbf{R}^{e\top}\mathbf{T}\mathbf{R}^e,$	stress conjugate to the elastic strain $\mathbf{E}^e$,
$\sigma = \frac{1}{3}\mathrm{tr}\mathbf{T},$	mean normal stress,
$\mathbf{T}^e_0 = \mathbf{T}^e - \sigma\mathbf{1},$	deviatoric stress,
$\mathbf{B}^p = \mathbf{F}^p\mathbf{F}^{p\top},$	left Cauchy-Green tensor corresponding to $\mathbf{F}^p$,
$\mathbf{B}^p_0 = \mathbf{B}^p - \frac{1}{3}(\mathrm{tr}\mathbf{B}^p)\mathbf{1},$	deviatoric part of $\mathbf{B}^p$,
$\lambda^p = \frac{1}{\sqrt{3}}\sqrt{\mathrm{tr}\mathbf{B}^p},$	effective plastic stretch,
$\mathbf{D}^p = \mathrm{sym}(\dot{\mathbf{F}}^p\mathbf{F}^{p-1}),\ \mathrm{tr}\mathbf{D}^p = 0,$	plastic stretching,

the constitutive equations, *under the approximative assumption of small elastic stretches*, are:

1. **Free Energy**:

   The Helmholtz free energy is taken in the noninteractive form

$$\psi = \psi^e(\mathbf{E}^e) + \psi^p(\lambda^p), \tag{3.1}$$

   where ψ^e is an elastic free energy, and ψ^p a plastic free energy. The elastic free energy is taken in the standard form for small elastic stretches

$$\psi^e = G|\mathbf{E}^e_0|^2 + \frac{1}{2}K|\mathrm{tr}\mathbf{E}^e|^2, \tag{3.2}$$

   where G and K are the elastic shear and bulk moduli, respectively. In amorphous polymeric materials the major part of ψ^p arises from an "entropic" contribution, and motivated by statistical mechanics models of rubber elasticity,[5]

[5]Cf., Treloar, 1975; Arruda & Boyce, 1993; Anand, 1996.

is taken in the specific form

$$\psi^p = \mu_R \lambda_L^2 \left[\left(\frac{\lambda^p}{\lambda_L} \right) x + \ln \left(\frac{x}{\sinh x} \right) - \left(\frac{1}{\lambda_L} \right) y - \ln \left(\frac{y}{\sinh y} \right) \right], \tag{3.3}$$

$$x = \mathcal{L}^{-1} \left(\frac{\lambda^p}{\lambda_L} \right), \qquad y = \mathcal{L}^{-1} \left(\frac{1}{\lambda_L} \right), \tag{3.4}$$

where $\mathcal{L}^{-1}$ is the inverse[6] of the Langevin function $\mathcal{L}(\cdots) = \coth(\cdots) - (\cdots)^{-1}$. This functional form for ψ^p involves two material parameters: μ_R, called the rubbery modulus, and λ_L, called the network locking stretch.

2. **Equation for the stress:**

$$\mathbf{T}^e = \frac{\partial \psi^e}{\partial \mathbf{E}^e} = 2G\mathbf{E}_0^e + K(\mathrm{tr}\mathbf{E}^e)\mathbf{1}. \tag{3.5}$$

3. **Equation for back stress:**[7]

$$\mathbf{S}_{\text{back}} = 2\mathrm{sym}_0 \left(\frac{\partial \psi^p}{\partial \mathbf{B}^p} \mathbf{B}^p \right) = \mu \mathbf{B}_0^p, \quad \text{with} \tag{3.6}$$

$$\mu = \frac{1}{3\lambda^p} \frac{\partial \psi^p}{\partial \lambda^p} = \mu_R \left(\frac{\lambda_L}{3\lambda^p} \right) \mathcal{L}^{-1} \left(\frac{\lambda^p}{\lambda_L} \right). \tag{3.7}$$

The back stress modulus $\mu \to \infty$ as $\lambda^p \to \lambda_L$, since $\mathcal{L}^{-1}(z) \to \infty$ as $z \to 1$.

4. **Flow rule:**

The evolution equation for $\mathbf{F}^p$ is

$$\dot{\mathbf{F}}^p = \mathbf{D}^p \mathbf{F}^p, \qquad \mathbf{F}^p(\mathbf{X}, 0) = \mathbf{1}, \tag{3.8}$$

[6]To evaluate $x = \mathcal{L}^{-1}(y)$ for a given y in the range $0 < y < 1$, we numerically solve the non-linear equation $f(x) = \mathcal{L}(x) - y = 0$ for x. For numerically intensive calculations we approximate the Langevin-inverse by the first 26 terms of its Taylor series expansion; see Appendix A.

[7]Also see Arruda & Boyce, 1993.

with $\mathbf{D}^p$ given by the flow rule

$$\mathbf{D}^p = \nu^p \left(\frac{\mathbf{T}_0^e - \mathbf{S}_{\text{back}}}{2\bar{\tau}} \right), \qquad \nu^p = \nu_0 \left(\frac{\bar{\tau}}{s - \alpha\sigma} \right)^{\frac{1}{m}}, \quad 0 < m \leq 1, \tag{3.9}$$

where

$$\bar{\tau} = \frac{1}{\sqrt{2}} |\mathbf{T}_0^e - \mathbf{S}_{\text{back}}|, \quad \text{and} \quad \nu^p = \sqrt{2}\, |\mathbf{D}^p|, \tag{3.10}$$

are an equivalent shear stress and equivalent plastic shear strain-rate, respectively. Here, ν_0 is a reference plastic shear strain-rate, α a pressure sensitivity parameter, and m a strain-rate sensitivity parameter. The limit $m \to 0$ renders (4.4) rate-independent, while $m = 1$ renders (4.4) linearly viscous. The equivalent plastic shear strain, γ^p, is defined by $\gamma^p = \int \nu^p \, dt > 0$.

5. **Evolution equations for the internal variables s and η:**

The evolution of s and η is taken to be governed by the coupled differential equations[8]

$$\left.\begin{aligned} \dot{s} &= h_0 \left(1 - \frac{s}{\tilde{s}(\eta)} \right) \nu^p, \qquad s(\mathbf{X}, 0) = s_0, \\ \dot{\eta} &= g_0 \left(\frac{s}{s_{\text{cv}}} - 1 \right) \nu^p, \qquad \eta(\mathbf{X}, 0) = 0, \end{aligned}\right\} \tag{3.11}$$

with

$$\tilde{s}(\eta) = s_{\text{cv}}[1 + b(\eta_{\text{cv}} - \eta)], \tag{3.12}$$

where $\{h_0, g_0, s_0, s_{\text{cv}}, b, \eta_{\text{cv}}\}$ are additional material parameters. Here $\tilde{s} = \tilde{s}(\eta)$ is a saturation value of s: $\dot{s}$ is positive for $s < \tilde{s}$ and negative for $s > \tilde{s}$. By definition ν^p is nonnegative. Assuming that $\nu^p > 0$, all solutions to the pair of

[8]We expect that $\tilde{s}$ (and perhaps h_0 and g_0) may, in general, depend on ν^p, but currently there is insufficient experimental evidence to warrant such a refinement.

evolution equations satisfy

$$s \to s_{\rm cv} \quad \text{and} \quad \eta \to \eta_{\rm cv} \quad \text{as} \quad t \to \infty.$$

We restrict attention to the initial conditions $s = s_0$ with

$$s_0 \leq s \leq s_{\rm cv}(1 + b\eta_{\rm cv}).$$

Also, as is tacit from $(3.11)_2$, the free-volume is measured from the value $\eta = 0$ in the virgin state of the material, and thus η at any other time represents a change in the free-volume from the initial state. Figure F-1 shows the evolution of s, $\tilde{s}$ and η with γ^p. We shall say that the flow has become "fully-developed" when $\eta \to \eta_{\rm cv}$ and $s \to s_{\rm cv}$.

3.2.1 Modification of the model for large elastic volume changes

As indicated previously, many experiments indicate that hydrostatic tension plays a key role in the nucleation of internal cracks. To accommodate this physical observation, we modify the elastic part of the constitutive model to allow for large elastic volume changes. Thus, instead of using the stress-strain pair

$$\mathbf{E}^e = \frac{1}{2}(\mathbf{C}^e - \mathbf{1}), \qquad \mathbf{T}^e = \mathbf{R}^{e\mathsf{T}}\mathbf{T}\mathbf{R}^e,$$

which is appropriate for small elastic stretches, we shall use the conjugate stress-strain pair

$$\mathbf{E}^e = \frac{1}{2}\ln \mathbf{C}^e, \qquad \mathbf{T}^e = (\det \mathbf{F}^e)\mathbf{R}^{e\mathsf{T}}\mathbf{T}\mathbf{R}^e, \tag{3.13}$$

which is appropriate for large elastic stretches in isotropic materials (Anand, 1979) to formulate the elastic stress-strain relations. Then denoting the volumetric and

deviatoric part of the logarithmic elastic strain $(3.13)_1$ by

$$\epsilon^e = \text{tr}\, \mathbf{E}^e, \qquad \mathbf{E}_0^e = \mathbf{E}^e - \frac{1}{3}\epsilon^e \mathbf{1}, \tag{3.14}$$

respectively, the elastic free energy is taken as[9]

$$\psi^e = G|\mathbf{E}_0^e|^2 + \left(K(\epsilon_c^e)^2\right)\left\{1 - (1 + \frac{\epsilon^e}{\epsilon_c^e})\exp\left(-\frac{\epsilon^e}{\epsilon_c^e}\right)\right\}, \tag{3.15}$$

where G, K, and ϵ_c^e are the shear modulus, the ground state bulk modulus, and a critical value of the elastic volumetric strain, respectively.

The conjugate stress $(3.13)_2$ is then given by

$$\mathbf{T}^e = \frac{\partial \psi^e}{\partial \mathbf{E}^e} = 2G\mathbf{E}_0^e + \left\{K \exp\left(-\frac{\epsilon^e}{\epsilon_c^e}\right)\right\}\epsilon^e \mathbf{1}. \tag{3.16}$$

and in this case the mean normal stress $\sigma = (1/3)\,\text{tr}\,\mathbf{T}^e$ is

$$\sigma = \left\{K \exp\left(-\frac{\epsilon^e}{\epsilon_c^e}\right)\right\}\epsilon^e. \tag{3.17}$$

Hence, the generalized bulk modulus in this constitutive model is

$$\tilde{K} = \frac{\partial \sigma}{\partial \epsilon^e} = K\left\{1 - \frac{\epsilon^e}{\epsilon_c^e}\right\}\exp\left\{\frac{\epsilon^e}{\epsilon_c^e}\right\}, \quad \text{with} \quad \tilde{K} \to K, \quad \text{as} \quad \epsilon^e \to 0. \tag{3.18}$$

Equation (3.17) for the mean normal stress σ may be rewritten as

$$\sigma = \sigma_c \left(\frac{\epsilon^e}{\epsilon_c^e}\right)\exp\left\{1 - \frac{\epsilon^e}{\epsilon_c^e}\right\}, \quad \text{where} \quad \sigma_c \equiv \frac{K\epsilon_c^e}{e}, \tag{3.19}$$

and e is the Neperian/Euler number. A plot of (σ/σ_c) versus $(\epsilon^e/\epsilon_c^e)$, Fig. F-31, clearly shows that σ attains a maximum value σ_c, when $\epsilon^e = \epsilon_c^e$. The quantity σ_c represents the *cavitation strength* of the material. Note that for most practical purposes the material loses any stress-carrying capacity when $\epsilon^e \geq (4 \text{ to } 10) \times \epsilon_c^e$.

[9]The form for the volumetric response is motivated by the Universal Binding Energy Relation (UBER) introduced by Rose et al. (1983) in a one-dimensional context of separation between atomic planes in metals.

Also note that the integral

$$\Gamma_C = \int_0^\infty \sigma d\epsilon^e = e\,\sigma_c\,\epsilon_c^e = K(\epsilon_c^e)^2, \tag{3.20}$$

represents a *cavitation fracture energy* per unit volume of the relaxed configuration.

In order to model fracture in polycarbonate we introduce two simple local fracture criteria:

1. Brittle fracture will be taken to occur when a local elastic volumetric strain ϵ^e reaches a failure value ϵ_f^e:

$$\epsilon^e \leq \epsilon_f^e. \tag{3.21}$$

2. Ductile fracture will be taken to occur when the effective plastic stretch λ^p reaches a critical value λ_f^p:

$$\lambda^p \leq \lambda_f^p. \tag{3.22}$$

We have implemented our constitutive model in the finite-element computer program ABAQUS/Explicit (ABAQUS, 2001) by writing a user material subroutine. This finite-element program permits the modeling of failure, when user-specified critical values of certain parameters are reached, by an element removal technique.

3.3 Estimation of material parameters for PC

As is well known, the mechanical response of amorphous thermoplastics is very sensitive to prior thermo-mechanical processing history. In our work, all experiments were conducted on specimens which were annealed at the glass transition temperature of the material, T_g = 145°C, for 2 hours, and then furnace-cooled to room temperature in approximately 15 hours. All experiments reported here were conducted under isothermal conditions at room temperature.

A representative true stress-true strain curve obtained from a simple compression experiment[10] conducted at a constant true strain rate of -0.001/s is shown in Fig. F-32. After an initial approximately linear region, the stress-strain curve becomes markedly nonlinear prior to reaching a peak in the stress; the material then strain-softens to a quasi-plateau before beginning a broad region of rapid strain hardening. While the existing models (e.g. Arruda & Boyce, 1993) account reasonably well for the large strain strain-hardening regime, they do not adequately capture the pre-peak nonlinearity and the subsequent strain softening,[11] a "transient response" which is not negligible, since the transient typically lasts for strain levels of $\approx$ 25 percent.

Various investigators have typically attributed the pre-peak nonlinearity to some sort of time-dependent recoverable "viscoelastic" response. To verify this conjecture, we performed some *plane strain tension* experiments in which the strains could be accurately measured using a sensitive extensometer. The engineering stress-engineering strain response[12] for a specimen loaded through its peak stress is shown in Fig. F-33. Note that the features of the stress-strain curve prior to the peak are similar to those observed in simple compression, Fig. F-32. The response in tension deviates from linearity at a stress level of $\approx$ 21 MPa and progresses in a nonlinear fashion to a peak stress of $\approx$ 56 MPa at a strain of $\approx$ 0.04. Five additional experiments were performed to stress levels below the peak value, and the specimens were subsequently unloaded, Fig. F-34; the resulting residual strains upon unloading from each stress level are also indicated in this figure. Note that there is a clear trend of increasing residual strain upon unloading from increasing stress levels in the non-linear pre-peak regime. To test how much of this residual strain is recovered at zero load, the testing machine was set to load-control after unloading each specimen, and the extensometer response was monitored. The specimens exhibited only a very small amount of recovery at zero load over a time period of about one hour; for example, the specimen

[10]The data has been corrected to account for compliance contributions from the loading system.

[11]See Hasan and Boyce (1995) for a viscoelastic-viscoplastic formulation which is capable of capturing the pre-peak nonlinearity and post-peak strain softening response of glassy polymers.

[12]Here, the engineering stress and engineering strain are used, because the specimen "necks" in tension, and the subsequent response becomes inhomogeneous.

unloaded from just prior to the peak recovered a strain of 0.09% in one hour out of an initial residual strain of 0.22%. Accordingly, for present purposes, we will neglect this small recovery at zero loads, and consider the measured residual strains after unloading as *plastic* strains. Thus, unloading from the initial approximately linear region[13] produces essentially no residual plastic strains and the response is considered to be "elastic", whereas unloading from any stress level above the stress at which the stress-strain curve deviates from initial linearity, produces residual plastic strains, and the response is considered to be "plastic".

With this as background, we discuss below the results of our efforts at estimation of the material parameters for our constitutive model, and also the failure values for the brittle and ductile fracture criteria. Recall that the material parameters that need to be determined are

1. The elastic shear and bulk moduli (G, K), and the critical value of the elastic volumetric strain ϵ_c^e in the elastic part of the free energy.

2. The parameters (μ_R, λ_L) in the plastic part of the free energy.

3. The parameters $\{\nu_0, m, \alpha, s_0, h_0, g_0, s_{cv}, b, \eta_{cv}\}$ in the flow rule and the evolution equations for (s,η).

4. The parameters ϵ_f^e and λ_f^p in the failure criteria.

The values of (G, K) are determined by measuring the Young's modulus and Poisson's ratio of the material in a compression experiment and using standard conversion relations of isotropic elasticity to obtain the elastic shear and bulk moduli. The parameters (ν_0, m) in the flow function are determined from a strain rate increment test in simple compression. The parameter α in the flow function is obtained by conducting tension or compression tests under various levels of imposed hydrostatic pressures. The parameters $\{h_0, g_0, s_{cv}, b, \eta_{cv}, s_0\}$ and (μ_R, λ_L) may be estimated by fitting a stress-strain curve in compression to large strains. The parameter λ_f^p for

[13]Within the accuracy of our strain-measuring techniques.

ductile failure is obtained by fitting a load-displacement curve obtained from a specimen which has been extended to failure in tension. And finally, the value of $(\epsilon_c^e, \epsilon_f^e)$ may be estimated from a load-displacement curve from a sharply notched-bar tension specimen extended to failure in tension.

An experimental result from a strain rate jump experiment on PC conducted in simple compression is shown in Fig. F-35. As the true strain rate is "instantaneously" increased from -0.001/s to -0.01/s, the response shows a transient peak which saturates to a steady-state value. Assuming that the deformation resistance s remains constant and neglecting the change in the term $\alpha\sigma$ as the increment is imposed, the relation for the equivalent plastic shear strain rate, Eq. 4.4_2, may be used to find $\{\nu_0, m\}$. The determination of ν_0 and m is shown graphically in Fig. F-36. Using these values, and a value of $\alpha = 0.08$ from the data reported by Spitzig & Richmond (1979), the parameters $\{G, K, \mu_R, \lambda_L, h_0, g_0, s_{cv}, b, \eta_{cv}, s_0\}$ are estimated by fitting a stress-strain curve for PC in simple compression, Fig. F-32.[14] The fit was performed by judiciously adjusting the values of these parameters in finite element simulations of a simple compression experiment using a single ABAQUS/C3D8R element. After multiple attempts, a reasonable fit was obtained, and this is shown in Fig. F-37. The list[15] of parameters obtained using this heuristic calibration procedure are:

$G = 0.857$ GPa	$K = 2.24$ GPa	$\mu_R = 11.0$ MPa	$\lambda_L = 1.45$
$\nu_0 = 0.0017$ s^{-1}	$m = 0.011$	$\alpha = 0.080$	
$s_0 = 20.0$ MPa	$s_{cv} = 24.0$ MPa	$h_0 = 2.75$ GPa	
$b = 825$	$g_0 = 6.0 \cdot 10^{-3}$	$\eta_{cv} = 0.001$	

In order to estimate the value of the parameter λ_f^p for ductile failure, we conducted several tension experiments. The experiments were performed under displacement control at 0.0125 mm/s on specimens with a gauge section of initial diameter of 6.35 mm, and length of 25.4 mm. A representative experimentally-measured load-displacement response is shown in Fig. F-38. At the peak load of about 2.3 kN, a pronounced neck forms in the gauge section, and the load subsequently decreases to

[14] See Appendix B for a guideline to calibration of the model.

[15] This list, although not unique, is adequate for present purposes.

an approximate plateau value of 1.6 kN. The neck then propagates along the gauge section until a displacement of 15.8 mm is reached. At the maximum displacement, the entire section over which the neck has propagated develops a profuse number of ring cracks around the circumference, and final separation occurs somewhere in the necked region. To check the repeatability of the failure response, five identical specimens were tested; the measured displacements at fracture varied less than 5%.

To numerically model a tension experiment, one half of a specimen was meshed with 390 ABAQUS/CAX4R axisymmetric elements. The constitutive parameters used in the simulation are those obtained from the fitting exercise for the compression experiments, and in this calibration step, the only adjustable parameter is the failure value of the effective plastic stretch, λ_f^p; this was adjusted to match the final displacements to "ductile" fracture. The fit shown in Fig. F-38 is obtained with

$$\lambda_f^p = 1.192.$$

Note that prior to the final ductile fracture, the load-displacement response from the numerical simulation shown in Fig. F-38 constitutes a prediction for this response. Contour plots of the effective plastic stretch λ^p are shown in Fig. F-39a,b,c at the three displacement levels which have been marked by arrows in Fig. F-38. As can be seen from the contour plots, the deformation is homogeneous until the peak load, location 1, is attained at a maximum value of λ^p of 1.003. Subsequent to the peak load, a localized neck forms at the center of the gauge section, location 2, and here the maximum value of λ^p reaches 1.120. As the neck propagates along the gauge section, λ^p continues to increase until it reaches a maximum value of 1.192, at location 3, at which stage ductile fracture occurs.

To complete the calibration procedure one needs to determine the remaining parameters $\{\epsilon_c^e, \epsilon_f^e\}$. To do this, notched-bar tension experiments were conducted. In such experiments a state of high mean normal stress is generated ahead of the notch, and brittle fracture is expected to occur if the notch is sufficiently sharp. The specimen geometry chosen to achieve this goal is a 12.7 mm cylindrical bar with a notch of

3.18 mm depth and 1.80 mm width; the radius at the notch root is 0.90 mm. An extensometer was used to measure the local relative displacement across the notch as the specimen was extended at a rate of 0.0125 mm/s. A representative experimentally-measured load-displacement response curve is shown in Fig. F-40. The specimen fails abruptly at a displacement of about 0.4 mm. The fracture surfaces show a smooth region with an rms roughness of 43 nm ahead of the notch root, indicative of a "brittle" mechanism of failure, together with an indication of a moreductile failure response at the notch root. In order to check the repeatability of the fracture response, five specimens were tested and the measured displacements at fracture were found to vary by less than 4%.

To numerically model a notched-bar tension experiment, one half of the specimen was meshed with 390 ABAQUS/CAX4R axisymmetric elements. We note that in this calibration step, the only adjustable parameters are $\{\epsilon_c^e, \epsilon_f^e\}$. Since, $\epsilon_c^e = (\sigma_c e)/K$, and the value of $K = 2.24\,\text{GPa}$ has been fixed, we adjust the value of σ_c and the ratio $\chi_f = \epsilon_f^e/\epsilon_c^e$, to fit the experimental load-displacement curve. The quality of the fit with the values[16]

$$\sigma_c = 83.5 \quad \text{MPa} \qquad \text{and} \qquad \chi_f = 4.0,$$

is shown in Fig. F-40. These values for $\{\sigma_c, \chi_f\}$ correspond to

$$\epsilon_c^e = 0.1013, \quad \text{and} \quad \epsilon_f^e = 0.4053.$$

Shown in Fig. F-41 are contour plots of the mean normal stress σ at two different displacement levels indicated by arrows in Fig. F-40. During the initial linear loading stage, σ is maximum at the root of the notch, as can be observed in Fig. F-41a. As deformation progresses, the load-displacement response becomes nonlinear, a plastic zone develops at the notch root, and the maximum value of σ becomes concentrated ahead of the zone of plastic deformation. Brittle fracture eventually initiates in the region of high triaxiality, and the crack propagates across the specimen. This response

[16]Note that this value of σ_c for polycarbonate is very similar to the value previous estimated by Narisawa and his colleagues, e.g. Narisawa & Yee (1993).

is consistent with the experimentally-observed mostly "brittle" fracture surface.

The parameters obtained from these three calibration steps complete the material parameter determination for PC. In the next section, we use the calibrated model to: (*i*) investigate the predictive capability of the model for the finite deformation response of PC in simple compression with monotonic loading/unloading and plane strain compression; (*ii*) compare numerical predictions for both the deformation and failure response in four-point bending of a "blunt"-notched specimen geometry and a "sharp"-notched specimen geometry against corresponding physical experiments.

3.4 Investigation of predictive capabilities of the model

3.4.1 Compression experiments

The purpose of this section is to illustrate some of the finite deformation features that our constitutive model is able to capture. In particular, we show model predictions for (*i*) the reverse yield effect observed upon unloading in simple compression experiments and (*ii*) the development of shear bands observed in plane strain compression experiments.

Simple compression

In the previous chapter, the material parameters for the finite deformation response were found by calibration to a monotonic compression experiment, where the effects of the back stress are manisfest in the resulting stress-strain curve. Upon elastic unloading, the existence of the back stress is observed as the cause of the so-called reverse yield effect. To investigate the extent of reverse yield with increasing strains, we performed simple compression experiments with a crosshead velocity of 0.0125 mm/s to a true strain of 17%, 59%, and 90% followed by unloading at the same displacement rate. The experimental stress-strain curves are shown in Fig. F-42, where a clear trend of an increasing extent of reverse yield with increasing strain is observed.

In order to model the compression experiment, we assume that the deformation is homogeneous and use a single ABAQUS/C3D8R element. The numerically predicted stress-strain curves are shown in Fig. F-43 for each experiment. As can be seen from the numerical curves, unloading in the experiments conducted to strains of 17% and 59% is predominantly elastic, with the reverse yield observed in the experiments under-predicted by the model. However, the model prediction of the experiment conducted to a strain level of 90% reasonably predicts both the stress level for yield upon unloading as well as the general curvature observed in the experiment during reverse yield.

Considering that the material parameters are determined from a monotonic compression experiment, the capability of the model to predict the features of reverse yield upon unloading is impressive.

Plane strain compression

The predictive capabilities of the model are further demonstrated by an investigation of plane strain compression experiments. A plane strain die set made of D2 tool steel was used to conduct plane strain compression experiments on PC at a constant true strain rate of -0.001/s. The resulting stress-strain curve assuming that the deformation is homogeneous is shown in Fig. F-44, where a simple compression experiment and the corresponding model fit are shown for comparison. A single ABAQUS/C3D8R element is used to model the plane strain compression experiment. As can be seen from the prediction of the plane strain compression curve in Fig. F-44, the model accurately predicts the peak stress and reasonably captures the full range of the stress-strain response.

It should be emphasized that these results for plane strain compression assume that the overall deformation is homogeneous. However, a post-mortem investigation of the specimen clearly reveals that the deformation is in fact non-homogeneous. In particular, evidence of shear bands throughout the specimen indicate that the deformation is a more complicated process. In order to demonstrate this important point, we have conducted two additional plane strain compression experiments uti-

lizing a specimen geometry with a gauge length of 12.4 mm and a cross-sectional area of 4.6 mm x 26 mm, with 4.6 mm in the constraint direction. The experiments were conducted at a cross-head velocity of 0.0125 mm/s, and the specimens were unloaded at the same rate. The experimental results are shown in Fig. F-45, where we have plotted the load-displacement curves to emphasize that the deformation is non-homogeneous. After testing, the specimens were carefully sectioned in half in the direction perpendicular to the constraint direction. The sectioned pieces were then polished down to a 1 μm alumina slurry in tap water and viewed through polarizers using a digital camera with a fiber optic light source. The experimental specimens corresponding to locations "A" and "B" of Fig. F-45 are shown in Fig. F-46 and Fig. F-47, respectively, where the loading axis is in the vertical direction. The figures indicate that at the initial location "A" of Fig. F-45 three pronounced sets of conjugate bands have formed throughout the specimen cross-section. Shear bands initiate from the edges due to the frictional effects in the experiments and a conjugate set of bands is observed in the center section, where the edge effects on the deformation should be minimized. The orientation of the bands with respect to the loading axis is $\pm 40.8°$. At location "B" of Fig. F-45, the orientation of the initial shear bands is seen to have evolved with the deforming background field, while new sets of bands have initiated with approximately the same orientation of $\pm 40.8°$ observed for the intial bands.

The experiments are modeled using a fine mesh of 3526 ABAQUS/CPE4R elements in order to accurately capture the details of the deformation process. The contact between the dies and the specimen are modeled by using analytical rigid surfaces and a coefficient of friction of 0.08 was assumed to model the inevitable effects of friction between the lubricated PC and tool steel. In order to constrain the specimen, a single node in the center of the bottom edge of the mesh is held fixed. The numerically predicted load-displacement curves are shown against the experiments in Fig. F-45, where the model prediction is observed to be reasonable.

The simulation results for unloaded specimens at locations "A" and "B" of Fig. F-45 are shown in comparison to the experimental specimens in Fig. F-46 and Fig. F-

47, respectively. In Fig. F-46, contour plots of the equivalent plastic shear strain γ^p indicate that the distinct nature of the bands[17] as well as the measured orientation of $\pm 42.6°$ to the loading axis are in good accord with the experimental results. The predicted bands in Fig. F-47 are seen to be diffuse in nature with an indication of initial bands that have deformed with continued deformation. The orientation of the bands is again in good accord with the experiment. As well, the overall morphology of the specimen is well-captured by the model. Clearly, the deformation process in plane strain compression is non-homogeneous.

We now investigate the predictive capability of our new constitutive model and fracture criteria for experiments involving brittle and ductile fracture.

3.4.2 Notched-beam bending

Four-point bending experiments were conducted on the specimen geometries shown in Fig. F-48. As indicated in this figure, specimens with a blunt notch of a root radius of 4.76 mm and specimens with a sharp notch of a root radius of 1.98 mm radius were tested. A specimen width of 50 mm was chosen so as to approximate plane strain conditions at the notch root. A four-point bending fixture was utilized with the specimen centerline coincident with the centerline of the fixture. The experiments were performed by displacing the center rollers relative to the outer rollers at a constant displacement rate of 2 mm/min. All rollers were constrained during the experiments to ensure that they did not rotate.

Bending of the blunt-notched beam

The load-displacement response for the blunt-notched specimen is shown in Fig. F-49. Three displacement levels of interest are marked on the load-displacement curve. Fig. F-50a,b,c show three micrographs, corresponding to the indicated displacement levels, of the specimen cross-section ahead of the notch. The micrographs were taken in the unloaded configuration from polished cross-sections of the specimen. The image

[17] We note that the width of the shear band is determined by the element size since the localization process occurs over a characteristic length scale.

taken at location 1 shows that a zone of plastic deformation (by the shear-yielding mechanism) has developed at the notch root. At location 2, the plastic zone has extended a significant distance through the thickness of the specimen, and plastic-deformation is also seen to have occurred at the back-face of the specimen. The abrupt drop in the load-displacement curve indicates the initiation of failure; this event is due to the nucleation of a crack at the notch root, and once the crack nucleates, it propagates in a stable manner through the thickness of the specimen. The crack is clearly visible in the micrograph corresponding to location 3. Thus, for the case of the blunt-notched specimen in bending, the macroscopic observation is that the structure fails in a ductile manner as evidenced by the attainment of large plastic stretches prior to crack initiation, and after initiation the crack propagates in a stable manner until final fracture.

To simulate bending of the blunt-notched beam, one-half of the beam is modeled using 1509 ABAQUS/CPE4R plane strain elements with reduced integration. A detail of the finite-element mesh and the mesh at the notch root are shown in Fig. F-51. The load-displacement curve from the numerical simulation is compared against the experimental response in Fig. F-52. A large part of the difference between the numerically-calculated and experimentally-measured curves is attributable to machine compliance effects of the bending apparatus. The overall characteristics of the load-displacement curve and final failure are reasonably well predicted by the constitutive model and the ductile fracture criterion.

Four displacement levels of interest are marked on the numerical load-displacement curve shown in Fig. F-52. In Fig. F-53 we show contour plots of the effective plastic stretch λ^p corresponding to these displacement levels:

- At location 1, Fig. F-53a, just prior to the initial peak on the load-displacement curve, a small plastic zone has developed around the notch root, and λ^p has a maximum value at the notch root of 1.014. This is physically similar to the plastic zone seen in Fig. F-50a at an approximately similar location on the load-displacement curve of the physical experiment.

- At location 2, Fig. F-53b, the plastic zone at the notch root has grown in size, with a maximum value of $\lambda^p = 1.110$ at a position slightly offset from the notch root; the back-face has deformed plastically. These features are physically similar to the plastic zone seen in Fig. F-50b at an approximately similar location on the load-displacement curve of the physical experiment.

- At location 3, Fig. F-53c, the plastic zone at the notch root has grown further in size. The effective plastic stretch has reached a maximum value of 1.192, which is equal to the failure value of λ_f^p, and ductile failure is seen to initiate at an element slightly offset from the centerline notch root. Recall that we are modeling failure by the element removal technique.

- By location 4, Fig. F-53d, additional elements have reached the ductile fracture condition $\lambda^p = \lambda_f^p$, and the corresponding elements have been removed. As the ductile failure process progresses from location 3 to location 4, the "crack" propagates both towards the specimen centerline and into the beam, as indicated in Fig. F-53d. These features of ductile fracture are physically similar to those seen in Fig. F-50c at an approximately similar location on the load-displacement curve of the physical experiment.

Bending of the sharp-notched beam

Fig. F-54 shows the load-displacement response when the sharp-notched beam is subjected to bending under the same loading conditions as were used for the blunt-notched beam. The initial load-displacement response of the sharp-notched specimen is similar to that of the blunt-notched experiment; here, however, the material fails abruptly at a displacement of 12.4 mm. An investigation of the fracture surface where the crack initiates reveals a surface roughness which varies in the nanometer range[18]; this indicates a fracture initiation mechanism which is "brittle" in nature. A separate experiment was conducted and stopped just prior to the point of fracture. An image of the polished cross-section is shown in Fig. F-55. Note that in addition

[18]The measured rms surface roughness is 43 nm.

to the shear-yielding plastic zone, one clearly sees a crack-like feature at the tip of the plastic zone[19]. For more exhaustive experimental observations of such features in sharp-notched beams, see Ishikawa et al. (1977) and Zuber (1985). The fracture surface of the beam shows a smooth surface ahead of the notch root and into the cross-section, indicative of brittle fracture, and also a small ligament at the notch root which appears to have failed in a ductile manner.

To simulate bending of the sharp-notched beam bending, one-half of the beam is modeled using 1370 ABAQUS/CPE4R plane strain elements with reduced integration. A detail of the finite-element mesh for the beam and a close-up of the fine mesh employed at the notch root is shown in Fig. F-56a and Fig. F-56b, respectively. Note that the mesh is refined at the contact locations with the rigid rollers in order to minimize contact noise in the simulation. The load-displacement curve from the numerical simulation is compared against the experimental response in Fig. F-57. The experimental curve has been corrected for an estimated machine and bending rig compliance of 0.57 mm/kN.

Four displacement levels of interest are marked on the numerical load-displacement curve shown in Fig. F-57. In Fig. F-58 and Fig. F-59 we show contour plots of the mean normal stress σ, and the effective plastic stretch λ^p corresponding to these displacement levels:

- At location 1, Fig. F-58a and Fig. F-59a, the maximum value of $\sigma = 82.1$ MPa occurs at a location just ahead of the notch root, while λ^p has a low value of only 1.100 at a location slightly offset from the notch root. Since the cavitation strength is $\sigma_c = 83.5$ MPa, location 1 is at a state of incipient brittle fracture.

- At location 2, Fig. F-58b and Fig. F-59b, we observe that brittle fracture has initiated at a location ahead of the plastic zone at the notch root. Comparison of the location of brittle fracture initiation with the micrograph in Fig. F-55 indicates that the model accurately predicts the initiation site of brittle fracture.

[19]Minor experimental misalignment may have offset the crack slightly from the loading centerline.

- By location 3, Fig. F-58c and Fig. F-59c, the "crack" has extended deeper through the thickness of the specimen, but by now the remaining ligament between the crack and the free-surface of the notch has also been sufficiently plastically stretched to initiate ductile fracture at the free surface of the notch root.

- By location 4, Fig. F-58d and Fig. F-59d, the remaining ligament has failed completely by the ductile mechanism, and the crack has propagated further in a brittle fashion through the thickness of the beam. During this stage of the process, the values of λ^p remain below the critical value, as indicated in Fig. F-59d.

Thus, in the sharp-notched beam the failure initiates due to the brittle fracture condition being met ahead of the plastic zone at the notch root, and the subsequent propagation of such a crack occurs by a competition between the brittle and ductile criteria being satisfied at different locations along the crack, depending on the local nature of the triaxiality constraints along the crack fronts. Our new constitutive model and fracture criteria capture the intricate interplay of both the brittle fracture and ductile failure mechanisms, and provide a reasonable prediction of the load-displacement response of the sharp-notched PC beam in four-point bending.

3.5 Concluding remarks

We have developed a constitutive model and fracture criteria which can capture the competition between the ductile mechanism of inelastic deformation by "shear-yielding" and eventual ductile tearing, typically observed in amorphous thermoplastic materials under states of low triaxial tension, and the "cracking" phenomenon that is observed in states of high triaxial tension. Our constitutive model builds upon the recent theory of Anand & Gurtin (2002) for plastic deformation of amorphous polymeric materials. Our extensions consist of (a) generalizing the theory to allow for large elastic volume changes; (b) introducing a brittle fracture criterion based

on the local elastic volumetric strain reaching a critical value; and (c) introducing a ductile fracture criterion based on an effective plastic stretch reaching a critical value. We have shown that the constitutive model and failure criteria, when suitably calibrated, are able to *quantitatively* predict the ductile failure response of blunt-notched beams of polycarbonate in bending, as well as the competition between the ductile and brittle mechanisms in more sharply-notched beams.

We recognize that our numerical modelling of the ductile and brittle fracture processes is "mesh-sensitive," and much needs to be done to refine the mesh (amongst other considerations) to be able to better represent such fracture processes. However, as a first attempt to model such highly nonlinear fracture processes in polymers, we consider that the proposed constitutive model and failure criteria adequately capture the competition between the ductile and brittle mechanisms of fracture initiation and propagation.

The present research needs to be extended by conducting more detailed experiments at various temperatures and strain-rates to see if the failure criteria continue to have predictive capabilities under different temperature and strain rate conditions,[20] and by conducting experiments on specimen geometries that might exhibit an even more complicated interplay between the ductile and brittle fracture mechanisms. In addition, statistical aspects of fracture criteria also need to be elucidated.

[20]The experiments of Narisawa and his colleagues (as summarized in Narisawa & Yee, 1993) indicate that the value of σ_c for polycarbonate is approximately independent of strain rate over a range of rates varying from 10^{-4} to 10^{-1} per second. However, given the strong dependence of the elastic moduli on temperature, we expect that the value of σ_c will decrease with increasing temperature (in this respect, the recent work of Johnson (2001) provides useful experimental results on fracture of notched-bars of PC under various loading rates and ambient temperatures). Thus, any adiabatic heating effects at higher strain rates are also expected to lower the value of σ_c.

Chapter 4

Micro-indentation of amorphous polymeric solids

4.1 Introduction

The development of very low-load depth-sensing indentation instruments, over the past twenty years or so, which allow one to make indents as shallow as a few nanometers, make these instruments particularly well-suited for indentation experiments on materials available only in small volumes, such as thin coatings (e.g., Pethica et al., 1983; Oliver & Pharr, 1992). Since these instruments allow one to continuously record both load, P, down to micro-Newtons, and indentation depths, h, down to nanometers during the indentation cycle, results from such nano/microindentation experiments hold the promise of the *in situ* estimation of mechanical properties of materials from the measured P-h curves.

Indentation experiments have long been used to measure the hardness of materials. Interest in instrumented indentation experiments as a means to estimate a wide variety of other mechanical properties (e.g, elastic moduli, yield strength, strain-hardening characteristics, residual stresses, and fracture toughness – for very brittle materials) has grown rapidly in recent years. It is clear from the recent literature (e.g., Giannakopoulos et al., 1994; Larsson et al., 1996; Dao et al., 2001), that the problem of estimating material properties from experimentally-measured P-h curves,

depends crucially on the availability of a large catalog of numerically calculated P-h curves, the attendant details of the time-varying "true projected contact areas", "pile-up/sink-in profiles", and stress and strain distributions in the inhomogeneously deforming volume of material under the indenter. Since in typical ductile metallic materials the plastic strain levels under sharp indenters exceed ≈ 0.15 in the majority of the plastically deforming volume directly beneath an indenter, and can reach as high as ≈ 1.5 just beneath the indenter tip (see, e.g., Fig. 6 of Dao et al., 2001) the numerical simulations of indentation need to be performed with accurate large deformation constitutive models for the material being indented. With a focus on *metallic materials*, most of the recent analyses of indentation (e.g., Cheng & Cheng, 1998; Cheng & Cheng, 1999; Dao et al., 2001) have been performed using a large deformation version of the classical isotropic, rate-independent, elasto-plastic J_2 flow theory,[1] in which the strain-hardening during plastic deformation is modeled by a flow condition of the form

$$\bar{\sigma} = Y(\bar{\epsilon}^p), \quad \text{with} \quad Y(\bar{\epsilon}^p) = \sigma_y \left(1 + \frac{\bar{\epsilon}^p}{(\sigma_y/E)}\right)^n, \tag{4.1}$$

where in standard notation, $\bar{\sigma}$ is the Mises equivalent tensile stress, $\bar{\epsilon}^p$ is the equivalent tensile plastic strain, σ_y is the tensile yield strength, n is the strain-hardening exponent, and E is the Young's modulus. Suresh and co-workers (e.g., Giannakopolous & Suresh, 1999; Venkatesh et al., 2000; Dao et al., 2001) have used the results from such numerical analyses *in conjunction with suitable scaling relations*[2] to develop a promising methodology for estimating the Young's modulus, yield strength, strain-hardening exponent, as well as the hardness of metallic materials from measured P-h curves in microindentation.[3]

A search of the literature reveals that although numerous investigators have con-

[1]Previous finite element analyses (e.g., Bhattacharya & Nix, 1991; Giannakopolous et al., 1994; Larsson et al., 1996) were typically performed using a small deformation theory.

[2]Also see Cheng & Cheng, 1998; Cheng & Cheng, 1999.

[3]Two of the earliest, and still widely-used, methods for estimating the hardness and Young's modulus (from the maximum load and the initial unloading slope of the P-h curves) are those of Doerner and Nix (1986) and Oliver and Pharr (1992).

ducted nano/microindentation experiments to obtain P-h curves for polymeric materials (e.g., Briscoe & Sebastin, 1996; Briscoe et al., 1998), a corresponding methodology for extracting material property information from the experimental data is not as well developed.[4] This situation exists primarily because baseline numerical analyses of sharp indentation of polymeric materials using appropriate large deformation constitutive models for the elastic-viscoplastic response of polymeric materials appear not to have been previously reported in the literature. Before one can use experimentally-measured P-h curves from indentation experiments to extract material property information for a given material, *a particular constitutive model must be assumed, the sensitivity of the P-h curves to variation in the values of the constitutive parameters in the model must be studied, and the key material parameters that dominate the P-h response must be determined.* For instance, it is well known that room temperature stress-strain curves obtained from large deformation compression[5] experiments are very sensitive to (a) *the range of strains*: at small strains some amorphous polymers show a strain softening phenomenon, but at large strains they show a very rapid strain-hardening response; (b) *changes in strain path*: at large strains polymeric materials exhibit a pronounced Bauschinger effect upon unloading; (c) *the effects of strain rate*: room temperature for polymeric materials is usually not far from their glass-transition or melt temperatures, and they show substantial strain-rate sensitivity of plastic flow; (d) *large hydrostatic pressures*: most amorphous polymeric materials show a sizable positive pressure-sensitivity of the resistance to plastic flow. Without detailed numerical analyses of sharp indentation, it is unclear as to which of these phenomena significantly effect the P-h curves, and which material properties one can even hope to extract with reasonable accuracy.

A simple, rate-independent, power-law strain-hardening Mises type model, as has been used to simulate the indentation response of metallic materials (e.g., Cheng & Cheng, 1998; Dao et al., 2001), does not represent the various physical phenomena — strain-softening and then strain-hardening, Bauschinger effects, strain-rate sensi-

[4]However, see Rikards et al. (1998) for a recent attempt.

[5]And also tension experiments on polymers which do not craze.

tivity, pressure sensitivity of plastic flow — observed in polymeric materials. A more sophisticated constitutive model which comprehends these effects is needed. Such a model for *amorphous polymeric materials* undergoing plastic deformation by shear-yielding has been developed by Parks, Argon, Boyce, Arruda, and their co-workers (e.g. Parks et al., 1985; Boyce et al., 1988; Arruda & Boyce, 1993), and by Wu & Van der Giessen (1993). Anand & Gurtin (2002) have recently reformulated the model within a rigorous thermodynamic framework. In this paper we shall use this model to study the sharp-indentation response of the amorphous polymeric materials polycarbonate (PC) and polymethylmethacrylate (PMMA). Specifically we will (a) first estimate the constitutive parameters in the model by fitting stress-strain curves from large deformation compression tests, and other information available for these materials in the literature; (b) next we will conduct instrumented micro-indentation experiments using both Berkovich and conical indenters, and then by comparing the measured P-h curves and residual indent morphologies against corresponding predictions from finite-element analyses show that for both PC and PMMA the predicted results are in reasonable agreement with the experiments; and finally, (c) with the suitability of the constitutive model for these materials confirmed, we perform a sensitivity study and dimensional analysis in order to find the key material parameters that determine the P-h response and the residual indent morphology resulting from sharp indentation of polymeric materials. Building upon these results, we propose a simple scheme for the inverse approach in sharp-indentation of polymeric solids and demonstrate an example application to indentation of polystyrene (PS).

The plan of the chapter is as follows. In Section 4.2 we summarize our constitutive model for isotropic solids undergoing large deformations. In Section 4.3 we report our experimental and numerical simulation procedures for micro-indentation. In order to calibrate these procedures, we first perform a brief study of the indentation response of the metallic alloy Al6061-T6; this is reported in Section 4.3.1. In section 4.3.2 we report on the indentation experiments and simulations for PC and PMMA. In Section 4.4 we present a parametric study to motivate a framework for the inverse approach for indentation of amorphous polymeric solids. We present a methodology

for the extraction of material properties from indentation data in Section 4.5 and demonstrate an example application of an inverse approach for indentation of PS in section 4.6. We close in Section 4.7 with some final remarks.

4.2 Constitutive model

The model is based on the multiplicative decomposition, $\mathbf{F} = \mathbf{F}^e\mathbf{F}^p$, of the deformation gradient $\mathbf{F}$ into elastic and plastic parts, $\mathbf{F}^e$ and $\mathbf{F}^p$ (Kroner, 1960; Lee, 1969).[6] We shall first consider a specialized form of this constitutive model which is suitable for isotropic metallic materials, and then consider a more generalized form suitable for amorphous polymeric materials.

4.2.1 Isotropic metallic materials

For metallic materials the theory uses one internal variable $s > 0$ that represents an isotropic resistance to plastic flow. Then, in terms of the variables

$\mathbf{T}$,	$\mathbf{T} = \mathbf{T}^{\mathsf{T}}$,	Cauchy stress,
$\mathbf{F}$,	$\det \mathbf{F} > 0$,	deformation gradient,
$\mathbf{F}^p$,	$\det \mathbf{F}^p = 1$,	plastic part of the deformation gradient,
s,	$s > 0$,	isotropic resistance to plastic flow,

and the definitions

[6] *Notation*: ∇ and Div denote the gradient and divergence with respect to the material point $\mathbf{X}$ in the *reference configuration*; grad and div denote these operators with respect to the point $\mathbf{x} = \mathbf{y}(\mathbf{X}, t)$ in the deformed configuration, where $\mathbf{y}(\mathbf{X}, t)$ is the motion; a superposed dot denotes the material time-derivative. Throughout, we write $\mathbf{F}^{e-1} = (\mathbf{F}^e)^{-1}$, $\mathbf{F}^{p-\mathsf{T}} = (\mathbf{F}^p)^{-\mathsf{T}}$, etc. We write sym$\mathbf{A}$ and skw$\mathbf{A}$, respectively, for the symmetric, and skew parts of a tensor $\mathbf{A}$. Also, the inner product of tensors $\mathbf{A}$ and $\mathbf{B}$ is denoted by $\mathbf{A} \cdot \mathbf{B}$, and the magnitude of $\mathbf{A}$ by $|\mathbf{A}| = \sqrt{\mathbf{A} \cdot \mathbf{A}}$.

$\mathbf{F}^e = \mathbf{F}\mathbf{F}^{p-1}$, $\det \mathbf{F}^e > 0$, elastic deformation gradient,

$\mathbf{E}^e = \frac{1}{2}(\mathbf{F}^{e\top}\mathbf{F}^e - \mathbf{1})$, elastic strain,

$\mathbf{T}^e = \mathbf{R}^{e\top}\mathbf{T}\mathbf{R}^e$, stress conjugate to the elastic strain $\mathbf{E}^e$,

$\sigma = \frac{1}{3}\mathrm{tr}\mathbf{T}$, mean normal pressure,

$\mathbf{T}_0^e = \mathbf{T}^e - \sigma\mathbf{1}$, deviatoric stress,

$\mathbf{D}^p = \mathrm{sym}(\dot{\mathbf{F}}^p\mathbf{F}^{p-1})$, $\mathrm{tr}\mathbf{D}^p = 0$, plastic stretching,

the constitutive equations, under the usual approximative assumption of small elastic stretches, are:

1. **Equation for the stress**:

$$\mathbf{T}^e = 2G\mathbf{E}_0^e + K(\mathrm{tr}\mathbf{E}^e)\mathbf{1}. \tag{4.2}$$

where G and K are the elastic shear and bulk moduli, respectively.

2. **Flow rule**:

The evolution equation for $\mathbf{F}^p$ is

$$\dot{\mathbf{F}}^p = \mathbf{D}^p\mathbf{F}^p, \qquad \mathbf{F}^p(\mathbf{X}, 0) = \mathbf{1}, \tag{4.3}$$

with $\mathbf{D}^p$ given by the flow rule

$$\mathbf{D}^p = \nu^p\left(\frac{\mathbf{T}_0^e}{2\bar{\tau}}\right), \qquad \nu^p = \nu_0\left(\frac{\bar{\tau}}{s}\right)^{\frac{1}{m}}, \quad 0 < m \leq 1, \tag{4.4}$$

where

$$\bar{\tau} = \frac{1}{\sqrt{2}}|\mathbf{T}_0^e|, \quad \text{and} \quad \nu^p = \sqrt{2}\,|\mathbf{D}^p|, \tag{4.5}$$

are an equivalent shear stress and equivalent plastic shear strain-rate, respectively. Here, ν_0 is a reference plastic shear strain-rate, and m a strain-rate sensitivity parameter. The limit $m \to 0$ renders (4.4) rate-independent, while

$m = 1$ renders (4.4) linearly viscous. The equivalent plastic shear strain, γ^p, is defined by $\gamma^p = \int \nu^p \, dt > 0$.

3. **Evolution equation for the internal variables** s:

   The evolution of s is taken to be governed by the differential equation

$$\dot{s} = h_0 \left(1 - \frac{s}{s_*}\right)^a \nu^p, \qquad s(\mathbf{X}, 0) = s_0, \tag{4.6}$$

   where $\{s_0, h_0, s_*, a\}$ are additional material parameters.

   To complete the constitutive model for a particular isotropic metal the constitutive parameters/functions that need to be specified are

$$\{G, K, \nu_0, m, s_0, h_0, s_*, a\}.$$

4.2.2 Amorphous polymeric materials

For polymeric materials, it is commonly believed that the evolution of the local free-volume is the major reason for the highly non-linear stress-strain behavior of glassy materials which precedes the yield-peak and gives rise to the post-yield strain-softening. Accordingly, in this case the model employs two internal variables: a variable $s > 0$ that represents an isotropic intermolecular resistance to plastic flow; and an unsigned variable η that represents the local free-volume. The model also explicitly accounts for the dependence of the free energy on the plastic deformation in a thermodynamically consistent manner. In amorphous polymeric materials the major part of this dependence arises from an "entropic" contribution due to the stretching of the molecular chains. This dependence leads directly to a *back stress* in the underlying flow rule, which allows the model to capture the rapid strain-hardening response after the initial yield-drop in monotonic deformations, as well as the Bauschinger-type reverse-yielding phenomena typically observed in amorphous polymeric solids upon unloading after large plastic deformations.

The constitutive equations for amorphous polymeric materials are summarized

below.

1. **Equation for the stress**:

$$\mathbf{T}^e = 2G\mathbf{E}_0^e + K(\mathrm{tr}\mathbf{E}^e)\mathbf{1}. \tag{4.7}$$

where G and K are the elastic shear and bulk moduli, respectively.

2. **Flow rule**:

$$\dot{\mathbf{F}}^p = \mathbf{D}^p\mathbf{F}^p, \qquad \mathbf{F}^p(\mathbf{X}, 0) = \mathbf{1}, \tag{4.8}$$

with

$$\mathbf{D}^p = \nu^p \left(\frac{\mathbf{T}_0^e - \mathbf{S}_{\text{back}}}{2\bar{\tau}} \right), \qquad \nu^p = \nu_0 \left(\frac{\bar{\tau}}{s - \alpha\sigma} \right)^{\frac{1}{m}}, \quad 0 < m \leq 1, \tag{4.9}$$

where

$$\bar{\tau} = \frac{1}{\sqrt{2}} |\mathbf{T}_0^e - \mathbf{S}_{\text{back}}|, \quad \text{and} \quad \nu^p = \sqrt{2}\,|\mathbf{D}^p|, \tag{4.10}$$

are an equivalent shear stress and equivalent plastic shear-strain rate, respectively. Here, ν_0 is a reference plastic shear-strain rate, m a strain-rate sensitivity parameter, and α a pressure sensitivity parameter.

The tensor $\mathbf{S}_{\text{back}}$ represents a *back stress*, which using the definitions

$\mathbf{B}^p = \mathbf{F}^p\mathbf{F}^{p\top}$, left Cauchy-Green tensor corresponding to $\mathbf{F}^p$,

$\mathbf{B}_0^p = \mathbf{B}^p - \frac{1}{3}(\mathrm{tr}\mathbf{B}^p)\mathbf{1}$, deviatoric part of $\mathbf{B}^p$,

$\lambda^p = \frac{1}{\sqrt{3}}\sqrt{\mathrm{tr}\mathbf{B}^p}$, effective plastic stretch,

is given by

$$\mathbf{S}_{\text{back}} = \mu \mathbf{B}_0^p, \quad \text{with} \tag{4.11}$$

$$\mu = \mu_R \left(\frac{\lambda_L}{3\lambda^p} \right) \mathcal{L}^{-1} \left(\frac{\lambda^p}{\lambda_L} \right), \tag{4.12}$$

where $\mathcal{L}^{-1}$ is the inverse of the Langevin function $\mathcal{L}(\cdots) = \coth(\cdots) - (\cdots)^{-1}$. The back stress modulus μ involves two material parameters: μ_R, called the *rubbery modulus*, and λ_L called the *network locking stretch*; this modulus $\mu \to \infty$ as $\lambda^p \to \lambda_L$, since $\mathcal{L}^{-1}(z) \to \infty$ as $z \to 1$.

3. **Evolution equations for the internal variables s and η:**

The evolution of s and η is taken to be governed by the coupled differential equations

$$\left.\begin{aligned} \dot{s} &= h_0 \left(1 - \frac{s}{\tilde{s}(\eta)} \right) \nu^p, \qquad s(\mathbf{X}, 0) = s_0, \\ \dot{\eta} &= g_0 \left(\frac{s}{s_{\text{cv}}} - 1 \right) \nu^p, \qquad \eta(\mathbf{X}, 0) = 0, \end{aligned}\right\} \tag{4.13}$$

with

$$\tilde{s}(\eta) = s_{\text{cv}}[1 + b(\eta_{\text{cv}} - \eta)], \tag{4.14}$$

where $\{h_0, g_0, s_{\text{cv}}, b, \eta_{\text{cv}}\}$ are additional material parameters. Here $\tilde{s} = \tilde{s}(\eta)$ is a saturation value of s: $\dot{s}$ is positive for $s < \tilde{s}$ and negative for $s > \tilde{s}$. By definition ν^p is nonnegative. Assuming that $\nu^p > 0$, all solutions to the pair of evolution equations satisfy

$$s \to s_{\text{cv}} \quad \text{and} \quad \eta \to \eta_{\text{cv}} \quad \text{as} \quad t \to \infty.$$

We restrict attention to the initial conditions $s = s_0$ with

$$s_0 \leq s \leq s_{\text{cv}}(1 + b\eta_{\text{cv}}).$$

Also, as is tacit from $(4.13)_2$, the free-volume is measured from the value $\eta = 0$ in the virgin state of the material, and thus η at any other time represents a change in the free-volume from the initial state.

To complete the constitutive model for a particular amorphous polymeric material the constitutive parameters/functions that need to be specified are

$$\{G, K, \nu_0, m, \alpha, \mu_R, \lambda_L, s_0, h_0, s_{cv}, a, g_0, b, \eta_{cv}\}.$$

We have implemented our constitutive models for metallic as well as polymeric materials in the finite-element computer program ABAQUS/Explicit (ABAQUS, 2001), by writing user material subroutines.

4.3 Experimental and numerical simulation of sharp-indentation

In order to calibrate our experimental and numerical simulation procedures for micro-indentation, we first perform a brief study of the indentation response of the metallic alloy Al6061-T6. Following this calibration step, we study the indentation response of the amorphous polymeric materials polycarbonate (PC) and polymethylmethacrylate (PMMA).

4.3.1 Indentation of Al6061-T6

Material parameters

We begin by estimating the material parameters for Al6061-T6 in our constitutive model for metallic materials. Recall that the material parameters that need to be determined are

1. The elastic shear and bulk moduli (G, K).

2. The reference shear strain rate ν_0 and the strain-rate sensitivity parameter m in the flow equation (4.4).

3. The initial deformation resistance s_0 in shear, and the strain hardening parameters (h_0, s_*, a) in (4.6).

The values of (G, K) are determined by measuring the Young's modulus of the material in a tension experiment, E=66.5 GPa, assuming a value of 0.33 for the Poisson's ratio, and using standard conversion relations of isotropic elasticity to obtain the elastic shear and bulk moduli. The parameters $\{\nu_0, m\}$ are estimated by conducting a strain rate jump experiment in simple tension to obtain $\nu_0 = 0.0017\ \text{s}^{-1}$ and $m = 0.002$. The parameters $\{s_0, h_0, s_*, a\}$ may be estimated by fitting a stress-strain curve in compression to large strains. The fit was performed by adjusting the values of these parameters in finite element simulations of a simple compression experiment using a single ABAQUS/C3D8R element. The fit shown in Fig. F-60 was obtained using the parameters:

$$\begin{array}{llll} G = 25.0\ \text{GPa} & K = 65.3\ \text{GPa} & \nu_o = 0.0017\ \text{s}^{-1} & m = 0.002 \\ s_o = 165.1\ \text{MPa} & s_* = 337.2\ \text{MPa} & h_o = 6.60\ \text{GPa} & a = 3.98. \end{array}$$

Indentation experiments and simulations

Indentation specimens from the same Al6061-T6 were machined as discs, 25.4 mm diameter and 6.35 mm high. The surfaces of the sample were polished in a 0.05 μm diamond slurry to a mirror finish and thoroughly cleaned by rinsing with acetone. These specimens were indented in a recently developed flexure-based instrumented micro-indenter; see Fig. F-90. This instrument has a maximum load capacity of 8 N with an accuracy of measurement of 80 μN, while the maximum possible indentation depth is 1.25 mm with an accuracy of measurement of 20 nm; further details concerning the indenter may be found in Appendix C.

Loading-unloading indentation experiments using a Berkovich diamond indenter were conducted under load control at a constant loading rate of 50 mN/s, to load levels of 1.02 N, 3.27 N and 7.40 N. The measured P-h curves are shown in Fig. F-

61a.[7] A surface map of the residual indent from a test conducted to a peak load of 3.27 N is shown in Fig. F-61b; this figure clearly shows a large amount of pile-up of the material around the indenter, the maximum height of the pile-up is approximately 1.45 μm.[8]

Using the inherent six-fold symmetry of Berkovich indentation, the finite element mesh used for the indentation simulation of Al6061-T6 is shown in Fig. F-62a; the mesh consists of 24713 ABAQUS/C3D8R elements. A detail of the mesh that directly contacts the indenter shown in Fig. F-62b. The indenter was modeled using a rigid surface (not shown), and contact was modeled as frictionless.

The numerically-predicted P-h curves are compared against the experimentally-measured ones in Fig. F-61a. The loading curvature as well as the initial unloading portions of the P-h curves of the simulations and the experiments are in excellent accord. The numerically predicted indent morphology for the test conducted to 3.27 N is shown in Fig. F-61c; this also compares reasonably well with the corresponding optical micrograph shown in Fig. F-61b. The contour plots of indentation depth shown in Fig. F-61c predict a large zone of piled up material around the indent, as is observed in the experiment.

Profiles of the residual indents were also measured using a white-light, interferometric non-contact surface profiler. The profiles were determined in a plane which is perpendicular to one of the faces of the indent, and which intersects the midpoint of the trace of the indent edge on the surface; that is along the plane of the maximum pile-up height. Fig. F-63 shows a comparison of experimentally-measured and numerically-predicted indentation profile corresponding to a maximum load of 3.27 N

[7]Repeatability of the P-h response was investigated by conducting ten tests to the 3.27 N load level; the maximum variation in the response is on the order of 5%.

[8]It is well known that in indentation of metallic materials which have been previously strain-hardened so that they exhibit an essentially perfectly plastic response to subsequent deformations, the plastically displaced material tends to flow up the faces of the indenter, and hence results in a "pile-up" in that location; the result is a barreling of the indentation impression along the flat faces of the indenter (cf., e.g., Fig.2 of Lim & Chaudhari, 1999). On the other hand, for well-annealed materials which still have a substantial strain-hardening capacity, the active plastically deforming region is pushed further away from the indenter, with the final imprint sinking below the initial surface level; this results in a pin-cushion like "sink-in" impression around the faces of the indenter (cf., e.g., Fig.3 of Lim & Chaudhari, 1999).

and 10μm depth, as well as a profile corresponding to a maximum load of 7.40 N and 15μm depth. The numerically predicted profiles were found by plotting the nodal displacements of the relevant elements as a function of position from the center of the indent. The experimental profiles exhibit a small amount of noise resulting from the experimental method utilized. Granted that a refinement of the mesh may lead to minor improvements in the predicted profiles, the relatively fine mesh presently employed reasonably well predicts the pile-up height.

Finally note that the size of the individual indents in the experiments is of the order of the grain size of the material $\approx$ 20-50 μm. Thus, during the indentation experiment we are probing the response of one or at most a few single crystals. The fact that our continuum isotropic plasticity model performs reasonably well in predicting not only the macroscopic P-h curves but also some of the details of the indent morphology with reasonable accuracy, is quite remarkable.

In order to reduce computation time, a study of Berkovich indentation using a coarse mesh of 3500 ABAQUS/C3D8R elements was conducted. As shown in Fig. F-62c, the mesh employs substantially less elements in the contact region as compared to that of Fig. F-62b and consequently, the simulation time was reduced by a factor of 10. The results of our study showed that while the P-h curves obtained from the fine mesh and coarse simulations were indistinguishable from each other, the details of the local fields under the indenter as well as the indent morphologies varied considerably. For example, values of the equivalent plastic shear strain γ^p were found to vary on the order of 22% between simulations under the same loading conditions. Thus, a coarse mesh[9] similar to that of Fig. F-62c is adequate to obtain the details of the P-h curves, however, in order to accurately capture the local details of the indentation process, a fine mesh similar to that of Fig. F-62b must be employed. For the remainder of our study on Berkovich indentation, we have used the computationally more efficient coarse mesh to obtain our P-h curves, while the indent morphologies have been obtained from simulations using the fine mesh.

[9]We note that our simulations use elements with reduced integration. The results using higher-order elements may vary from our study.

4.3.2 Indentation of PC and PMMA

Material parameters

We begin by estimating the material parameters for PC and PMMA in our constitutive model for amorphous polymeric materials. To ensure consistent initial conditions of the PC and PMMA samples for compression and indentation experiments, all specimens were annealed at their glass transition temperatures (PC: $T_g = 145°C$, PMMA: $T_g = 105°C$) for two hours and then furnace-cooled for fifteen hours.

Recall that the material parameters that need to be determined are

1. The elastic shear and bulk moduli (G, K).
2. The reference shear strain rate ν_0, the strain-rate sensitivity parameter m, and the pressure sensitivity parameter α in the flow equation (4.9).
3. The parameters (μ_R, λ_L) for the back stress modulus, (4.12).
4. The parameters $\{h_0, g_0, s_{cv}, b, \eta_{cv}, s_0\}$ in the evolution equations for (s, η), (4.13, 4.14).

Focusing first on PC, the values of (G, K) are determined by measuring the Young's modulus $E = 2.28\,\text{GPa}$ of the material from a tension experiment, assuming a Poisson's ratio of $\nu = 0.33$, and using standard conversion relations of isotropic elasticity to obtain the elastic shear and bulk moduli. The parameters $\{\nu_0, m\}$ are estimated by conducting a strain rate jump experiment in simple compression; this gave $\nu_0 = 0.0017\,\text{s}^{-1}$ and $m = 0.011$. The pressure sensitivity parameter $\alpha = 0.08$ was estimated from the data reported by Spitzig and Richmond (1979). The parameters $\{h_0, g_0, s_{cv}, b, \eta_{cv}, s_0\}$ and (μ_R, λ_L) were estimated by fitting a stress-strain curve in compression to large strains. The fit was performed by adjusting the values of these parameters in finite element simulations of a simple compression experiment (assuming homogeneous deformation) using a single ABAQUS/C3D8R element. After a few attempts, a reasonable fit was obtained, and this is shown in Fig. F-64a. The list of

parameters obtained using this calibration procedure is:[10]

$G = 0.857$ GPa	$K = 2.24$ GPa	$\mu_R = 11.0$ MPa	$\lambda_L = 1.45$
$\nu_o = 0.0017$ s^{-1}	$m = 0.011$	$\alpha = 0.080$	
$s_o = 20.0$ MPa	$s_{cv} = 24.0$ MPa	$h_o = 2.75$ GPa	$a = 1$
$b = 825$	$g_o = 6.0 \cdot 10^{-3}$	$\eta_{cv} = 0.001$.	

The material parameters for PMMA are found in an analogous manner as that used for PC. The quality of the curve fit to the simple compression experiment is shown in Fig. F-64b. The list of parameters is:

$G = 1.17$ GPa	$K = 3.04$ GPa	$\mu_R = 7.70$ MPa	$\lambda_L = 1.51$
$\nu_o = 0.0017$ s^{-1}	$m = 0.043$	$\alpha = 0.204$	
$s_o = 37.8$ MPa	$s_{cv} = 43.7$ MPa	$h_o = 1.30$ GPa	$a = 1$
$b = 790$	$g_o = 7.5 \cdot 10^{-3}$	$\eta_{cv} = 0.00025$.	

The value $\alpha = 0.204$ for the pressure sensitivity parameter is from the data reported by Rabinowitz et al. (1970). The values $\nu_0 = 0.0017$ s^{-1} and $m = 0.043$ were obtained from a strain rate jump experiment. Note that PMMA shows a higher strain rate sensitivity than PC at room temperature.

Indentation experiments and simulations

We have performed two types of sharp-indentation experiments: (a) using a Berkovich diamond tip, and (b) using a conical diamond tip. The projected contact area for a Berkovich indenter is $A = 24.5h^2$ where h is the depth of indentation, while that for a conical indenter, with semicone angle θ, is $A = (\pi \tan^2\theta)\, h^2$. The semicone angle of the conical indenter was designed to be $\theta = 70.3°$ so that the projected area per unit depth for the conical indenter was the same as that for a Berkovich indenter. The utility of experiments using conical indenters is that they allow the corresponding numerical simulations to be performed as axisymmetric two-dimensional calculations, rather than full-three dimensional calculations which are needed for Berkovich indents.

[10]These parameters, while not unique, are adequate for present purposes.

Berkovich indentation of PC and PMMA

The indentation samples were machined from a 6.35 mm thick rolled sheet and are 12.7 mm x 25.4 mm in cross-section. All surfaces were polished in a 0.05 μm alumina slurry to ensure that the surface roughness is negligible in comparison to the indent sizes. In the present experiments on PC and PMMA, the rms surface roughness is two to three orders-of-magnitude smaller than the indent edge lengths. After polishing, the samples were annealed at their respective glass transition temperatures and then furnace-cooled for fifteen hours.

The experiments were conducted in load control at a rate of 50 mN/s to nominal load levels of 1 N, 3 N and 7-8 N.[11] Due to the low strain rate sensitivity of PC at room temperature, our indentation experiments did not incorporate a dwell time at the peak load. However, as we shall demonstrate, the P-h curve and more specifically, the initial unloading slope, obtained during indentation of materials of high strain rate sensitivity, such as PMMA, depend critically on the loading profile. We perform a brief study on incorporating a dwell time in our loading profile for Berkovich indentation of PMMA to elucidate the effects of creep in indentation of polymers.

Representative results from our study of Berkovich indentation of PC are shown in Fig. F-65. We have used the course mesh of Fig. F-62c to obtain the P-h curves shown in Fig. F-65a. The model predictions are in good accord with the experimentally obtained curves. An optical micrograph of a residual indent from a test conducted to a peak load of 2.50 N is shown in Fig. F-65b, where the indent morphology is consistent with material "sink-in" around the indenter tip. The fine numerical mesh of Fig. F-62b was used to obtain the numerically predicted morphology shown in Fig. F-65c. We note that while the overall residual indent morphology is indicative of material "sink-in" around the indenter, a surface trace intersecting the center of one of the pyramidal sides reveals that a small amount of material "piles-up" around the indenter. The extent of this pile-up is only approximately 2% relative to the

[11]Repeatability of the P-h curves was investigated by conducting five experiments to the 3 N nominal load level; the variation in the curves is on the order of 5%.

depth of the indent, while for aluminum at a commensurate depth, the pile-up is approximately 20%. The constitutive model accurately captures the general shape of the residual indent, including the characteristic edge-curvature of the sink-in indent morphology.

The P-h curves obtained from Berkovich indentation of PMMA are shown in Fig. F-66a in comparison to the numerically predicted responses, where we note that we have used the course mesh of Fig. F-62c to obtain the numerical curves. A residual indent from the experiment conducted to a peak load of 3.30 N is shown in the optical micrograph of Fig. F-66b; similarly to our results on PC, the residual indent is indicative of a "sink-in" morphology. A comparison of this image with the numerically predicted profile of Fig. F-66c demonstrates the capability of the model and the fine mesh of Fig. F-62b to adequately capture the features of the residual indent morphology.

While the general characteristics of the P-h curves for Berkovich indentation of PMMA, Fig. F-66a, are similar to those observed in our study of PC, Fig. F-65a, we note that a salient discrepancy between the initial unloading slopes is seen. Particularly, the initial unloading slope obtained for PMMA exhibits a feature typically referred to as the "nose" effect (e.g. Briscoe & Sebastin, 1996), which causes the initial unloading curvature to have a negative slope. The physical mechanism behind this effect is creep of the material during the initial unloading period. To mitigate the effects of creep, and to thus obtain a positive initial unloading slope, researchers incorporate a dwell time, which may range from 10 s to 10 minutes, at the peak load.

We have conducted a dwell time experiment on PMMA. The material was loaded at a constant loading rate of 30 mN/s and a dwell time of 300 s was imposed at the peak load. The resulting experimental P-h curve is shown in Fig. F-67a in comparison to the model prediction. Clearly, the incorporation of a dwell period of 300 s has eliminated "nose" effects during unloading in the experiment. As can be seen from the comparison of the model to the experiment, the model somewhat underpredicts the displacement observed during the dwell period. This is observed more clearly in Fig. F-67b, where the dwell displacement is shown as a function of the imposed

dwell time. Granted that the discrepancy between the results is considerable, we emphasize that the model presently employed is an elastic-viscoplastic formulation. For time scales such as those encountered during our 300 s dwell period, the experimental response may indicate both viscoplastic as well as viscoelastic effects.[12] In Fig. F-68 we show loading curves for Berkovich indentation of PMMA conducted at three different loading rates of 25 mN/s, 50 mN/s, and 250 mN/s. Corresponding model predictions are also shown in comparison to the experimental results. The load and displacement levels as well as the trend indicated by the rate-sensitive response of the experiments are well-captured by the constitutive model. For the time scale associated with the experiments in Fig. F-68, our numerical predictions indicate that the response is dominated by the viscoplastic response of the material over any viscoelastic effects. In contrast, the displacement measured during the 300 s dwell period, Fig. F-67b, indicates a combination of the effects of both creep strains due to the viscoplastic nature of the material as well as displacements due the viscoelasticity of the material.

Comparison of Berkovich and conical indentations for PC and PMMA

A comparison of experimental results for Berkovich and conical indentation of PC is shown in Fig. F-69, where the loading rate for both experiments was 50 mN/s. As can be seen from Fig. F-69, the P-h curves obtained using a conical indenter with a semicone angle of $\theta = 70.3°$ provide a good approximation for the P-h curves resulting from Berkovich indentation.

Experimental and numerical results from our study on conical indentation of PC and PMMA are shown in Fig. F-70a and Fig. F-70b, respectively. A mesh density study was conducted to obtain a converged numerical result for both the P-h curves and the residual indent morphologies; we have used this mesh to obtain the numerical

[12]See Hasan and Boyce (1995) for a viscoelastic-viscoplastic formulation for glassy polymers which was shown to accurately capture the strains due to creep under uniaxial conditions.

results shown in Fig. F-70. The model results are in good accord with the experimentally obtained P-h curves. We note that the general features of the P-h curves shown in Fig. F-70 are similar to those of the P-h curves obtained from Berkovich indentation on PC and PMMA. Furthermore, a comparison of the strain levels observed under the indenter tip at the same load level revealed that the local fields are in fact similar. Thus, we propose to use conical indentation as a computationally efficient method for our parametric studies. In the next section, we present results from our parametric study and dimensional analysis to motivate a framework for the inverse approach in indentation of polymeric solids.

4.4 Parametric study

The results of the previous section serve to validate the suitability of our constitutive model for capturing the P-h curves and indent characteristics for Berkovich and conical indentation of PC and PMMA. In this section, we present a parametric study to motivate guidelines for property extraction from indentation data.

With recourse to our constitutive model, the indentation response for the class of amorphous polymeric solids under consideration may be sufficiently determined by the list of parameters:

$$\{E, \nu, s_0, \mu_R, \lambda_L, \nu_0, m, \alpha, \mathrm{h}, \dot{\mathrm{h}}, \theta\}, \tag{4.15}$$

where h represents the indenter displacement, $\dot{\mathrm{h}}$ is the indenter displacement rate, and θ is the semicone angle of the conical indenter. We expect that the effects of the hardening/softening behavior of s coupled with the evolution of the local free-volume η do not dominate the response of the polymer to indentation, therefore in (4.15) we use an average value of the deformation resistance s_0 to capture the effects of the local resistance to plastic flow.

The sensitivity of the P-h curve to changes of $\pm 10\%$ in the included angle of the conical indenter is shown in Fig. F-71 for conical indentation of PC. While the P-h

response is observed to be highly sensitive to the semicone angle, we emphasize that in the present experiments, we concentrate on micro-indentation where the depths of indentation are in the μm range. Thus, the indentation experiments sample a portion of the conical indenter tip which is orders of magnitude greater than the typical radii[13] associated with the as-machined tips. Accordingly, for the present study, we assume that the semicone angle is fixed at 70.3°. Furthermore, we shall assume a value of $\nu = 0.33$ is adequate for a considerable range of polymers. The list of parameters that determine the indentation response reduces to

$$\{E, s_0, \mu_R, \lambda_L, \nu_0, m, \alpha, \mathrm{h}, \dot{\mathrm{h}}\}. \tag{4.16}$$

In Fig. F-72a, we show a contour plot of the equivalent plastic shear strain at a peak load of 2.80 N for conical indentation of PC. As can be seen from Fig. F-64a, the effect of the back stress is dominant for strain levels exceeding $\approx$ 90%. The contour plot of Fig. F-72a indicates that the region of material where strains exceed 90% only comprises approximately 22% of the zone of plastically deformed material under the indenter tip. This result suggests that perhaps a material model of the form shown in Fig. F-72b as a fit to simple compression of PC may be adequate to capture the indentation P-h curve. We note that this model is an elastic-perfectly plastic rate-dependent constitutive model with pressure-sensitive plastic flow. Numerical predictions resulting from the model shown in Fig. F-72b are shown in Fig. F-73 compared against the experiments as well as the previous numerical calculations for conical indentation of PC. Clearly, for the range of sharp-indentation under consideration, the effects of the back stress may be neglected in determining the P-h response and residual indent morphology predicted by the two models; the list of parameters that determine the indentation P-h curve is accordingly approximated by

$$\{E, s_0, \nu_0, m, \alpha, \mathrm{h}, \dot{\mathrm{h}}\}. \tag{4.17}$$

[13]The conical indenter tip used in the present experiments has a tip radius of approximately 100 nm and is machined to within 1% of the design semicone angle of 70.3°.

The sensitivity of the P-h curve to changes in the pressure sensitivity parameter α are shown in Fig. F-74, where α is varied from zero to a maximum value of 0.30. We expect that this range should account for the majority of amorphous polymers under consideration. We show the sensitivity of the P-h curves to changes in both E and s_0 in Fig. F-75a and Fig. F-75b, respectively. For both sets of P-h curves, the parameter under consideration is varied by $\pm 20\%$, as indicated on the plots. Comparison of these curves indicates that the loading and unloading portions of the P-h curve are sensitive to variations in E, whereas variations in s_0 are seen to significantly effect only the loading portion of the P-h curve. We shall draw upon this observation in the next section when we present a methodology for property extraction from indentation data.

Note as well that the effects of variations of 40% in both E and s_0 are commensurate with variations in α from zero to 0.30, thus the P-h curve is more sensitive to variations in E and s_0. The determination of α from a single indentation P-h curve is generally not feasible. Indeed, at macroscopic scales, the pressure sensitivity must be determined from a set of experiments involving tension and compression tests conducted with a range of superposed hydrostatic pressures. In the next section, we present a methodology for determining an experimental estimate of α using Berkovich indentation in conjunction with spherical indentation.

In summary, the list of *material parameters* that dominate the indentation P-h curve is given by

$$\{E, s_0, \nu_0, m, \alpha, \mathrm{h}, \dot{\mathrm{h}}\}. \tag{4.18}$$

With our parametric study as background, we proceed with a guideline for property extraction from indentation data on amorphous polymeric solids.

4.5 Guidelines for property extraction

In this section, we present our methodology for the determination of the list of material parameters

$$\{E, s_0, \nu_0, m, \alpha\}. \tag{4.19}$$

given an experimental data set for indentation of a sample of an amorphous polymeric material. The procedure for property extraction consists of the following steps:

1. *Determination of E.* Previous researchers (e.g. Briscoe et al., 1998) have typically used an unloading analysis such as the approach of Oliver and Pharr (1992) to estimate values of E from instrumented indentation data. However, caution must be exercised when using an unloading analysis due to the effects of creep on the estimate of the initial unloading slope, which is assumed to be associated with purely elastic unloading when using the approach of Oliver and Pharr. Since the strains due to creep depend upon both the peak load as well as the unloading rate, the incorporation of a dwell period may not completely mitigate the effects of creep on the estimated values of E.

   To experimentally determine a valid approach for the estimation of E, we have conducted Berkovich indentation on PMMA over a range of peak loads with various loading and unloading rates and have analyzed the initial unloading slopes to obtain values of Young's modulus E. In Fig. F-76a, three experiments were conducted to a peak load of approximately 205 mN at a loading rate of $\dot{P}_l = 25$ mN/s followed by a dwell period of 300 s. The experiments were then unloaded at three different rates of $\dot{P}_u = 25$ mN/s, 50 mN/s and 250 mN/s. As can be seen from the results, the highest unloading rate provides a final unloading slope which is somewhat stiffer than that corresponding to the lower unloading rates.

   An unloading analysis following the approach of Oliver and Pharr (1992) was

conducted by first estimating the initial unloading slope[14] $S_m = \left.\frac{dP}{dh}\right|_{h=h_m}$, and measuring the maximum depth h_m and the maximum load P_m. The contact depth h_c was estimated from $h_c = h_m - 0.75(P_m/S_m)$ with the corresponding contact area A_c given by $A_c = 24.5h_c^2$. The value of E was estimated by assuming a value of $\nu = 0.33$ and calculating

$$E = f(1-\nu^2)\frac{S_m}{2.16}\sqrt{\frac{\pi}{A_c}}, \tag{4.20}$$

where the factor of 2.16 is introduced following the work of Cheng and Cheng (1999). The factor f was estimated from our finite element calculations by performing an unloading analysis on the *simulation* P-h data and comparing the estimated value of E to that of 3.11 GPa used for the simulation. The predicted value of E was found to vary from 3.11 GPa as a linear function of the peak load P_m according to

$$f = 1 - 0.0539P_m. \tag{4.21}$$

Table G.1 summarizes the values obtained from each experiment and the corresponding values of E are indicated for each curve in Fig. F-76. As can be seen from Fig. F-76a, the experiment conducted at the highest unloading rate of 250 mN/s provides the best estimate of E relative to the values found when lower unloading rates are used. Since the extent of strain due to creep depends upon the peak load and the unloading rate, our results indicate that the best estimate of elastic properties is obtained from an experiment conducted at a relatively low peak load with a high unloading rate.

In Fig. F-76b and Fig. F-76c, we present additional experimental results on Berkovich indentation of PMMA to support our conclusion. For each set of experiments, a dwell period of 300 s was used at the peak load. The effect

[14]For each test, unloading data corresponding to a range of 5% of the peak load was fit with a linear regression to obtain an estimate of the initial unloading slope.

of peak load on estimates for E is shown in Fig. F-76b, where the loading and unloading rates were 25 mN/s for each experiment. The results appear to indicate overestimation of E with increasing peak load. The effects of loading and unloading rates on the calculated values of E are shown in Fig. F-76c, where the experiments were conducted at loading and unloading rates of 25 mN/s, 250 mN/s and 1020 mN/s. The corresponding estimates of E shown for each test clearly indicate gross error in estimating elastic properties from an unloading analysis when the material shows considerable rate-sensitivity.

2. *Determination of ν_0 and m.* In order to estimate the parameters ν_0 and m, we take the reference value ν_0 to be 0.001/s and propose to determine the rate-sensitivity parameter m from indentation data which incorporates loading rate-jump experiments. In order to determine the feasibility of this approach, we have conducted a loading rate-jump experiment in Berkovich indentation of PMMA as shown in Fig. F-77. Two rate-jumps were imposed; the jump from the indicated stage 1 to stage 2 was for a rate jump from 25 mN/s to 250 mN/s and that from stage 3 to stage 4 was from 250 mN/s to 1025 mN/s. The displacement rates measured as the jump was imposed were $\dot{h}_1 = 0.353\,\mu$m/s, $\dot{h}_2 = 2.154\,\mu$m/s for stages 1 and 2, respectively, and $\dot{h}_3 = 1.397\,\mu$m/s, $\dot{h}_4 = 3.328\,\mu$m/s for stages 3 and 4, respectively. The value of m was estimated by assuming that the state of the material, as characterized by the deformation resistance s, remains constant as the jump is instantaneously imposed. To estimate a nominal measure of the stress-state under the indenter, we use the values of $P_1 = 0.337$ N and $P_2 = 0.390$ N, where P_2 is estimated by extrapolating the curve during stage 2 back to the displacement level at which the jump is enforced. In a similar manner, the values of $P_3 = 1.63$ N and $P_4 = 1.74$ N were estimated. The value of m for the jump from stage 1 to stage 2 was then calculated from

$$m = \frac{\ln(P_2/P_1)}{\ln(\dot{h}_2/\dot{h}_1)}, \tag{4.22}$$

with an analogous calculation yielding an estimation of the value of m for the

jump from stages 3 to 4. The nominal strain-rates during the jump have been approximated by $\dot{h}_i/h_*$, where the displacement rate at stage i is $\dot{h}_i$ and the displacement at the instant the jump is imposed is h_*. This procedure gives a value of $m = 0.081$ for the jump from stage 1 to stage 2 and $m = 0.075$ for that corresponding to stages 3 and 4. While the estimated values of m from our indentation rate-jump experiments are higher than that of $m = 0.043$ approximated from simple compression, we note that the value from simple compression was estimated from the steady-state response of the material after a strain-rate increment was imposed. However, an estimation of m from the initial rate-jump response in simple compression provides a bound for m on the order of 0.15, which provides a bound for our estimates from the indentation rate-jump experiments.

3. *Determination of s_0 and α.* As noted previously, in order to determine the pressure sensitivity parameter α, experiments conducted in tension and compression with various levels of superposed hydrostatic pressure must in general be performed. While experimental results from a single indentation P-h curve would not allow for a direct determination of α, we propose to introduce a different stress-state under the indenter than that realized in Berkovich indentation by using a spherical indenter. Our numerical results indicate that for indentation of PMMA at 25 mN/s at a load level of 2.5 N for Berkovich and spherical indentation using a 1.59 mm diameter stainless steel tip, the maximum value of the hydrostatic pressure under the indenters is approximately 190 MPa and 130 MPa for Berkovich and spherical indentation, respectively. This difference of 60 MPa allows us to obtain a marked difference between the stress-states under the indenter tips which provides a convenient method to estimate α between two different indentation experiments. As a methodology to obtain an estimate of s_0 and α, we propose to use our predetermined values of E, ν_0 and m and to numerically fit the loading curve for Berkovich indentation by adjusting s_0 and α. Once a reasonable fit of the loading curve for Berkovich indentation is

obtained, the loading curve for spherical indentation is independently predicted. The process of fitting to Berkovich indentation data and predicting the spherical indentation data is repeated until both numerical curves are in good accord with the experimental results. Our method thus provides an independent method to fit for values of s_0 and α. As validation of the predictive capability of our constitutive model for spherical indentation, we show a comparison of the predicted loading curves for Berkovich and spherical indentation in Fig. F-78, where the model predictions are seen to be in good accord with the experimental results.

In the next section, we demonstrate an application of our inverse approach to the amorphous glassy polymer polystyrene.

4.6 Application to sharp-indentation of polystyrene

In this section, we apply our inverse approach to indentation data obtained for polystyrene (PS). Recall that the list of material parameters that may be determined from indentation data is given by

$$\{E, s_0, \nu_0, m, \alpha\}. \tag{4.23}$$

The indentation and compression samples were machined from 12.3 mm thick stock and polished in a 0.05μm alumina slurry. The samples were then annealed for two hours at the glass transition temperature of 100°C followed by quenching in ice-water for 20 minutes.

Following our methodology, we have estimated the material parameters for PS from (*i*) A Berkovich indentation experiment conducted at a suitably low-load with a relatively high unloading rate for the estimation of E, (*ii*) a Berkovich indentation experiment incorporating a loading rate-jump for the determination of ν_0 and m, and (*iii*) a spherical indentation experiment used in conjunction with our Berkovich indentation data to determine s_0 and α. We proceed in a step-by-step manner to detail our process of property extraction from indentation data:

1. The Berkovich indentation experiment shown in Fig. F-79a was conducted to a peak load of approximately 19 mN at 2 mN/s. A dwell time of 300 s was incorporated at the peak load and unloading was conducted at 20 mN/s. An unloading analysis following the procedure outlined in the previous section was performed. In performing the analysis, an initial unloading slope of $S_m = \left.\frac{dP}{dh}\right|_{h=h_m} = 37.92$ mN/μm measured at $h_m = 3.69$ μm and a maximum load of $P_m = 19.04$ mN at initial unloading were calculated from the P-h data. The contact depth h_c was then estimated from $h_c = 3.31h_m - 0.75(P_m/S_m)$, which gives $h_c = $ μm. Using the relation for the contact area A_c for a Berkovich geometry tip of $A_c = 24.5h^2$, the value of E was estimated from $E = (1 - \nu^2)\frac{S_m}{2.16}\sqrt{\frac{\pi}{A_c}}$, where upon assuming a value of $\nu = 0.33$ yields a value of $E =$ 1.691 GPa for our PS samples.

2. The next step in the analysis is to perform a Berkovich indentation experiment with a loading rate-jump imposed during loading; the experimental response is shown in Fig. F-79b. The initial portion of the test, stage 1, was conducted at a loading rate of 30 mN/s. Upon reaching a displacement of $h_* = 23.7\,\mu$m, the rate was instantaneously increased one order-of-magnitude to stage 2. The positive rate-sensitivity of the material is clearly seen in Fig. F-79b, as evidenced by the increased stiffness of the P-h response with increasing loading rate. The displacement rates measured as the jump was imposed were $\dot{h}_1 = 0.384\,\mu$m/s and $\dot{h}_2 = 2.27\,\mu$m/s for stages 1 and 2, respectively. A value of $\nu_0 = 0.001$/s was assumed and m is calculated was estimated by following the procedure outlined in the previous section. To estimate a nominal measure of the stress-state under the indenter, we use the values of P_1 and P_2, where P_2 is estimated by extrapolating the curve during stage 2 back to the displacement level h_* at which the jump is enforced. The value of m was estimated from:

$$m = \frac{\ln(P_2/P_1)}{\ln(\dot{h}_2/\dot{h}_1)} \qquad \text{with} \qquad \nu_0 = 0.001 \quad s^{-1}. \tag{4.24}$$

This procedure gives a value of $m = 0.0741$.

3. Using our the values of E, m and ν_0 thus obtained, we perform a numerical fit of the loading portion of the P-h curve for Berkovich indentation conducted at 25 mN/s and independently predict the loading curve for spherical indentation conducted at 25 mN/s. The results of our iterative fitting process are shown in Fig. F-79c, where the values of $s_0 = 18.2$ MPa and $\alpha = 0.10$ were found to provide a reasonable fit to both sets of indentation data.

With the values of $\{E, s_0, \nu_0, m\}$ thus estimated, the next step was to perform a validation of our data by conducting simple compression experiments on our PS samples and comparing the predicted stress-strain response to the experimental response. A stress-strain curve obtained from a simple compression experiment conducted at a constant true-strain rate of -0.001/s is shown in Fig. F-80a in comparison to the predicted response obtained with the material parameters estimated from indentation. We emphasize that this is a predicted response in simple compression based upon two indentation experiments, with no a priori knowledge of the material behavior. Considering that frictional effects in the compression simulation have been neglected, our initial approach for the reverse problem in indentation of amorphous polymers is encouraging. As a final validation of our procedure, a strain-rate jump experiment was performed in simple compression; the strain-rate was increased one order-of-magnitude from -0.001/s to -0.01/s. The resulting experimentally obtained stress-strain curve is shown in Fig. F-80b compared to the predicted response obtained using our material parameters from indentation. The trend of the macroscopic stress-strain curve as well as the levels are reasonably well-predicted by the constitutive model. The strain-rate sensitivity parameter was estimated to be approximately $m = 0.04$ from the strain-rate jump experiment in simple compression. While the value of $m = 0.0741$ estimated from indentation is somewhat higher, it provides a reasonable bound for our estimation of m.

4.7 Concluding remarks

This chapter presents a study of the forward problem in instrumented sharp indentation of amorphous polymeric solids, with application to PC and PMMA. We use the constitutive model of Anand & Gurtin (2002) to model the material behavior. Calibration of the model to the response of both PC and PMMA in simple compression yields an excellent fit to the overall stress-strain response for strains up to approximately 120%.

After calibrating our testing and modeling approach to a study of Berkovich indentation of Al6061-T6, we predict the P-h curves and indent morphologies for PC and PMMA subjected to both conical and Berkovich indentation. The general features of the P-h curves as well as the load and displacement levels are well predicted by our constitutive model. A parametric study reveals that the dominant material parameters that determine the indentation response are the Young's modulus E, an average value of the deformation resistance s_0, and the rate-sensitivity parameter of the material m. The back-stress and the pressure sensitivity of plastic flow are shown to have a negligible effect on the P-h curves.

Our parametric study and dimensional analysis motivate a framework for a reverse approach for sharp-indentation of amorphous polymeric solids. As an example application of a first attempt at an inverse scheme for the extraction of the material parameters E, s_0 and m we consider indentation of PS. From two indentation experiments, we show that our approach is capable of reasonably-well predicting the stress-strain response of PS in simple compression in monotonic loading as well as in loading with a strain-rate jump imposed.

This work may be further developed by formulating a more rigorous framework for the reverse problem in instrumented sharp-indentation of amorphous polymeric solids. Our validation of the applicability of the constitutive model for predicting the P-h curves and indent morphologies observed in micro-indentation of PC and PMMA combined with our parametric study and simple framework for the reverse problem establish a starting point for accomplishing this goal.

References

ABAQUS Reference manuals. (2001). Pawtucket, R.I.

Anand, L. (1979). On H. Hencky's approximate strain-energy function for moderate deformations. *ASME Journal of Applied Mechanics, 46,* 78-82.

Anand, L. (1993). A constitutive model for interface friction. *Computational Mechanics, 12,* 197-213.

Anand, L. (1996). A constitutive model for compressible elastomeric solids. *Computational Mechanics, 18,* 339-352.

Anand, L., & Gurtin, M. (2002). A theory of amorphous solids undergoing large deformations, with applications to polymers and metallic glasses. *International Journal of Solids and Structures, submitted.*

Andrews, E. H. (1973). Cracking and crazing in polymeric glasses. In R. N. Haward (Ed.), *The Physics of Glassy Polymers. First Edition* (p. 394-453). Applied Science, New York.

Argon, A. (1999). Craze plasticity in low molecular weight diluent-toughened polystyrene. *Journal of Applied Polymer Science, 72,* 13-33.

Argon, A., & Hannoosh, J. G. (1977). Initiation of crazes in polystyrene. *Philosophical Magazine, 36,* 1195-1216.

Argon, A., Hanoosh, J. G., & Salama, M. M. (1977). Initiation and growth of crazes in glassy polymers. *Fracture 1977, 1,* 445-470.

Arruda, E. M., & Boyce, M. C. (1993). Evolution of plastic anisotropy in amorphous polymers during finite straining. *International Journal Of Plasticity, 9*, 697-720.

Barenblatt, G. I. (1959). The formation of equilibrium cracks during brittle fracture: general ideas and hypotheses, axially symmetric cracks. *Applied Mathematics and Mechanics (PMM), 23*, 622-636.

Bhattacharya, A. K., & Nix, W. D. (1991). Finite element analysis of cone indentation. *International Journal of Solids and Structures, 27*, 1047-1058.

Bhushan, B. (1995). *Handbook of Micro/Nano Tribology.* CRC Press.

Boyce, M. C., Parks, D. M., & Argon, A. S. (1988). Large inelastic deformation of glassy polymers. part 1: rate-dependent constitutive model. *Mechanics of Materials, 7*, 15-33.

Briscoe, B. J., Fiori, L. , & Pelillo, E. (1998). Nano-indentation of polymeric surfaces. *Journal of Physics D: Applied Physics, 31*, 2395-2405.

Briscoe, B. J., & Sebastin, K. S. (1996). The elastoplastic response of poly(methyl methacrylate) to indentation. *Proceedings of the Royal Society, London, A, 452*, 439-457.

Camacho, G. T., & Ortiz, M. (1996). Computational modeling of impact damage in brittle materials. *International Journal of Solids and Structures, 33*, 2899-2938.

Cheng, Y. T., & Cheng, C. M. (1998). Scaling approach to conical indentation of elastic-plastic solids with work-hardening. *Journal of Applied Physics, 84*, 1284-1291.

Cheng, Y. T., & Cheng, C. M. (1999). Scaling relationships in conical indentation of elastic-perfectly plastic solids. *International Journal of Solids and Structures, 36*, 1231-1243.

Chong, C. M. , & Lam, C. C. (1999). Strain gradient plasticity effect in indentation hardness of polymers. *Journal of Materials Research, 14*, 4103-4110.

Courtney-Pratt, J. S. , & Eisner, E. (1957). The effect of a tangential force on the contact of metallic bodies. *Proceedings of the Royal Society A, 238*, 529-550.

Dao, M., Chollacoop, N., Van-Vliet, K. J., Venkatesh, T. A., & Suresh, S. (2001). Computational modeling of the forward and reverse problems in instrumented sharp indentation. *Acta Materialia, 49*, 3899-3918.

Doerner, M. F., & Nix, W. D. (1986). A method for interpreting the data from depth-sensing indentation instruments. *Journal of Materials Research, 1*, 601-609.

Donald, A. M. (1997). Crazing. In R. N. Haward & R. J. Young (Eds.), *The Physics of Glassy Polymers. Second Edition* (p. 295-341). Chapman & Hall, New York.

Dugdale, D. S. (1960). Yielding of steel sheets containing slits. *Journal of the Mechanics and Physics of Solids, 8*, 100-104.

Estevez, R., Tijssens, M. G. A., & VanderGiessen, E. (2000). Modeling of the competition between shear yielding and crazing in glassy polymers. *Journal of the Mechanics and Physics of Solids, 48*, 2585-2617.

Gearing, B. P., Gudlavalleti, S. , & Anand, L. (2002). Novel testing apparatuses for mechanical testing at the small scale. *Experimental Mechanics, to be submitted.*

Gearing, B. P., Moon, H. S. , & Anand, L. (2001). A plasticity model for interface friction: application to sheet metal forming. *International Journal of Plasticity, 17*, 237-271.

Giannakopolous, A. E., Larsson, P. L., & Vestergaard, R. (1994). Analysis of vickers indentation. *International Journal of Solids and Structures, 31*, 2679-2708.

Giannakopolous, A. E., & Suresh, S. (1999). Determinantion of elastoplastic properties by instrumented sharp indentation. *Scripta Materialia, 40*, 1191-1198.

Hasan, O. A., & Boyce, M. C. (1995). A constitutive model for the nonlinear viscoelastic viscoplastic behavior of glassy polymers. *Polymer Engineering and Science, 35*, 331-344.

Ishikawa, M., Narisawa, I., & Ogawa, H. (1977). Criterion for craze nucleation in polycarbonate. *Journal of Polymer Science, 15*, 1791-1804.

Johnson, M. D. (2001). *Deformation and fracture of polycarbonate and rubber-modified polycarbonate under controlled temperature, deformation rate, and notch stress triaxiality.* Unpublished master's thesis, Massachusetts Institute of Technology.

Kambour, R. P. (1973). A review of crazing and fracture in thermoplastics. *Journal of Polymer Science, 7*, 1-154.

Kinloch, A. J., & Young, R. J. (1983). *Fracture behavior of polymers.* Elsevier.

Kramer, H. H. (1983). Microscopic and molecular fundamentals of crazing. *Advances in Polymer Science, 52*, 1-56.

Kroner, E. (1960). Allgemeine kontinuumstheorie der versetzungen und eigenspannungen. *Archive for Rational Mechanics and Analysis, 4*, 273-334.

Larsson, P. L., Giannakopolous, A. E., Soderlund, E., Rowcliffe, D. J., & Vestergaard, R. (1996). Analysis of berkovich indentation. *International Journal of Solids and Structures, 33*, 221-248.

Lee, E. H. (1969). Elastic plastic deformation at finite strain. *ASME Journal of Applied Mechanics, 36*, 1-6.

Lim, Y. Y., & Chaudhari, M. M. (1999). The effect of indenter load on the nanohardness of ductile metals: an experimental study on polycrystalline work-hardened and annealed oxygen-free copper. *Philosophical Magazine A, 79*, 2979-3000.

Narisawa, I., & Yee, A. F. (1993). Crazing and fracture of polymers. *Materials Science and Technology. A comprehensive Treatment, 12*, 699-765.

Nimmer, R., & Woods, J. (1992). An investigation of brittle failure in ductile notch-sensitive thermoplastics. *Polymer Engineering and Science, 32*, 1126-1137.

Oliver, W. C., & Pharr, G. M. (1992). An improved technique for determining hardness and elastic modulus using load and displacement sensing indentation experiments. *Journal of Materials Research, 7*, 1564-1583.

Oxborough, R. J., & Bowden, P. B. (1973). A general critical-strain criterion for crazing in amorphous polymers. *Philosphical Magazine, 28*, 547-559.

Parks, D. M., , Argon, A. S., & Bagepalli, B. (1985). Large elastic-plastic deformation of glassy polymers. part 1: constitutive modeling. *MIT, Program in Polymer Science and Technology Report.*

Pethica, J. B., Hutchings, R., & Oliver, W. C. (1983). Hardness measurements at penetration depths as small as 20 nm. *Philosophical Magazine A, 48*, 593-606.

Rabinowitz, S., Ward, I. N., & Parry, J. C. (1970). The effect of hydrostatic pressure on the shear yield behavior of polymers *Journal of Materials Science, 5*, 29-39.

Rikards, R., Flores, A., Ania, F., Kushnevski, V., & Balta-Calleja, F. (1998). Numerical-experimental method for identification of plastic properties of polymers from microhardness tests . *Computational Matetrials Science, 11*, 233-244.

Rose, J., Smith, J. R., & Ferrante, J. (1983). Universal features of bonding in metals. *Physical Review B, 28*, 1835-1845.

Socrate, S., Boyce, M., & Lazzeri, A. (2001). A micromechanical model for multiple crazing in high-impact polystyrene. *Mechanics of Materials, 33*, 155-175.

Spitzig, W. A., & Richmond, O. (1979). Effect of hydrostatic pressure on the deformation behavior of polyethylene and polycarbonate in tension and compression. *Polymer Engineering and Science, 19*, 1129-1139.

Sternstein, S. S., & Meyers, F. A. (1973). Yielding of glassy polymers in the second quadrant of principal stress space. *Journal of Macromolecular Science, Phys. B8*, 539-571.

Sternstein, S. S. , & Ongchin, L. (1969). Yield criteria for plastic deformation of glassy high polymers in general stress fields. *Polymer Preprints, 10*, 1117-1124.

Tijssens, M. G. A., VanderGiessen, E., & Sluys, L. J. (2000a). Modeling of crazing using a cohesive surface methodology. *Mechanics of Materials, 32*, 19-35.

Tijssens, M. G. A., VanderGiessen, E., & Sluys, L. J. (2000b). Simulation of Mode I crack growth in polymers by crazing. *International Journal of Solids and Structures, 37*, 7307-7327.

Treloar, L. R. G. (1975). *The Physics of Rubber Elasticity.* Oxford.

Venkatesh, T. A., Van Vliet, K. J., Giannakopoulos, A. E., , & Suresh, S. (2000). Determination of elasto-plastic properties by instrumented sharp indentation: guidelines for property extraction. *Scripta Materialia, 42*, 833-839.

Weber, G., & Anand, L. (1990). Finite deformation constitutive equations and a time-integration procedure for isotropic, hyperelastic-viscoplastic solids. *Computer Methods in Applied Mechanics and Engineering, 79*, 173-220.

Williams, J. G. (1984). *Fracture mechanics of polymers.* Ellis Horwood.

Wu, P. D., & VanderGiessen, E. (1993). On improved network models for rubber elasticity and their applications to orientation hardening of glassy polymers. *Journal of the Mechanics and Physics of Solids, 41*, 427-456.

Xu, X. P., & Needleman, A. (1994). Numerical simulations of fast crack growth in brittle solids. *Journal of the Mechanics and Physics of Solids, 42*, 1397-1434.

Zuber, P. J. (1985). *Initiation of ductile fracture from shear bands in u-notched four-point bend tests.* Unpublished master's thesis, Massachusetts Institute of Technology.

Appendix A

Function inverse to the Langevin function

To evaluate $a = \mathcal{L}^{-1}(b)$ for a given b in the range $0 < b < 1$, we may numerically solve the non-linear equation $f(a) = \mathcal{L}(a) - b = 0$ for a. However, for numerically intensive calculations, it is desirable to avoid an iterative solution scheme for $\mathcal{L}^{-1}$. We instead use the following series expansion to approximate the function inverse to the Langevin function:

$$\begin{aligned}\mu/\mu_R &= 1 + 0.6c^2 + 0.5657c^4 + 0.5863c^6 + 0.6240c^8 + 0.6657c^{10} + \\ &\quad 0.7043c^{12} + 0.7340c^{14} + 0.7510c^{16} + 0.7520c^{18} + 0.7353c^{20} + \\ &\quad 0.7020c^{22} + 0.6547c^{24} + 0.5987c^{26} + 0.5417c^{28} + 0.4933c^{30} + \\ &\quad 0.4643c^{32} + 0.4650c^{34} + 0.5042c^{36} + 0.5860c^{38} + 0.7094c^{40} + \\ &\quad 0.8654c^{42} + 1.0368c^{44} + 1.1978c^{46} + 1.3158c^{48} + 1.3547c^{50}, \qquad \text{(A.1)}\end{aligned}$$

where $c = \dfrac{\lambda^p}{\lambda_L}$. The series expansion is compared to an iterative solution in Fig. F-81, where the expansion is seen to match the iterative solution to within 1% at a value of $\lambda^p = 0.99\lambda_L$. Utilizing this series expansion is less expensive computationally than an iterative approach when solving three-dimensional finite element simulations.

Appendix B

Guideline for model calibration

In this appendix we present a guideline for our calibration procedure to obtain material parameters for shear-yielding. For illustrative purposes, we demonstrate the estimation of our material parameters for PC. Recall that the material parameters that must be determined for our constitutive model for shear-yielding are:

1. The elastic shear and bulk moduli (G, K) in the elastic part of the free energy.
2. The parameters (μ_R, λ_L) in the plastic part of the free energy.
3. The parameters $\{\nu_0, m, \alpha, s_0, h_0, g_0, s_{cv}, b, \eta_{cv}\}$ in the flow rule and the evolution equations for (s,η).

The experimental estimates of (ν_0, m) are obtained by conducting a strain rate jump experiment. In Fig. F-82, we show three simple compression experiments conducted on PC, two of which were conducted at constant true strain rates of -0.001/s and -0.01/s. The third experiment shows the response to a jump in the true strain rate from -0.001/s to -0.01/s. As can be seen from Fig. F-82, the rate jump experiment indicates an initial transient response upon the imposed jump followed by a gradual saturation to a steady-state stress level which is approximately equal to that of the corresponding experiment conducted monotonically at a strain rate of -0.01/s. Using this result, we shall approximate a strain rate sensitivity parameter m from the steady-state level attained after the strain rate jump is imposed. In Fig. F-83 we show

the calculation of m from the strain-rate jump experiment in Fig. F-82. As indicated in Fig. F-83, the reference equivalent shear strain rate ν_0 is taken as $\nu_0 = 0.0017/s$, which is a factor of $\sqrt{3}$ times the reference equivalent strain rate of 0.001/s. Recall that the equivalent shear strain rate is given by

$$\nu^p = \nu_0 \left(\frac{\bar{\tau}}{s - \alpha\sigma} \right)^{\frac{1}{m}}. \tag{B.1}$$

Assuming that the state of the material stays constant as the jump is imposed and neglecting the change in $\alpha\sigma$, the value of m may be estimated from

$$m = \frac{\ln(\bar{\tau}_2/\bar{\tau}_1)}{\ln(\nu_2^p/\nu_1^p)}, \tag{B.2}$$

where the subscripts 1 and 2 denote the true strain rate prior to and after the rate jump is imposed, respectively. The construction line indicated in Fig. F-83 is extrapolated back to the strain at which the rate increment is imposed. Note as well that the strain rate jump is imposed prior to the strain range where the effects of the back-stress become dominant on the material stress-strain response. Thus, the values of $\bar{\tau}_1$ and $\bar{\tau}_2$ may be estimated from the experiment by dividing the uniaxial values by a factor of $\sqrt{3}$.

Using our values of (ν_0, m) and a value of $\alpha = 0.08$ from Spitzig & Richmond (1979), the remaining material parameters $\{G, K, \mu_R, \lambda_L, h_0, g_0, s_{cv}, b, \eta_{cv}, s_0\}$ are determined from a stress-strain curve for simple compression of PC under monotonic loading. A stress-strain curve for simple compression conducted at a constant true strain rate of -0.001/s is shown in Fig. F-84, where we have indicated specific regions of the stress-strain response and the corresponding material parameters that dominate these regions. For the elastic constants, (G, K), it is convienient with respect to the simple compression stress-strain response to work with the pair the Young's modulus E and Possion's ratio ν. The standard transformations of linear elasticity

relate (E, ν) to (G, K)

$$E = \frac{9KG}{3K+G} \qquad \text{and} \qquad \nu = \frac{1}{2}\left[\frac{3K-2G}{3K+G}\right]. \tag{B.3}$$

As indicated in Fig. F-84, with a value of $\nu = 0.33$, the Young's modulus E determines the initial linear slope of the stress-strain response. In general, if ν is not known a priori, a value of E may be determined from the initial loading slope of the simple compression experiment,[1] and a value for ν may then be determined from a plane strain compression or tension experiment since the initial slope is given by $E/(1-\nu^2)$.

The deviation from initial linearity in Fig. F-84 is determined by the value of s_0, and the slope during the initial nonlinearity is dominated by the value of h_0, with higher values of h_0 yielding a higher slope. The region of the stress-strain curve just prior to the peak and until strains of approximately 35% is determined predominantly by the paramters $\{b, \eta_{cv}, g_0\}$. In Fig. F-85, Fig. F-86 and Fig. F-87, we show the sensitivity of the stress-strain curve to variations of 25% and 50% relative to the fit values for PC for b, η_{cv} and g_0, respectively. Following this region, the value of s_{cv} determines the level at which the experimental response will tend to saturate following the post-peak strain-softening response.

The parameters (μ_R, λ_L) in the plastic part of the free energy dominate the stress-strain response at strain levels exceeding approximately 50%. The sensitivity of the stress-strain response to variations of 25% and 50% in μ_R and λ_L relative to our fit values for PC is shown in Fig. F-88 and Fig. F-89, respectively.

[1]Note that due to compliance effects in simple compression, the preferred experiment to determine E is a tension test using an extensometer to isolate the displacement of the material over the gauge section.

Appendix C

Instrumented indentation apparatus

C.1 Microindentation apparatus

The instrumented microindentation apparatus[1] is shown in Fig. F-90. The system uses a double compound spring, which consists of two identical compound springs symmetrically disposed around a common centerline. The use of a double compound spring minimizes the potential for rotations or parasitic deflections due to either machining imperfections or to variations in the properties of the frame material. Design and manufacturing issues concerning the indenter as well as several other novel small scale testing devices recently developed at MIT may be found in Gearing et al. (2002). All vendor information is contained in a vendor list in Appendix E. An extension of the single apparatus indentation devices to a biaxial compression/shear apparatus is presented in Appendix D.

The apparatus is an integral design machined from a 12.7 mm thick Al7075-T6 rolled plate. Key dimensions of the design are shown in Fig. F-91, where tabs securing the compound flexures to the frame are shown. These anchoring tabs ensure that the flexure is not damaged when final milling is performed to level critical edges. The

[1] Various aspects of the design are patent pending.

tabs are milled off in the last machining step.

The monolithic system is cut by water-jet machining and is composed of a limited number of assembled parts. Thus, errors due to assembly of multiple components are eliminated. As well, the design incorporates "hard-stops" so that the bending stressses in the compound springs do not exceed 100 MPa. For the Al7075 plate used, this maximum stress gives a safety factor of about 5 for yielding and allows for a fatigue life of greater than 10^8 cycles. The design is scaleable, therefore a large range of forces and displacements may be achieved simply by changing the geometry of the system, the material used for the frame, and/or the actuators incorporated into the system.

The "centerpiece" of the indenter indicated in Fig. F-90 is displaced by a voice coil driven by a precision amplifier which receives an input signal from a 16-bit computer-controlled data acquisition board. Flexure displacements are measured with commercially available non-contacting eddy-current sensors with a resolution of 20 nm over a range of 1.25 mm. The sensors may be changed to achieve better displacement resolution if desired. The system stiffness of $K_S = 2.13$ N/mm is found by precision weight calibration, and the electronics have a linear transfer function of $K_E = 1.31$ N/V. If a voltage divider is incorporated, the best achievable electronic transfer function with the current system is 13.1 mN/V. Calibration curves for the spring stiffness and the driving electronics are shown in Figs. F-92 and F-93, respectively. The resolutions of the electronics and the displacement sensors along with the appropriate transfer functions determine the load resolution of 80 μN over a range of 8 N. In order to minimize environmental disturbances, the indentation system is secured to an isolation table.

The specimen is held on a stiff vertical displacement stage which holds the displacement sensor as close as possible to the specimen in order to minimize compliance contributions from the specimen stage and the centerpiece. The system compliance is estimated to be approximately 1200 N/mm, which is about 560 times as stiff as the system spring constant. Various indenter geometries may be threaded into the indenter frame as indicated in Fig. F-90.

A test is conducted by driving the indenter tip into a specimen and monitoring the displacement as a function of output voltage from the computer. A curve demonstrating the acquired data is shown in Fig. F-94. The mechanical and electrical transfer functions are then used to find the load on the specimen as a function of the indentation depth, or P-h curve via
No contact with specimen:

$$K_E \cdot \text{Output Voltage} = K_S \cdot \text{Displacement}, \tag{C.1}$$

where Fig. F-94 shows this initial linear region prior to contact. This approach allows for real-time calibration of K_E with each indentation test. Once contact occurs as indicated in Fig. F-94:

$$P = K_E \cdot \text{Output Voltage} - K_S \cdot h \tag{C.2}$$

and thus the P-h curve may be extracted from the acquired data. The Labview 6.0 virtual instruments (vi) also acquire elasped time as the test progresses. A graph of P versus time allows for a calculation of the loading rate during the indentation test.

As a calibration of our experimental device and procedures, we have conducted indentation experiments on fused silica, which has been suggested recently in the literature as a benckmark material for indentation studies. Since fused silica is known to fracture at loads exceeding about 300 mN, all tests were conducted below this limit. Five experiments conducted at 5 mN/s are shown in Fig. F-95, where the repeatibility of the results is excellent. Note as well that the displacement sensor resolution is apparent in the experimental P-h curves. Following the approach of Oliver-Pharr (1992), an analysis of the unloading slopes was conducted to find an approximate value for the Young's modulus E of the fused silica. The analysis yielded a value of $E = 69.5$ GPa, which compares well with the published value of 73 GPa. The

hardness was calculated as approximately 6.6 GPa, which falls within the reported range of values varying from 5.5 GPa to 9.7 GPa. The values for the Young's modulus of fused silica appear to vary far less from source to source as compared to the values of hardness. Thus, it appears that E is a more consistent value upon which to base our experimental calibration.

Further examples of the capabilities of the apparatus are shown in Figure F-96, which demonstrates the range of displacements attainable for a variety of soft materials. The drastic difference in material response for an unfilled rubber versus a polycarbonate sample is saliently observed.

C.2 Nanoindentation apparatus

The ability to scale the design of our flexure-based systems has been exploited to produce the instrumented nanoindentation apparatus shown in Fig. F-97, where the features of the system are similar to those of the microindenter of Fig. F-90. In contrast to the microindenter, the nanoindenter uses a smaller capacity voice coil and is designed to have a system spring stiffness of 0.25 N/mm, which is an order of magnitude lower than that of the previous design. The key dimensions of the nanoindenter are shown in Fig. F-98. The design is machined from a 6.35 mm thick plate of Al7075-T6. Once the design is machined via water-jet cutting, the tabs seen in Fig. F-98 serve to secure the compound flexures. Edges that must be parallel are milled or smoothed with EDM machining, and the tabs are carefully removed as the final machining step. The design is machined from a 6.35 mm thick plate of Al7075-T6.

System calibration yields a spring constant of $K_S = 0.253$ N/mm and an electronic transfer function of $K_E = 0.622$ mN/V as shown in Figs. F-99 and F-100, respectively. The nanoindenter has a force resolution of 4 μN over a range of 400 mN. With the mechanical and electrical transfer functions known, data from an indentation test is analyzed in a manner identical to that followed for the microindenter.

As a calibration of the nanoindentation apparatus, we conduct Berkovich indenta-

tion of fused silica. The experiments were conducted at 1.20 mN/s, and the resulting P-h curves are shown in Fig. F-101. A representative P-h curve obtained with the nanoindentation apparatus is compared to a result from the microindentation apparatus in Fig. F-102. The new testing range spanned by the nanoindenter is clearly observed from Fig. F-102. This result underscores the scalable nature of our designs.

An analysis of the initial unloading slope yields a Young's modulus of $E = 72.0$ GPa and a hardness of 9.87 GPa. Whereas the value of E compares well both with the bulk value of 73 GPa and with the microindentation result of 69.5 GPa, the hardness of 9.87 GPa, albeit this value falls within the reported ranges of hardness, is higher than the value of 6.6 GPa obtained with the microindenter. However, an investigation of the residual Berkovich indent shows salient cracking at the edges of the indents obtained with the microindenter and no apparent edges cracks on the indents obtained in the load range of the nanoindenter. Thus, the Young's modulus appears to be a more consistent value upon which to base calibration of different indentation apparatuses if the candidate material chosen to benchmark from is fused silica.

Appendix D

Biaxial compression/shear apparatus

The biaxial testing apparatus is shown in Fig. F-103. Two flat bodies whose interfacial response is to be investigated are brought together in the space denoted as "specimen." One body is attached at the base of the "flexure for normal force," and the opposing body is secured to the "shear displacement flexure." Normal forces on the interface are applied using a voice-coil actuator acting through the "flexure for normal force." Tangential displacements at the interface are achieved by actuating the "shear displacement flexure" with a piezo-electric inchworm actuator. The tangential force arising from the interfacial interaction is measured by the resulting displacement of the "flexure for shear force." All displacements are measured using non-contacting eddy current sensors with a resolution of 20 nm over a range of 1.25 mm.

The design incorporates compound spring flexures within a monolithic frame and possesses only a limited number of assembled parts. Thus, device assembly errors and backlash are minimized. The use of the double compound springs for actuation in the normal direction minimizes the potential for rotations or parasitic deflections due to either machining imperfections or to variations in the properties of the frame material. The frame is a monolithic, light weight design made of 12.7 mm thick Al7075-T6 plate and is 440 mm x 460 mm in size. Hard-stops ensure that the maximum bending stress

in the spring webs does not exceed 5 MPa, which provides essentially infinite fatigue life. The normal axis is nested within the shear load cell and has been designed using FEA to minimize cross-talk between normal force application and shear force measurement. The design also allows for the measurement of relative separation or approach of the surfaces in the normal direction as a test is conducted.

The normal force is controlled with a resolution of 80 μN over a range of 5 N, the shear force is measured with a resolution of 225 μN up to 15 N, tangential displacement is imposed in 4 nm steps up to 6.35 mm, and the relative motion of the surfaces in the normal direction is measured with a resolution of 20 nm over a range of 1.25 mm.[1] Imposed displacement rates range from 0.5 μm/s to 600 μm/s. The entire system rests upon a vibration-isolated table to minimize environmental disturbances.

Calibration of the flexure stiffness for each axis is achieved by measuring the displacement of the axis under precision weights. In the present embodiment of the design, the normal axis has a stiffness of 9.53 N/mm, and the stiffness of the tangential axis is 43.2 N/mm as shown by the calibration curves in Fig. F-105. The electronics driving the normal axis are calibrated by measuring the normal displacement due to known computer output voltage ramps. The electronic system (consisting of a 16-bit data acquisition board, a precision amplifier powered by a low-noise source, and the voice coil) has a transfer function of 1.31 N/V, which yields the same calibration curve as that shown in Fig. F-93 since the driving electronics are the same. All system responses are highly linear over their operating ranges. The transfer functions of the mechanical and electrical systems are utilized to apply a precise normal load on an interface under compression.

The simple, compact physical design of the apparatus may be scaled to allow for testing over a wide range of normal and shear forces, as well as a large range of imposed tangential displacements.[2] Design and manufacturing issues concerning the compression/shear apparatus as well as several other novel small scale testing devices

[1] Displacement sensors with improved sensitivity may be used for better force and displacement resolution.

[2] Various aspects of the design are patent pending.

recently developed at MIT may be found in Gearing et al. (2002).

An example of experimental data obtained with the biaxial apparatus is shown by the tangential force-sliding distance response in Fig. F-106. The interface is an Al6111-T4 2 mm x 2 mm coupon (with an as-received surface texture) against polished tool steel. A normal force of 1 N was imposed on the interface, and the tangential sliding velocity was 6 μm/s, with regions where the tangential displacement was reversed and then imposed again in the initial sliding direction. The negative sign on the tangential force axis indicates motion in the opposite direction to that initially imposed on the interface. The ability to precisely measure the tangential stiffness of an interface (represented by the slope of the linear "unloading-reloading" regions) is a novel capability of our apparatus. These "unloading-reloading" portions are reminiscent of the classical results (at a more macroscopic scale) of Courtney-Pratt and Eisner (1957), and serve as experimental motivation for adhering-slipping models of interface friction (e.g. Anand, 1993; Gearing et al., 2001). The slope of the "unloading-reloading" curve is termed the tangential stiffness in adherence in Anand (1993), and previously was experimentally difficult to measure. The coefficient of friction (defined as the ratio of the tangential force to the applied normal force) as a function of sliding distance is shown in Fig. F-107, where we note that the measured values of the coefficient of friction are consistent with previous standard pin-on-disk friction tests.

A second diagnostic test was conducted to demonstrate the range of tangential displacement rates attainable with the apparatus. A 1 mm thick 2 mm x 2 mm coupon of polycarbonate (PC) was loaded against the polished tool steel surface with a normal force of 750 mN. A sliding velocity of 100 μm/s was applied and the PC specimen was displaced cyclically relative to the tool steel until the tangential force reached a steady-state value of 171 mN, which occurred at a total displacement of about 11 mm. At this state, the sliding velocity was reduced to 10 μm/s for an additional 2 mm of sliding. The velocity was then increased to 500 μm/s at the final stage of sliding. Figure F-108 shows the tangential force as a function of sliding distance as the sliding rate decrement and increment are imposed. The solid lines are

the average value of the tangential force at the corresponding sliding velocity. We note that this interface exhibits *positive rate sensitivity.* This result demonstrates the range of displacement rates that may be obtained with the apparatus.

As further validation of our new testing capabilities, we investigate the frictional response of two interfaces of relevance to MEMS. The first interface is single crystal silicon (Si) contacting Si, and the second interface is a 1 μm thick diamond-like carbon (DLC) thin film on Si contacting DLC on Si. Both tests were conducted on *as-fabricated* 0.8 mm thick 2.2 mm x 2.2 mm diced square coupons against 0.8 mm thick 12.7 mm x 12.7 mm pieces.

The normal load was held constant at 2 N as the interfaces were displaced relative to each other at a velocity of 10 μm/s. Figure F-109 shows the measured tangential force-sliding distance response, and Fig. F-110 shows the coefficient of friction as a function of the imposed tangential sliding distance. At a sliding distance of 400 μm, the coefficient of friction is 0.32 for the Si/Si interface, which compares to the much lower value of 0.11 for the DLC/DLC interface. These results serve as confirmation of the current trend to use DLC as low friction bearing surfaces for MEMS. The evolution of the tangential force with sliding distance at imposed normal forces may be utilized to develop improved friction models for the design of low friction and low wear interfaces for MEMS.

The relative displacement of the interface in the normal direction is shown in Fig. F-111, where it is noted that both interfaces showed a small amount of *relative approach* as the tangential displacement was imposed. At a sliding distance of 400 μm, the relative displacement between the surfaces is about 621 nm for the Si/Si interface as compared to 200 nm for the DLC/DLC interface.

We demonstrate an additional testing capability of the biaxial compression/shear apparatus by conducting scratch testing of PC at various imposed normal forces as shown in Fig. F-112 and Fig. F-113. The tests were conducted with a conical indenter tip designed to have the same nominal contact area per unit depth as a Berkovich indenter, which corresponds to an included angle of 140.6°. The imposed scratch velocity was 10 μm/s. The residual scratch morphology for the test performed at

a normal force of 174 mN shown in Fig. F-112 indicates the excellent alignment of the apparatus. Current research is underway to assess the utility of the scratch test for extracting deformation and fracture information for polymeric materials with no *a priori* knowledge of the material behavior. We note that in the conical scratch tests results for PC with a conical indenter of 140.6° included angle, there was no discernible evidence of fracture. Thus, studies into indenter tip geometries, normal loads, sliding velocities, and material classes appropriate for extraction of fracture properties are warranted.

Appendix E

Vendor list

The following vendors are recommended sources for the indicated items:

- Al7075-T6 sheet, Fused-silica: Goodfellow, www.goodfellow.com.
- Water-jet machining at MIT: Building 35 machine shop; Pappalardo Laboratory; Media Lab
- Final machining, EDM machining: RAMCO Machine, LLC, MA, 978-948-3778, Randy Jezowski.
- Voice coils: BEI Sensors and Systems Co., CA, Model LA13-12-000A for the micorindenter and Model LA05-05-000 for the nanoindenter.
- Precision current sources: Precision MicroDynamics, CA, Model BTA-28V-6A Linear.
- Data acquisition and software: National Instruments, TX, PCI-6035E board.
- Displacment sensors: Kaman Instrumentaion, CO, Model SMU9000-5U.
- Isolation tables: Newport, CA, Model RG Series.
- Precision displacement stages: New Focus, Inc., CA, Model 9065-Z.
- Indentation tips: Gilmore Diamond Tools, Inc., RI, 401-438-0717, Mike Mihalec.

- Piezo-electric inchworm actuator: Burleigh Instruments, NY, Model IW700.

Appendix F

Figures

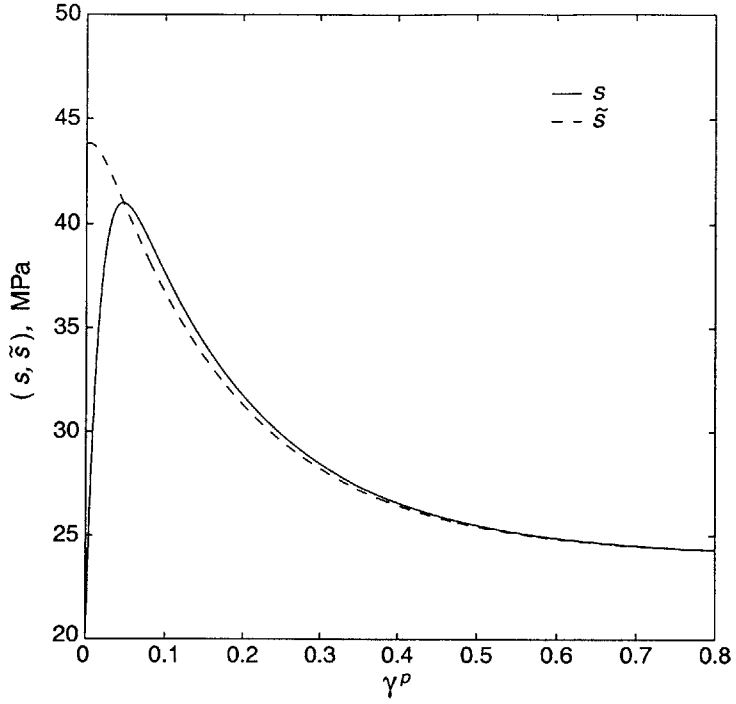

(a)

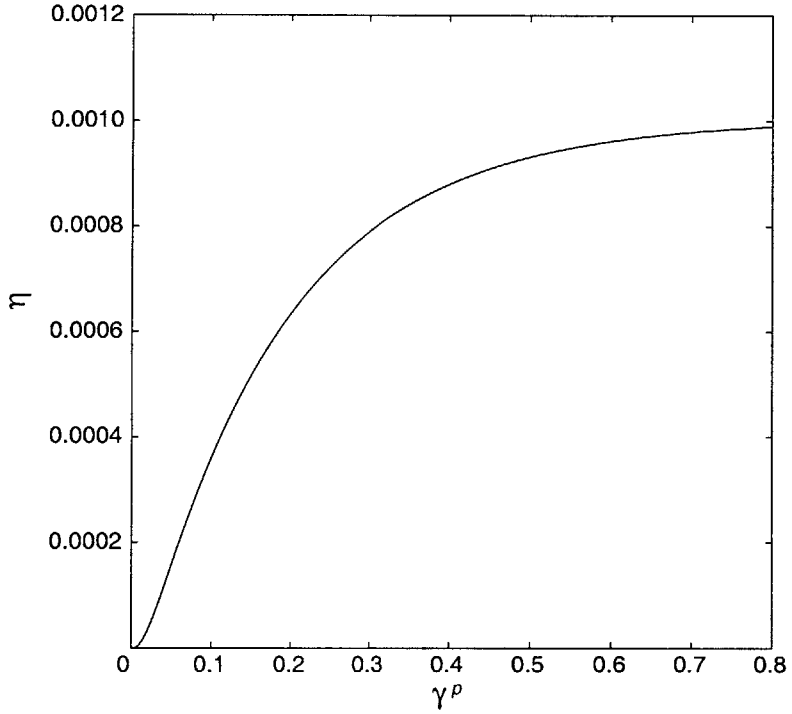

(b)

Figure F-1: Evolution of s, $\tilde{s}$ and η with γ^p.

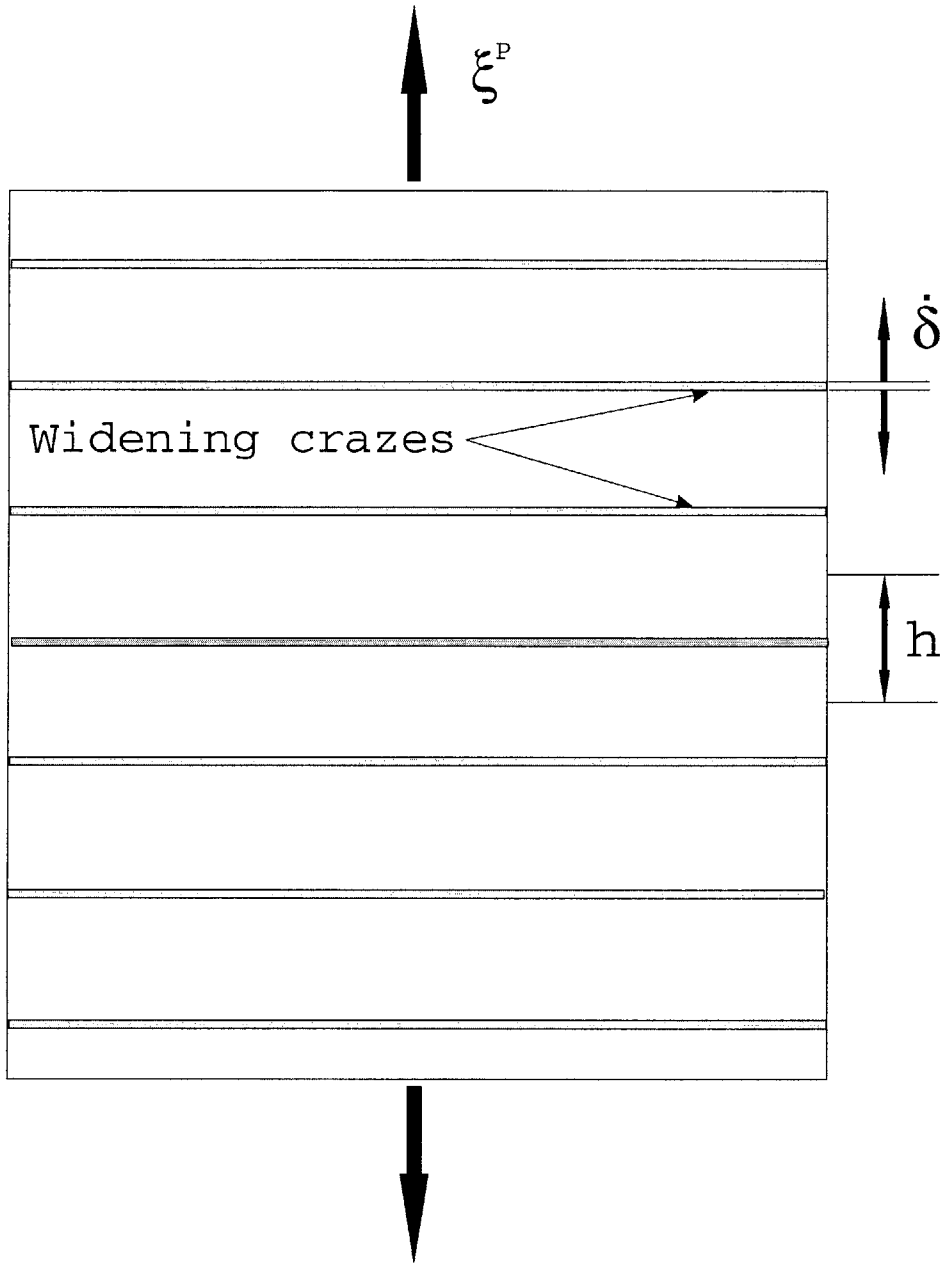

Figure F-2: An idealization of craze plasticity where the macroscopic averaged tensile craze strain rate ξ^p is determined by the thickening rate $\dot{\delta}$ of crazes at an average spacing h. After Argon (1999), Figure 7.

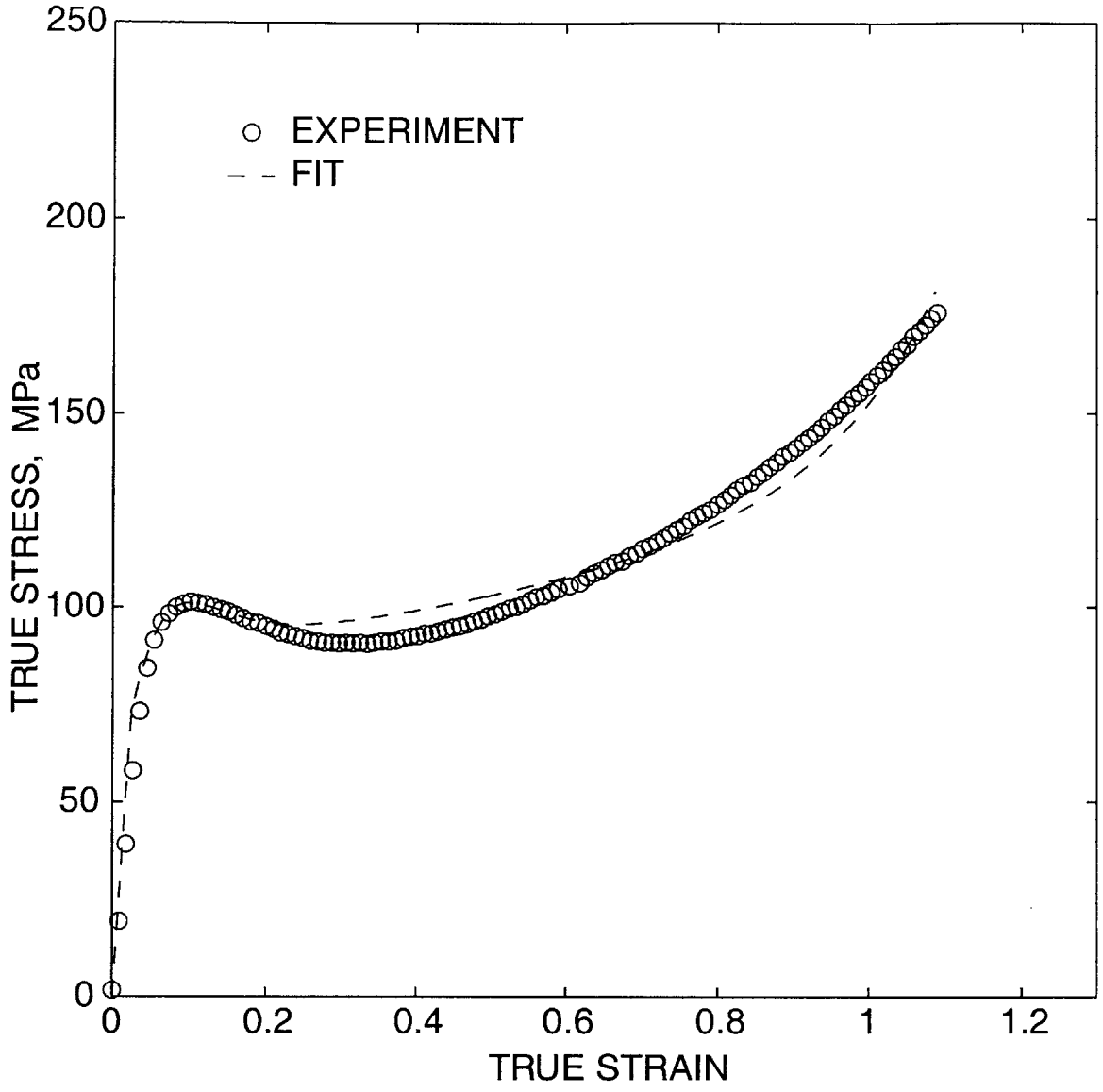

Figure F-3: Stress-strain response of PMMA in simple compression, together with a fit of the constitutive model.

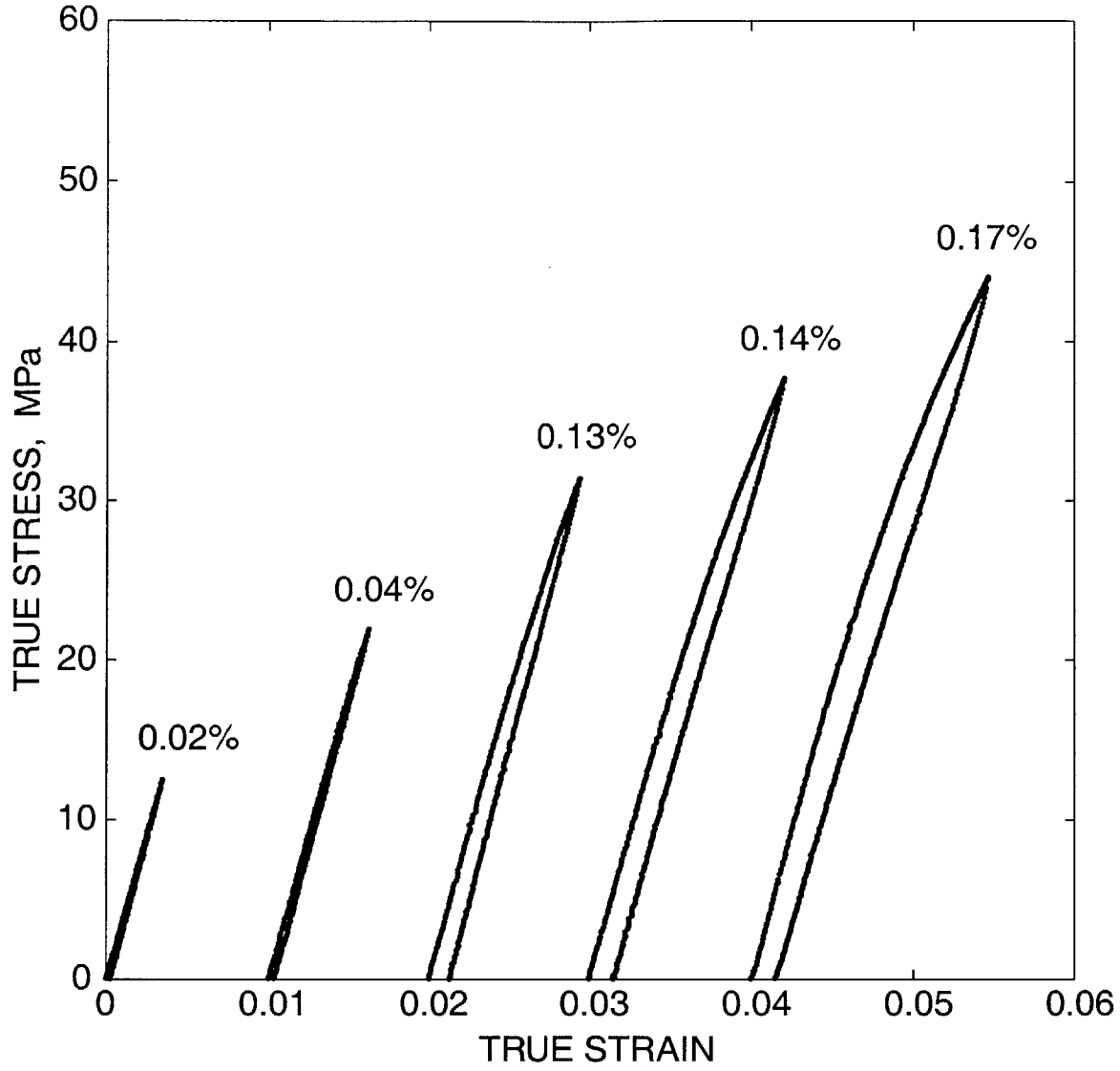

Figure F-4: Plane strain tension of PMMA. True stress-strain responses for specimens loaded to stress levels prior to the peak stress. Each test has been shifted horizontally in order to elucidate individual responses. The residual strain upon unloading is indicated above each curve.

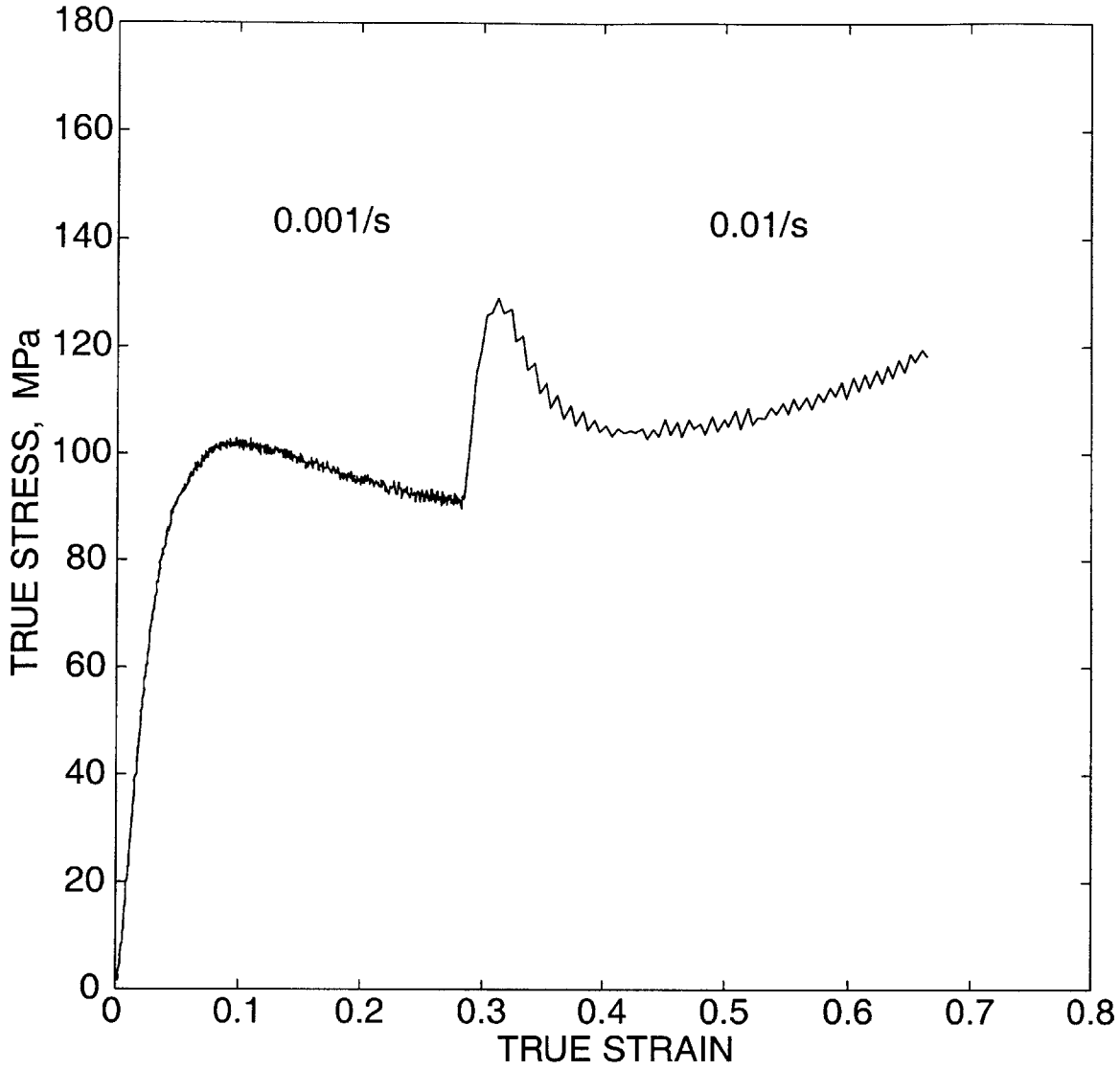

Figure F-5: Strain rate increment experiment on PMMA in simple compression. The strain rate of -0.001/s is increased to -0.01/s.

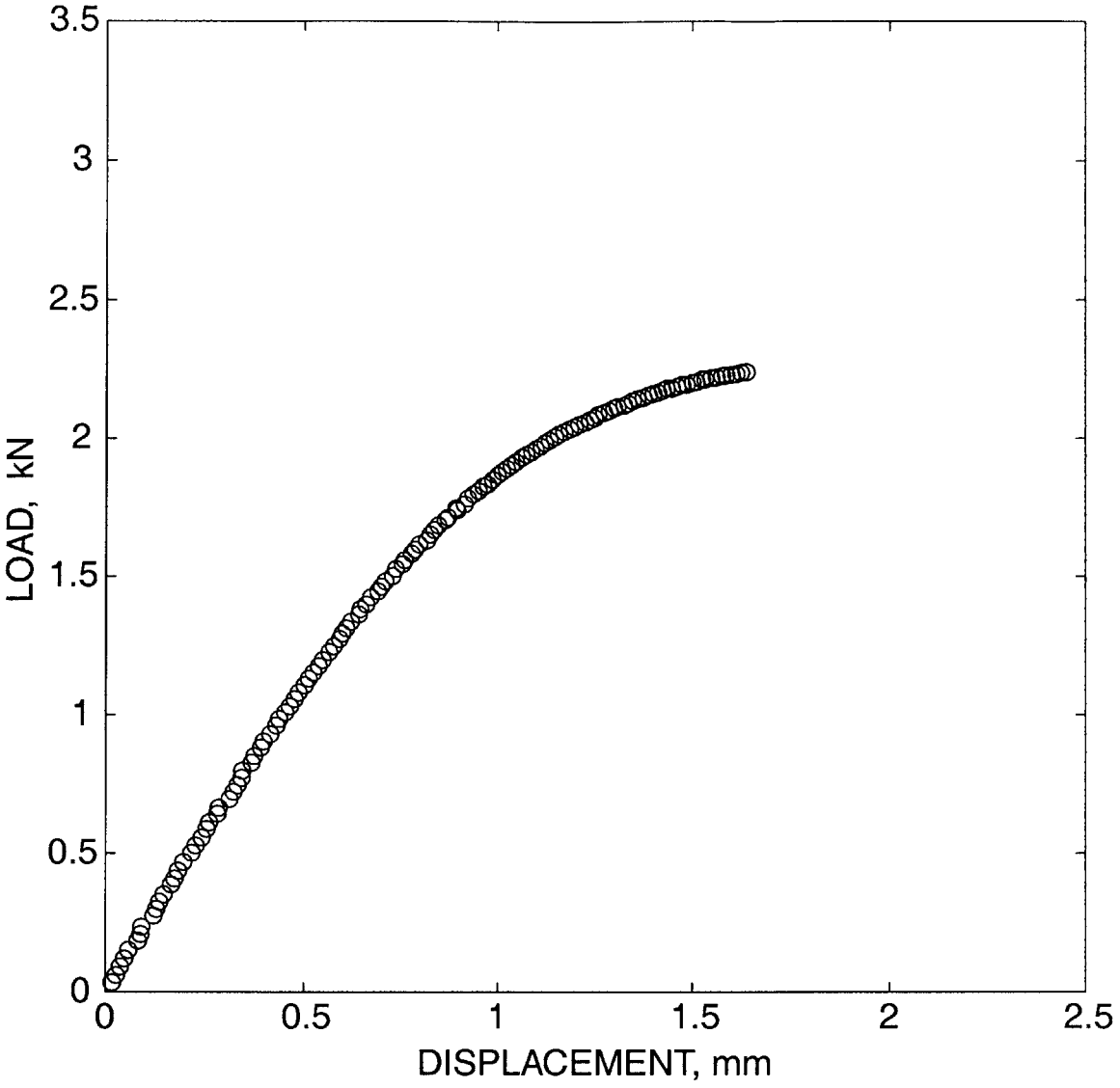

Figure F-6: Experimental load-displacement curve for a smooth-bar tension experiment on PMMA.

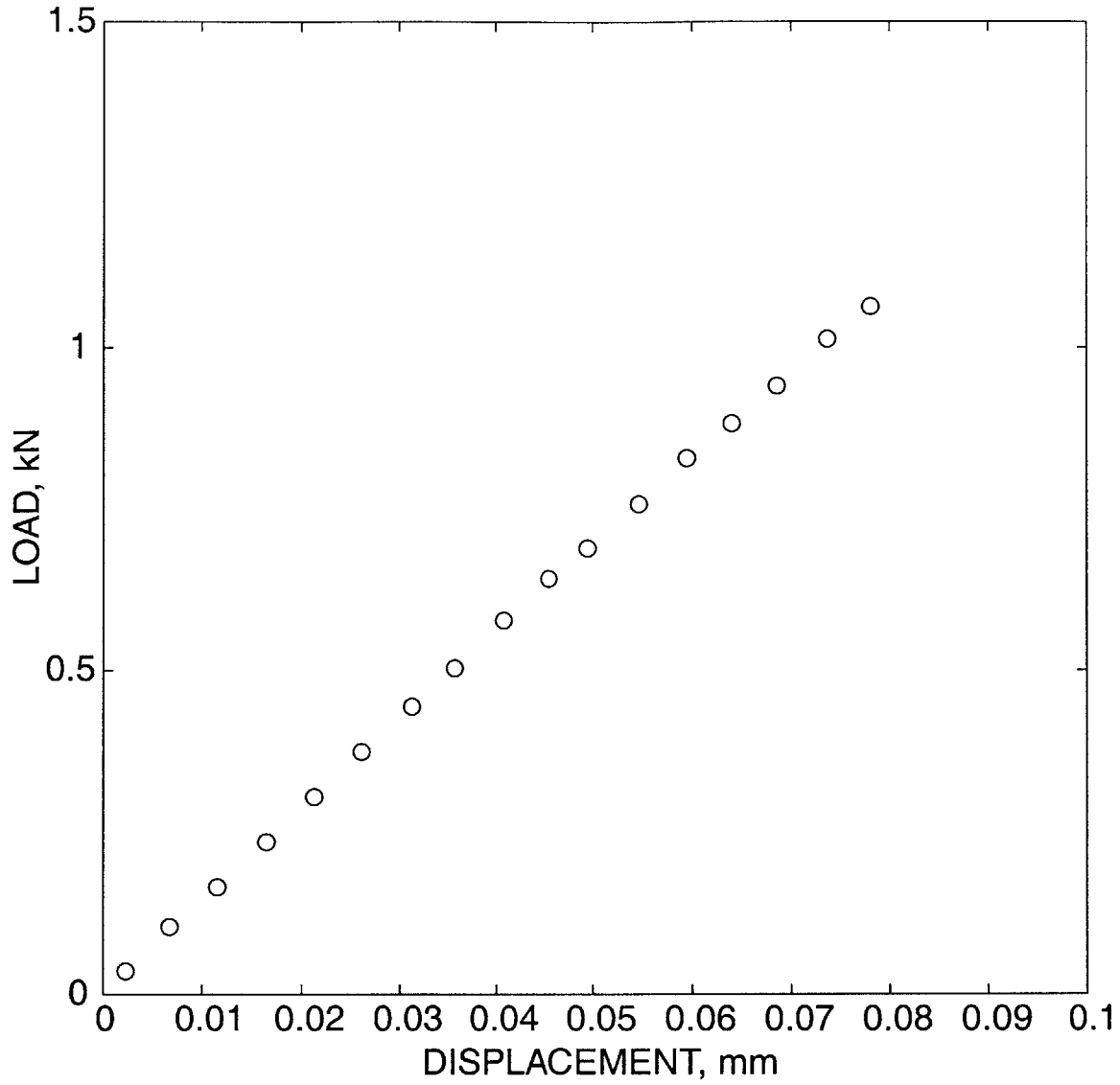

Figure F-7: Experimental load-displacement curve for a notched-bar tension experiment on PMMA.

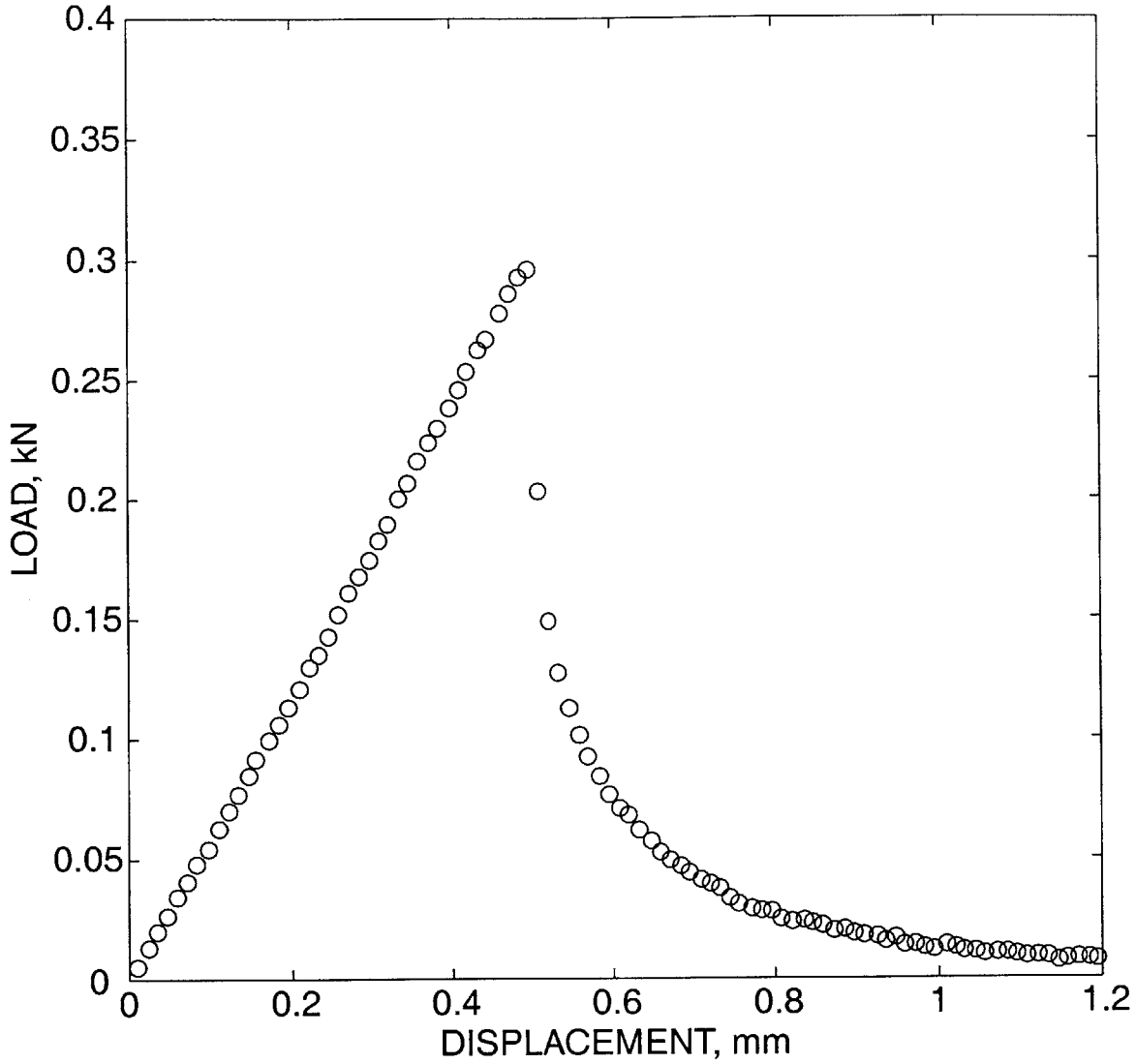

Figure F-8: Experimental load-displacement curve for an ASTM standard PMMA compact tension specimen (without a sharp fatigue pre-crack).

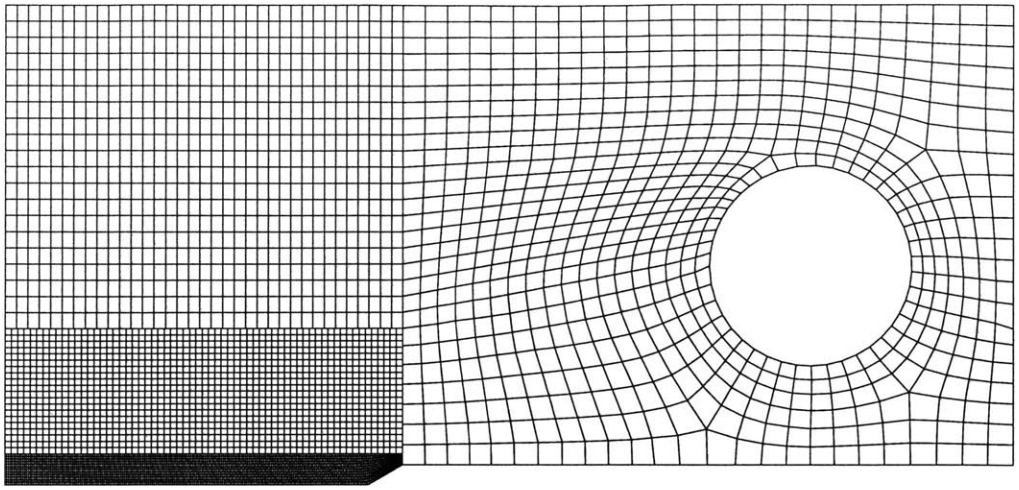

(a)

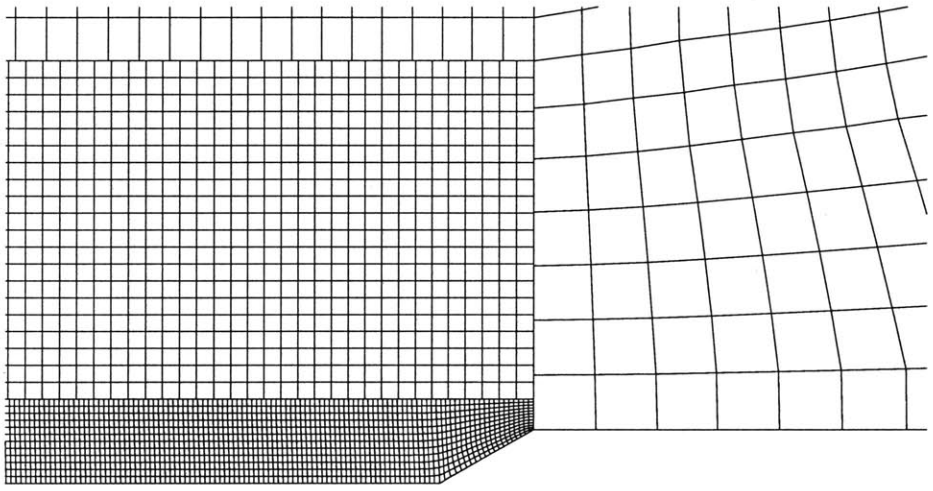

(b)

Figure F-9: Mesh design used to simulate the CTS experiment under mode I loading conditions: (a) full mesh and (b) detail of fine mesh at the notch-root.

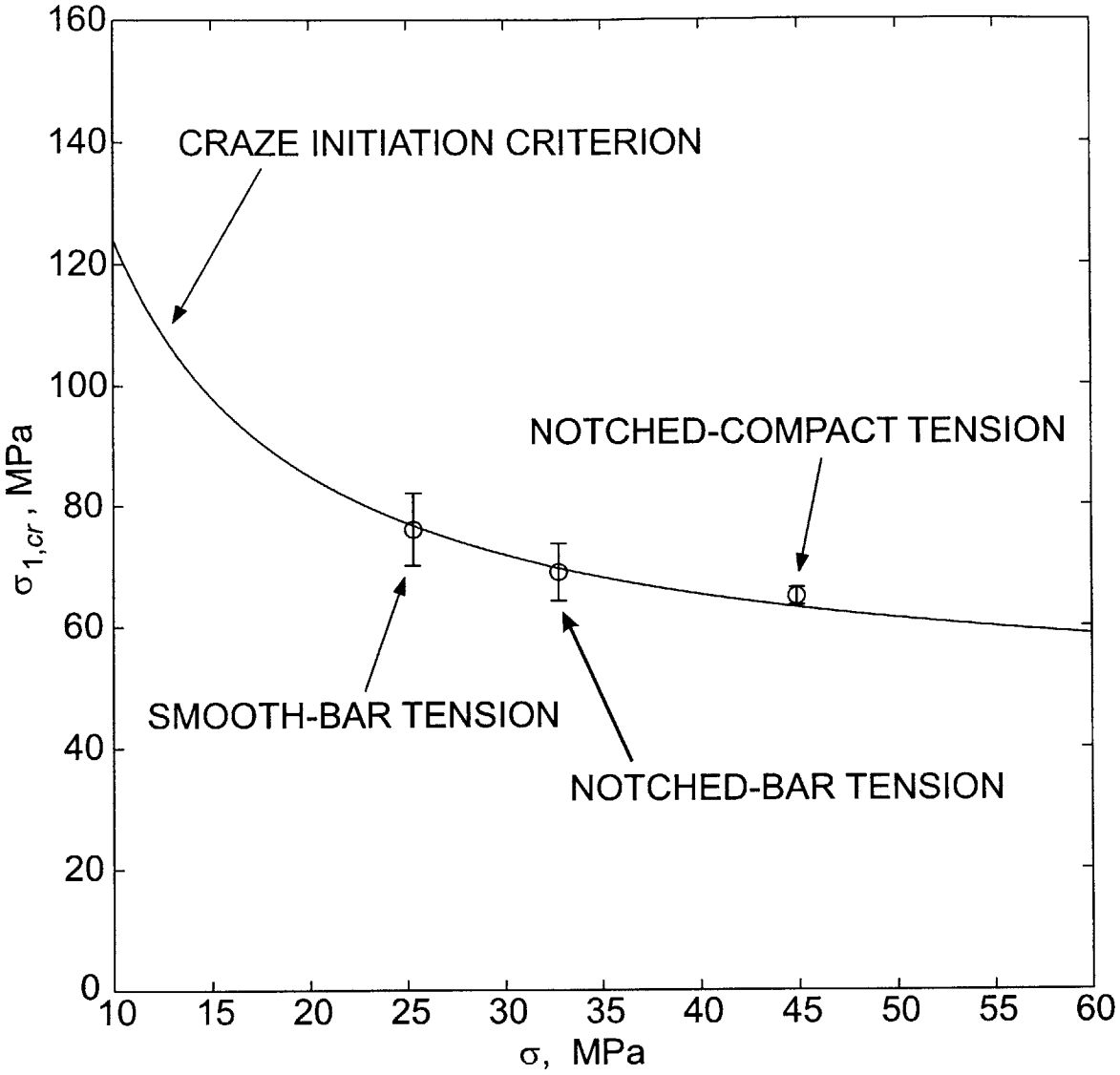

Figure F-10: Fit of the craze-initiation criterion to the experimental data from smooth-bar, notched-bar, and notched compact tension specimens.

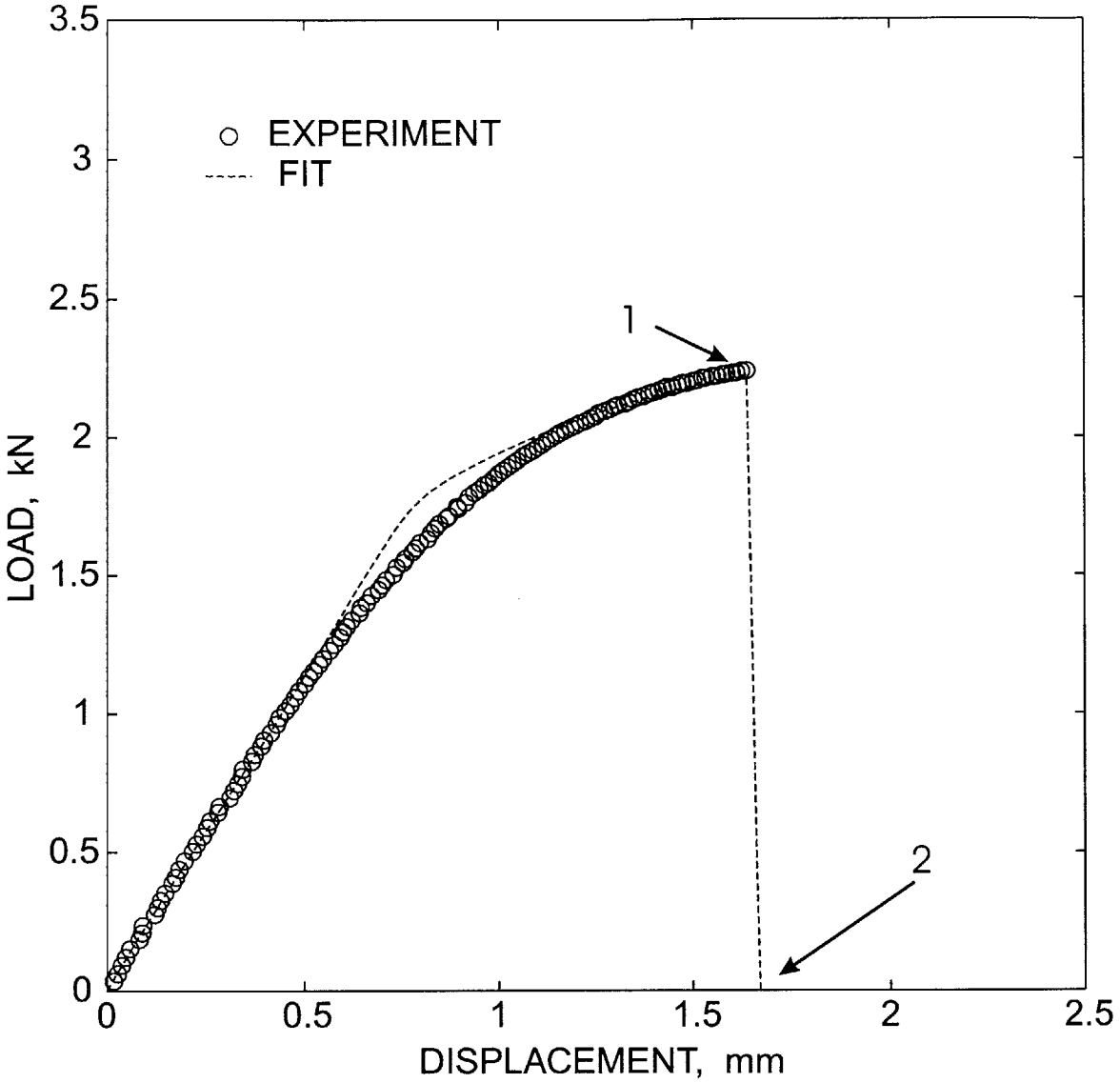

Figure F-11: Experimental and calculated load-displacement curves for a smooth-bar tension specimen.

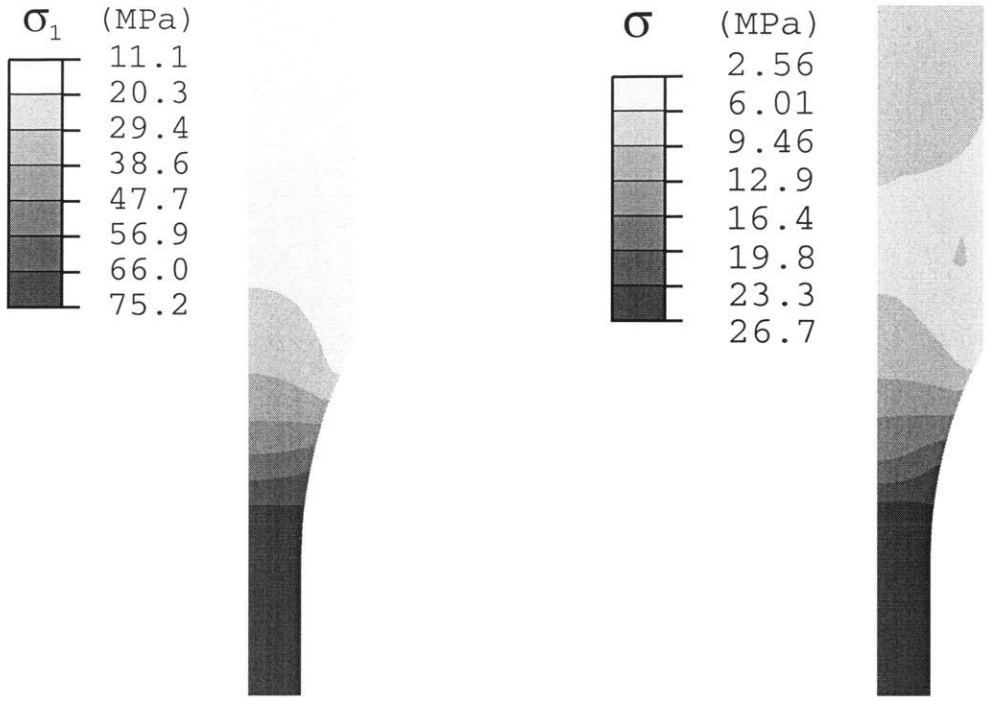

(a) (b)

(c)

Figure F-12: Contours of (a) σ_1 and (b) σ at incipient craze-flow, location 1 of Fig. F-11; (c) Mesh at location 2 of Fig. F-11 showing fracture. Note that fracture has occurred at multiple locations in the gauge section.

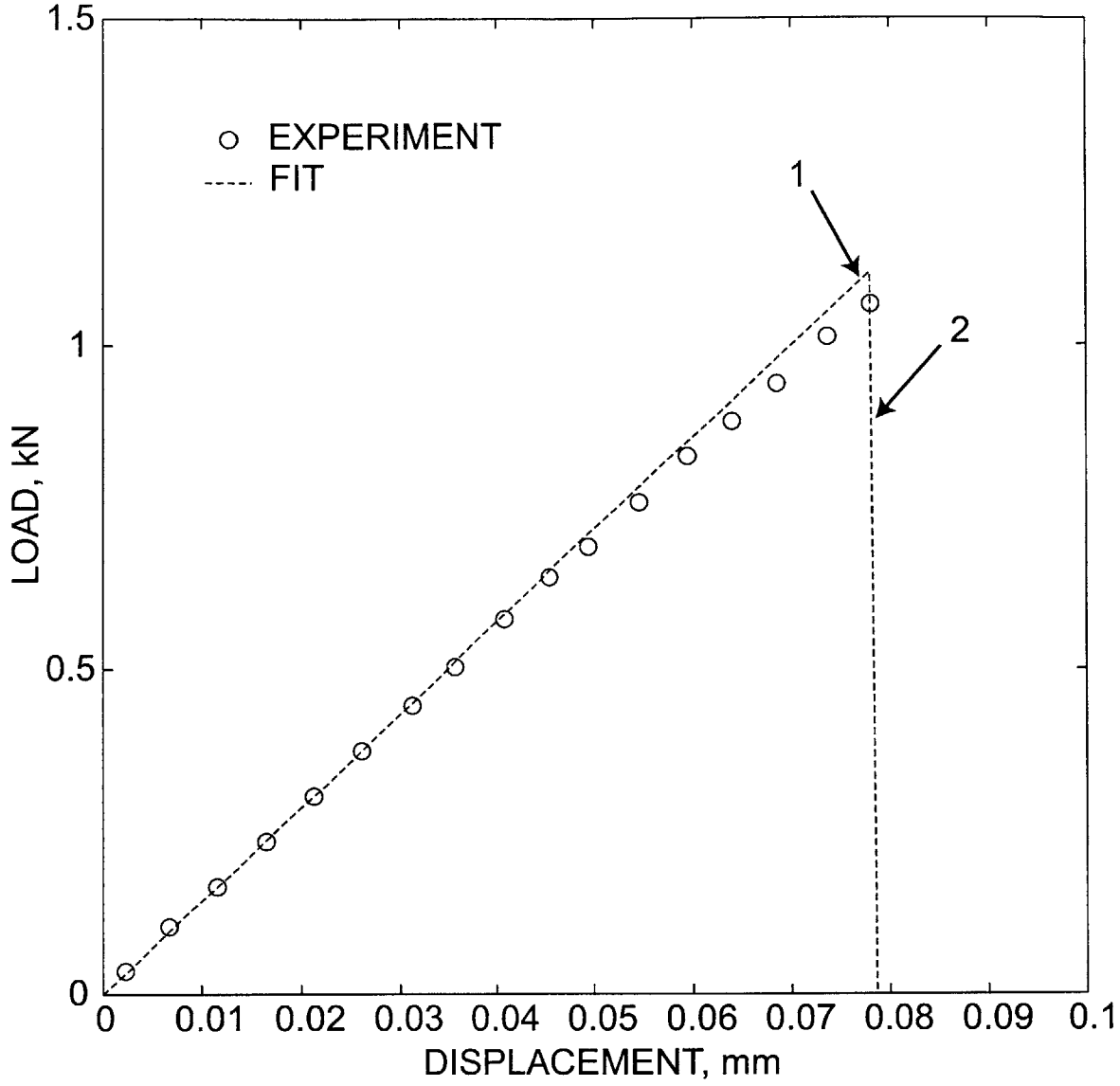

Figure F-13: Experimental and calculated load-displacement curves for a notched-bar tension specimen.

(a)

(b)

Figure F-14: Contours of (a) σ_1 and (b) σ at incipient craze-flow, location 1 marked in Fig. F-13.

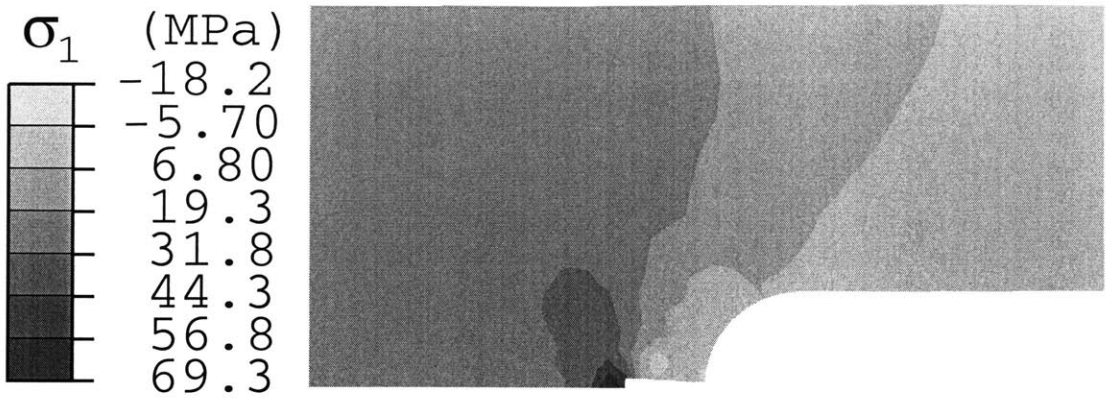

(a)

(b)

Figure F-15: Contours of (a) σ_1 and (b) σ after craze-fracture has propagated part of the way into the cross-section, location 2 marked in Fig. F-13.

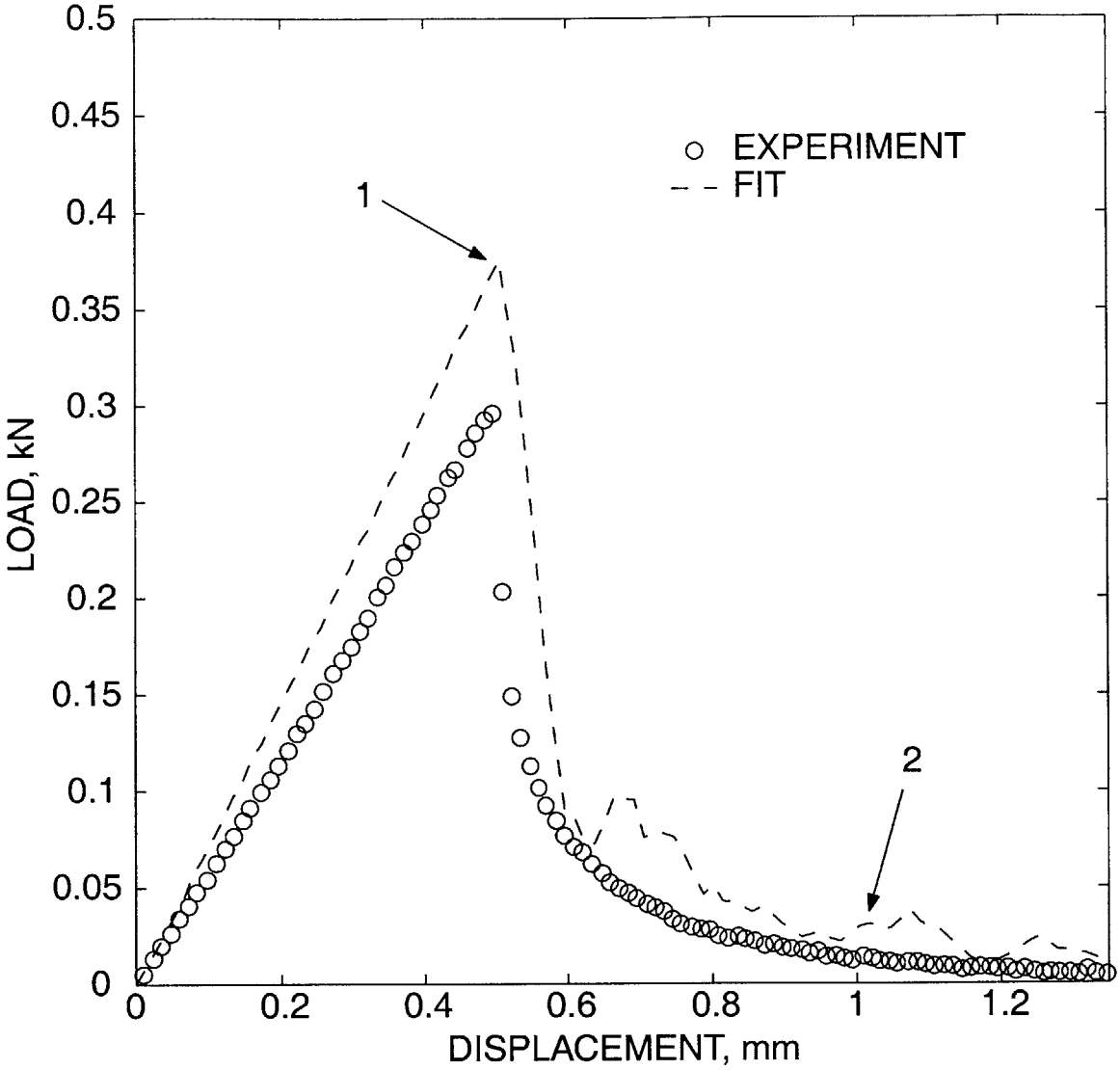

Figure F-16: Experimental and calculated load-displacement curves for a notched compact tension specimen.

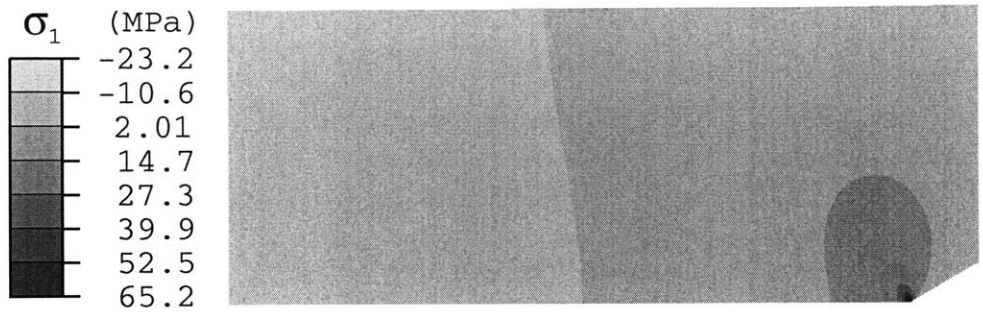

(a)

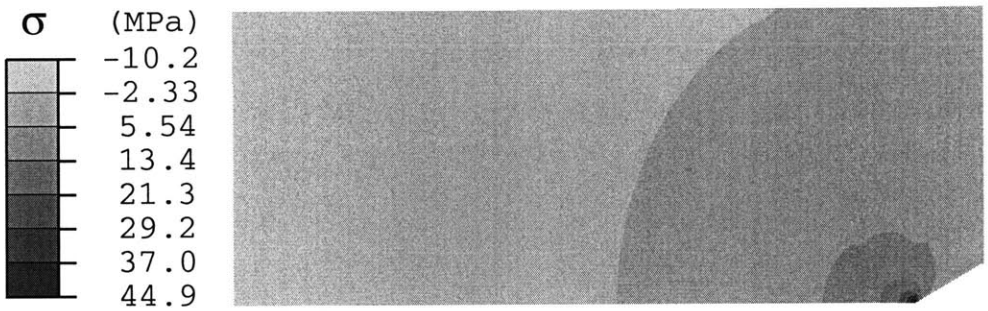

(b)

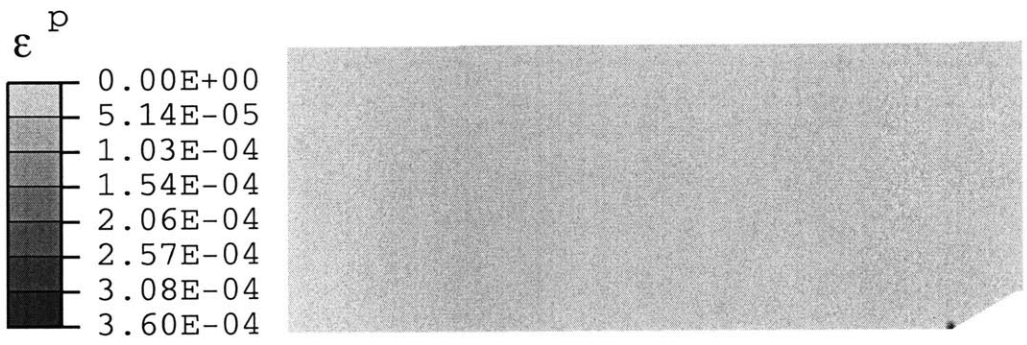

(c)

Figure F-17: Contour plots of (a) σ_1, (b) σ, and (c) ϵ^p at incipient craze-flow, location 1 marked in Fig. F-16. For clarity of presentation, the contour plots are focused on the region in the vicinity of the notch-root.

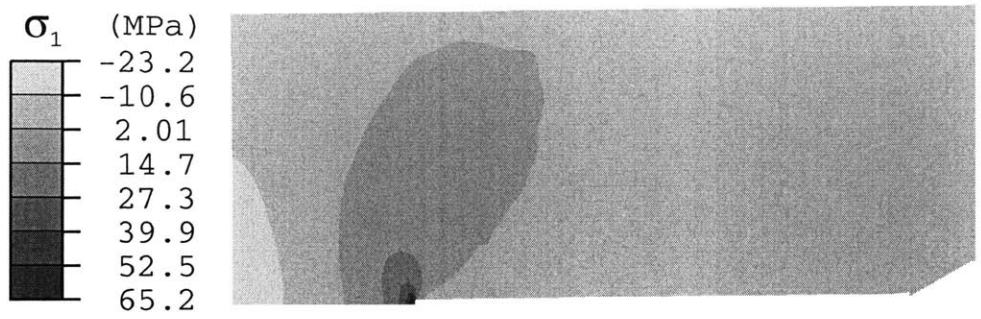

(a)

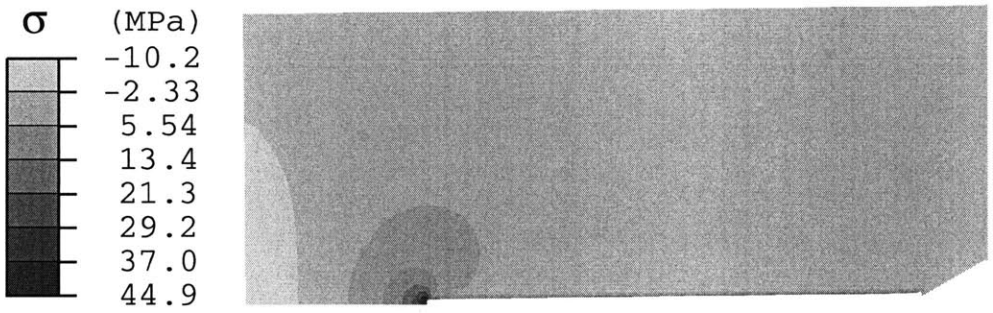

(b)

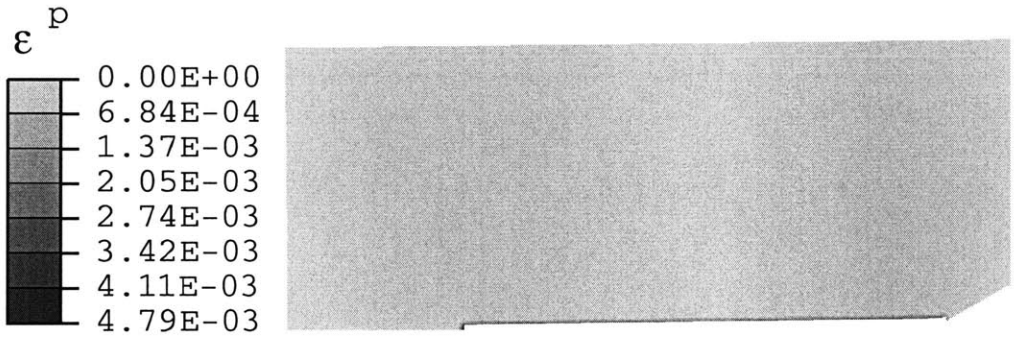

(c)

Figure F-18: Contour plots of (a) σ_1, (b) σ, and (c) ϵ^p after craze-fracture has propagated part of the way into the cross-section, location 2 marked in Fig. F-16. For clarity of presentation, the contour plots are focused on the region in the vicinity of the notch-root.

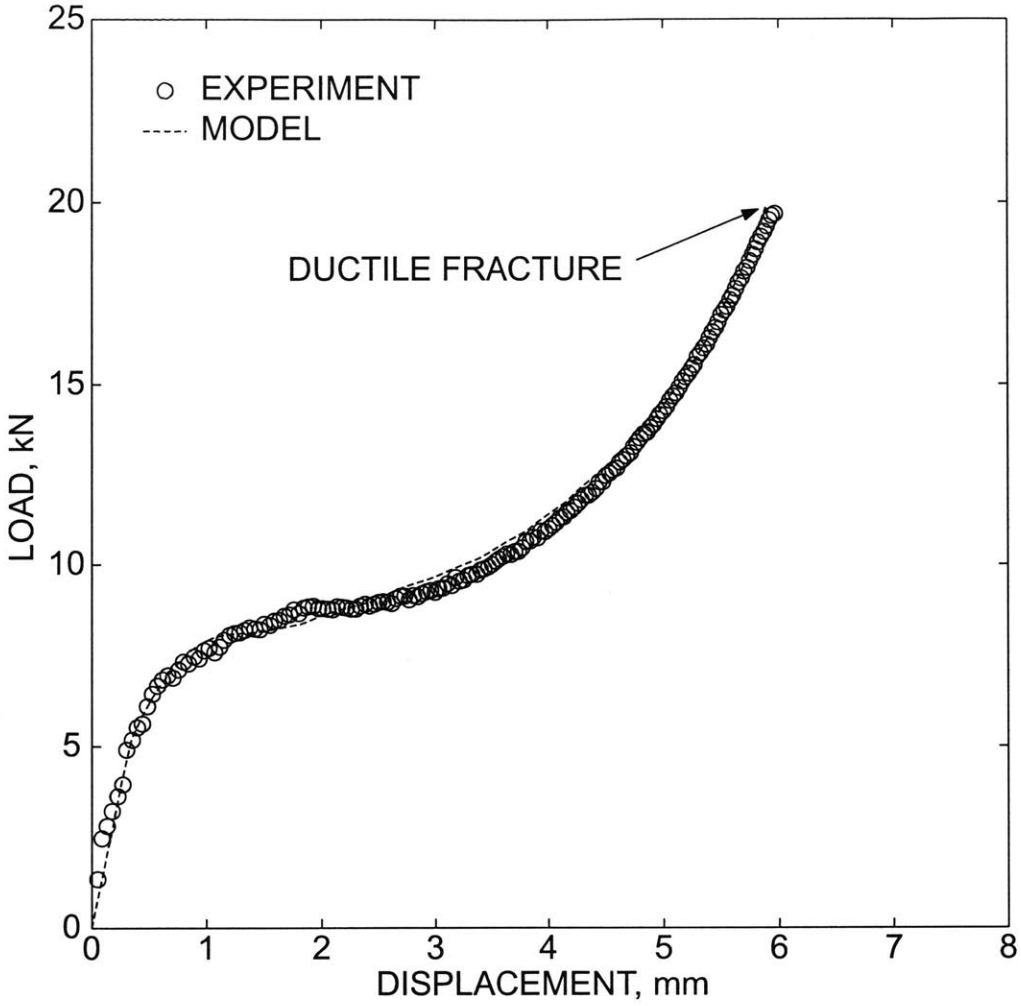

(a)

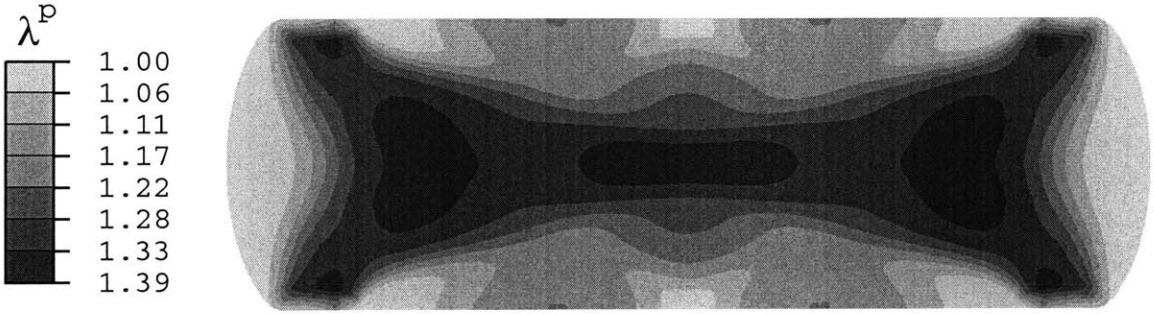

(b)

Figure F-19: Fit of the ductile failure criterion in plane strain compression: (a) Load-displacement curve. (b) Contour plot showing values of λ^p at the point of ductile fracture.

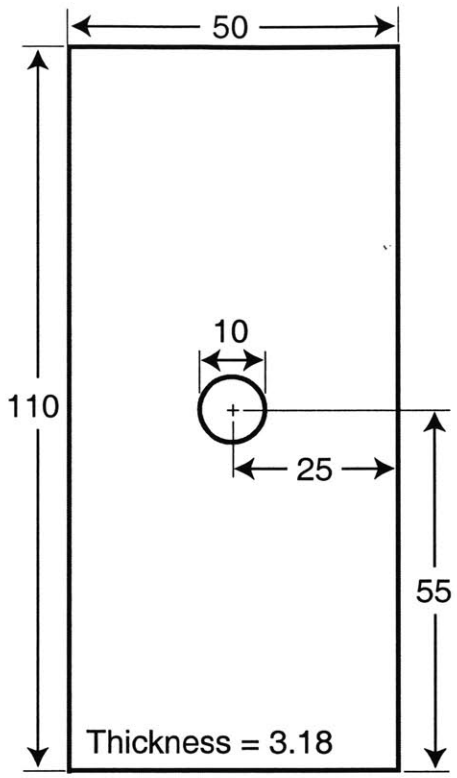

(a)

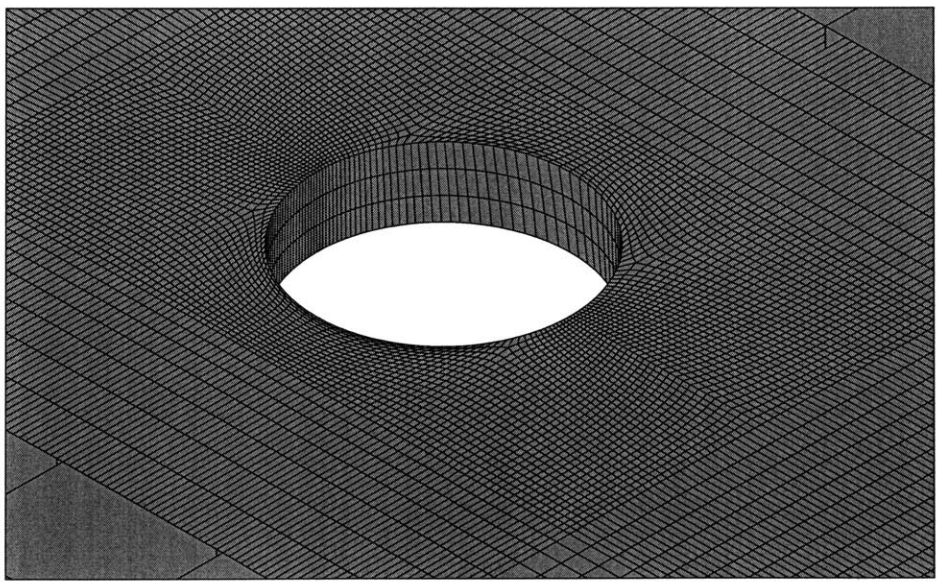

(b)

Figure F-20: Fracture of thin PMMA plates with circular windows; (a) Specimen geometry with dimensions in mm. (b) Detail of the finite element mesh in the vicinity of the hole.

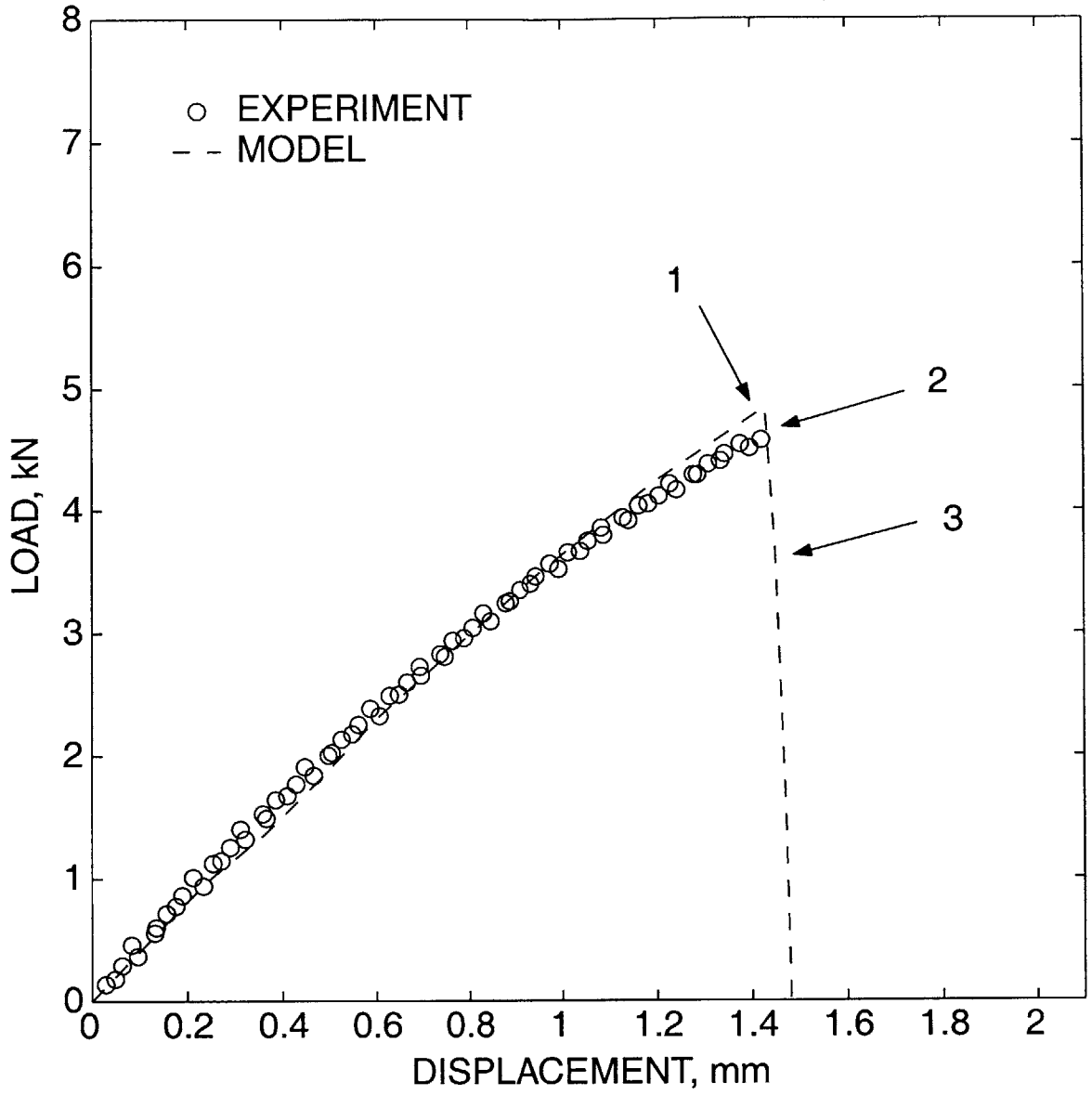

Figure F-21: Fracture of thin PMMA plates with circular windows; comparison of the experimentally-measured and numerically-predicted load-displacement curves.

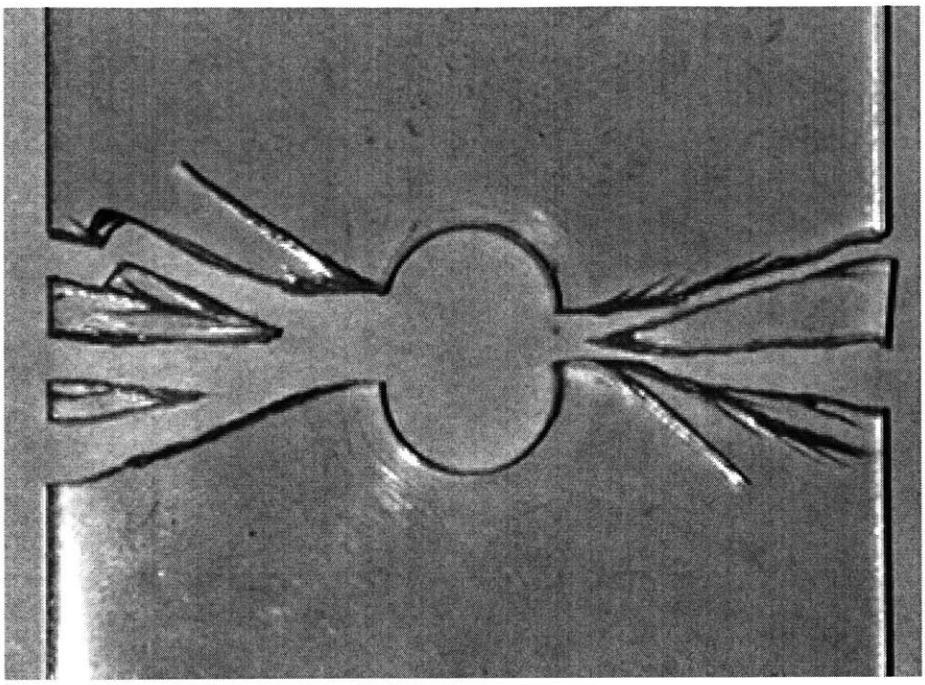

(a)

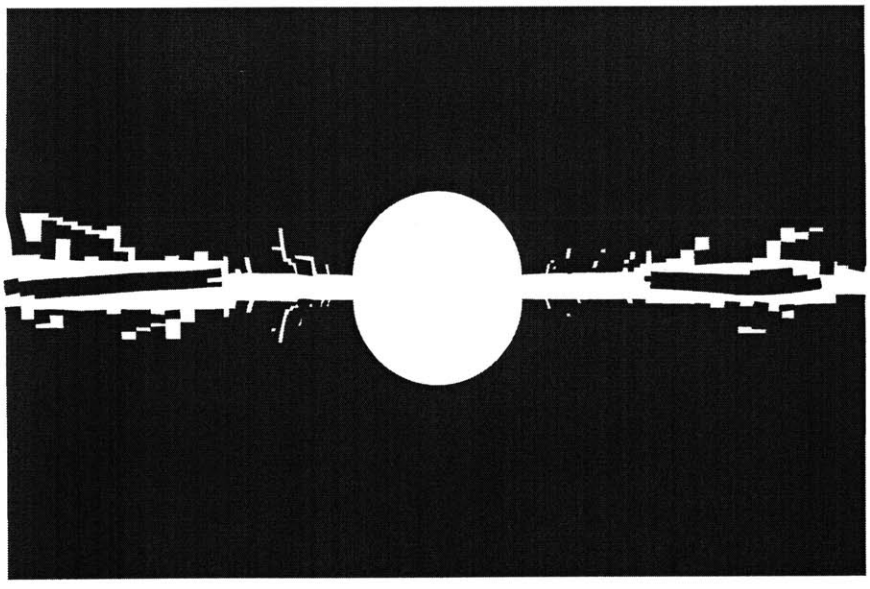

(b)

Figure F-22: (a) Image of fractured specimen showing crack-branching and fractured ligaments. Loading direction is vertical. (b) Result from corresponding numerical calculation.

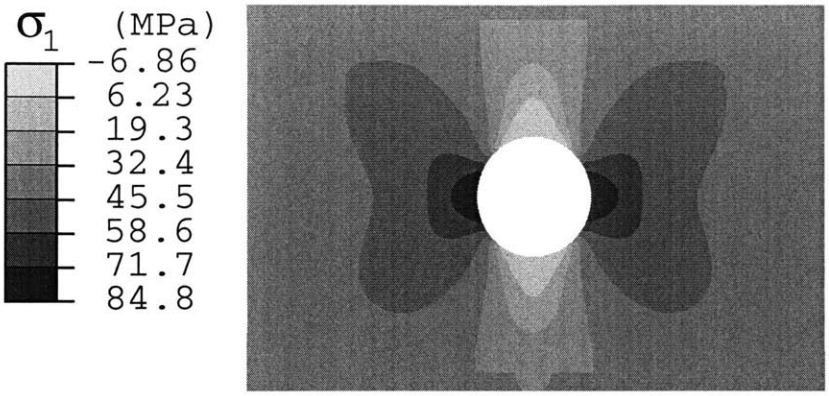

(a)

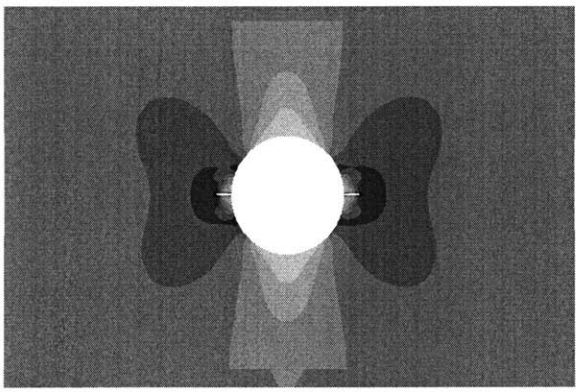

(b)

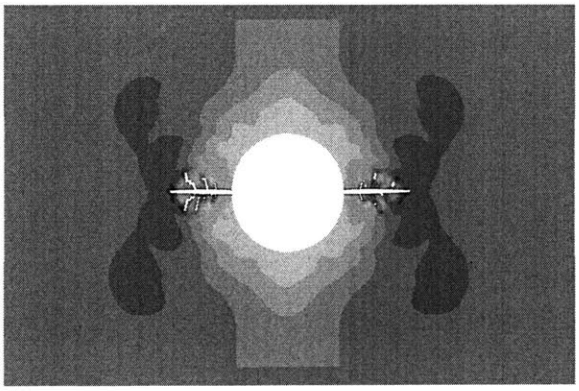

(c)

Figure F-23: Contour plots of σ_1 at (a) location 1, (b) location 2, and (c) location 3 indicated on the numerical curve in Fig. F-21. Loading direction is in the vertical.

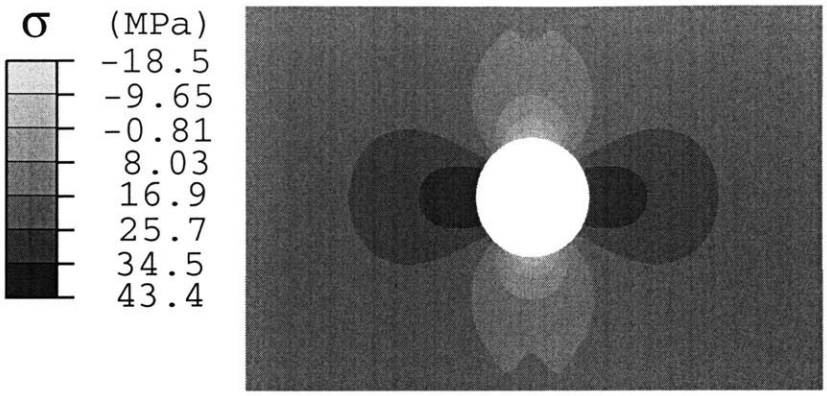

(a)

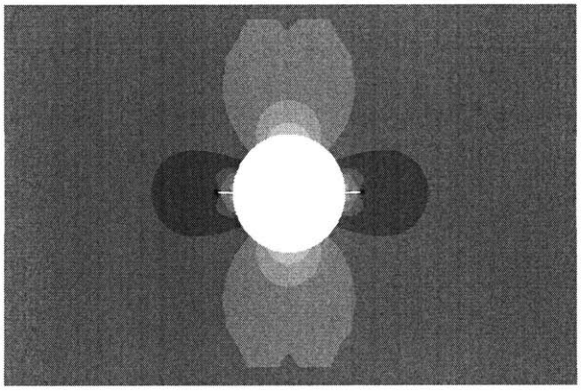

(b)

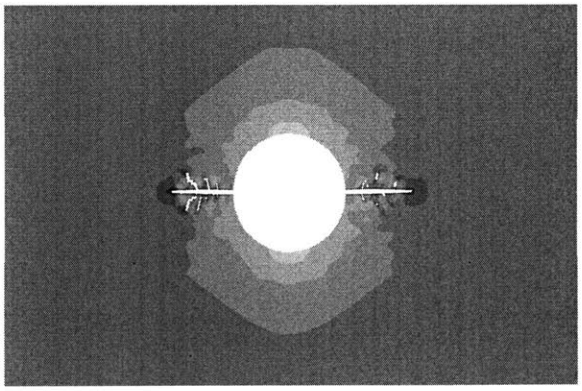

(c)

Figure F-24: Contour plots of σ at (a) location 1, (b) location 2, and (c) location 3 indicated on the numerical curve in Fig. F-21. Loading direction is in the vertical.

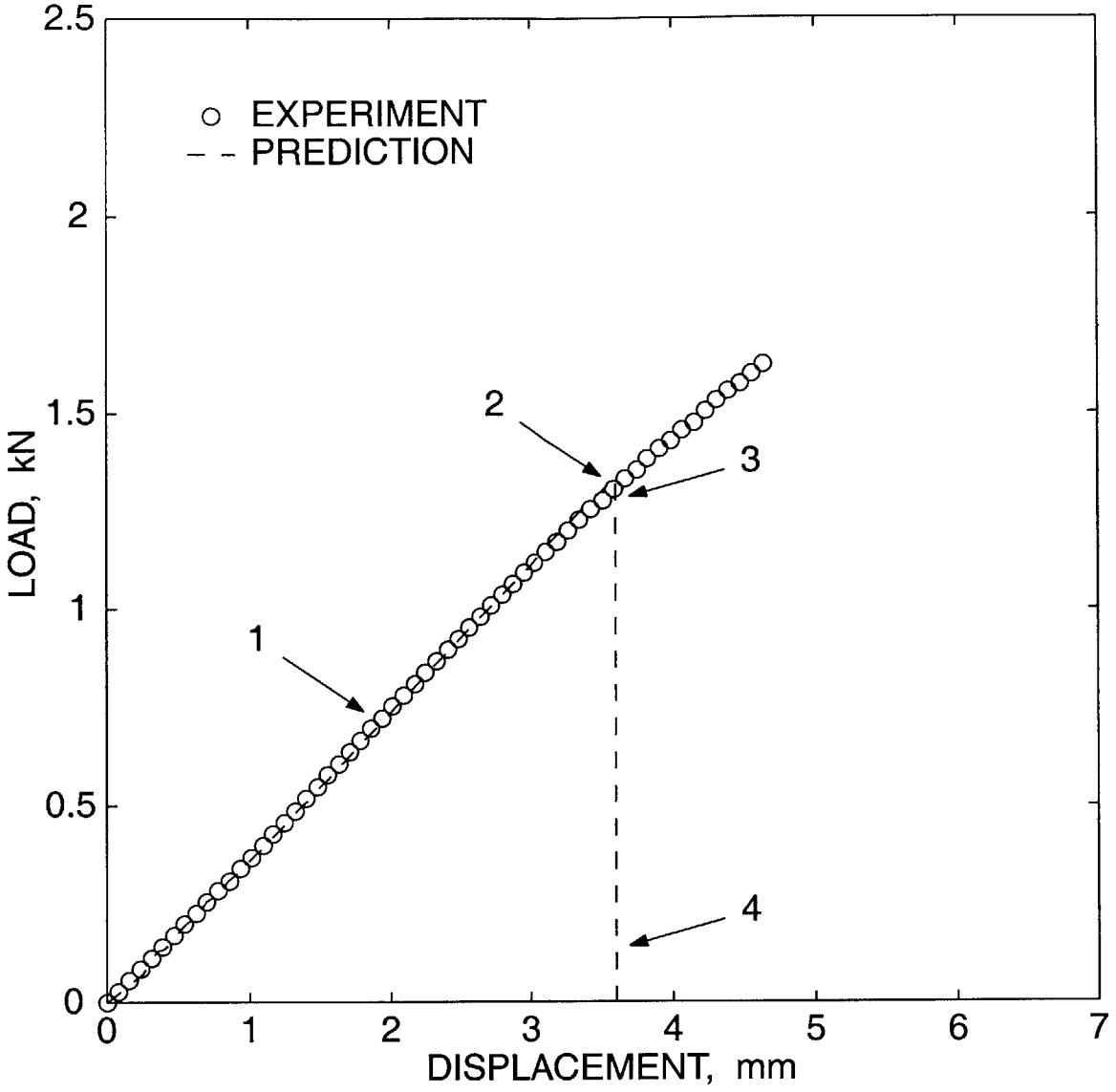

Figure F-25: Comparison of the predicted load-displacement response for the blunt-notched beam in bending against the experiment.

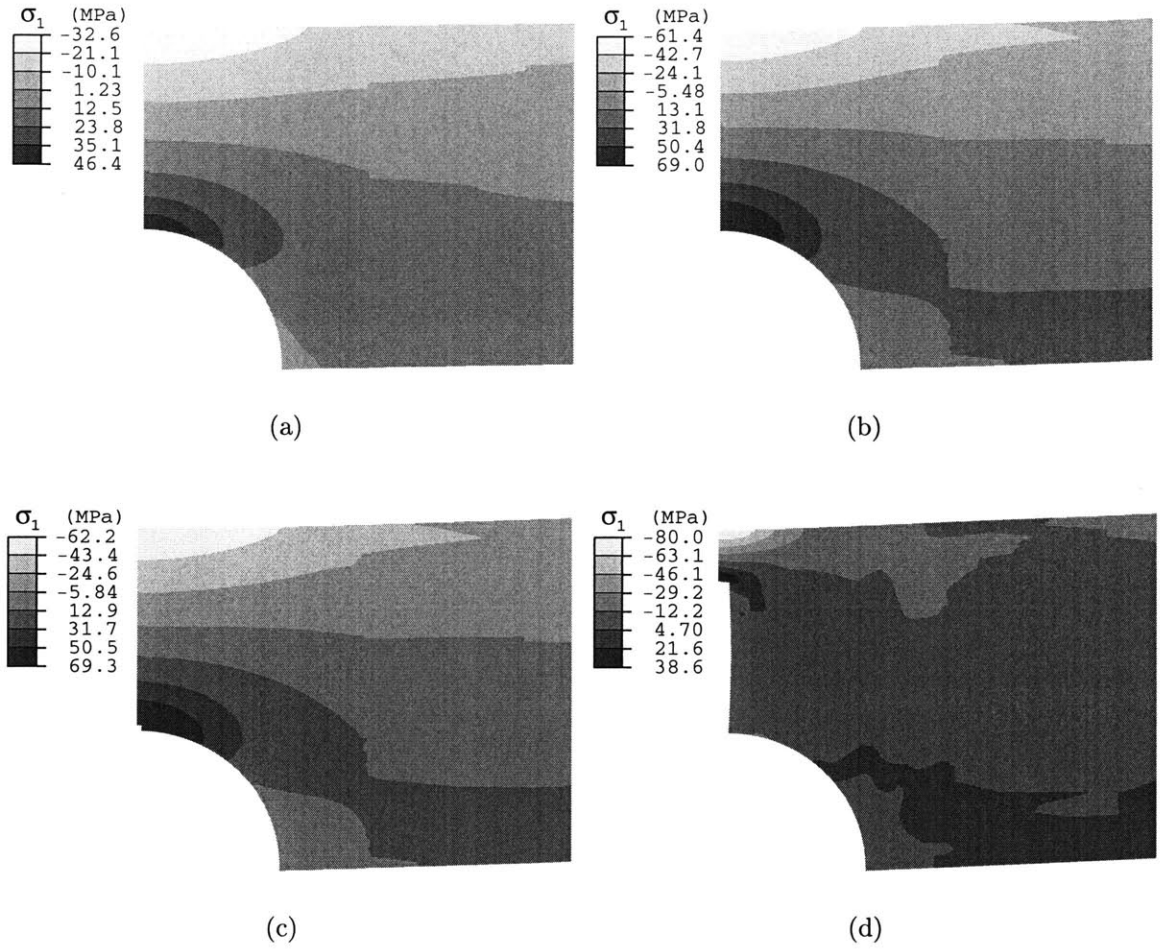

Figure F-26: Prediction of the fracture process in blunt-notch beam bending. Contour plots of σ_1 corresponding to (a) location 1, (b) location 2, (c) location 3, and (d) location 4, as indicated on the predicted curve in Fig. F-25. Brittle fracture initiates at the notch-root as indicated in (c).

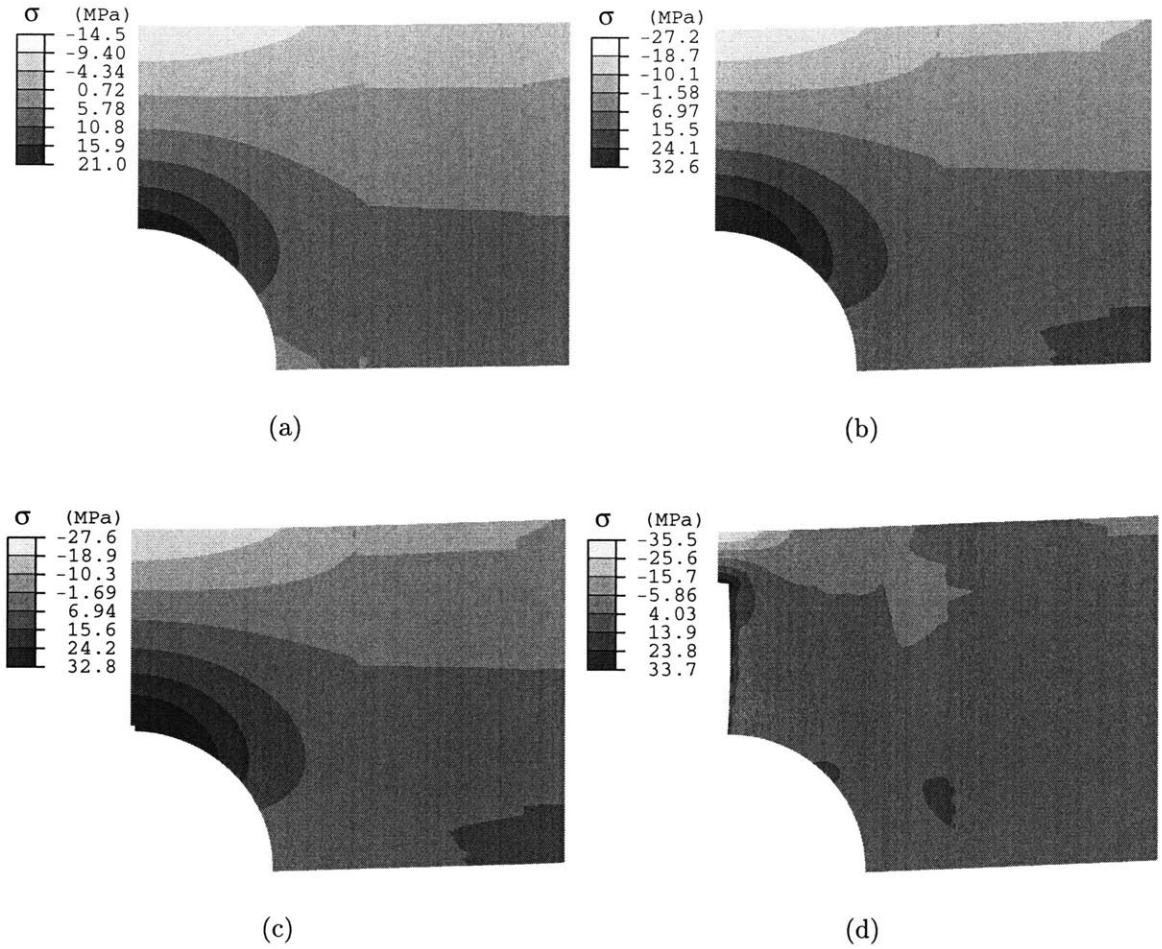

Figure F-27: Prediction of the fracture process in blunt-notch beam bending. Contour plots of σ corresponding to (a) location 1, (b) location 2, (c) location 3, and (d) location 4, as indicated on the predicted curve in Fig. F-25. Brittle fracture initiates at the notch-root as indicated in (c).

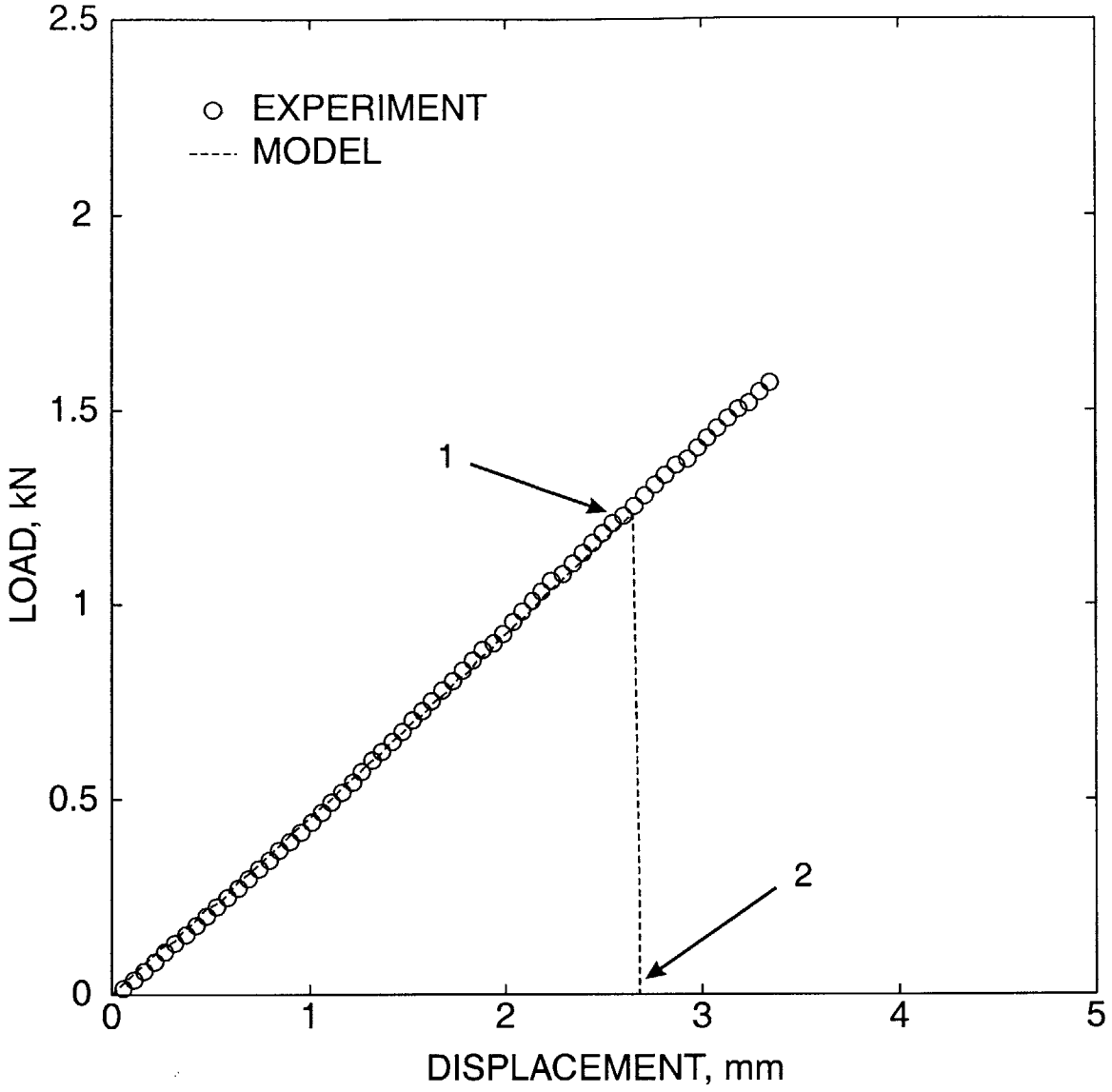

Figure F-28: Comparison of the predicted load-displacement response for the sharp-notched beam in bending against the experiment.

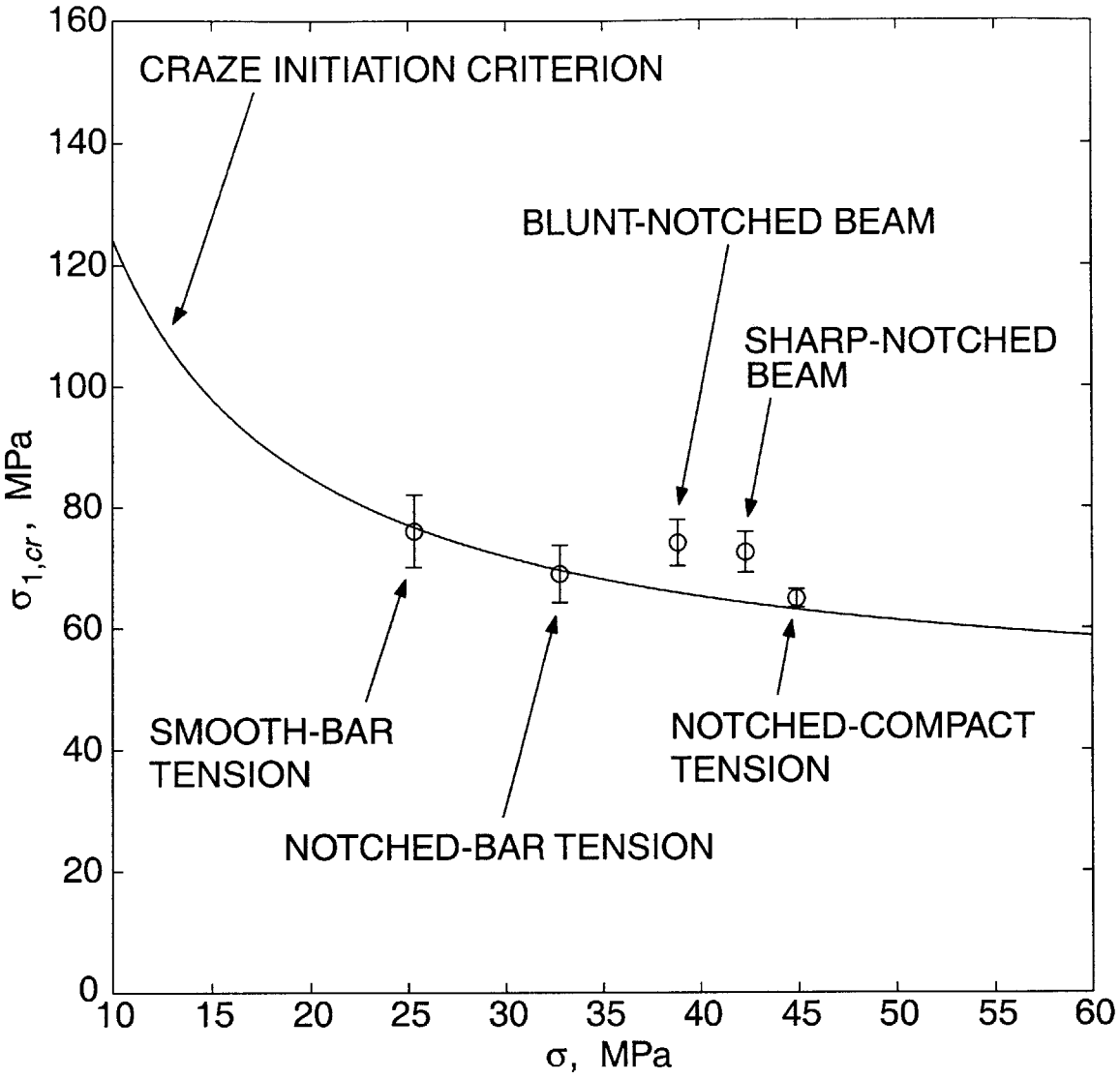

Figure F-29: Craze initiation criterion showing the location of experimental points for the blunt and sharp-notched beam bending experiments.

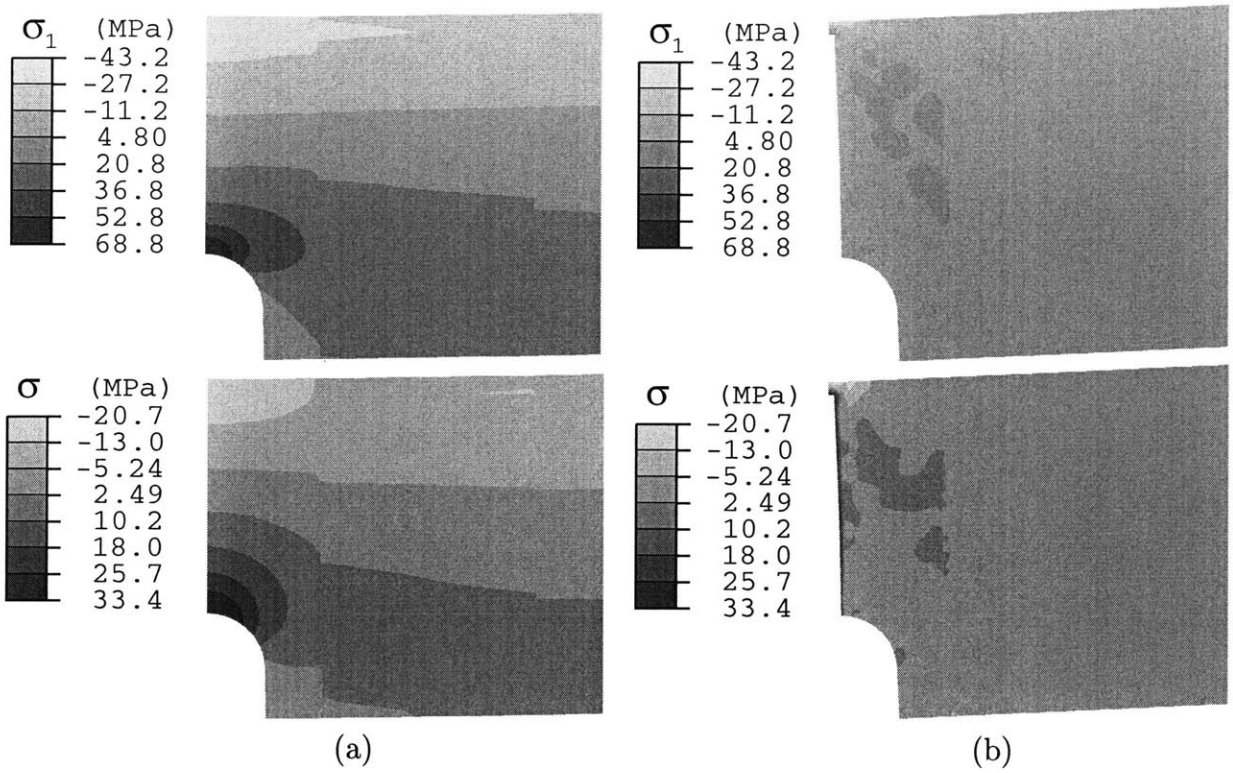

Figure F-30: Four-point bending of a sharp-notched beam. Contour plots of σ_1 and σ at (a) location 1, and (b) location 2 indicated in Fig. F-28. Brittle fracture occurs along the specimen centerline.

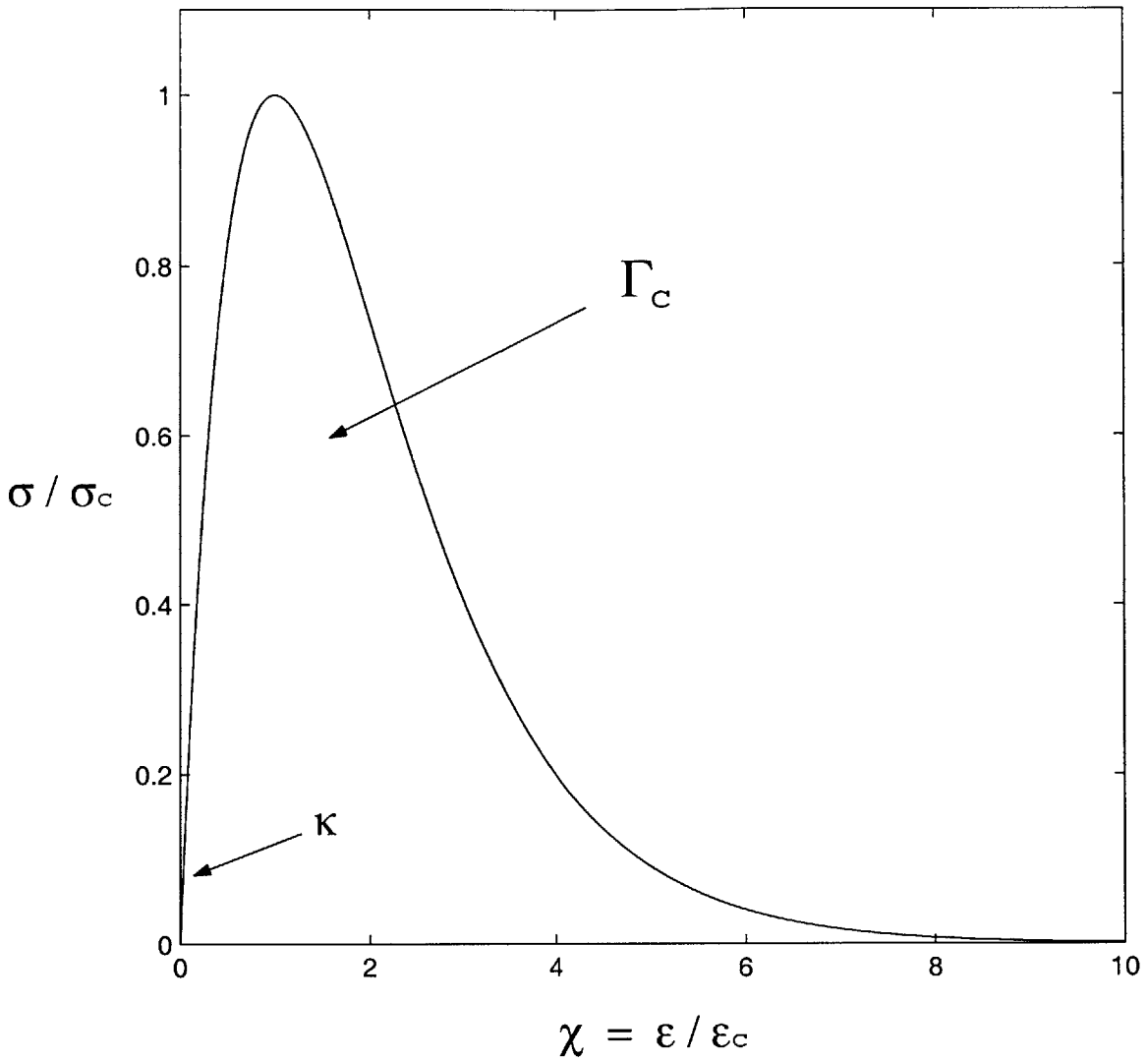

Figure F-31: Functional relationship prescribed between the mean normal stress and the elastic volumetric strain. The initial slope is the ground state bulk modulus K, and the cavitation fracture energy per unit volume is Γ_c.

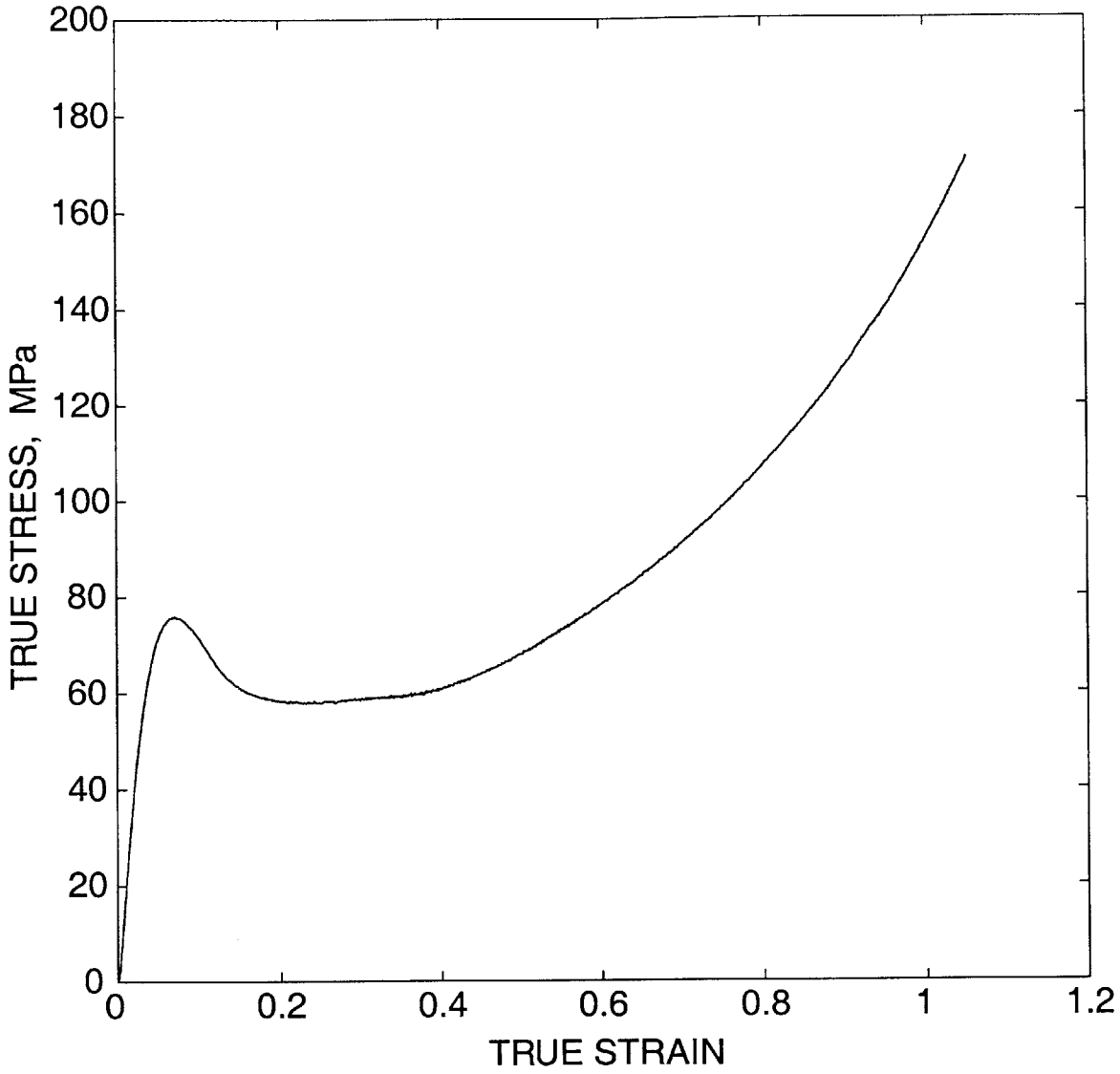

Figure F-32: Stress-strain response for simple compression of PC.

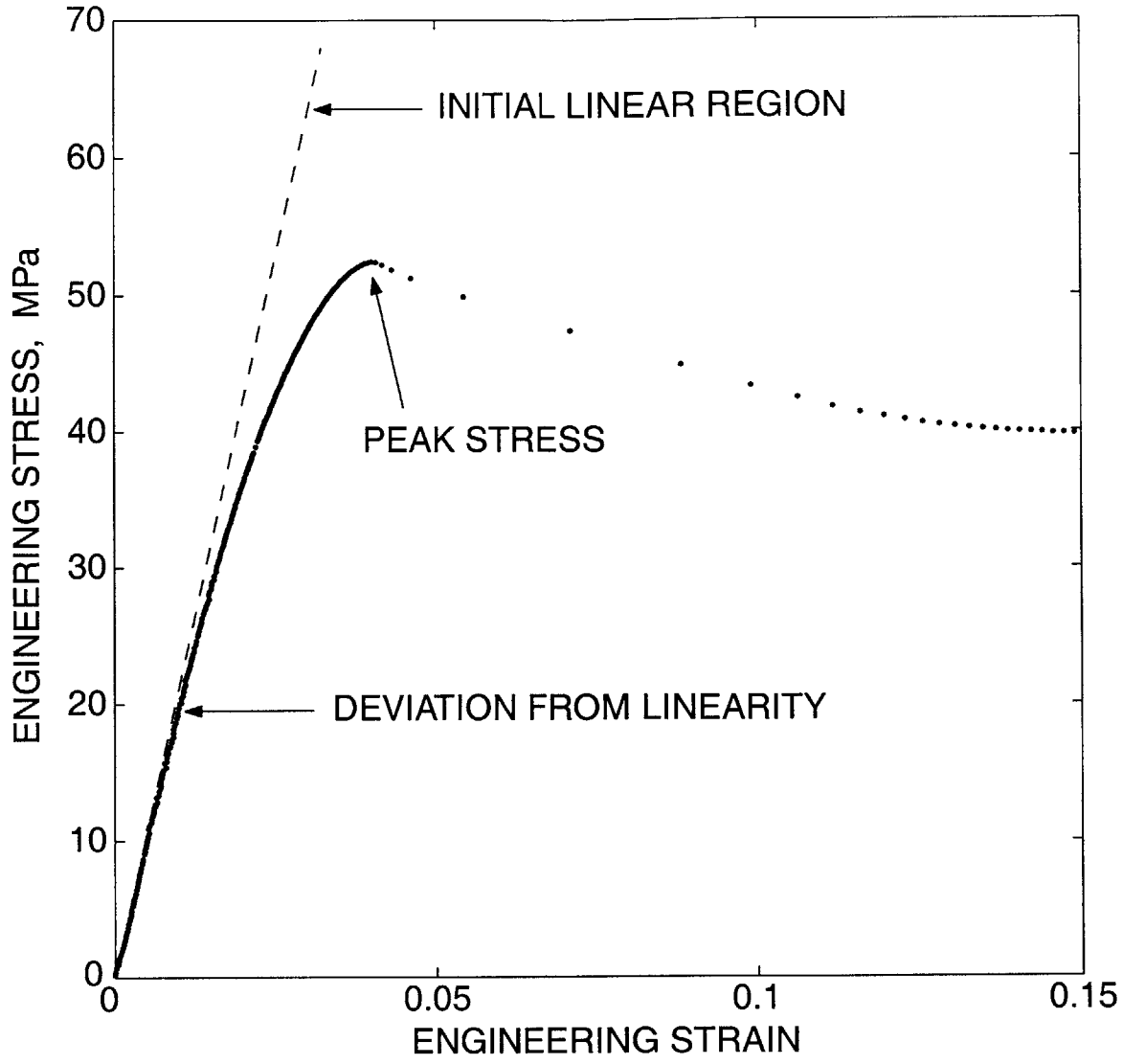

Figure F-33: Plane strain tension of PC. Engineering stress-strain response for a specimen loaded through its peak load.

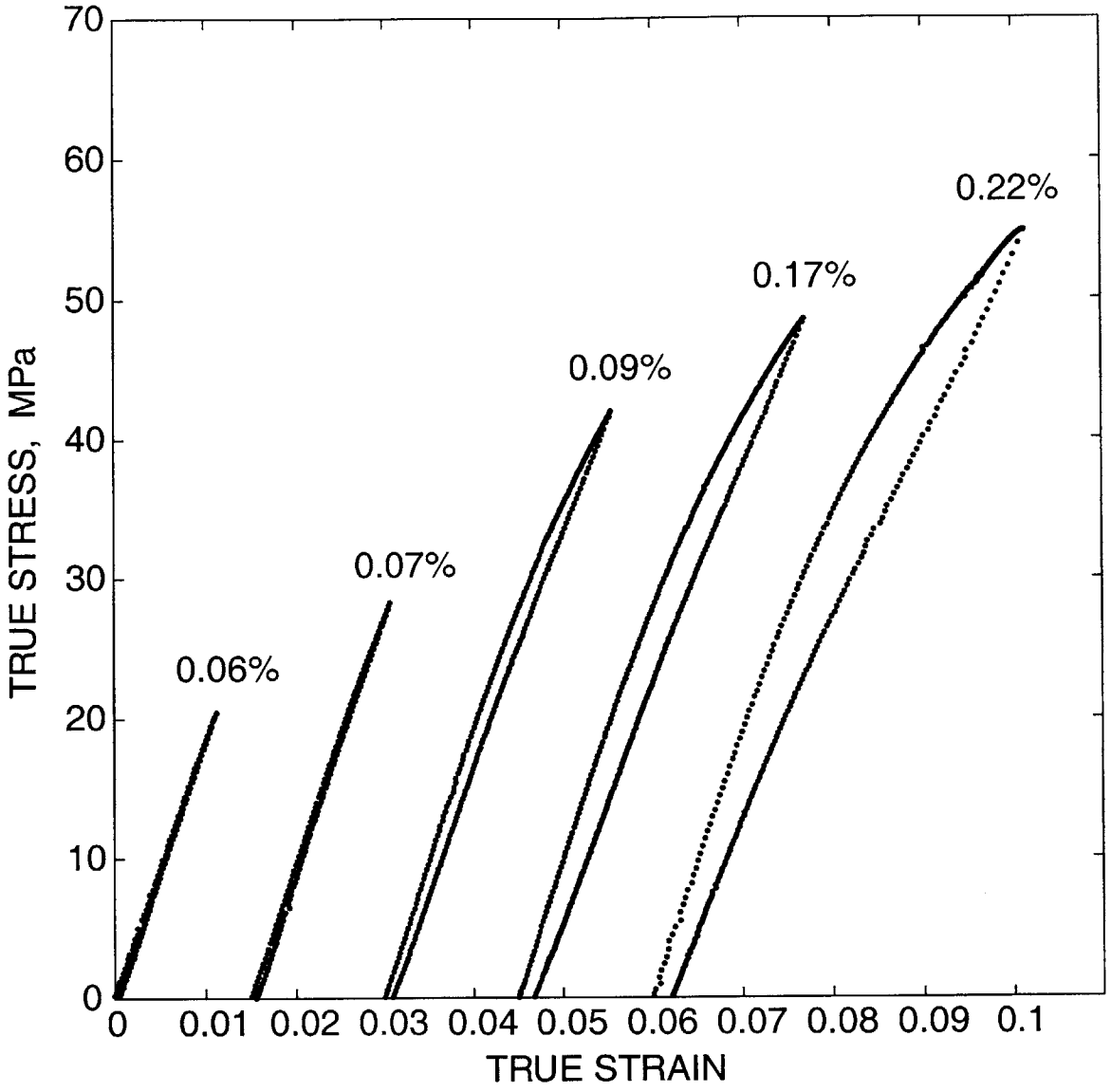

Figure F-34: Plane strain tension of PC. True stress-strain responses for specimens loaded to stress levels prior to the peak stress. Each test has been shifted horizontally in order to elucidate individual responses. The residual strain upon unloading is indicated above each curve.

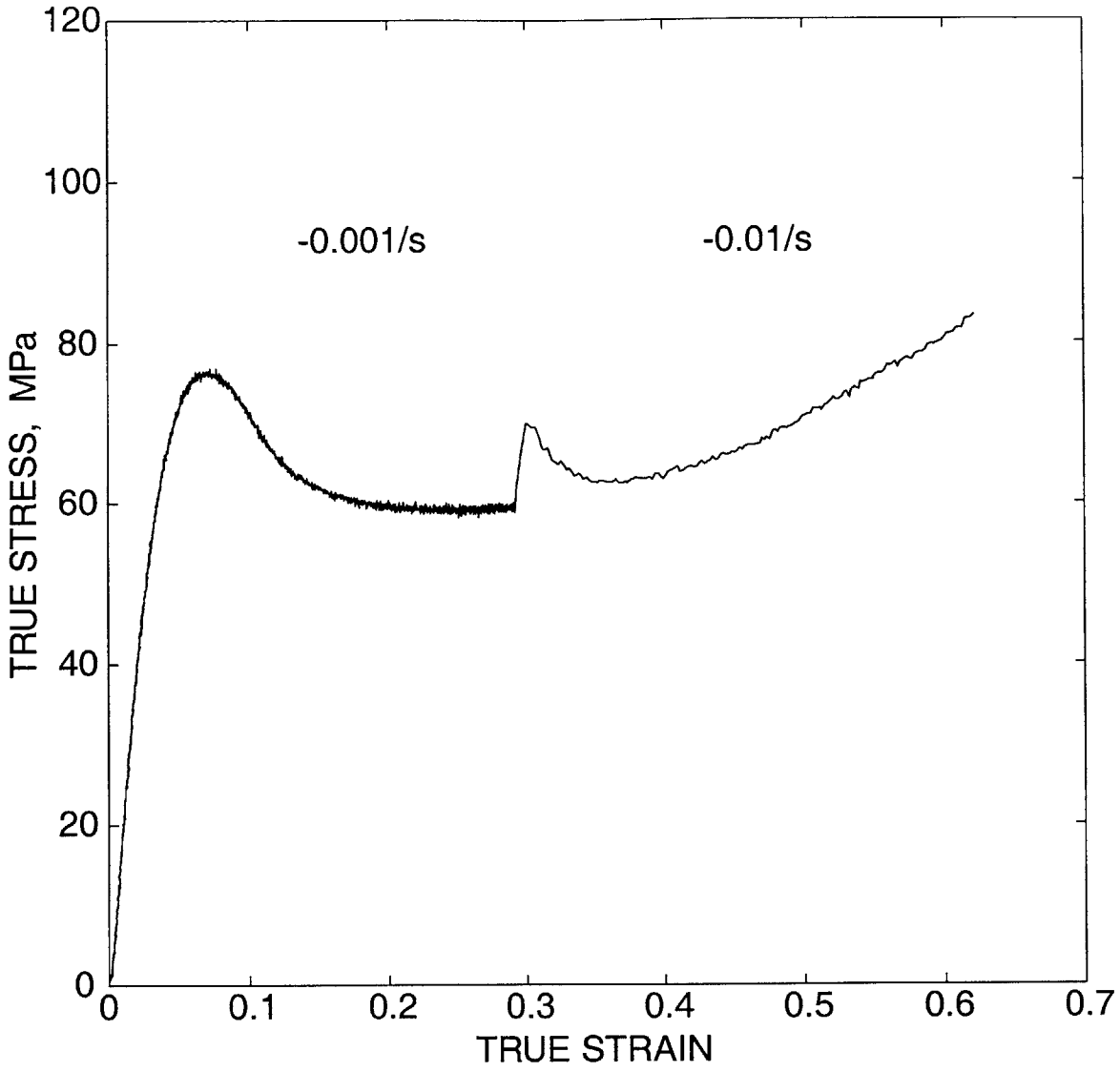

Figure F-35: Strain rate increment experiment on PC in simple compression. The initial true strain rate of -0.001/s is increased to -0.01/s as indicated.

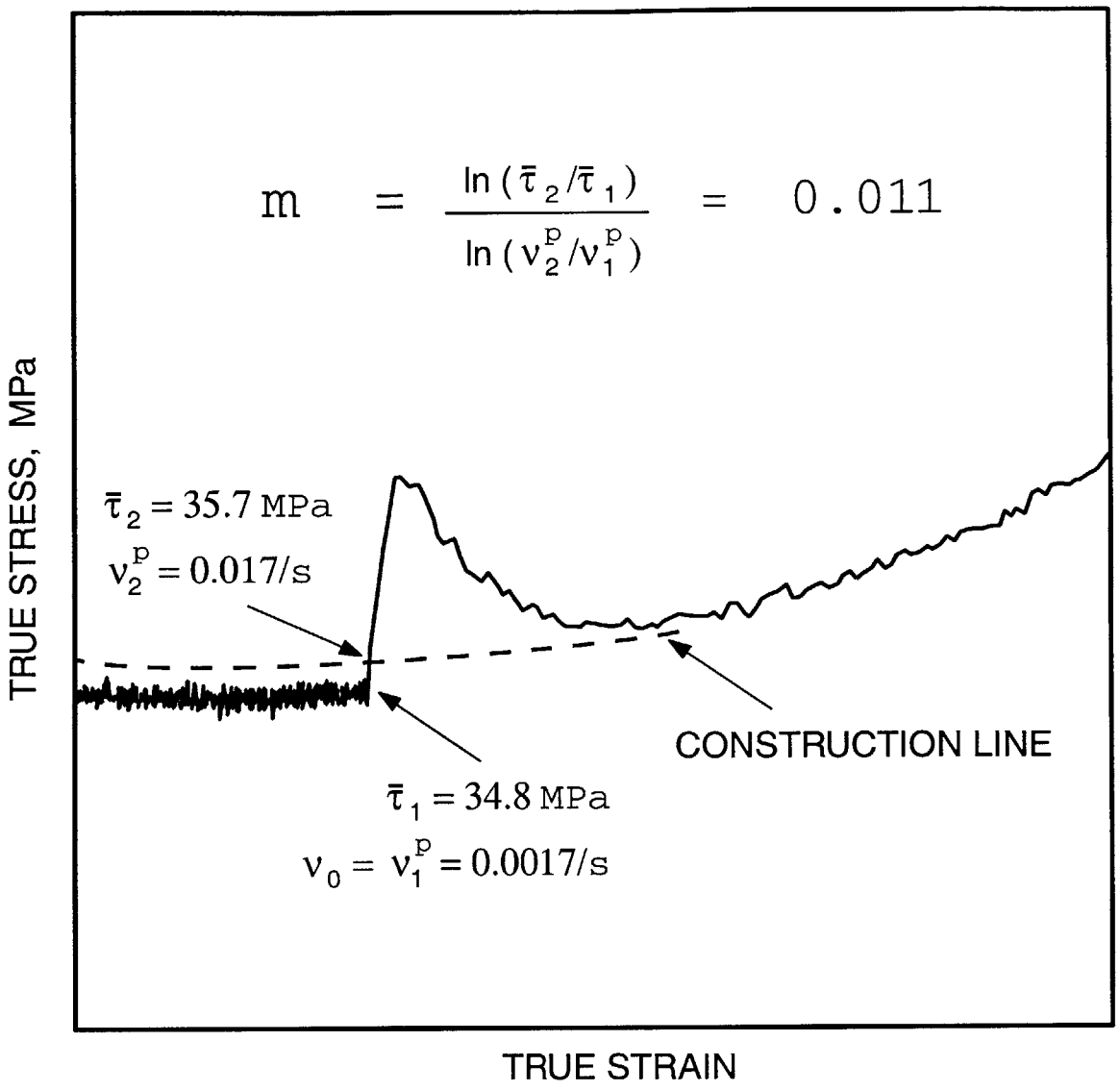

Figure F-36: Detail of the stress-strain curve of Fig. F-35 showing the calculation of the strain-rate sensitivity parameter m. The indicated construction line is extrapolated back to the strain at which the rate increment is imposed.

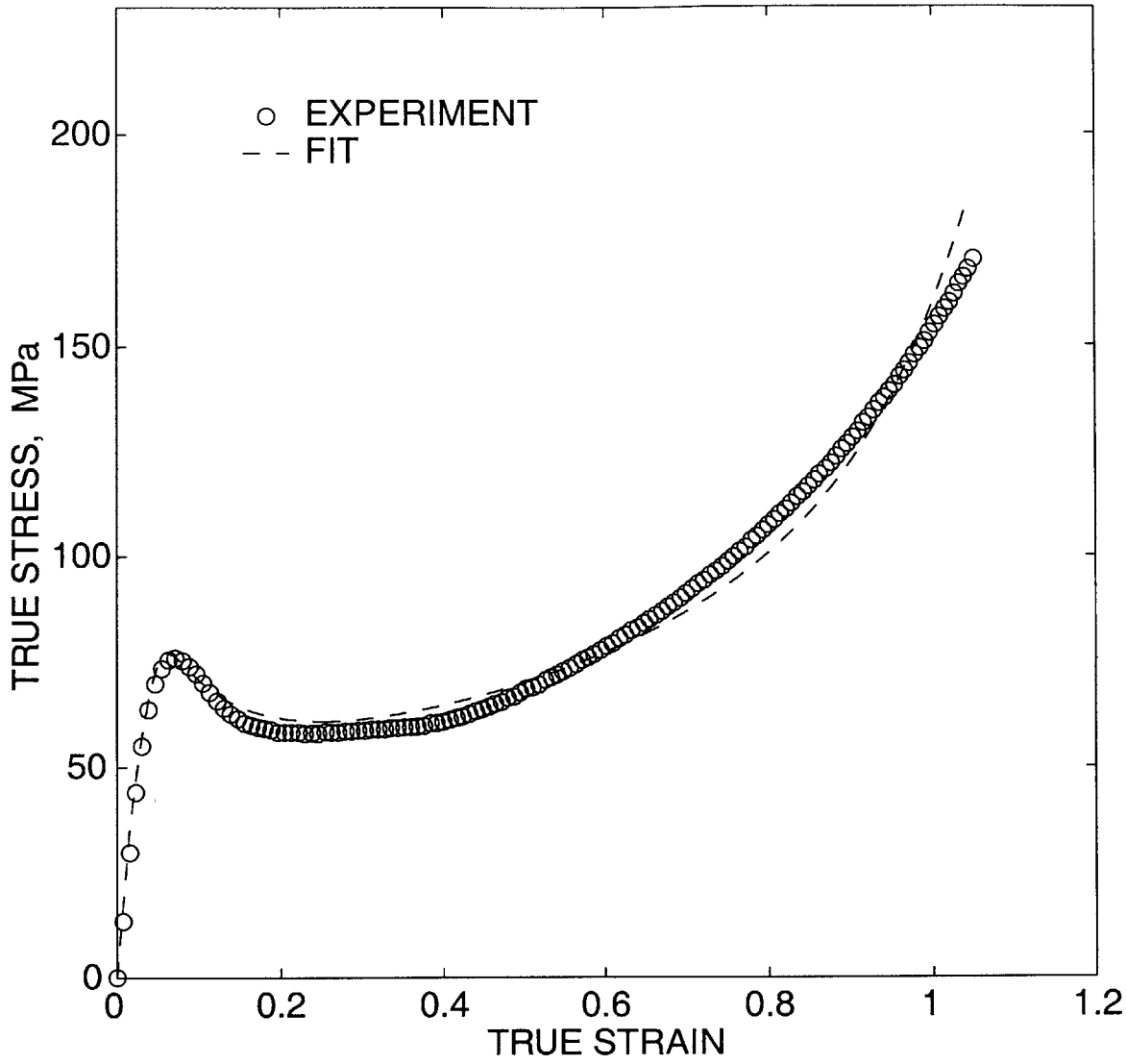

Figure F-37: Fit of the constitutive model to the stress-strain response of PC in simple compression.

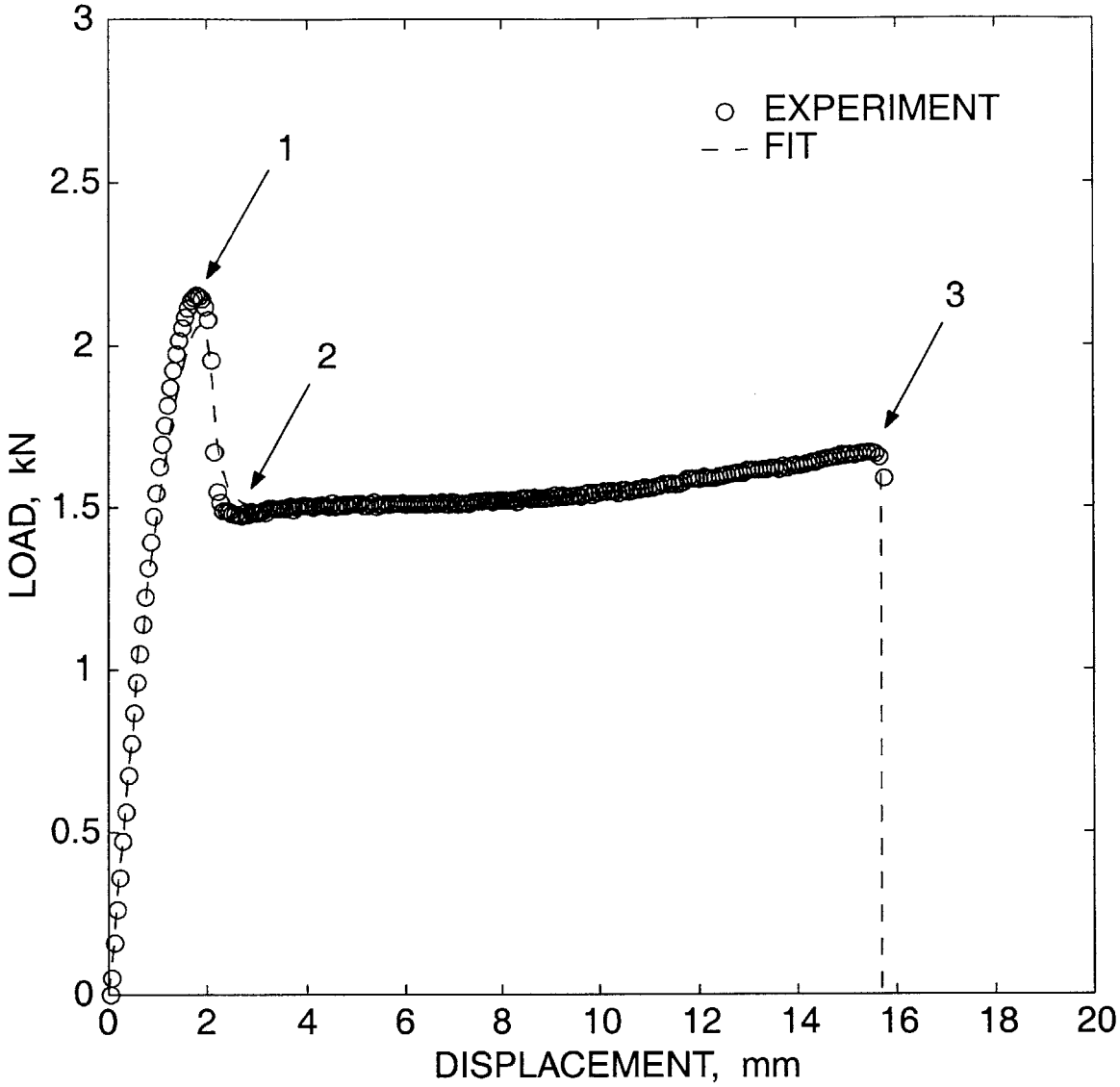

Figure F-38: Fit of the ductile fracture criterion in simple tension; experimental and numerical load-displacement curves.

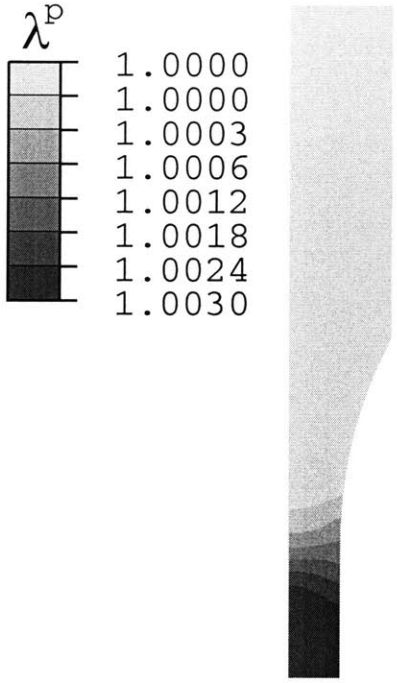

(a)

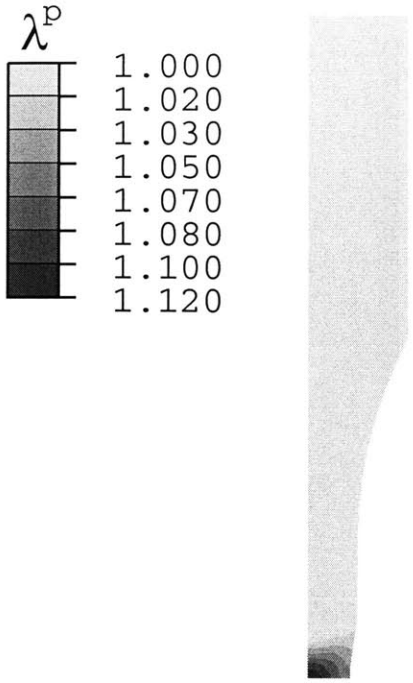

(b)

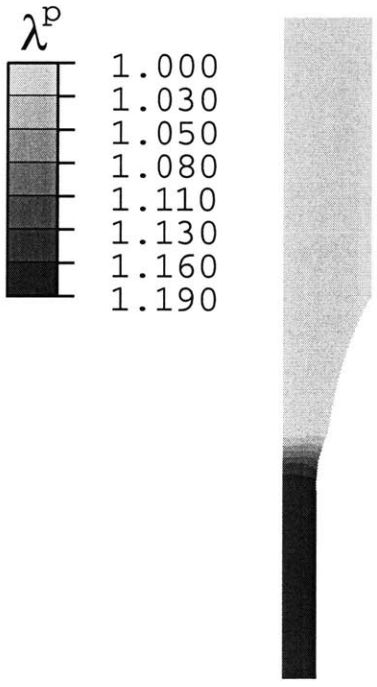

(c)

Figure F-39: Model fit of ductile fracture in uniaxial tension: Contour plots of evolution of λ^p for locations (b) 1, (c) 2, and (d) 3 as indicated on the numerical curve in Fig. F-38

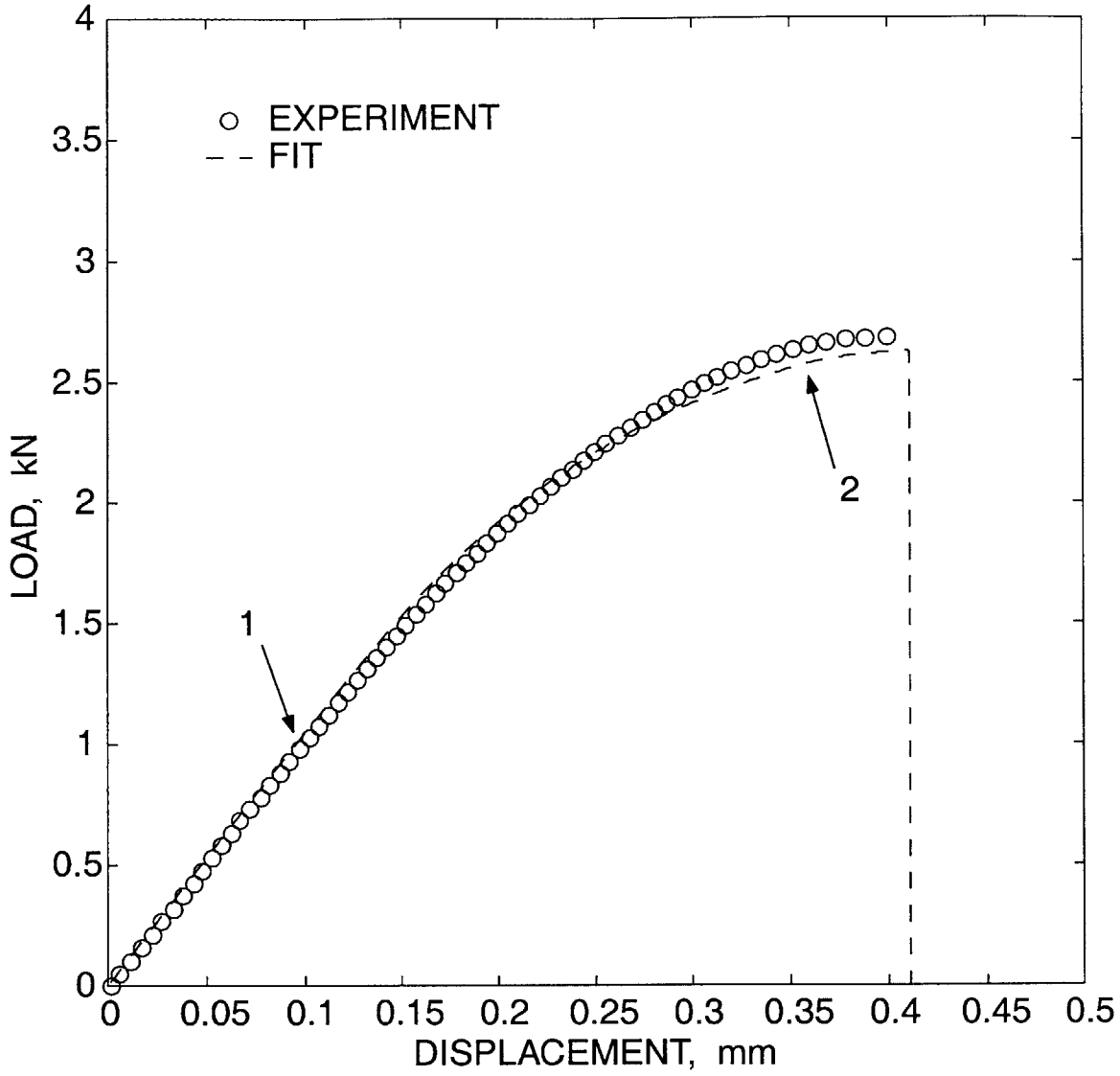

Figure F-40: Fit of the brittle fracture criterion in tension of a notched bar PC specimen; experimental and numerical load-displacement curves.

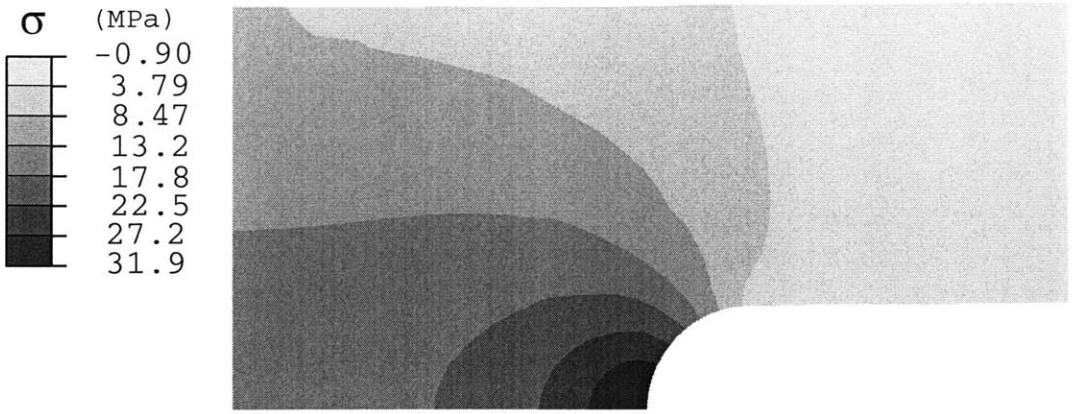

(a)

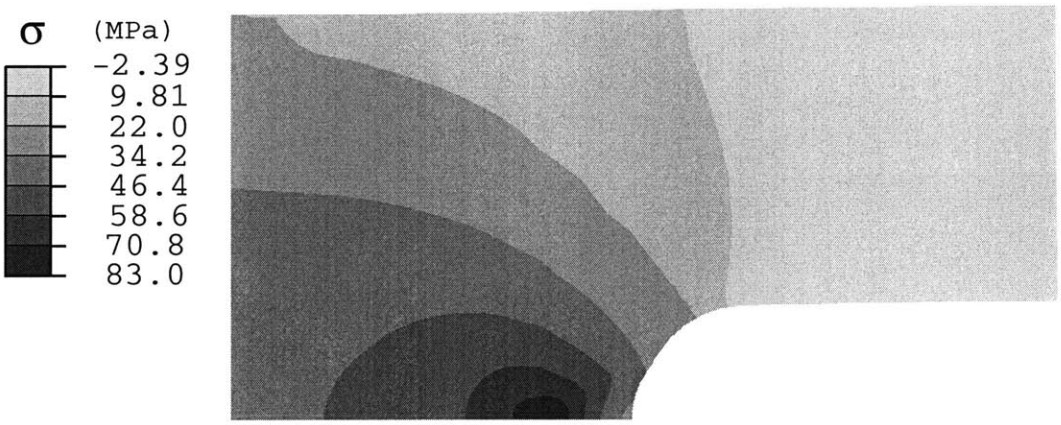

(b)

Figure F-41: Fit of the brittle fracture criterion in tension of a notched-bar PC specimen; contour plots of σ at (a) location 1 and (b) location 2 as indicated in Fig. F-40.

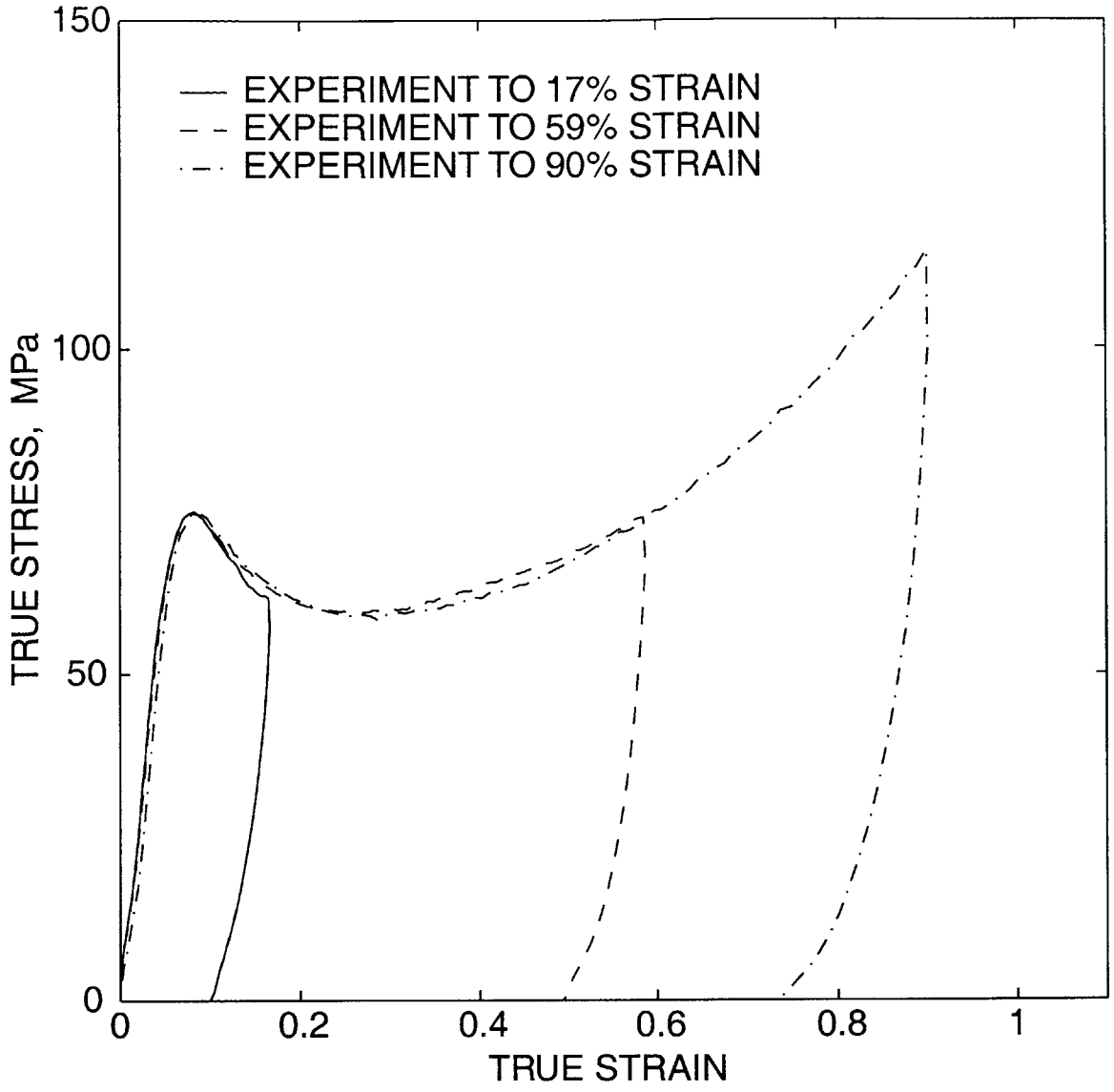

Figure F-42: Experimental stress-strain curves showing the reverse yield effect observed for PC in simple compression.

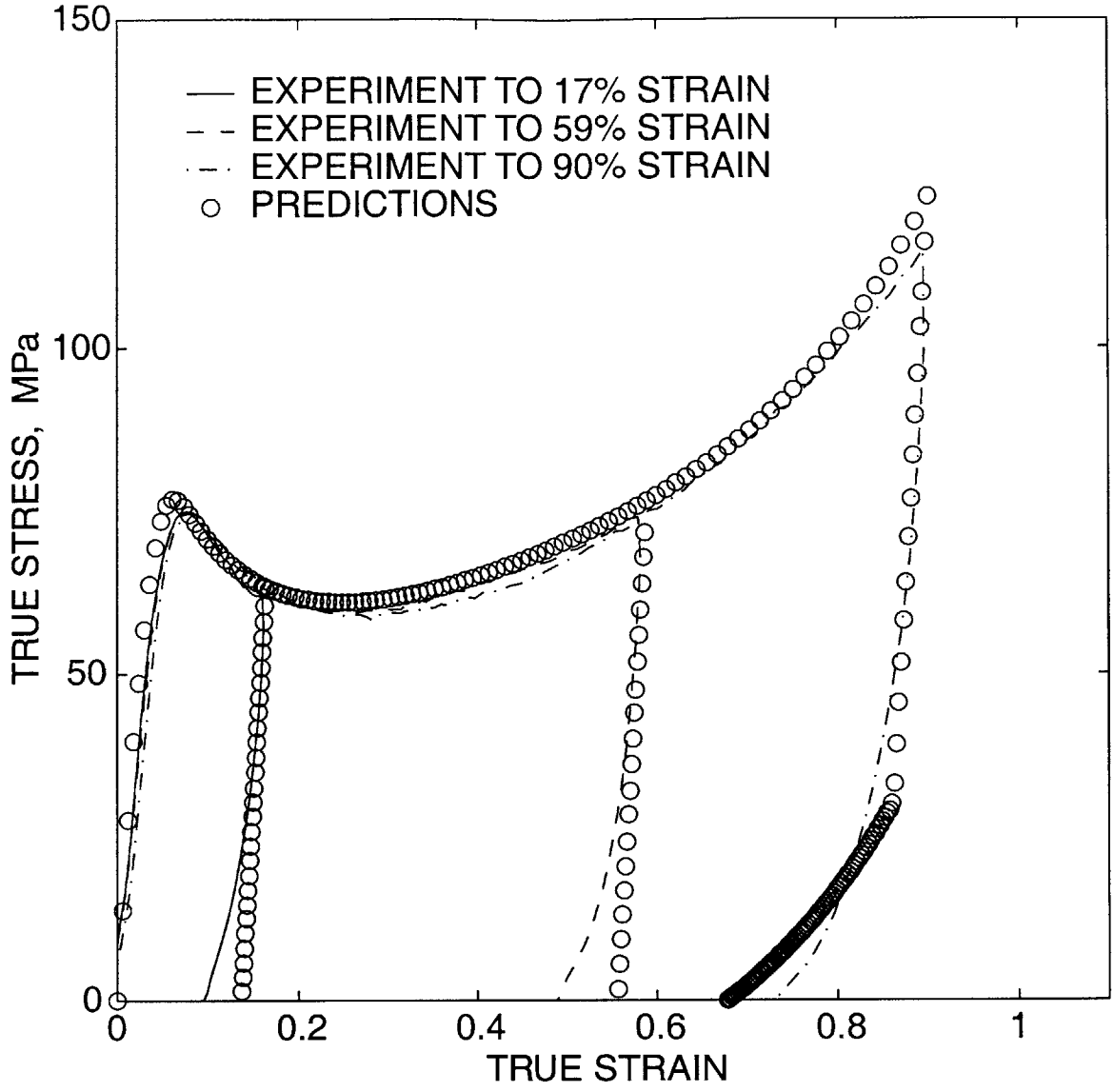

Figure F-43: Numerically predicted stress-strain curves for the loading-unloading response of PC in simple compression.

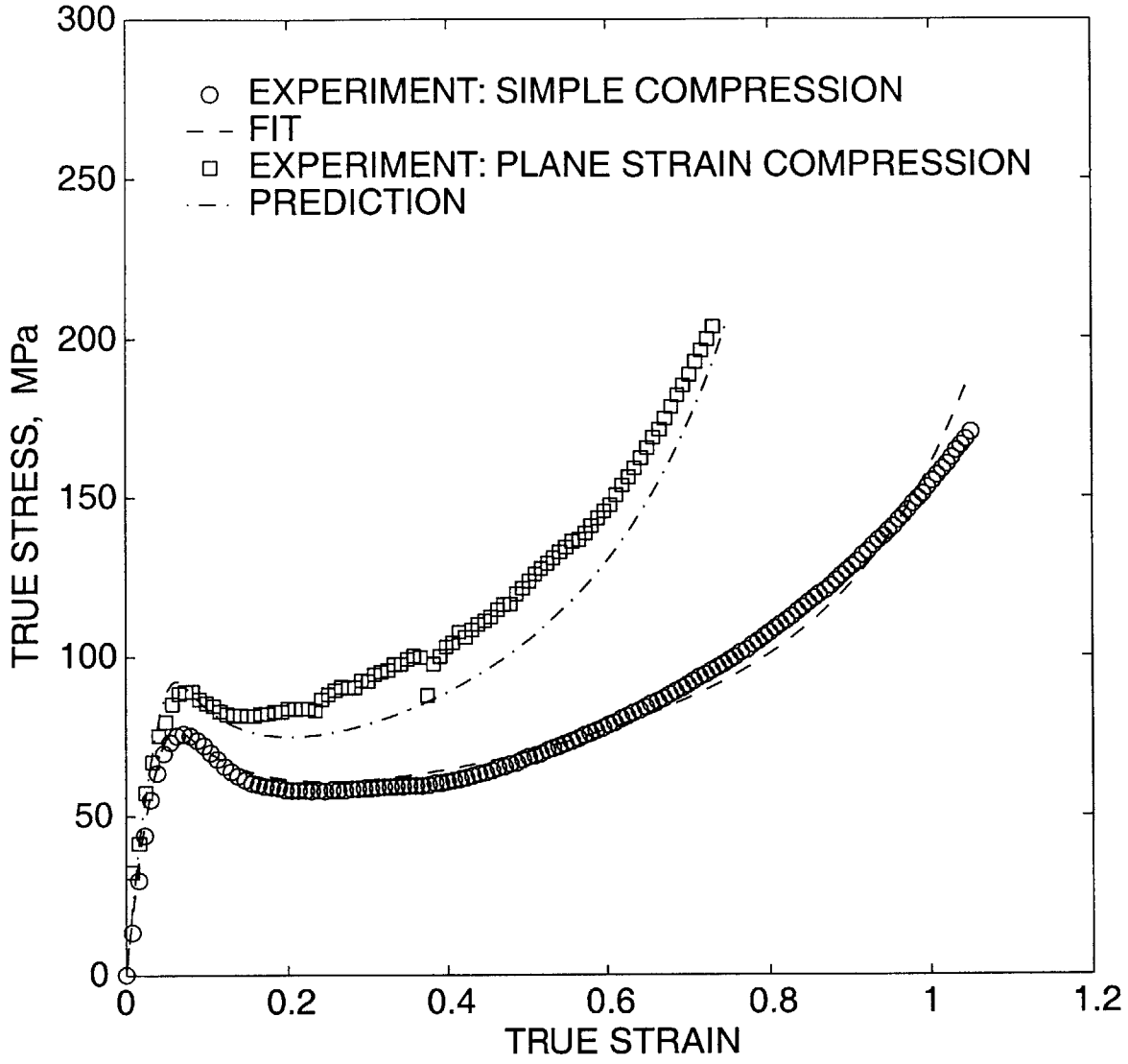

Figure F-44: Simple and plane strain compression experiments on PC with corresponding model results.

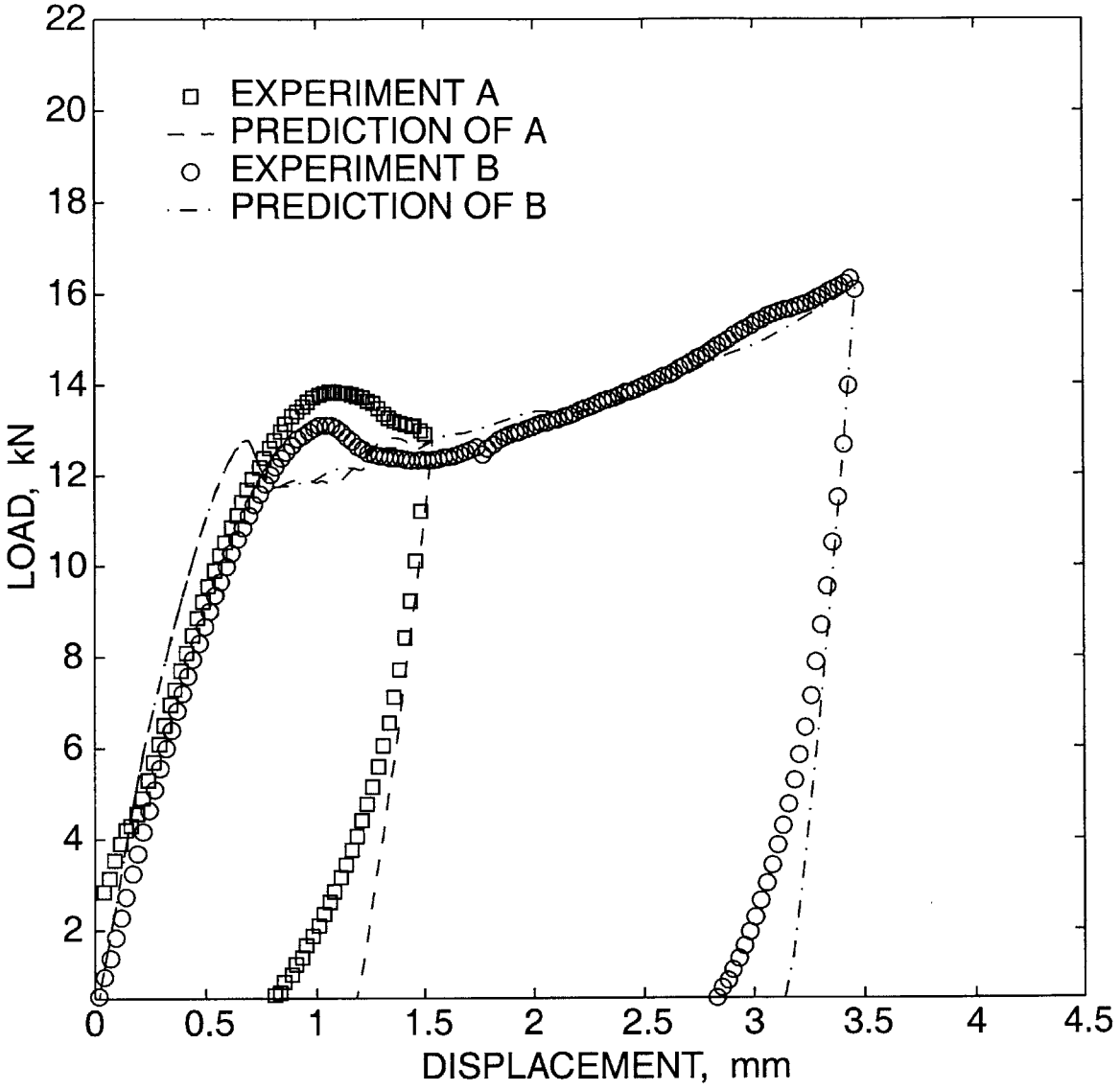

Figure F-45: Load-displacement curves for plane strain compression experiments on PC with corresponding model results.

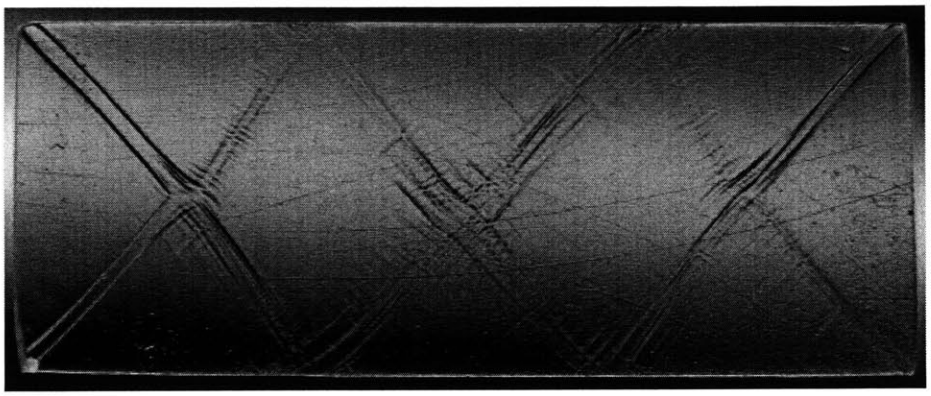

(a)

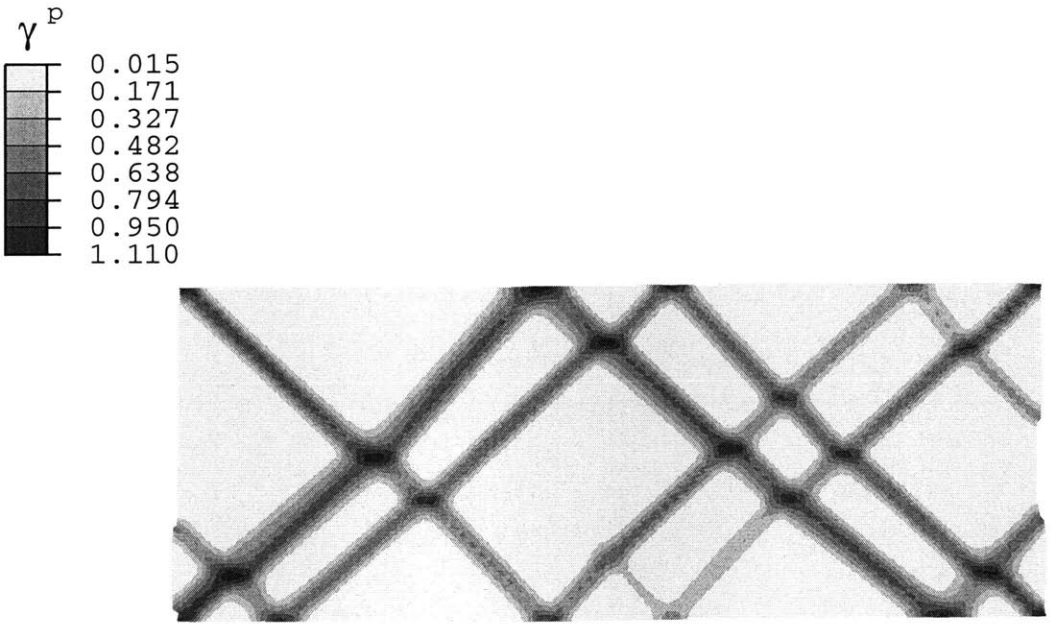

(b)

Figure F-46: Plane strain compression experiment "A" of Fig. F-45: (a) Experimental specimen. (b) Numerically predicted specimen showing contours of γ^p for direct comparison with (a).

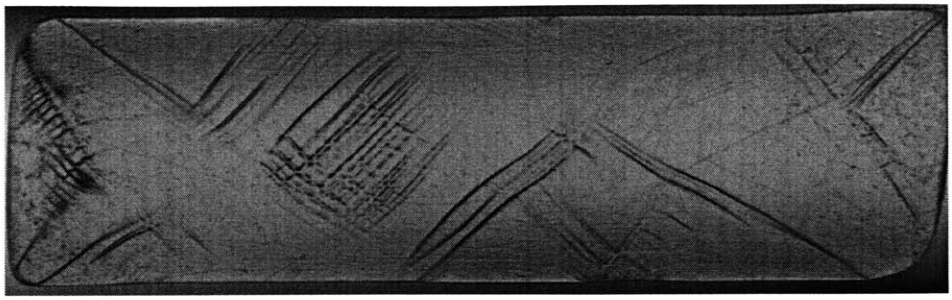

(a)

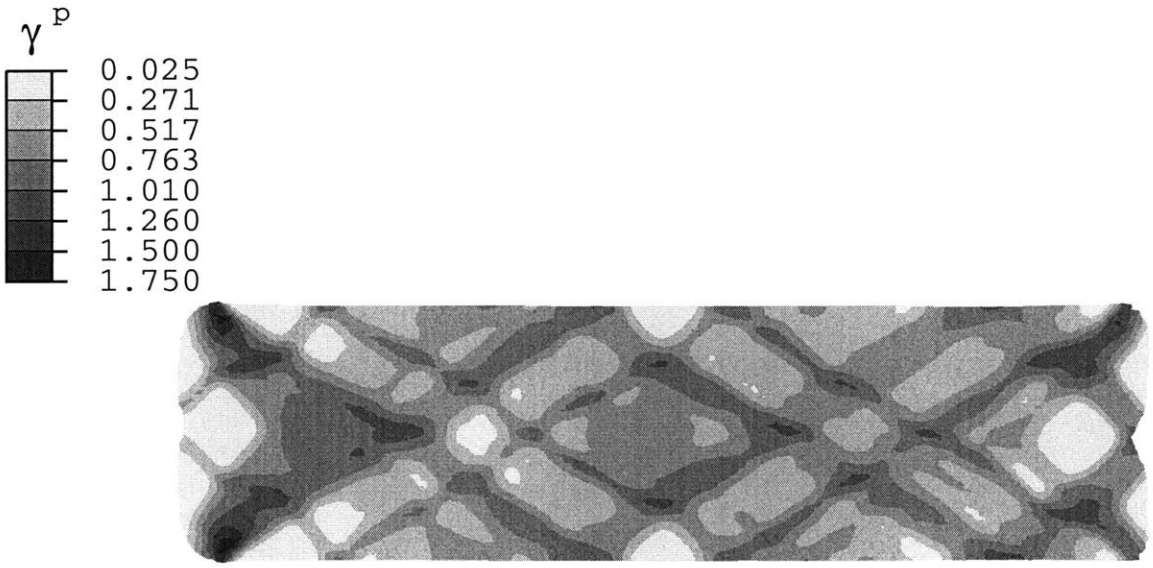

(b)

Figure F-47: Plane strain compression experiment "B" of Fig. F-45: (a) Experimental specimen. (b) Numerically predicted specimen showing contours of γ^p for direct comparison with (a).

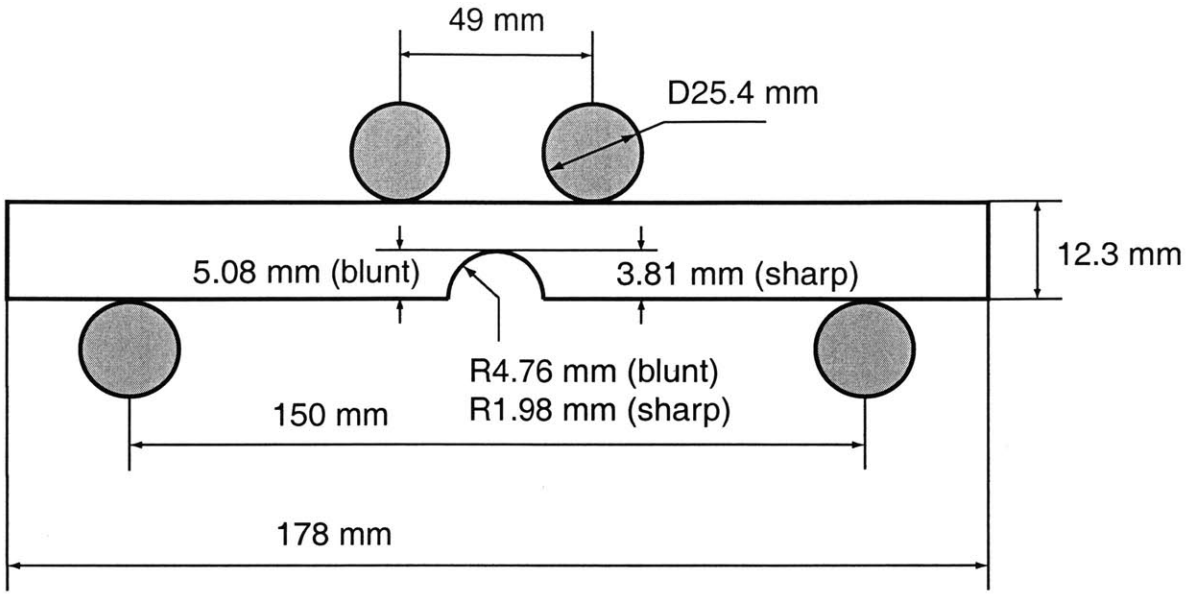

Figure F-48: Geometry of four-point bending experiments. All specimens have a 50 mm nominal width.

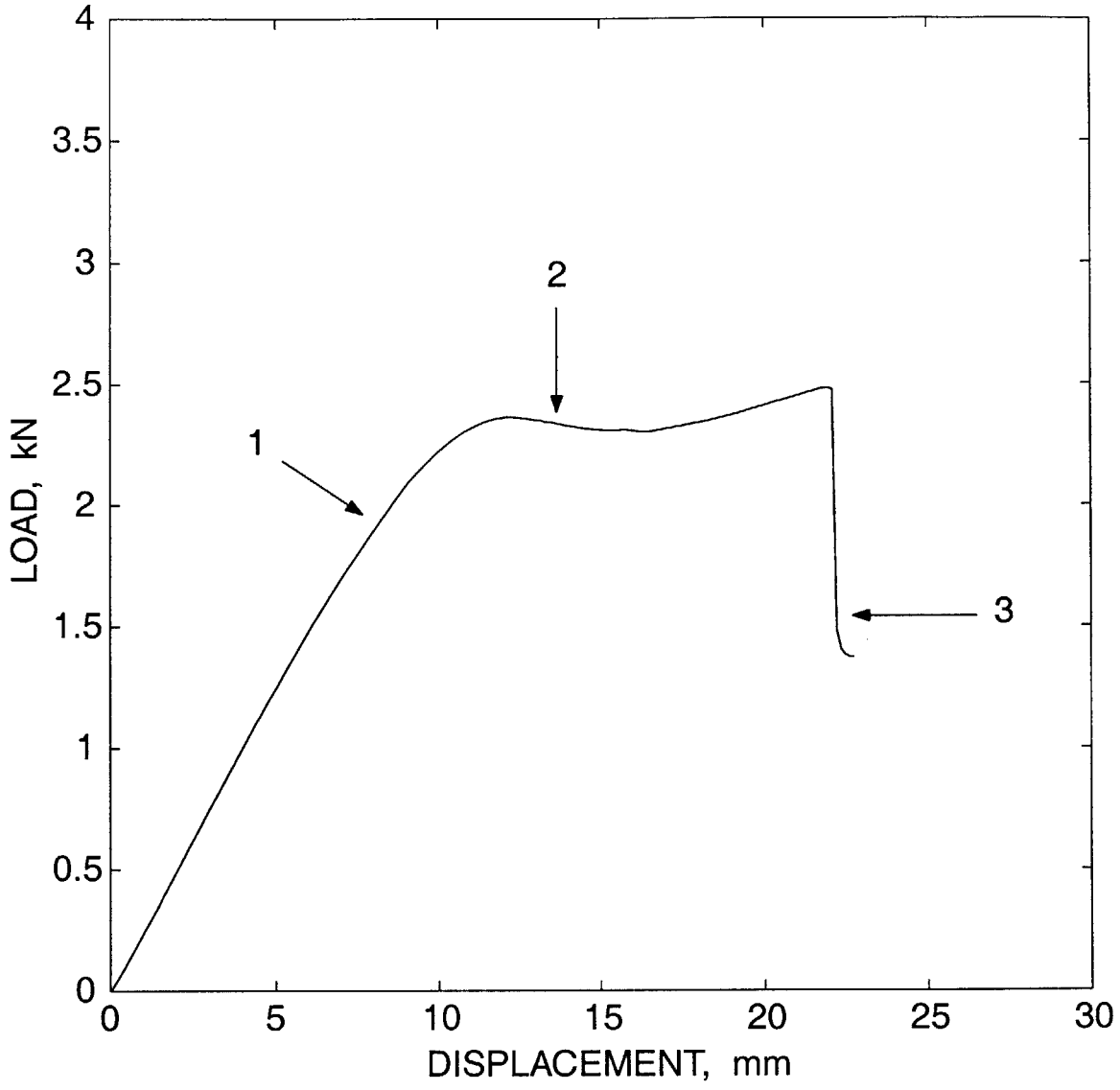

Figure F-49: Load-displacement curve for four-point bending of a blunt-notched PC beam.

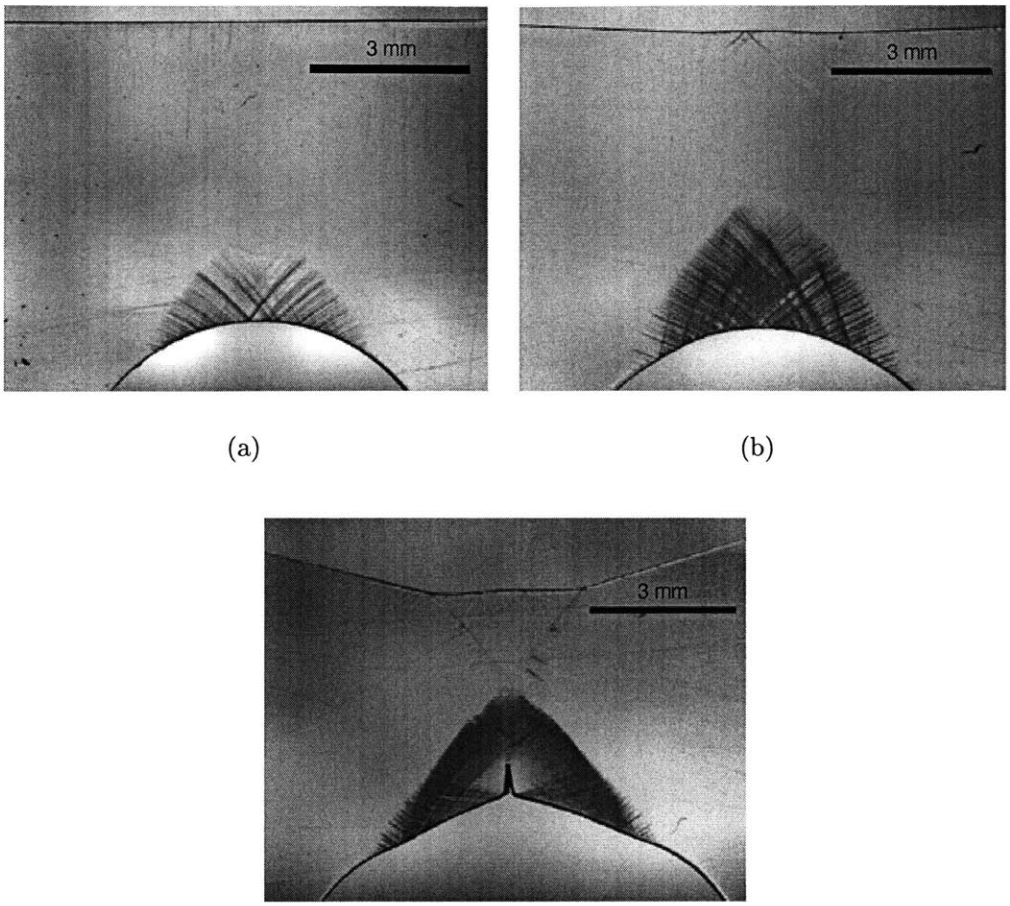

(a) (b)

(c)

Figure F-50: Four-point bending of a blunt notched PC specimen: Micrographs of unloaded specimen cross-sections are shown at: (a) location 1, (b) location 2, and (c) location 3 as indicated on the load-displacement curve in Fig. F-49.

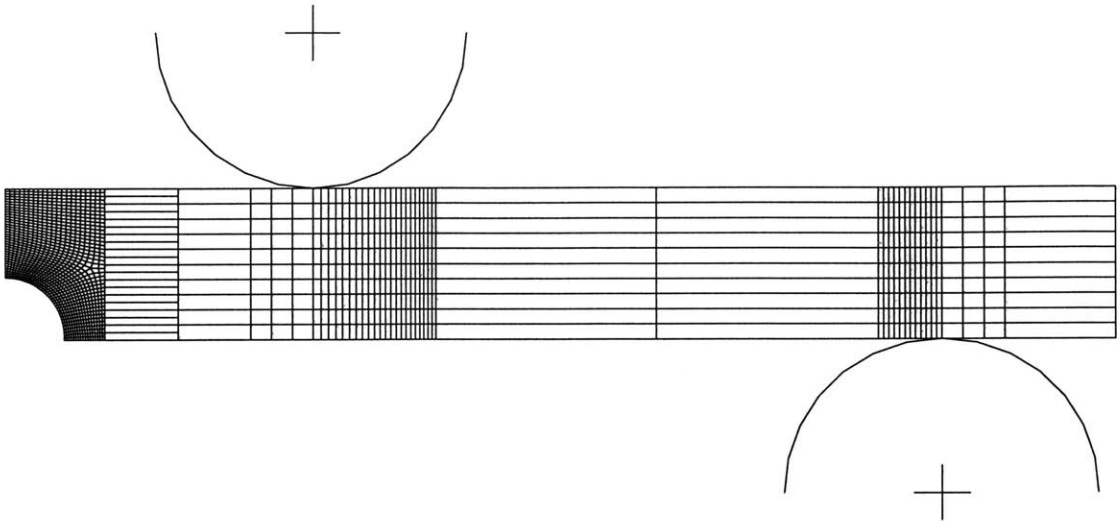

(a)

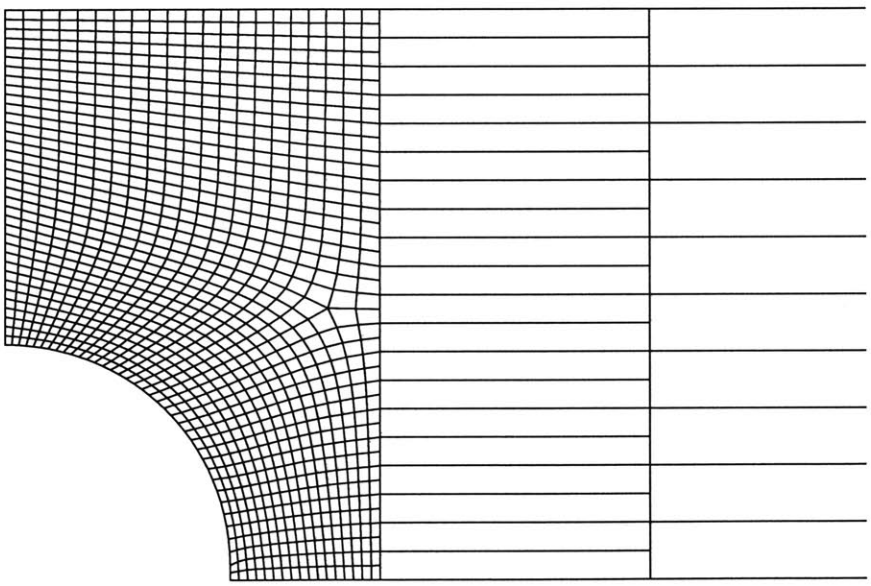

(b)

Figure F-51: Mesh used for four-point bending of the blunt-notched beam: (a) whole mesh using half-symmetry. (b) detail of the mesh at the notch-root.

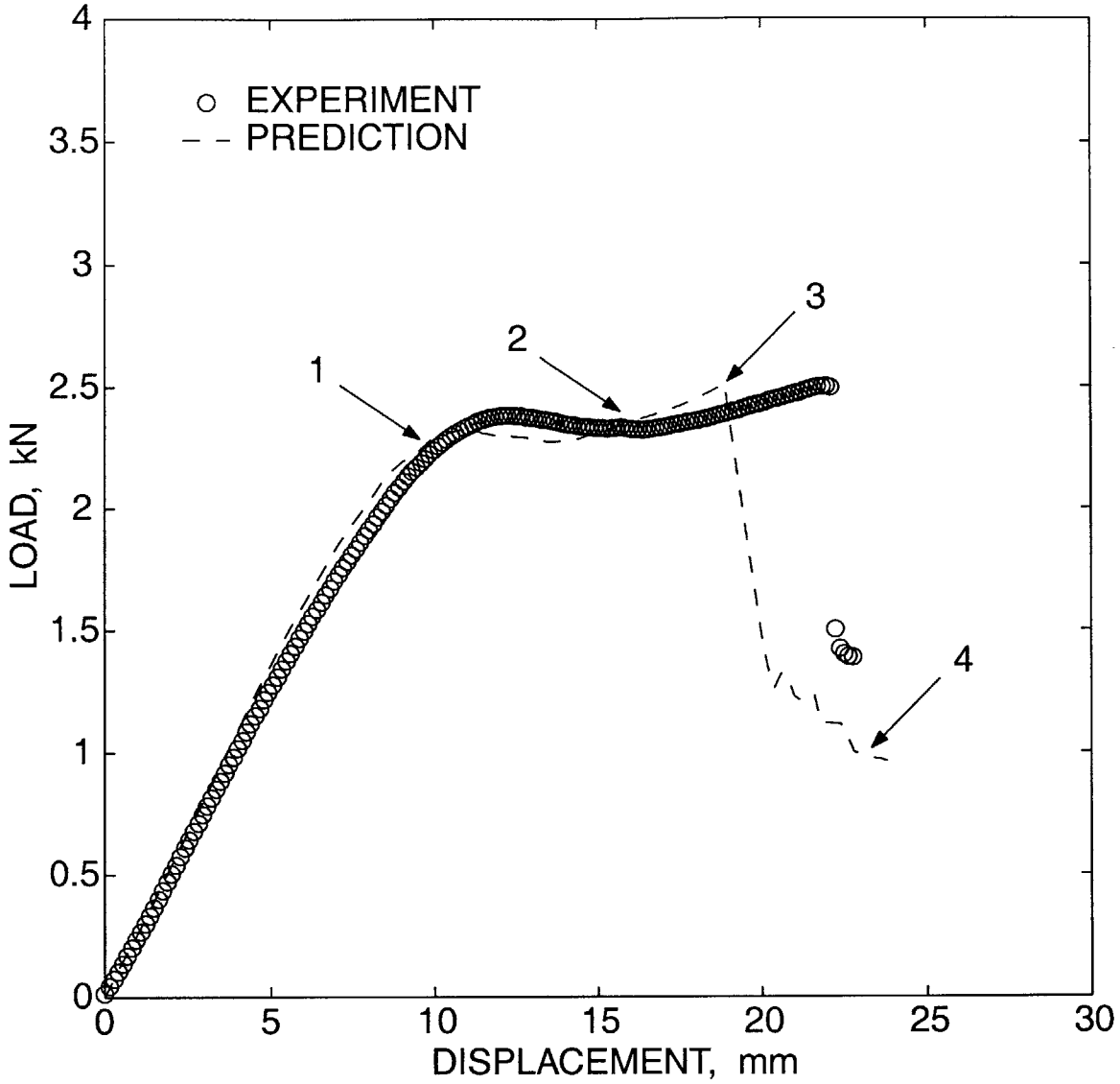

Figure F-52: Experimental and numerically predicted load-displacement curves for four-point bending of a blunt-notched PC beam.

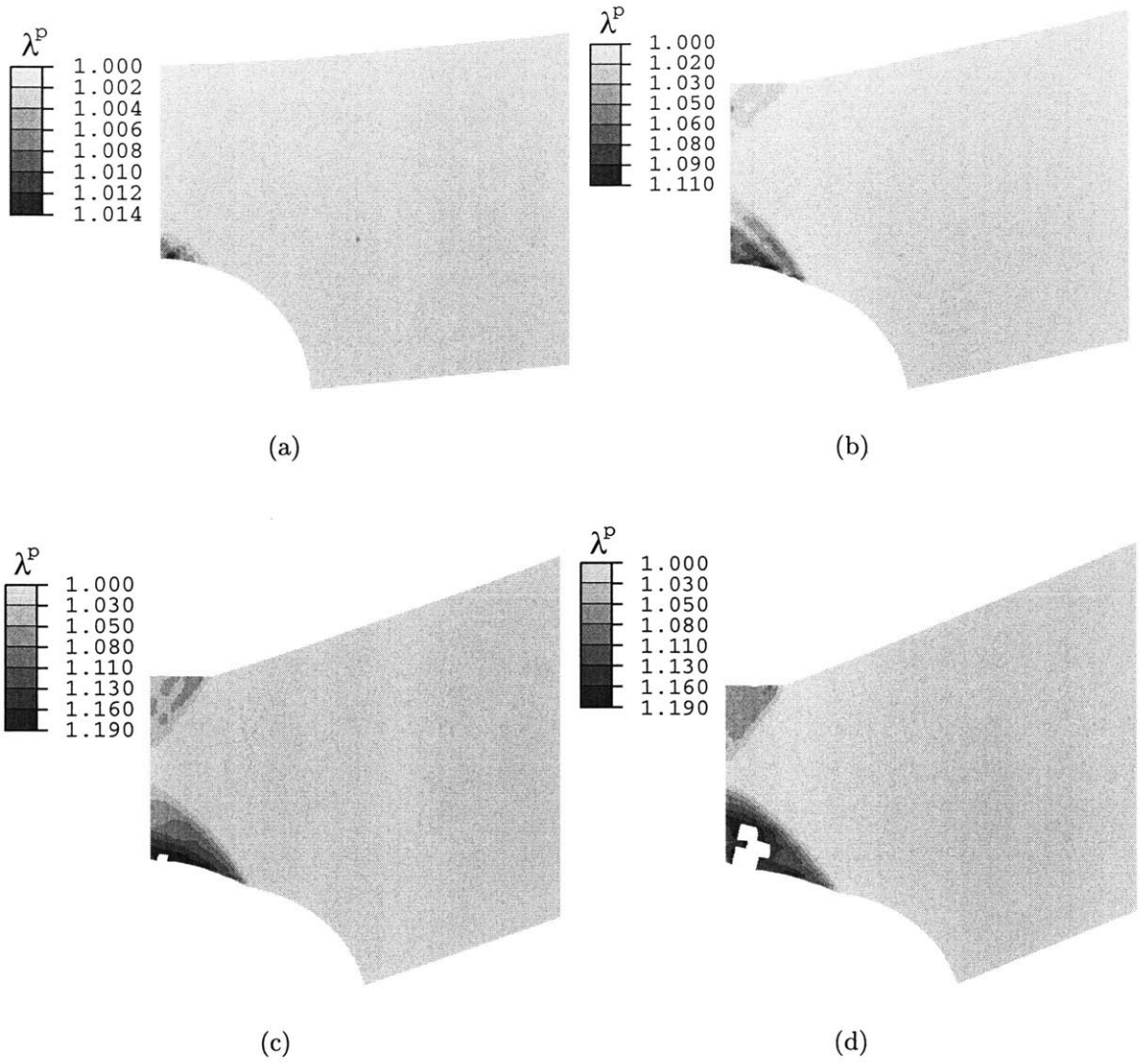

Figure F-53: Prediction of the fracture process in blunt-notch beam bending. Contour plots of λ^p corresponding to (a) location 1, (b)location 2, (c) location 3, and (d) location 4 as indicated on the predicted curve in Fig. F-52. Ductile failure initiates at the notch root as indicated in (c) and propagates into the beam as seen in (d).

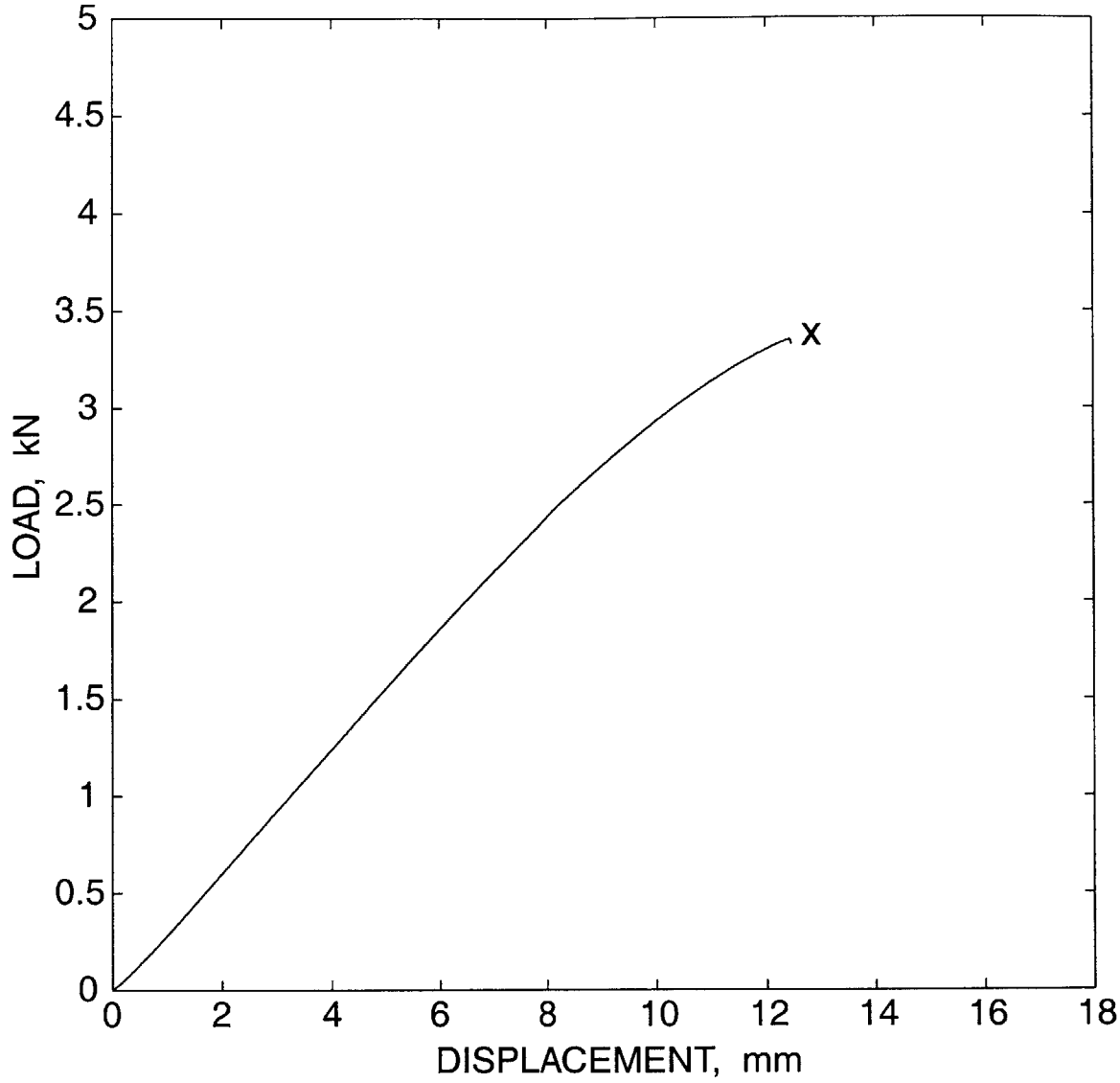

Figure F-54: Load-displacement curve for four-point bending of a sharp-notched PC beam. The location indicated by "x" is the location of fracture.

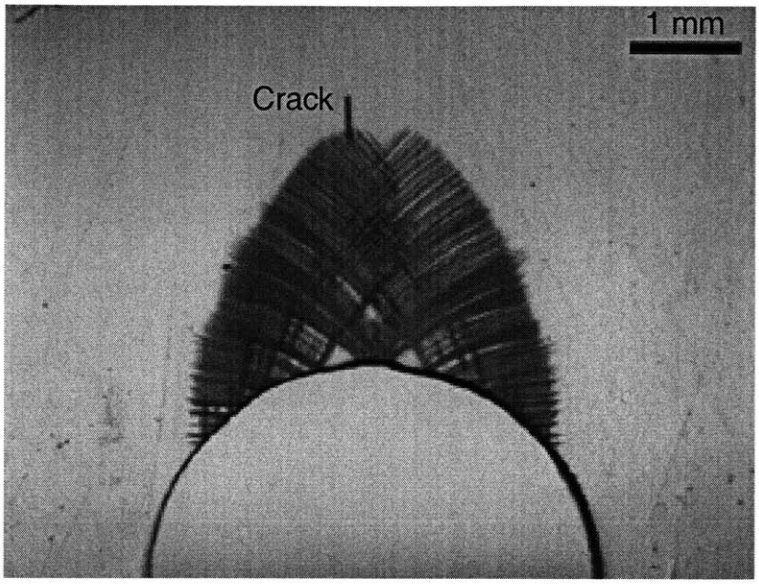

(a)

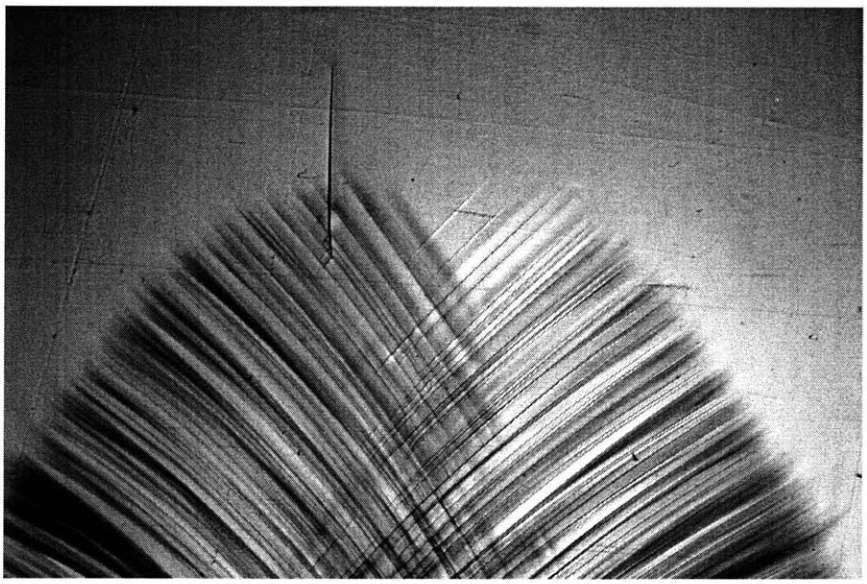

(b)

Figure F-55: (a) Micrograph of unloaded specimen cross-section at incipient fracture. The crack initiates at the apex of the plastic zone; (b) close-up of the crack at the apex of the plastic zone.

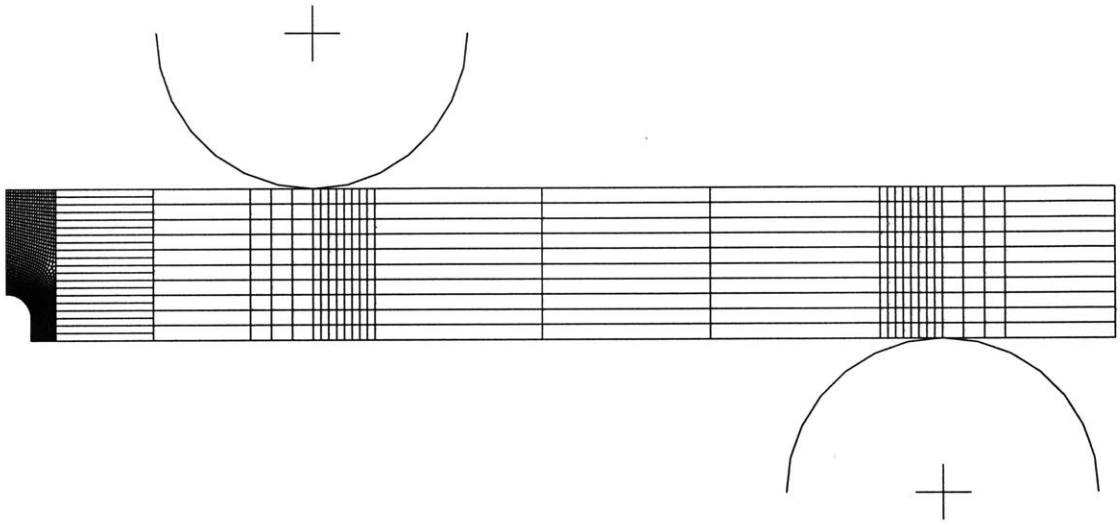

(a)

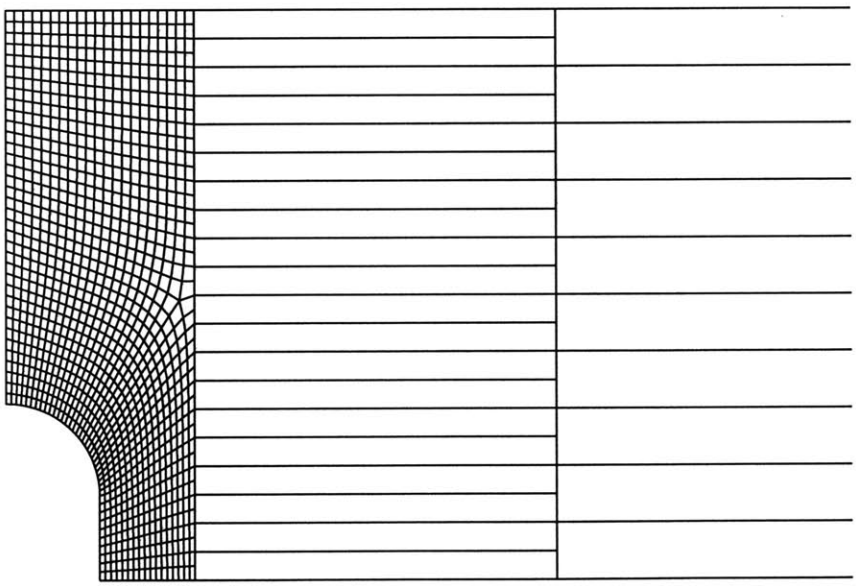

(b)

Figure F-56: Mesh used for four-point bending of the sharp-notched beam: (a) whole mesh using half-symmetry. (b) detail of the mesh at the notch-root.

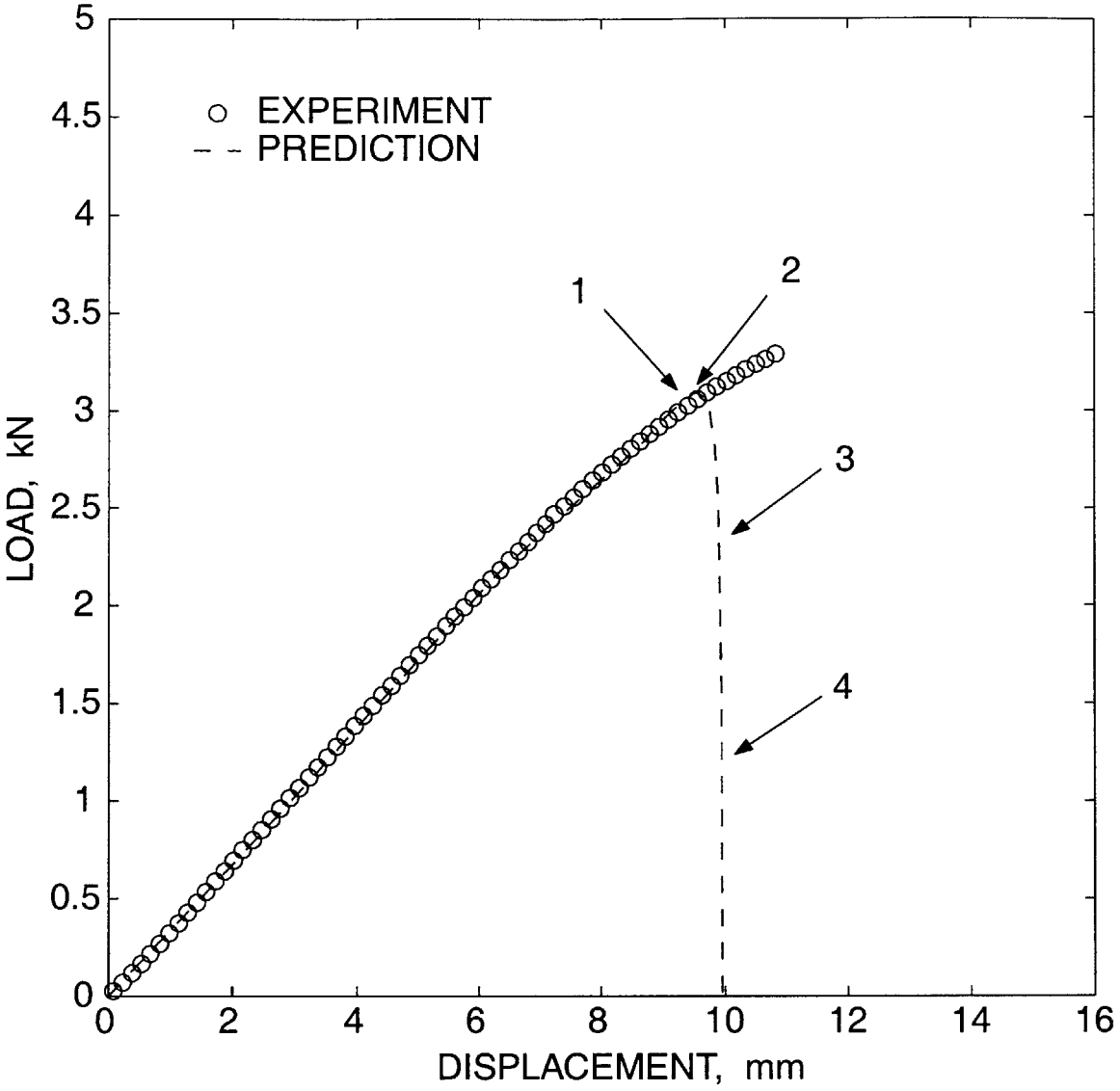

Figure F-57: Experimental and numerically predicted load-displacement curves for four-point bending of a sharp-notched PC beam.

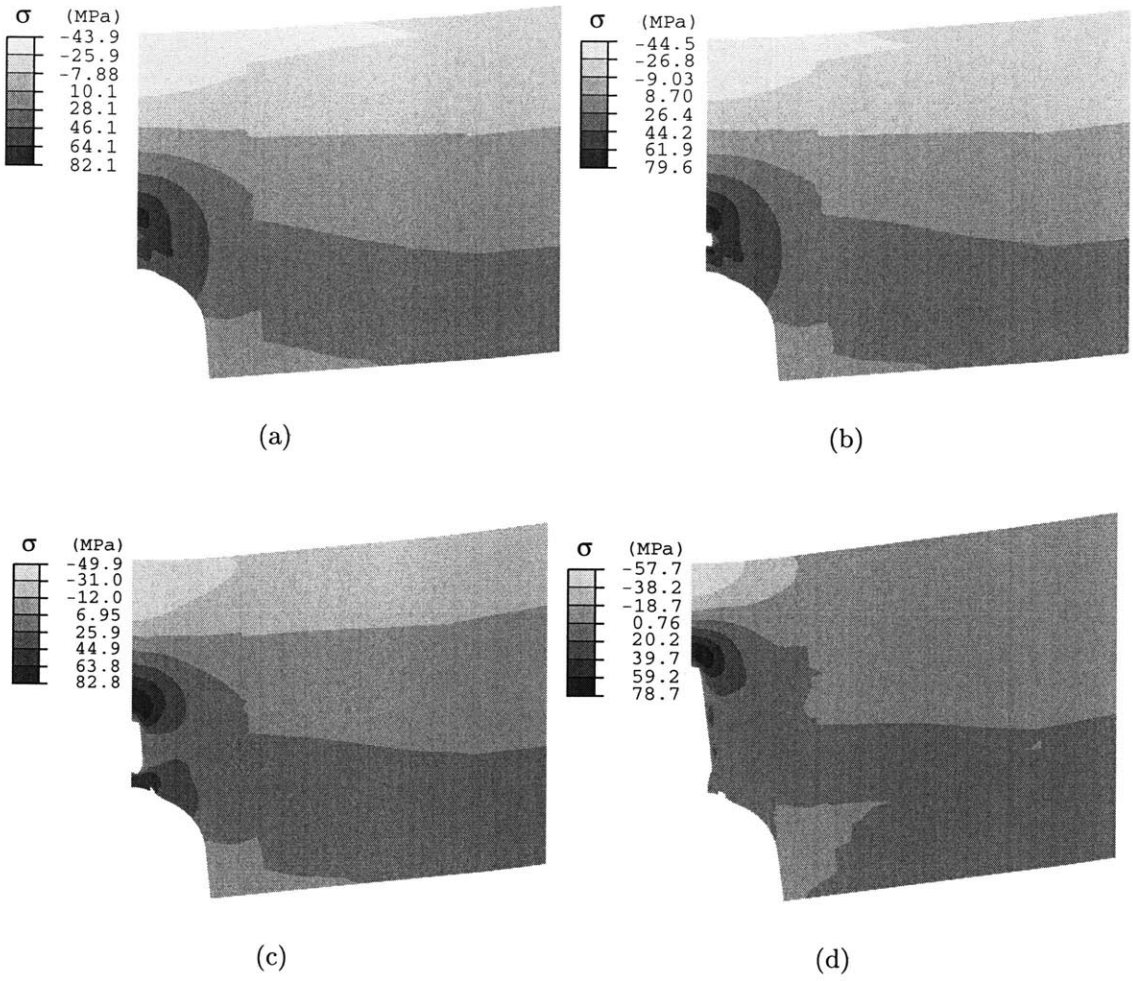

Figure F-58: Prediction of the fracture process in sharp-notch beam bending. Contour plots of σ corresponding to (a) location 1, (b) location 2, (c) location 3, and (d) location 4, as indicated on the predicted curve in Fig. F-57. Brittle fracture initiates ahead of the notch root as indicated in (b).

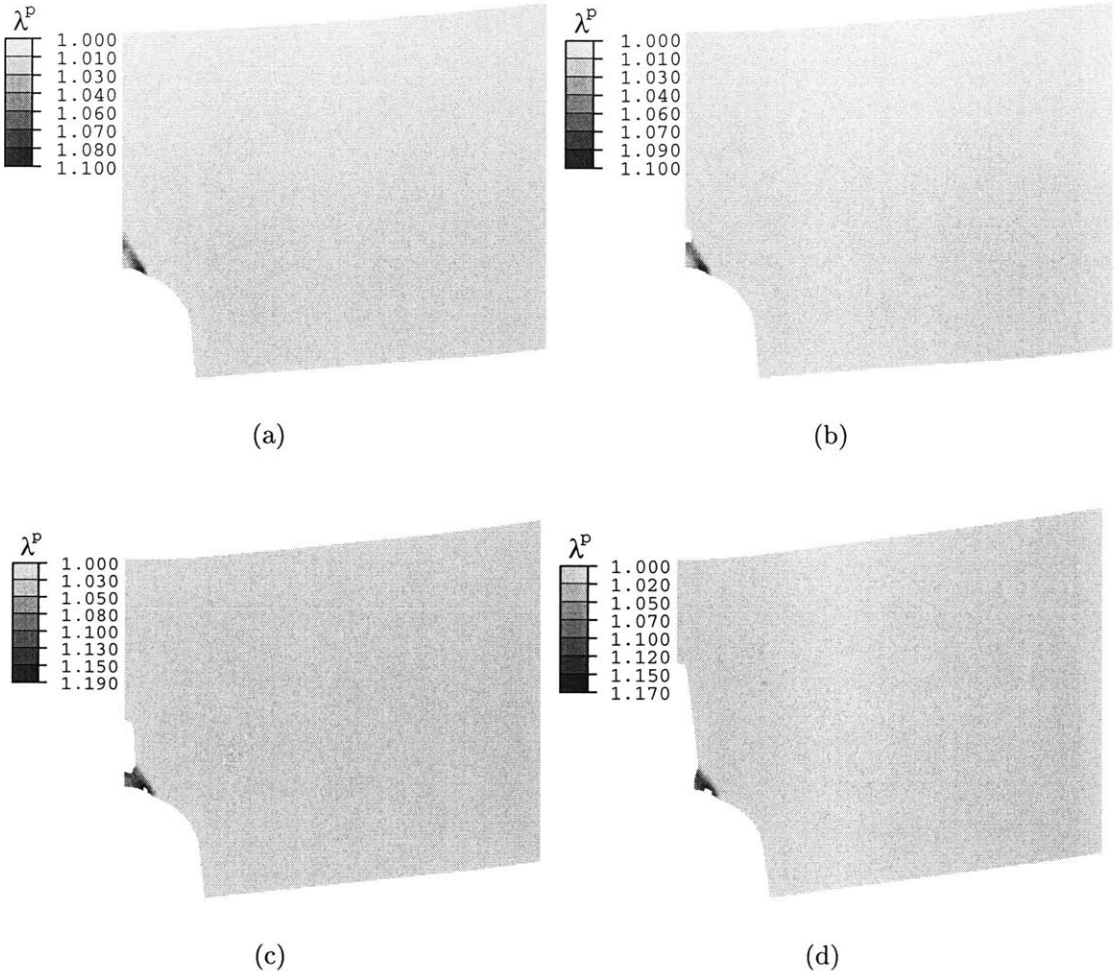

Figure F-59: Prediction of the fracture process in sharp-notch beam bending. Contour plots of λ^p corresponding to (a) location 1, (b)location 2, (c) location 3, and (d) location 4 as indicated on the predicted curve in Fig. F-57. Ductile failure initiates at the notch root as indicated in (c) after brittle fracture initiates ahead of the notch.

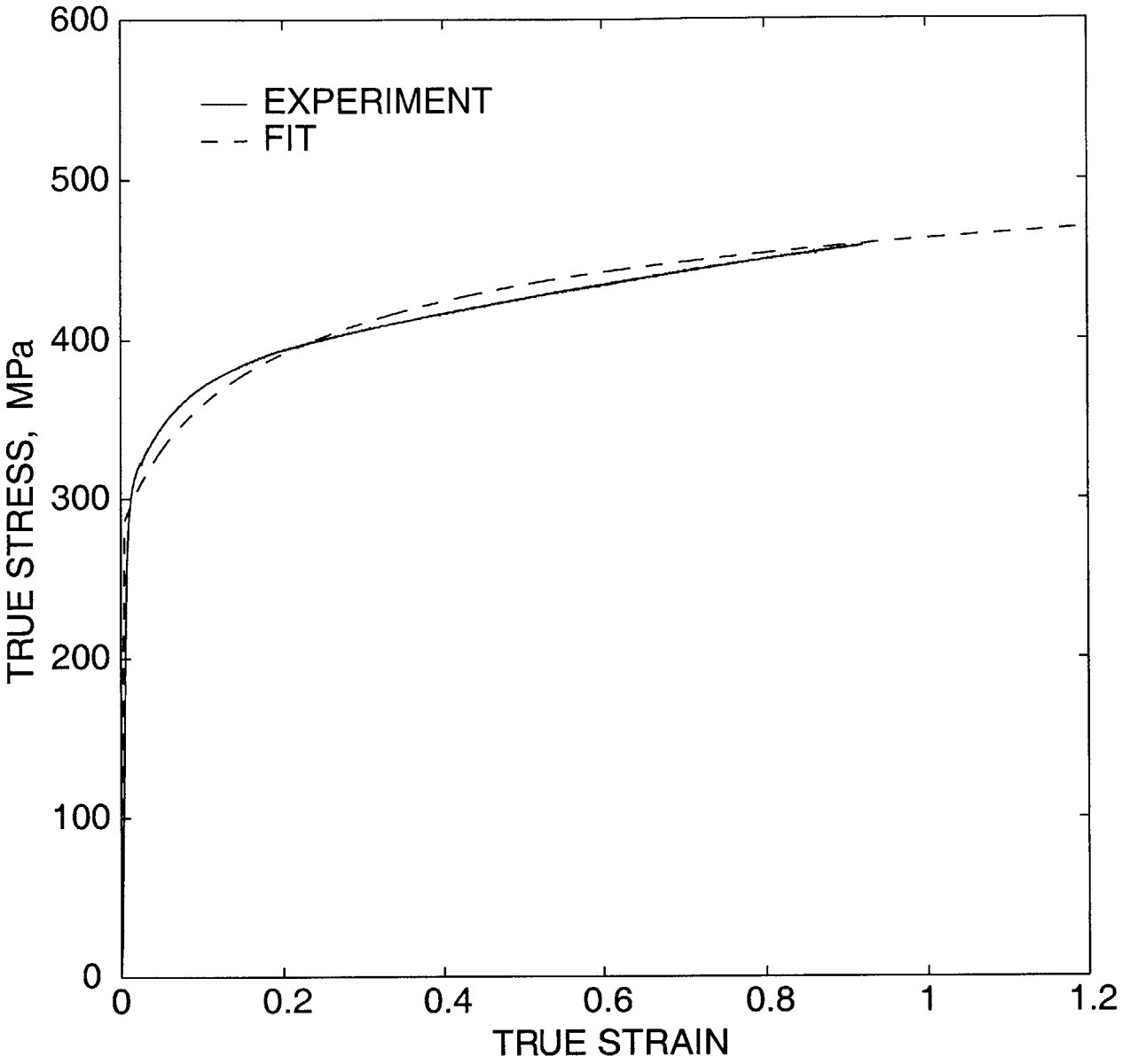

Figure F-60: Fit of the constitutive model for isotropic polycrystalline metals to large deformation simple compression of Al6061-T6.

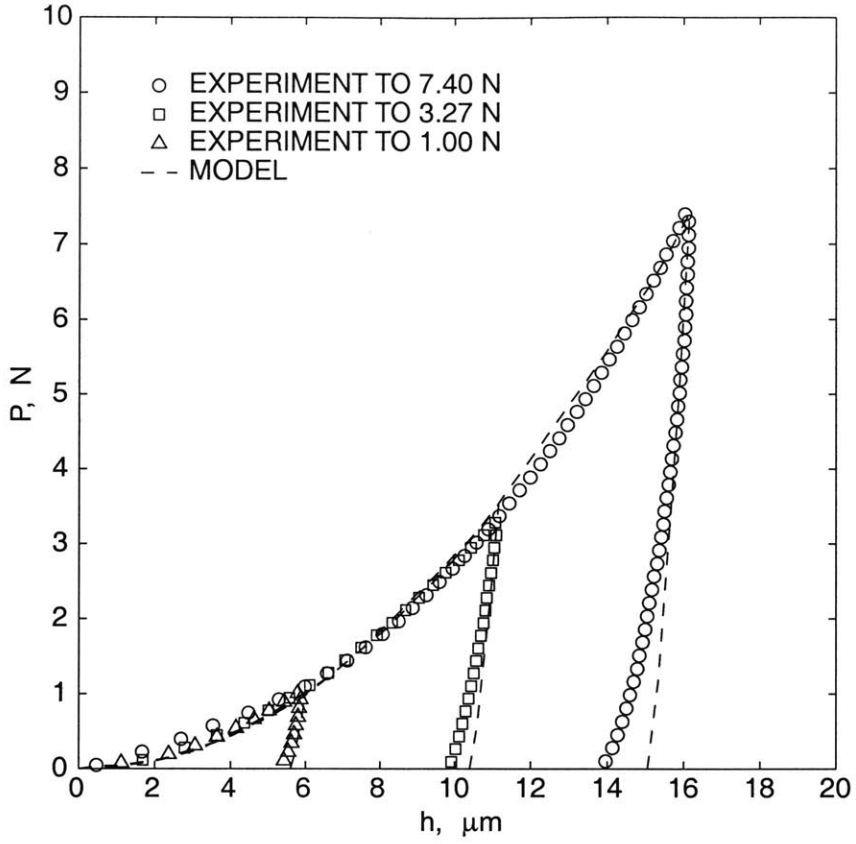

(a)

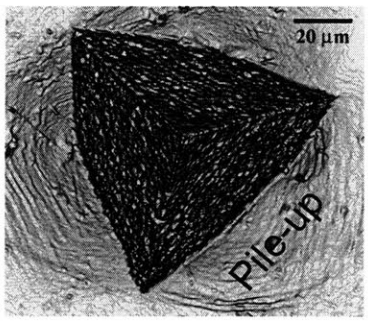

(b)

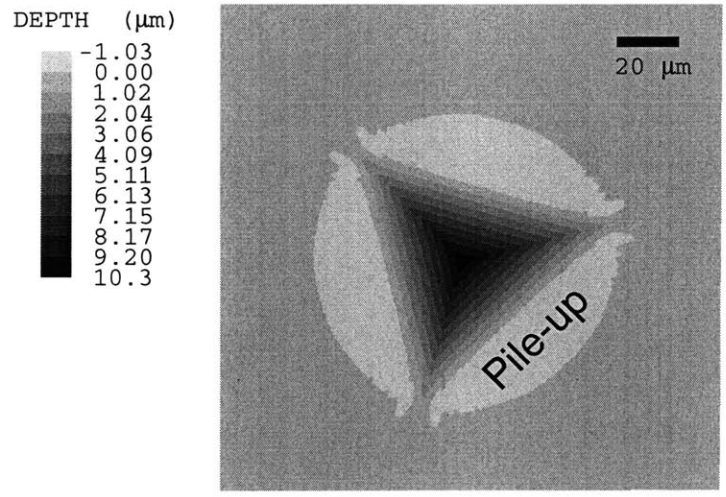

(c)

Figure F-61: Berkovich indentation of Al6061-T6: (a) P-h curves with model predictions. (b) Optical micrograph of residual indent morphology for test to 3.27 N. (c) Numerically predicted morphology for test to 3.27 N.

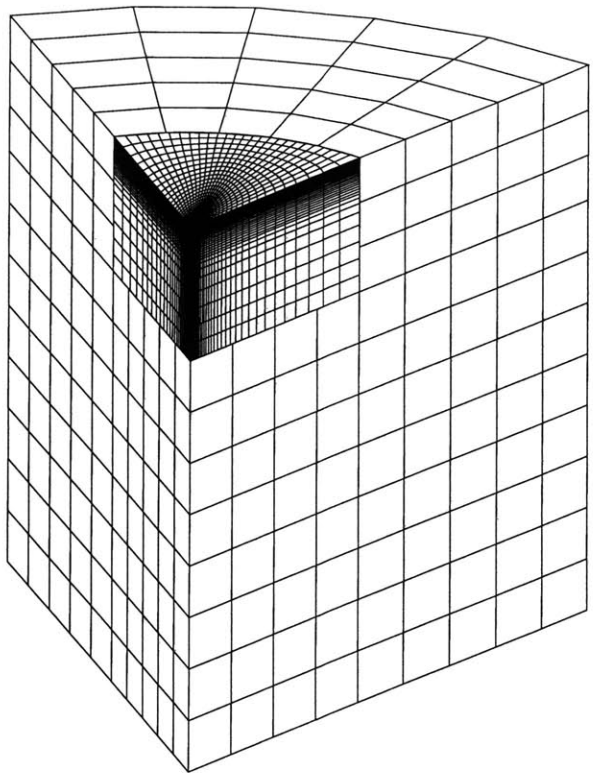

(a)

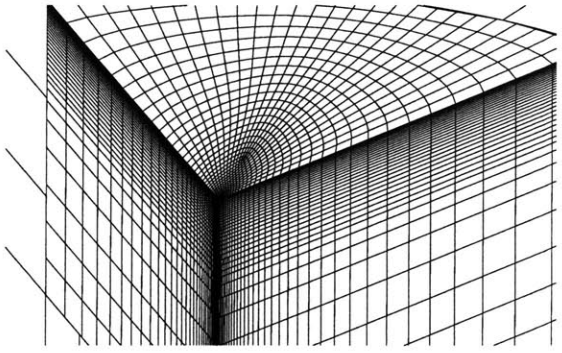

(b)

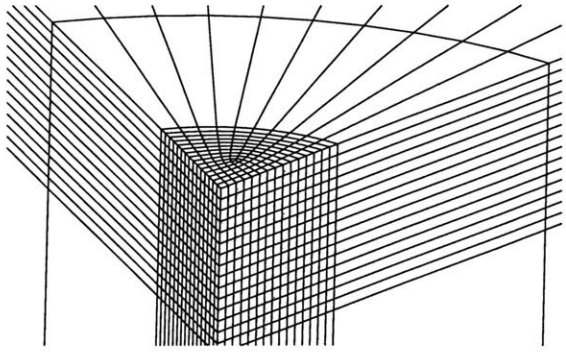

(c)

Figure F-62: (a) Mesh design used for Berkovich indentation simulations; (b) Detailed view of area in direct contact with the indenter tip. (c) Detailed view of a coarse mesh design. The indenter is modeled using a rigid surface (not shown).

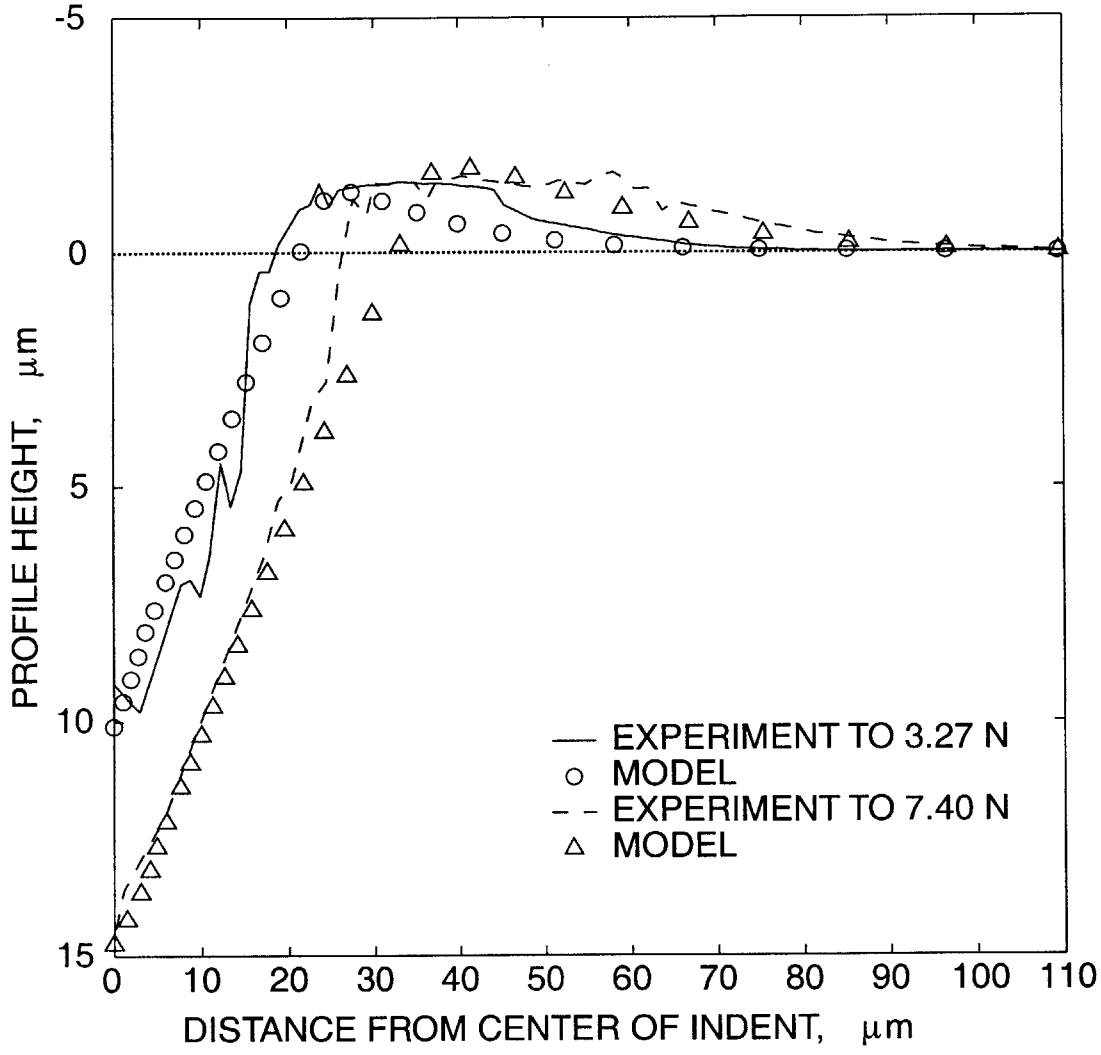

Figure F-63: Comparison of experimentally-measured and numerically-predicted indentation profiles corresponding to a maximum load of 3.27 N and 10μm depth, as well as a maximum load of 7.40 N and 15μm depth are shown. Each profile is shown in a plane which is perpendicular to one of the faces of the indent; the trace from the deepest point of the indent, up the indent and onto and along the surface being indented is shown. The baseline for the profile height is at 0 μm. Material: Al6061-T6.

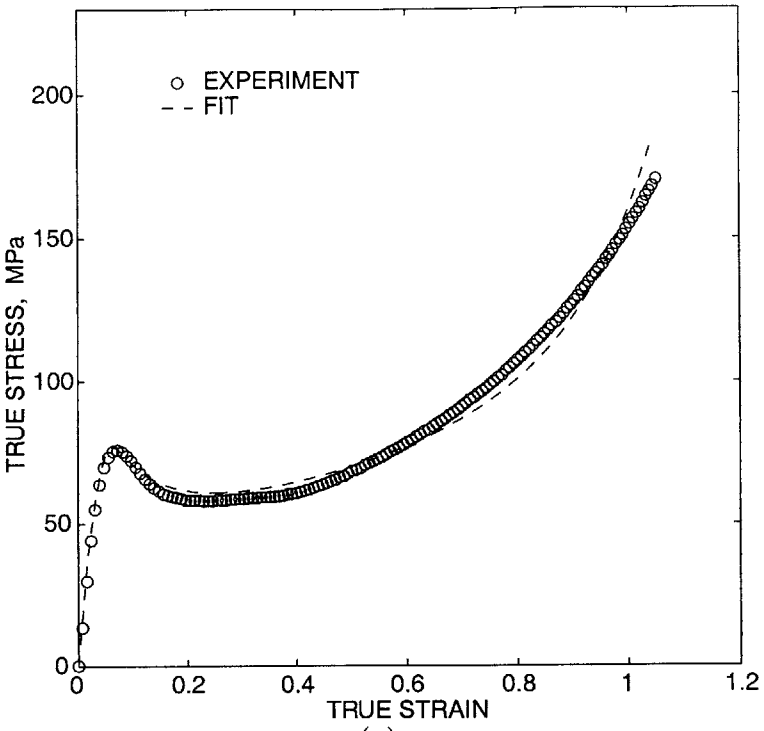

(a)

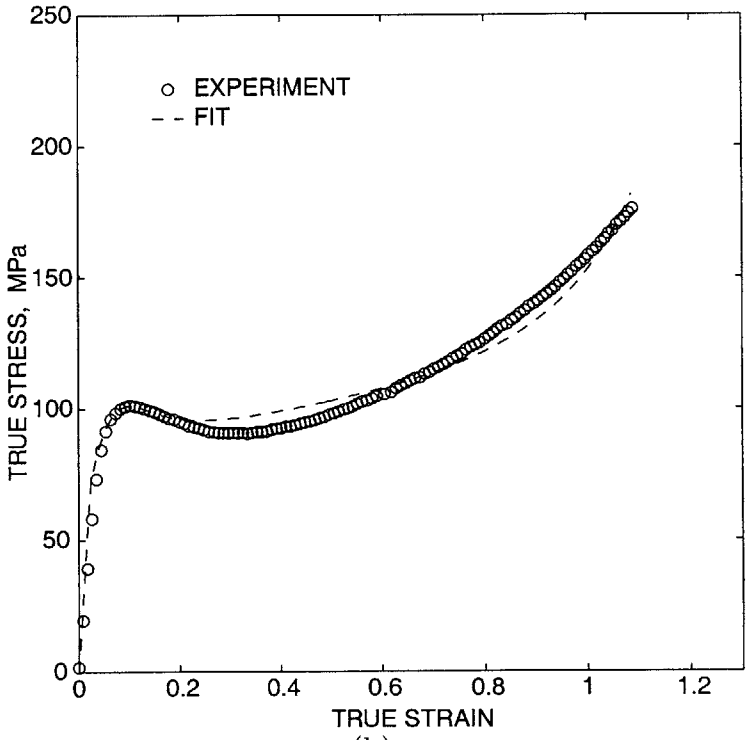

(b)

Figure F-64: Fit of the constitutive model to simple compression of (a) PC and (b) PMMA.

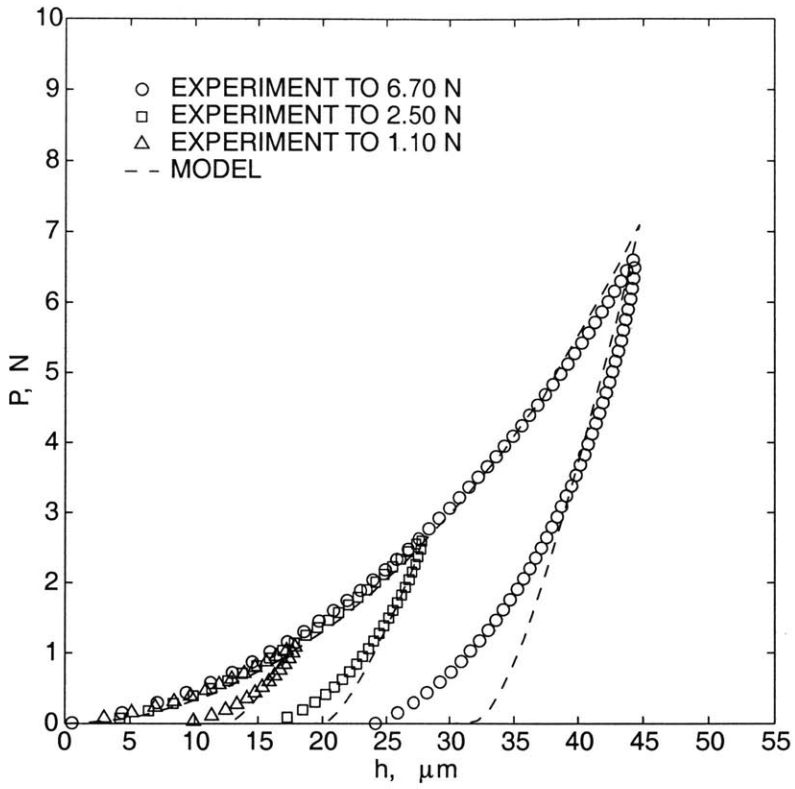

(a)

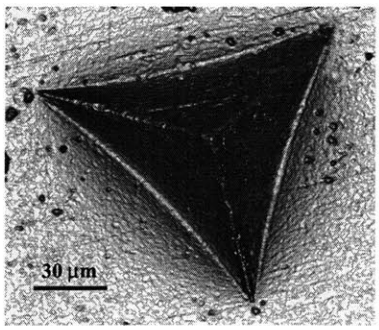

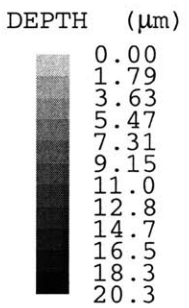

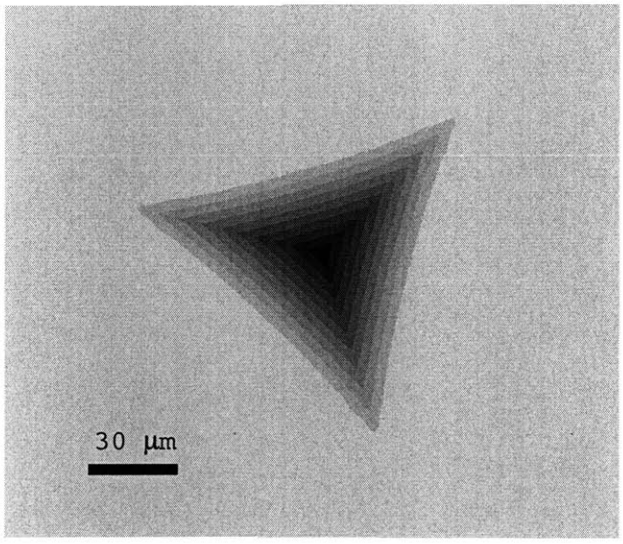

(b) (c)

Figure F-65: Berkovich indentation of PC: (a) P-h curves with model predictions. (b) Optical micrograph of residual indent morphology for test to 2.5 N. (c) Numerically predicted morphology for test to 2.5 N.

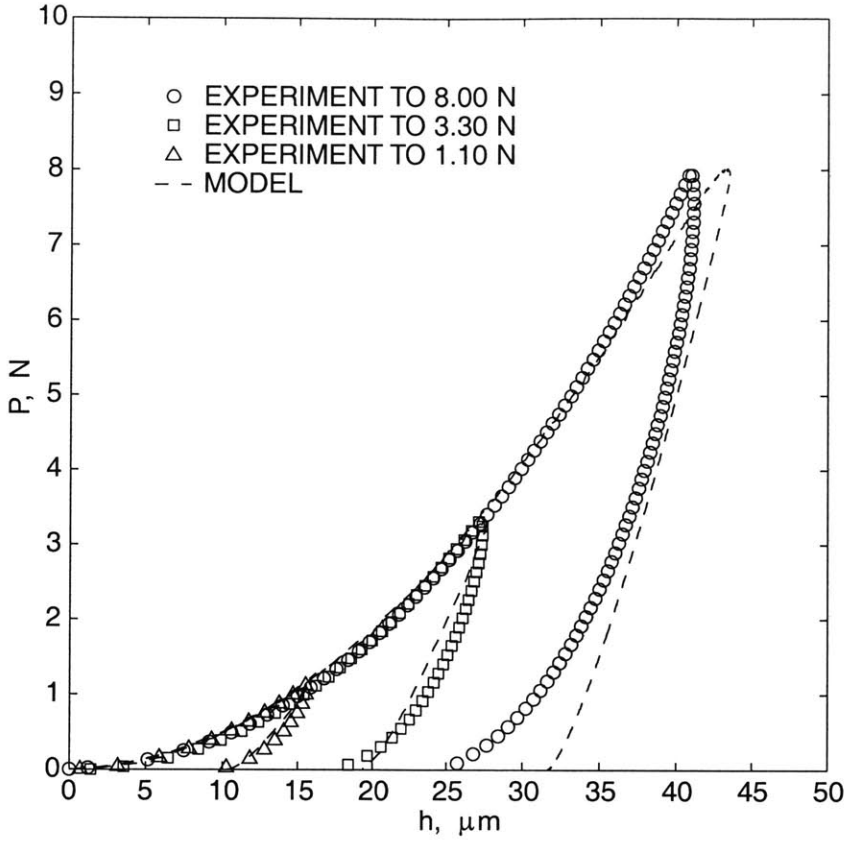

(a)

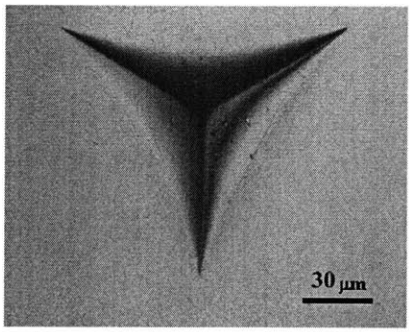

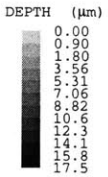

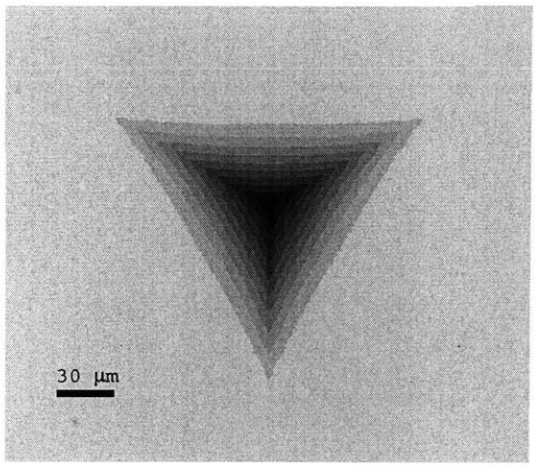

(b) (c)

Figure F-66: Berkovich indentation of PMMA: (a) P-h curves with model predictions. (b) Optical micrograph of residual indent morphology for test to 3.30 N. (c) Numerically predicted morphology for test to 3.30 N.

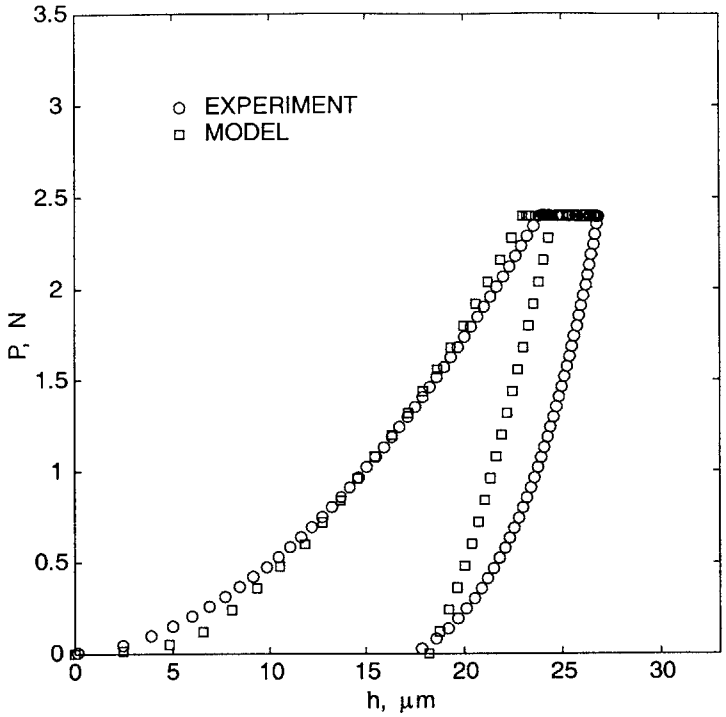

(a)

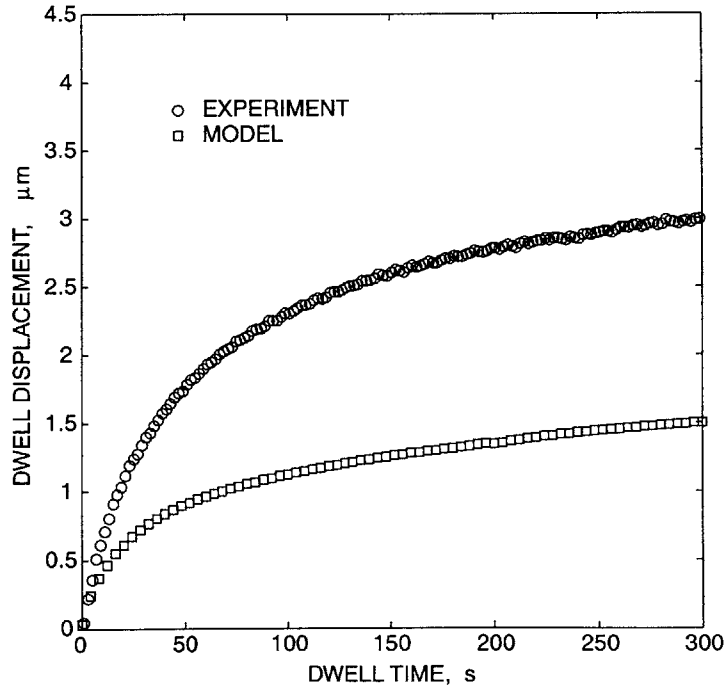

(b)

Figure F-67: Model result compared with experimental data for Berkovich indentation of PMMA with a dwell time of 300 s at a peak load of 2.40 N.

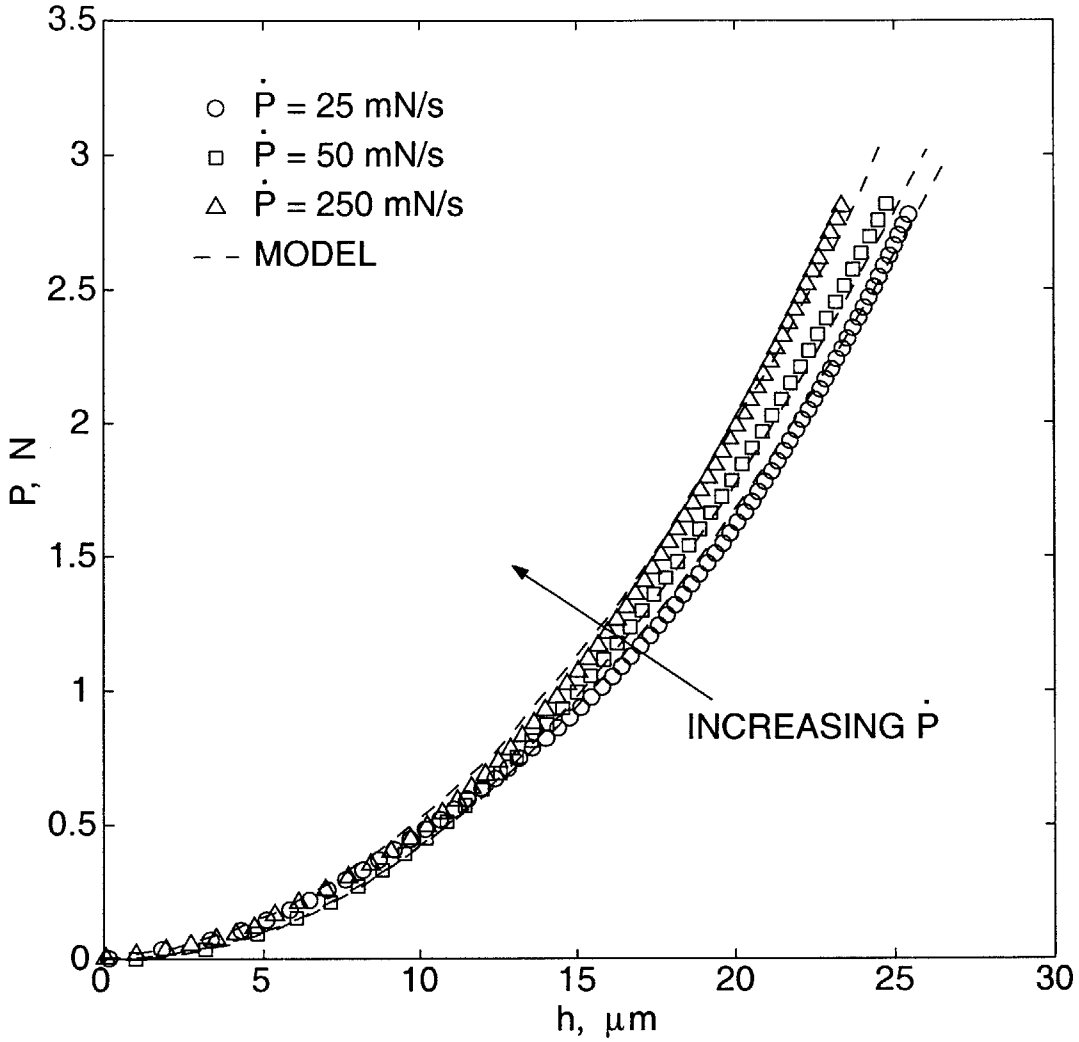

Figure F-68: Model predictions of the loading curve for Berkovich indentation of PMMA conducted at the three indicated loading rates.

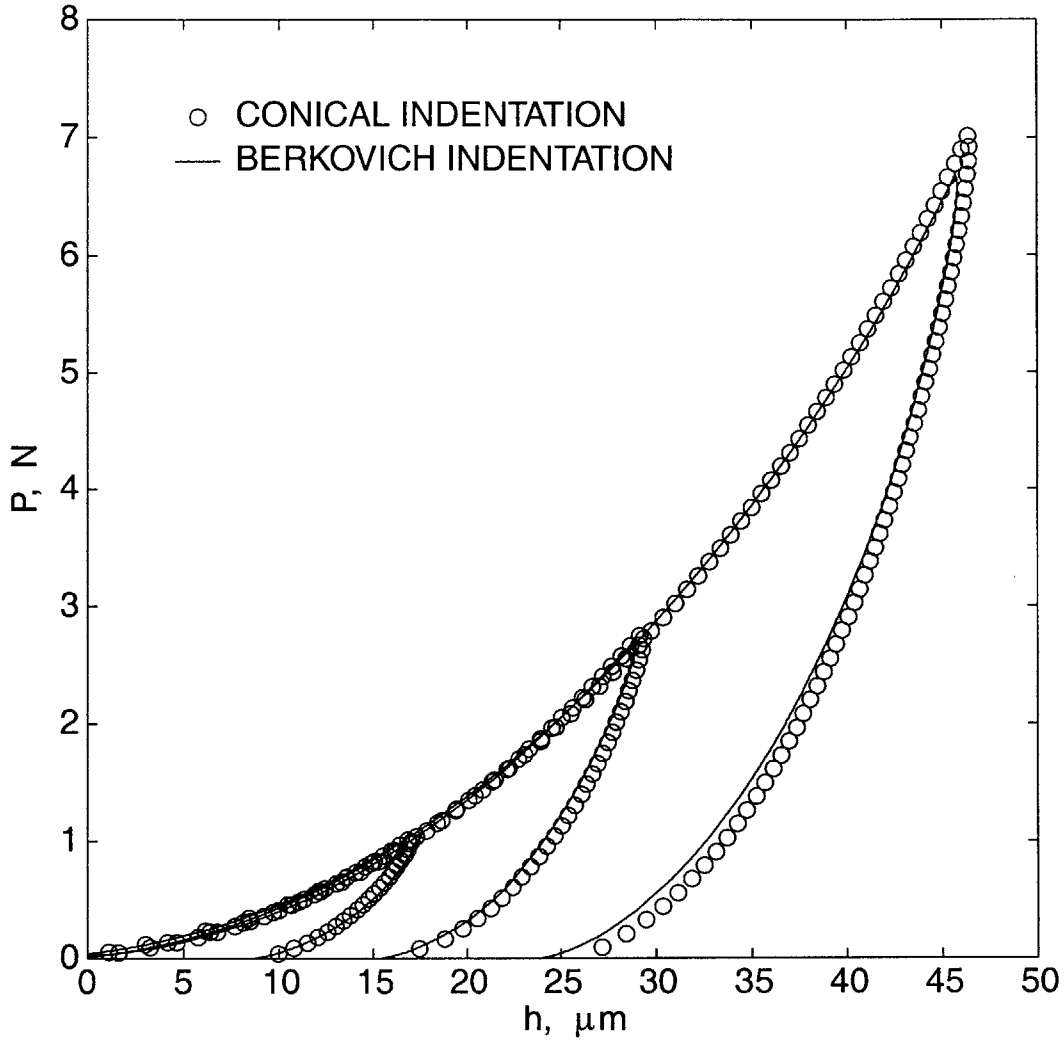

Figure F-69: Comparison of experimentally obtained P-h curves for PC using a conical indenter versus a Berkovich indenter geometry.

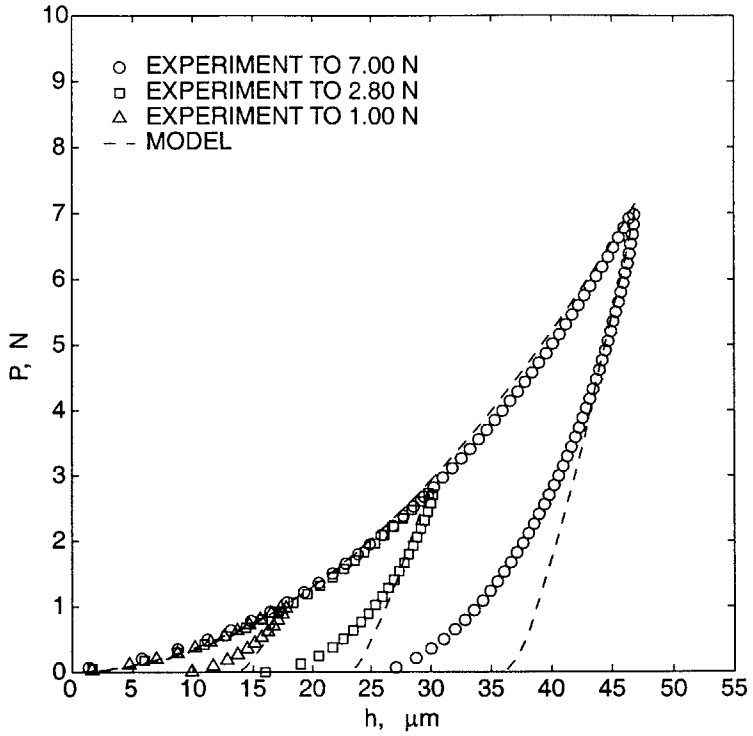

(a)

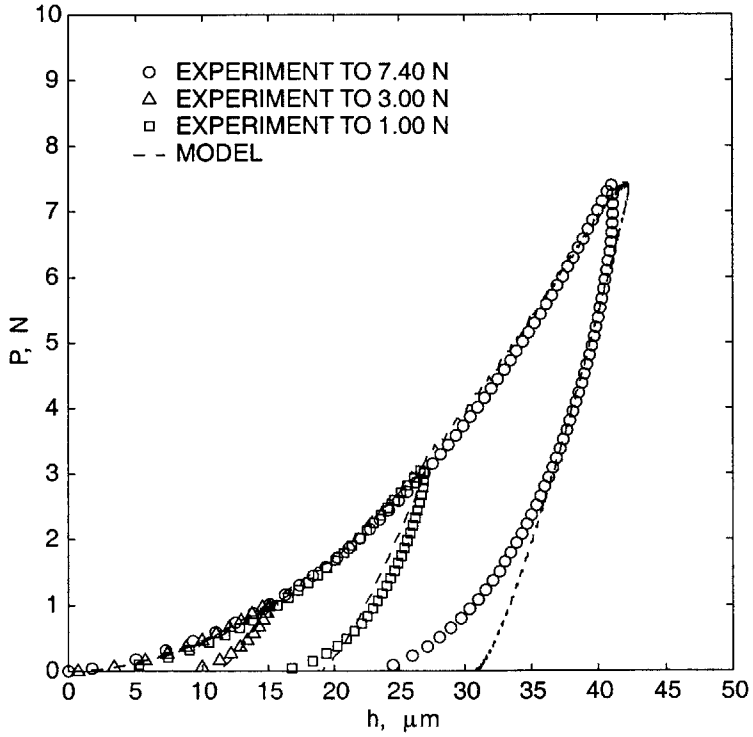

(b)

Figure F-70: Conical indentation with model predictions: (a) P-h curves for PC. (b) P-h curves for PMMA.

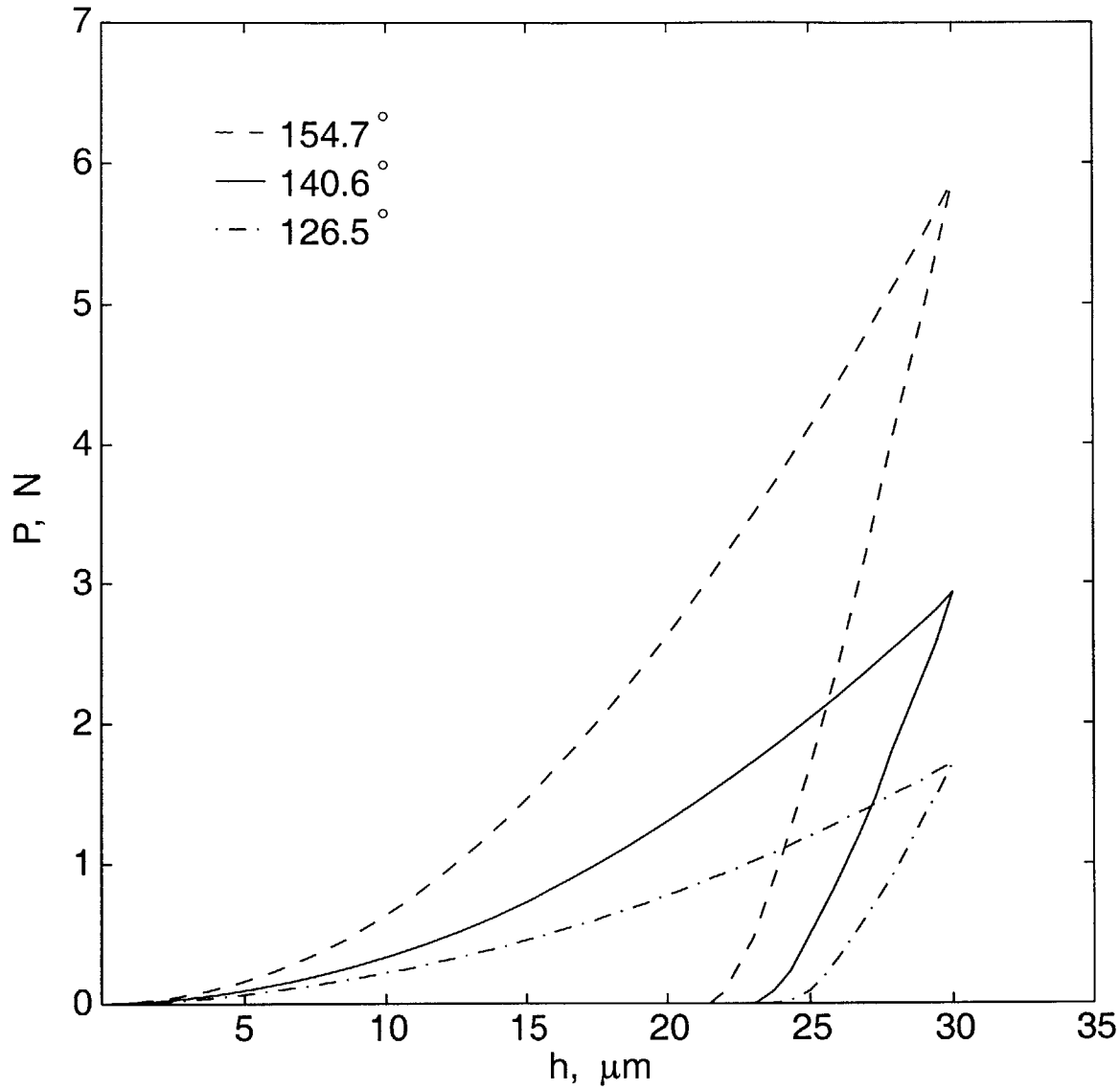

Figure F-71: Sensitivity of the P-h curves for indentation of PC to variations of ±10% in the included angle of the conical indenter.

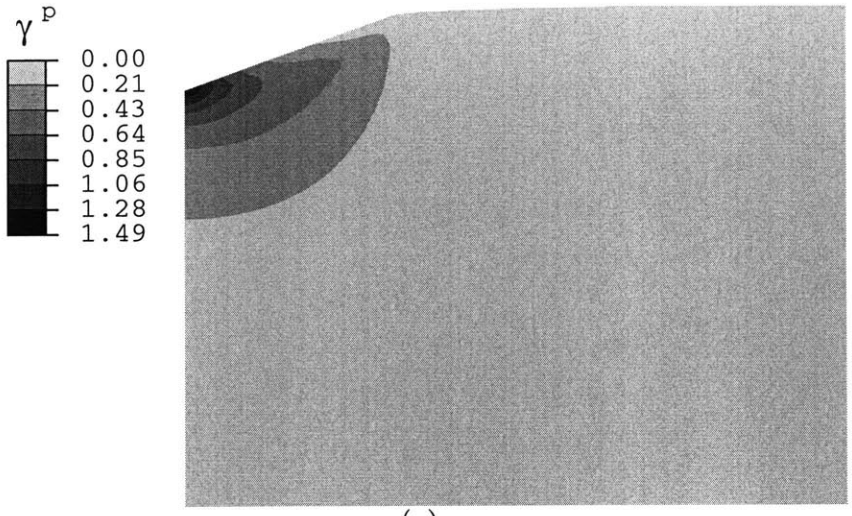

(a)

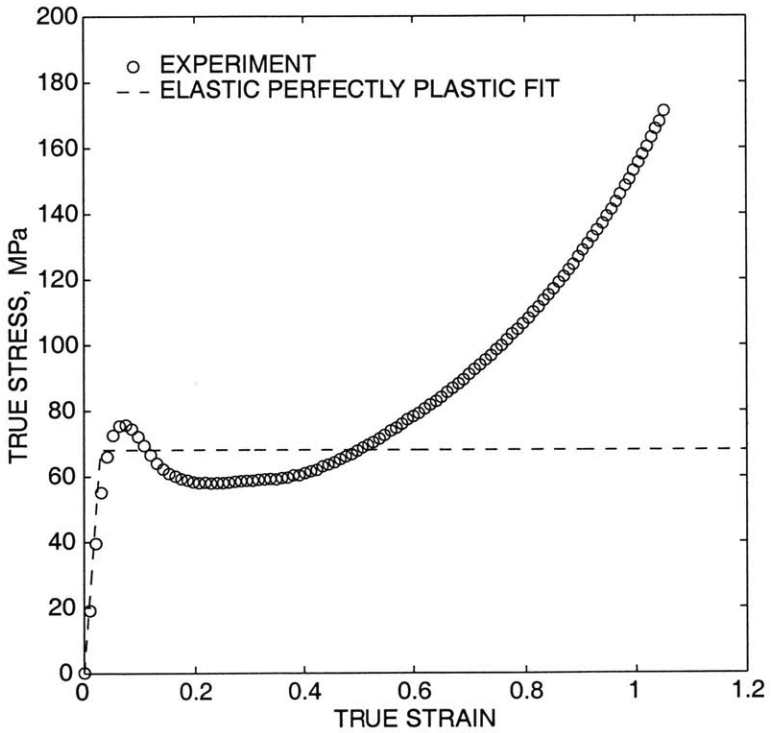

(b)

Figure F-72: (a) Contour plot of the equivalent plastic shear strain γ^p at a peak load of 2.80 N for conical indentation of PC. (b) Fit of an elastic-perfectly plastic model to simple compression of PC.

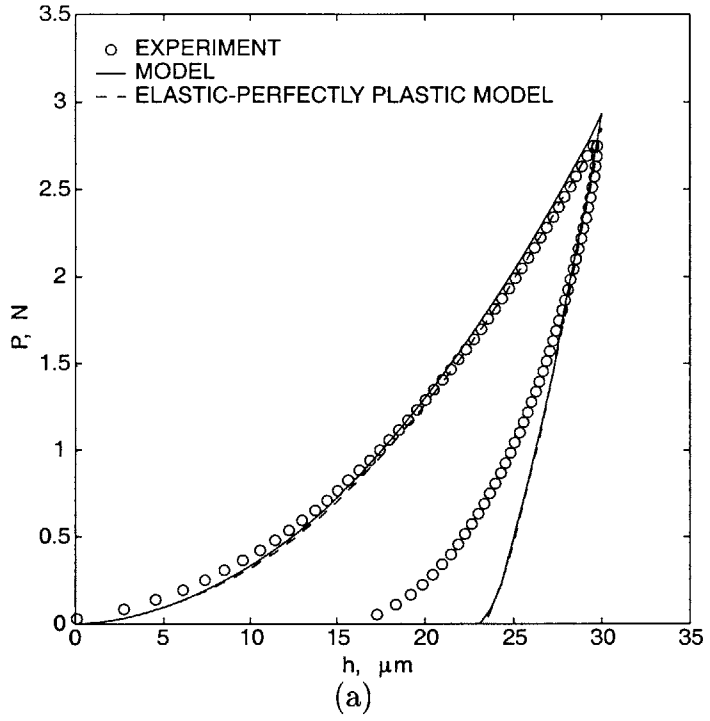

(a)

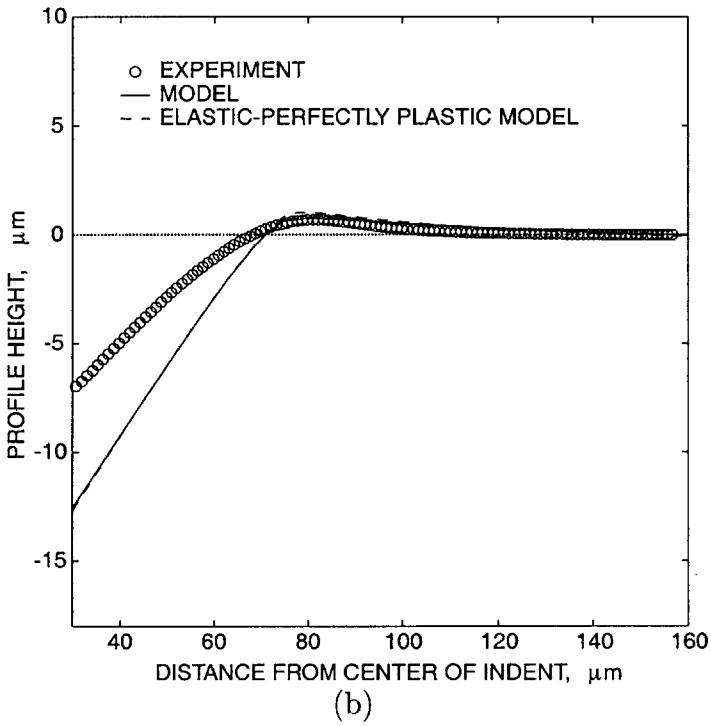

(b)

Figure F-73: Prediction of conical indentation of PC using an elastic-perfectly plastic rate-dependent model with pressure sensitive plastic flow: (a) P-h curves; (b) Residual indent profile focused on the region of material pile-up.

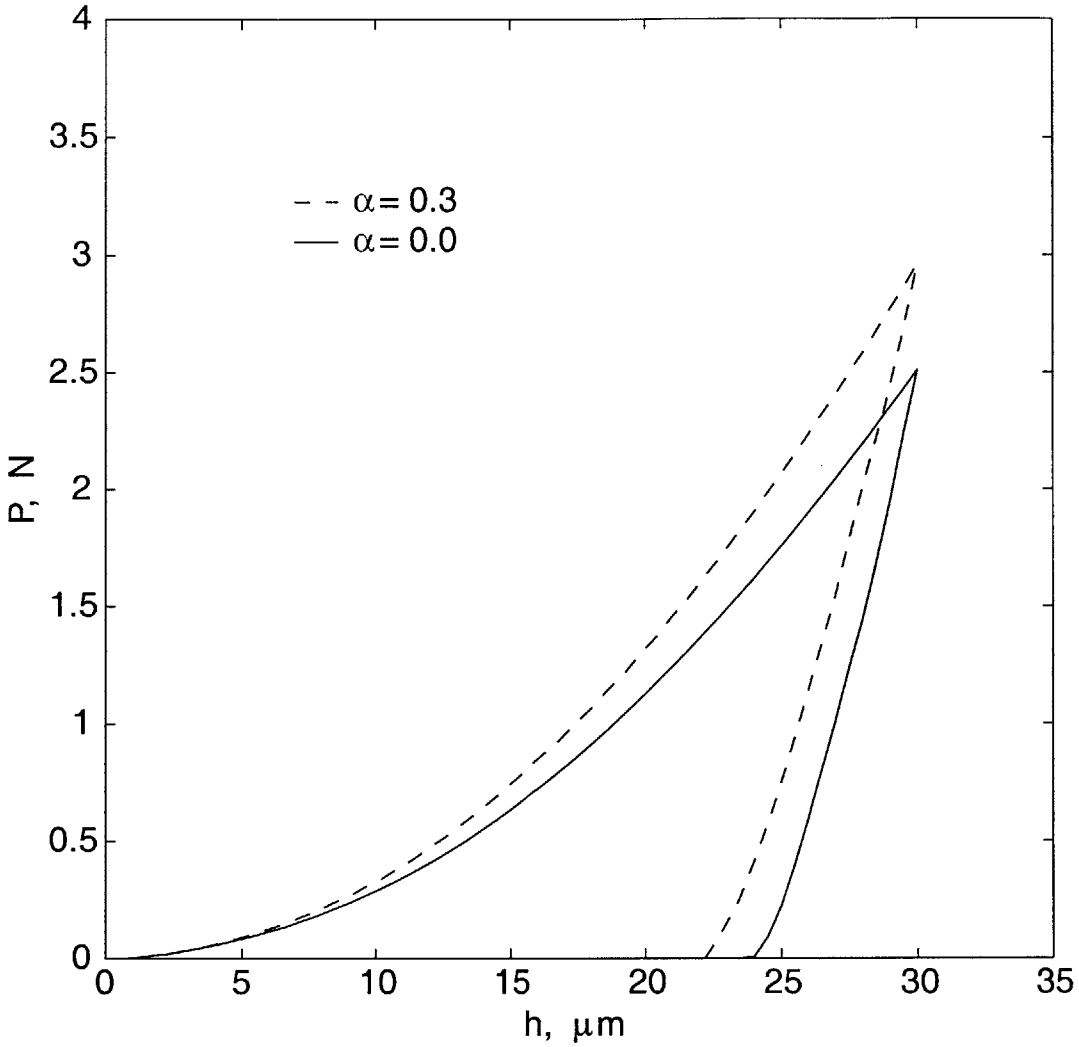

Figure F-74: Model predictions of the sensitivity of the P-h curve to variations in the pressure sensitivity parameter α.

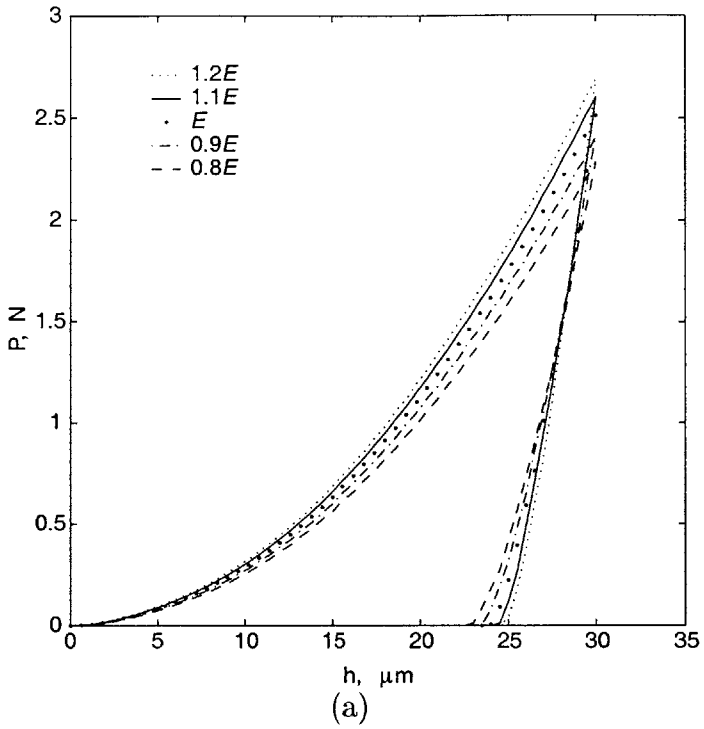

(a)

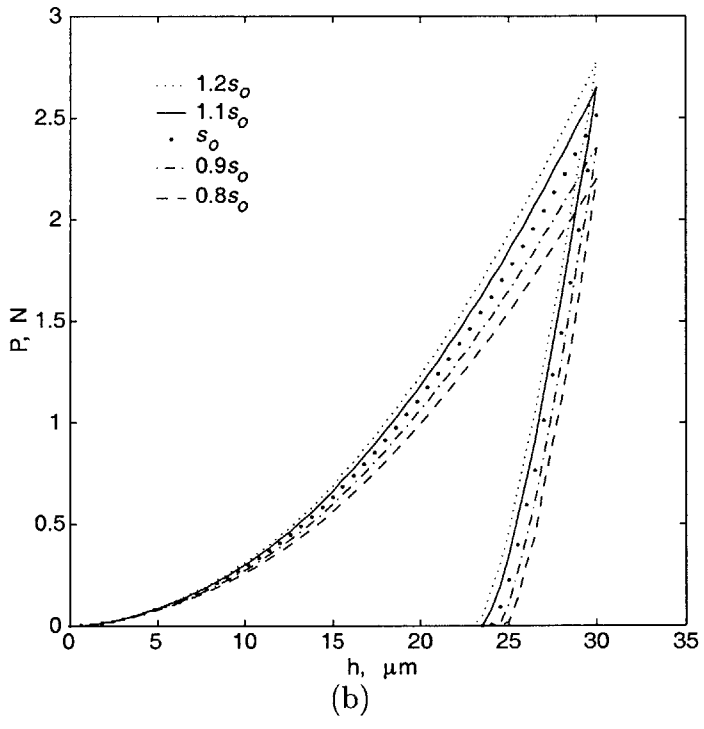

(b)

Figure F-75: Sensitivity of the P-h curves for conical indentation of PC to variations of $\pm 20\%$ in (a) E and (b) s_0.

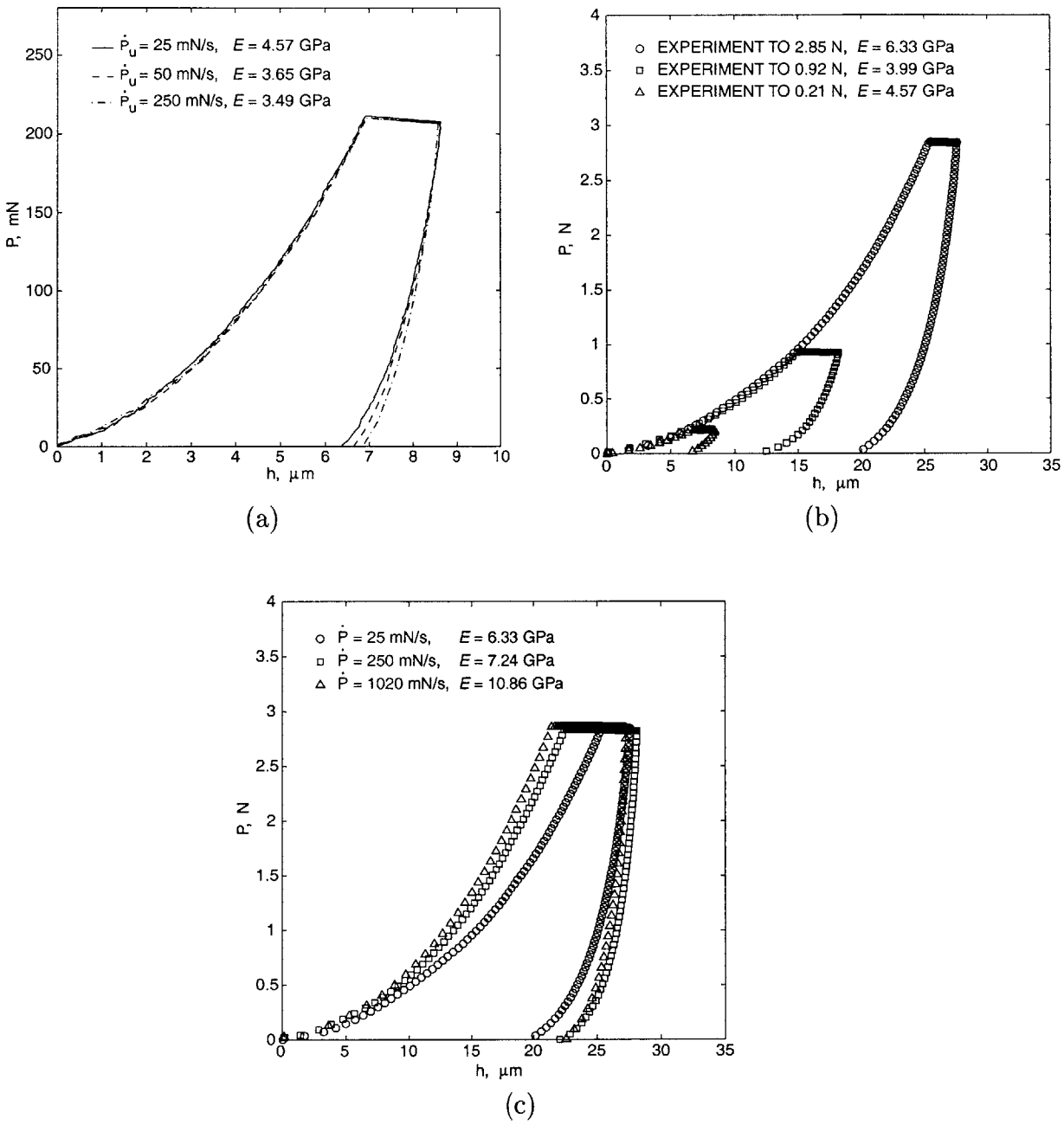

Figure F-76: Unloading analysis for Berkovich indentation of PMMA: (a) Results for a 205 mN peak load with a loading rate of 25 mN/s and various unloading rates. (b) Results for three peak load levels at equal loading and unloading rates. (c) P-h curves for a peak load of 2.80 N and three different loading and unloading rates. The values of E were calculated using the data given in Table I.

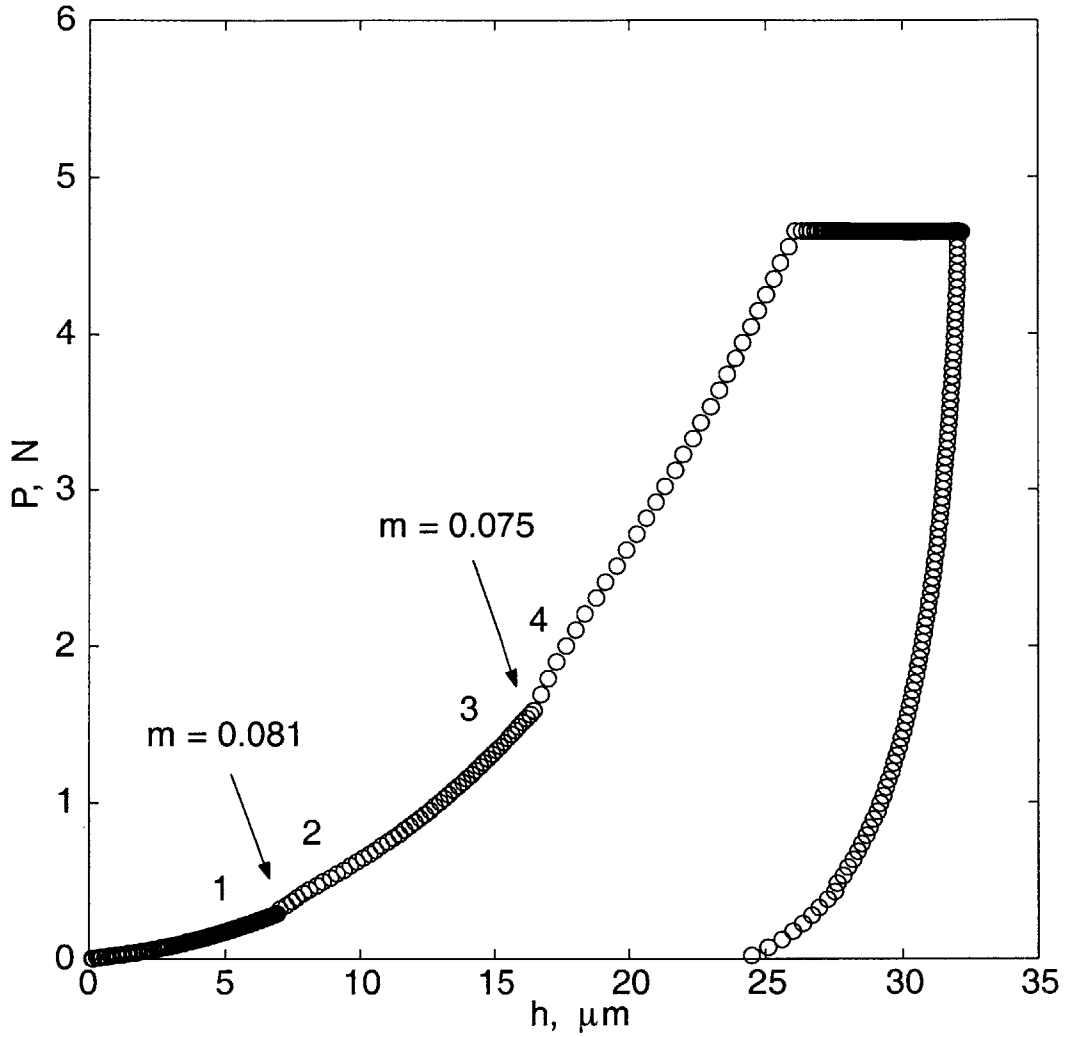

Figure F-77: Berkovich indentation of PMMA with loading rate-jumps imposed from stages 1 to 2 and from stages 3 to 4. Values of the calculated rate sensitivity parameter m are given for each rate-jump test.

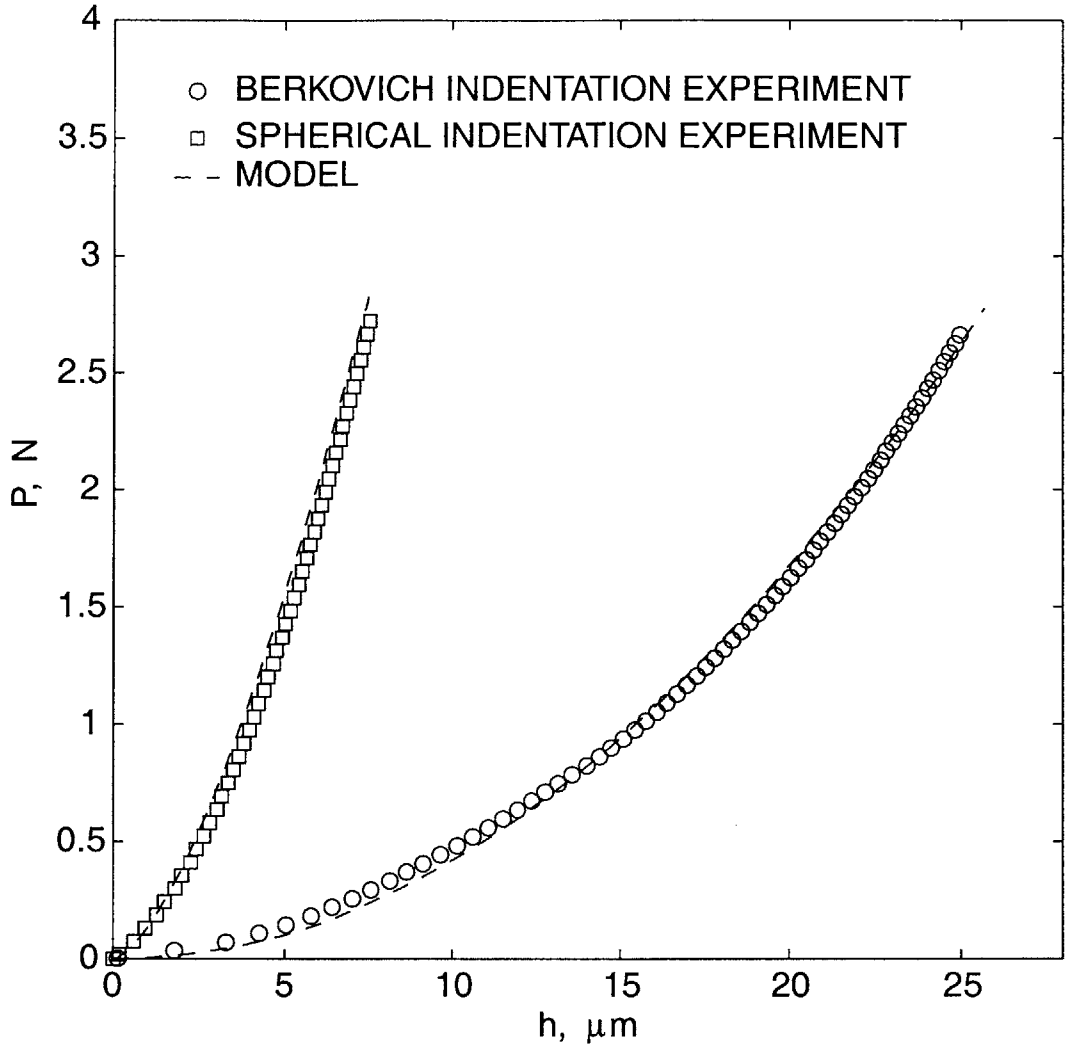

Figure F-78: Berkovich and spherical indentation of PMMA with corresponding model predictions of the loading curves.

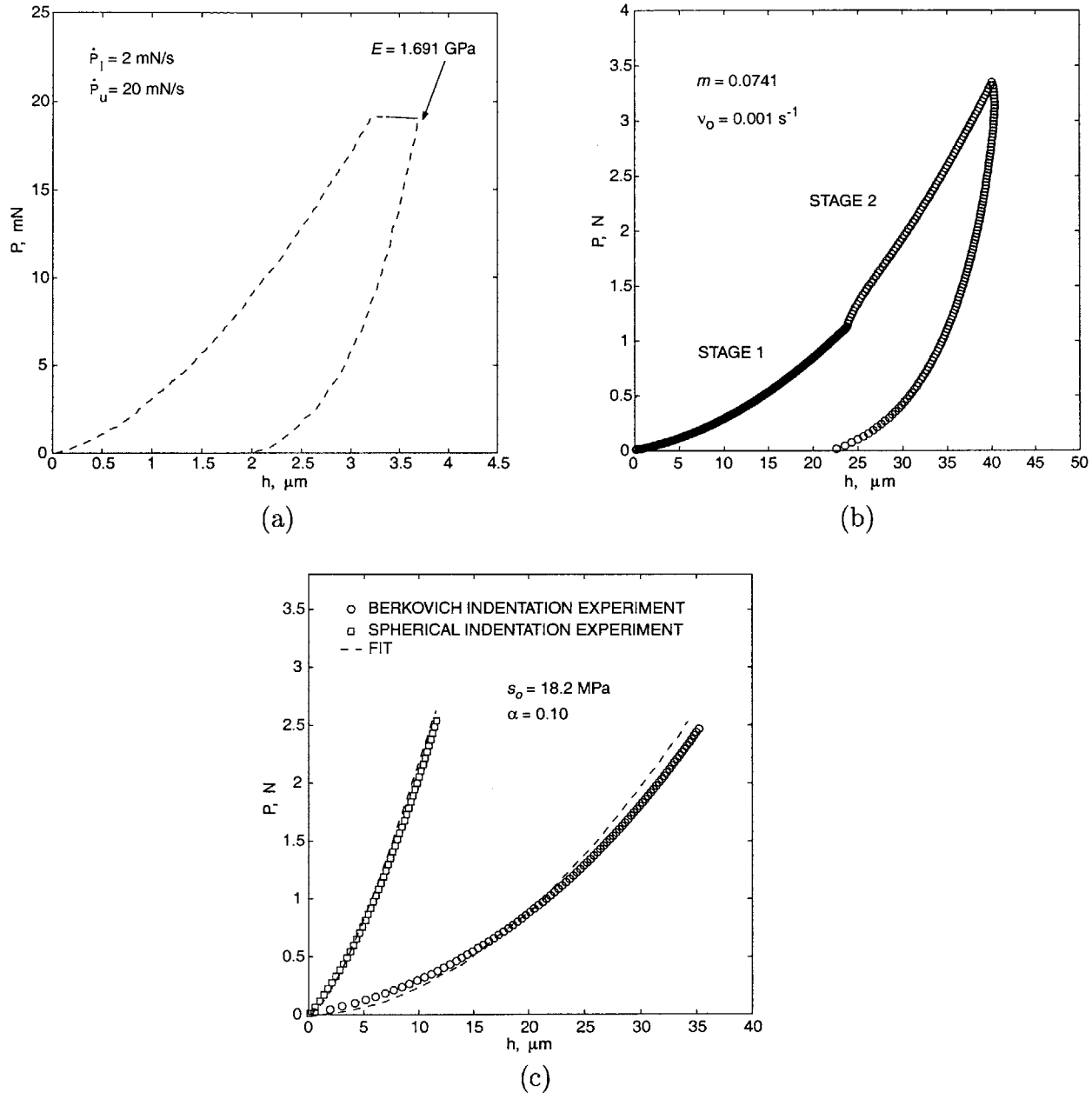

Figure F-79: Berkovich indentation of polystyrene: (a) P-h curve used to estimate E from the initial unloading slope. (b) P-h curve with a rate-jump imposed during the loading portion for the estimation of m and ν_0. (c) Fit to the loading curves of Berkovich and spherical indentation to estimate s_0 and α.

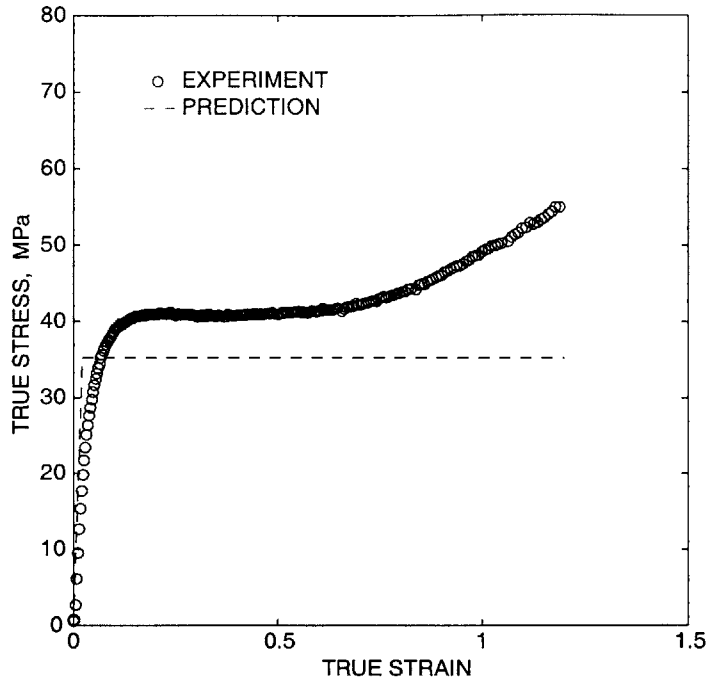

(a)

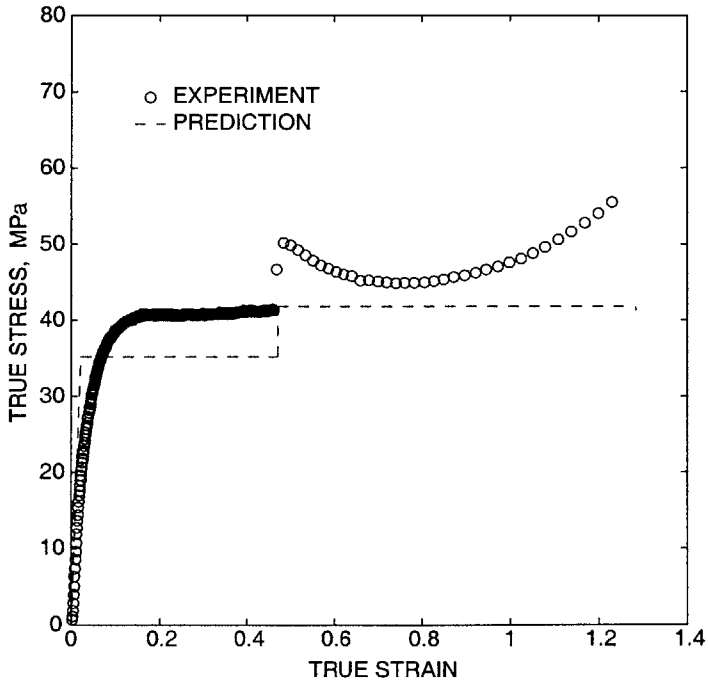

(b)

Figure F-80: Comparison of the experimentally obtained stress-strain curves in simple compression against the predicted responses based upon a reverse approach for sharp-indentation: (a) Monotonic loading at -0.001/s. (b) Strain-rate jump experiment.

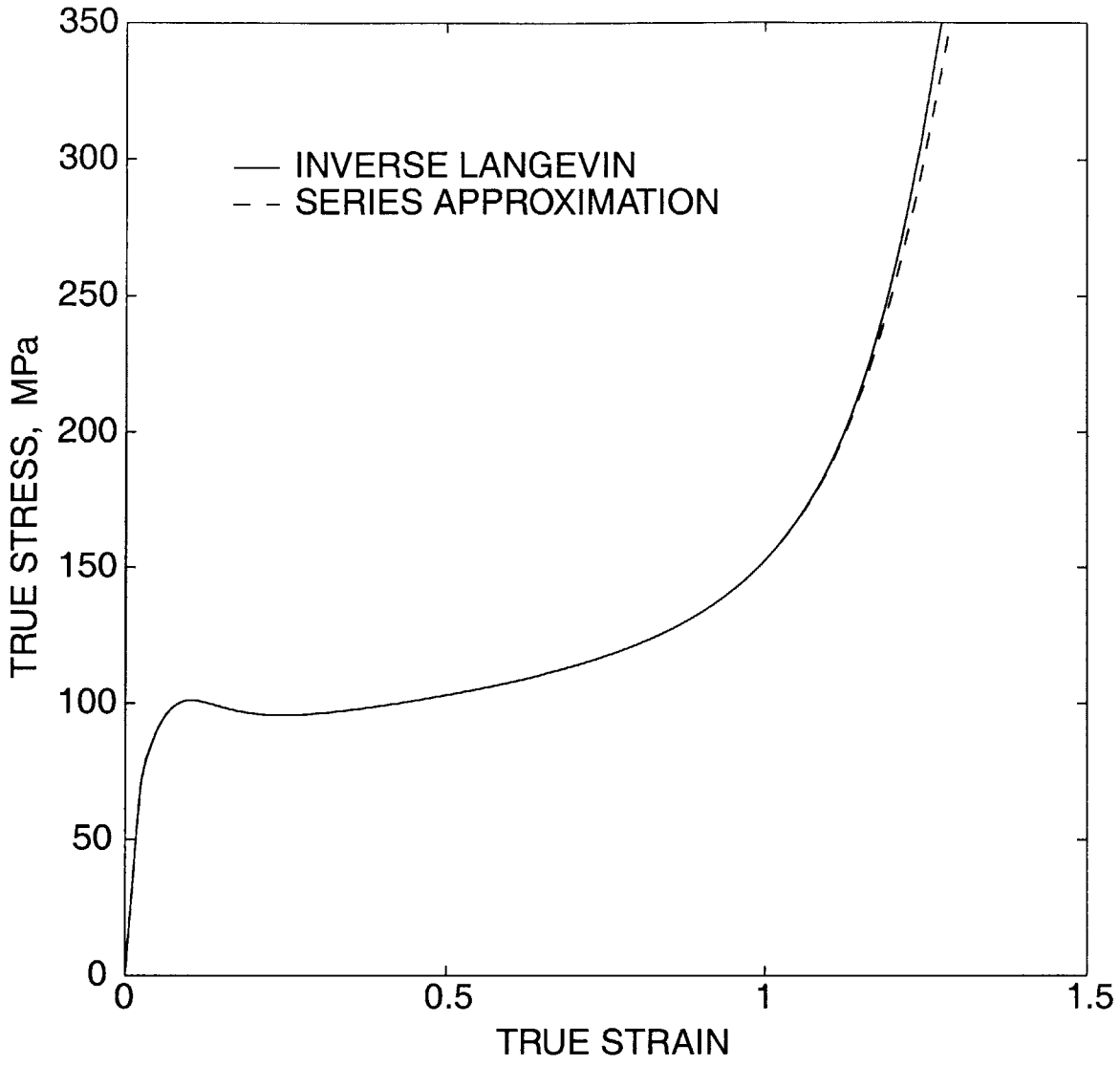

Figure F-81: Comparison of the numerical solution of $\mathcal{L}^{-1}(\lambda^p/\lambda_L)$ to a series approximation using twenty-five terms. The comparison is shown for a single element fit of our model to the stress-strain curve of PMMA in compression. The series approximation is within 1% of the numerical solution at a value of $\lambda^p/\lambda_L = 0.99$.

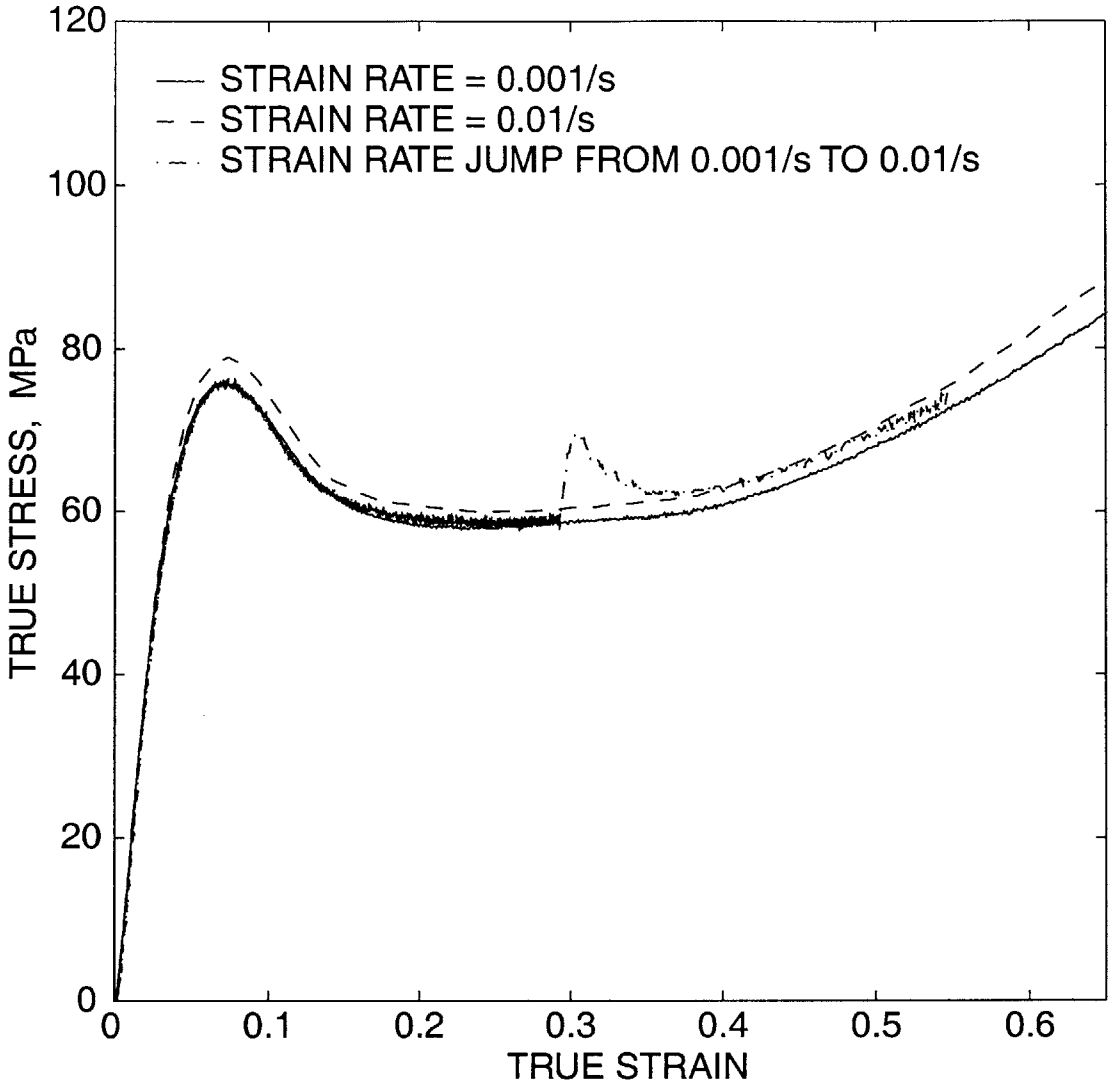

Figure F-82: Stress-strain curves for simple compression of PC under monotonic loading at -0.001/s and -0.01/s compared to a strain rate jump experiment from -0.001/s to -0.01/s.

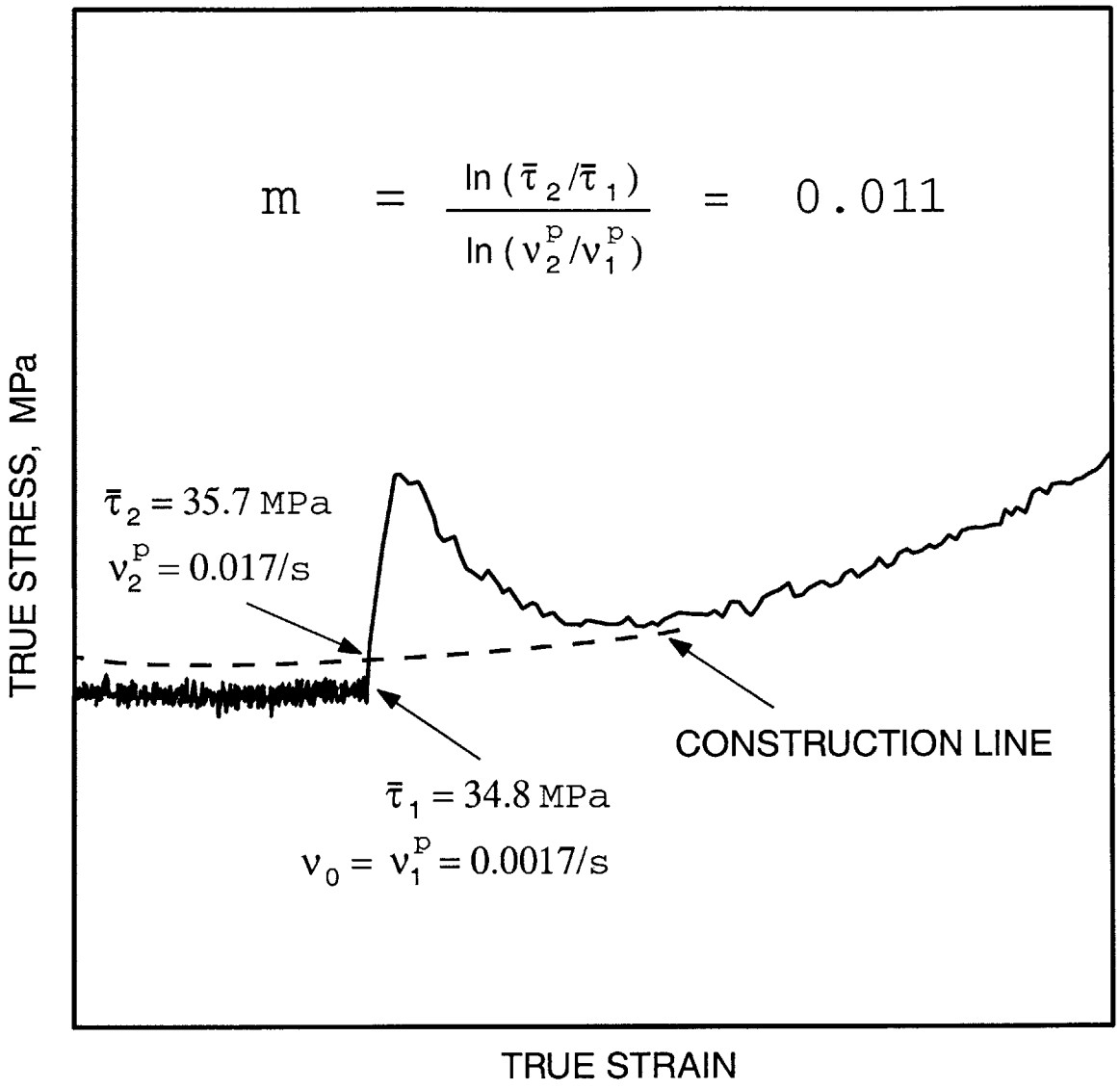

Figure F-83: Detail of the stress-strain curve for the strain rate jump experiment in Fig. F-82 showing the calculation of the strain rate sensitivity parameter m. The indicated construction line is extrapolated back to the strain at which the rate increment is imposed.

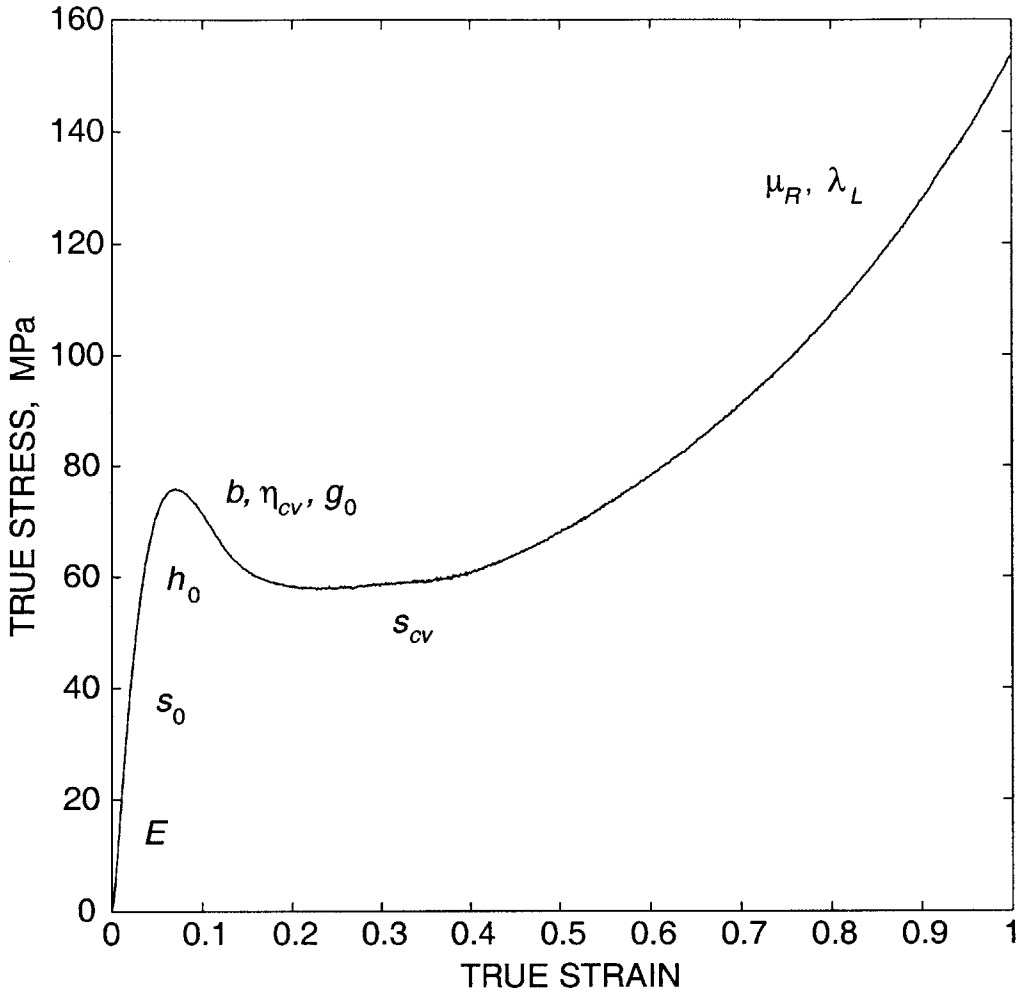

Figure F-84: Stress-strain curve for simple compression of PC at a constant true strain rate of -0.001/s. The material parameters that dominate the indicated regions are displayed on the curve.

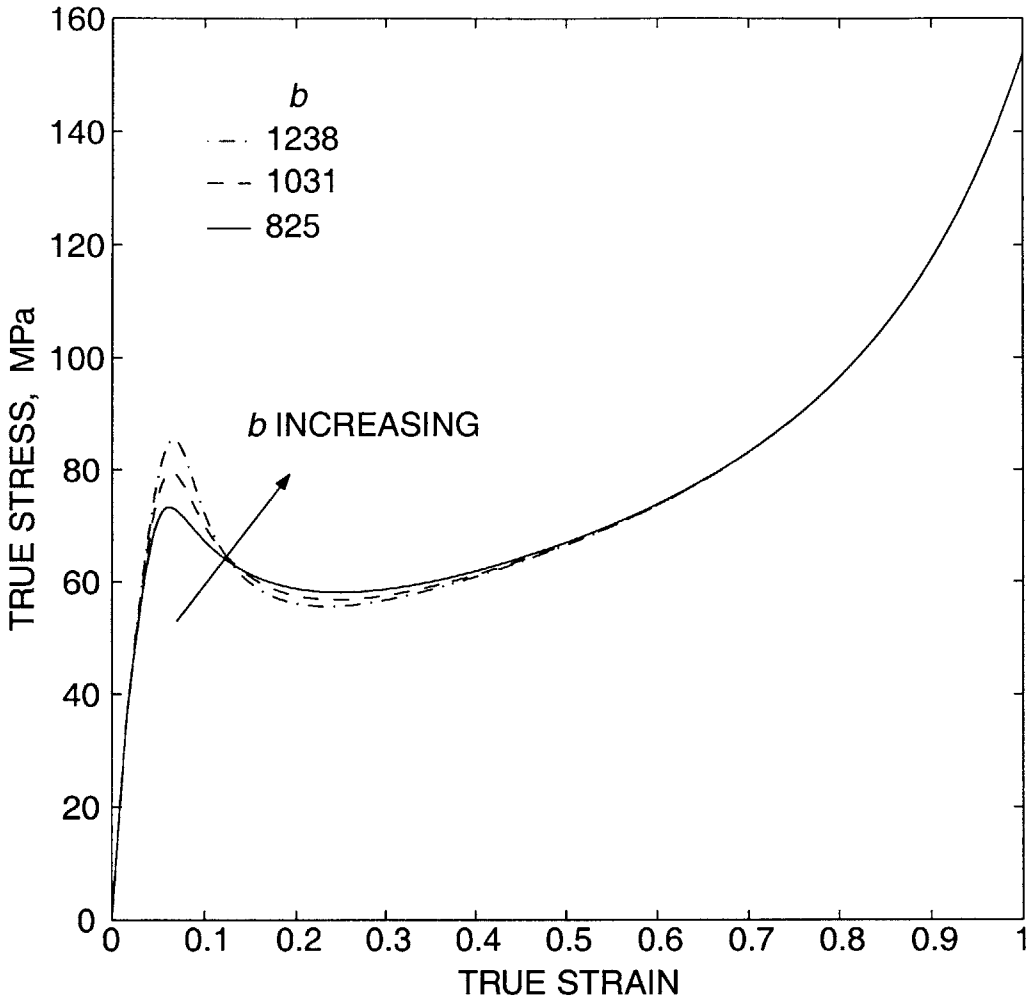

Figure F-85: Sensitivity of the model stress-strain curve for PC to variations in b.

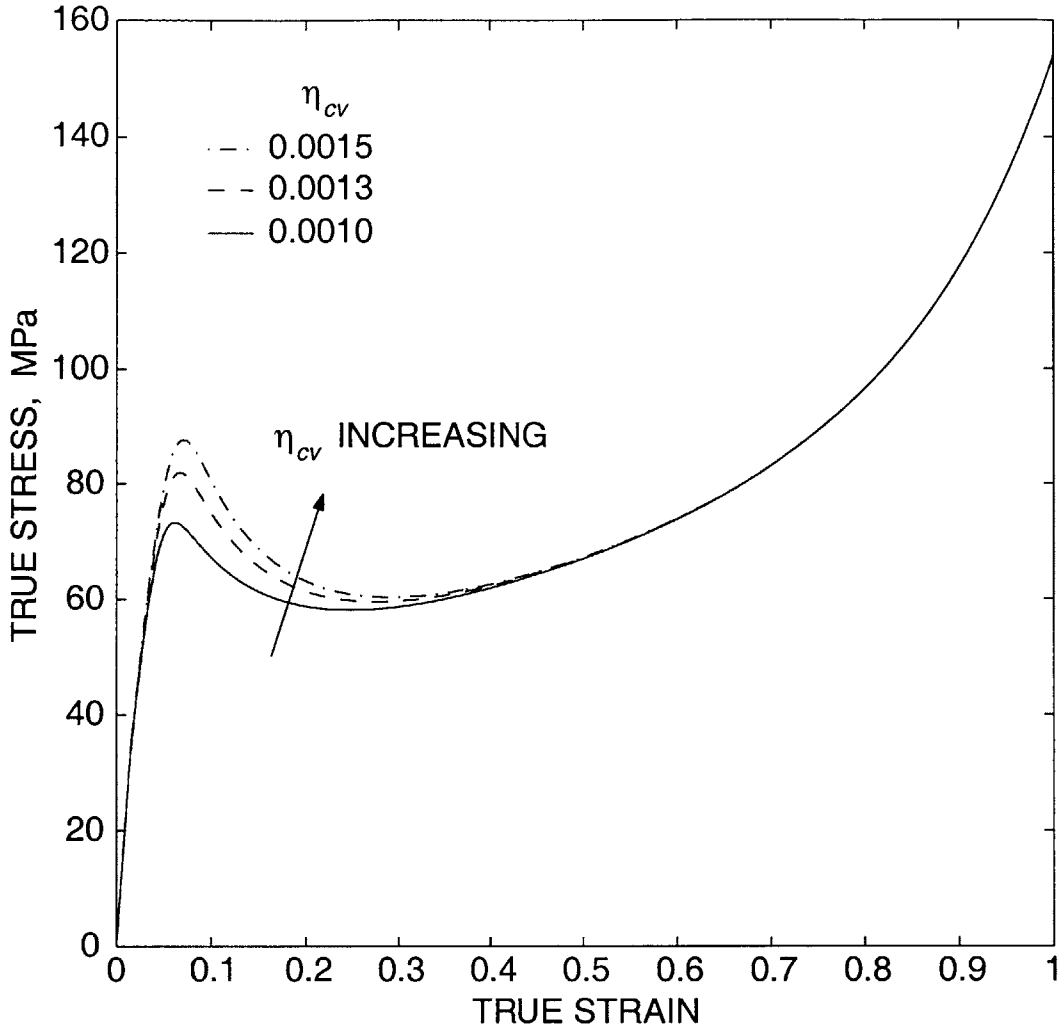

Figure F-86: Sensitivity of the model stress-strain curve for PC to variations in η_{cv}.

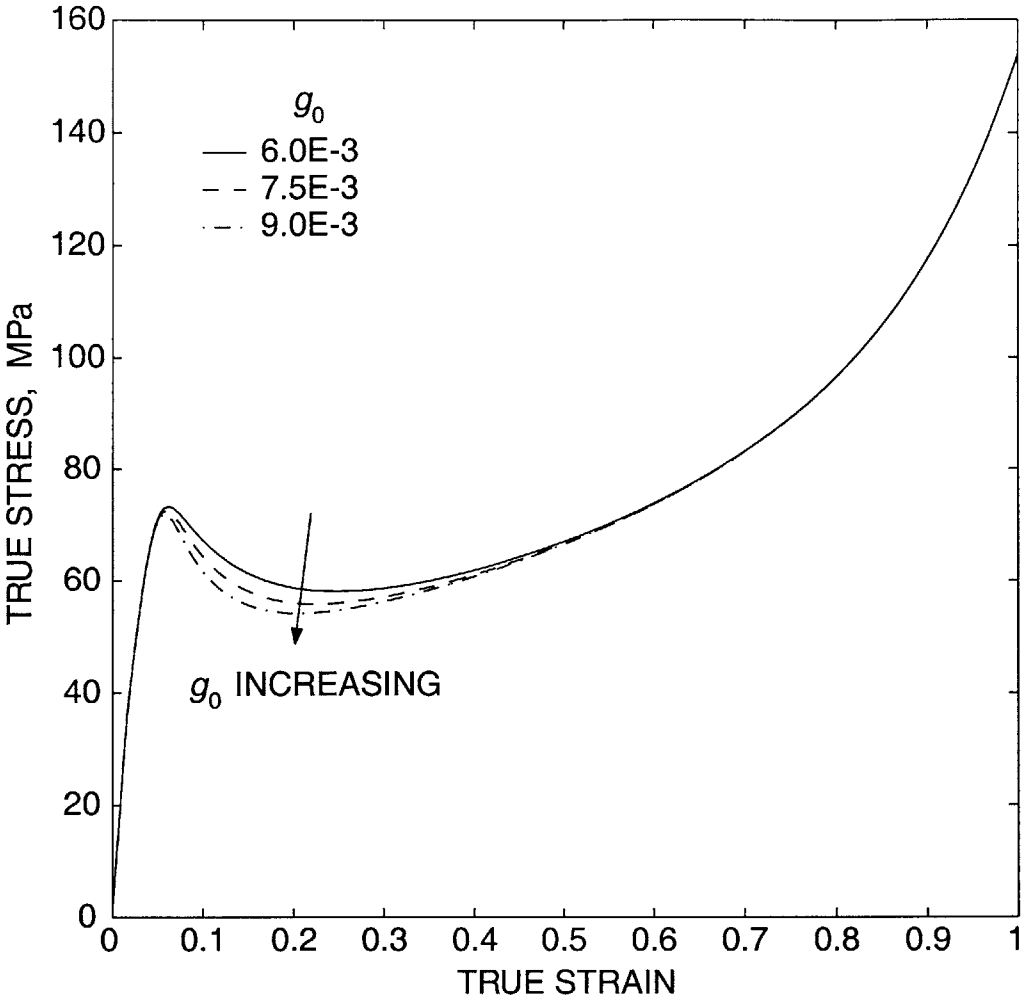

Figure F-87: Sensitivity of the model stress-strain curve for PC to variations in g_0.

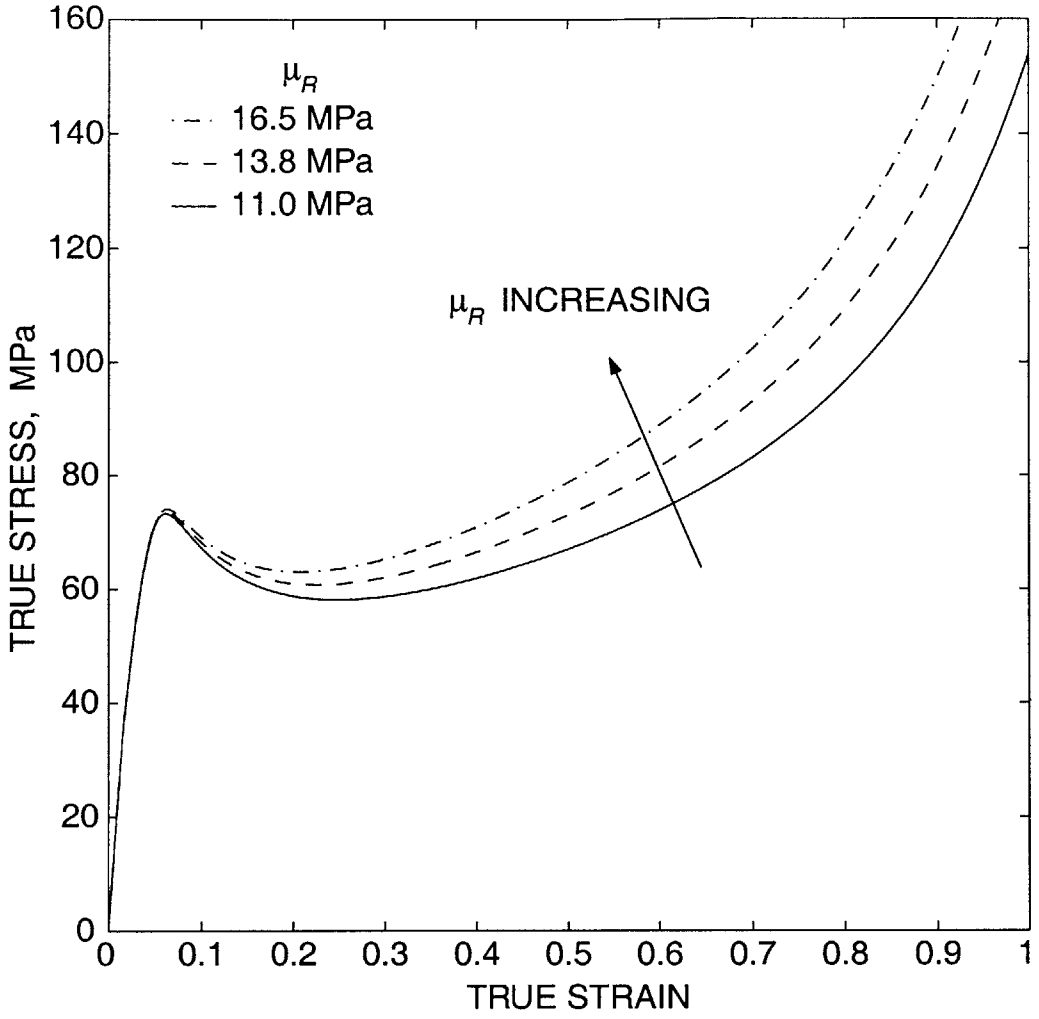

Figure F-88: Sensitivity of the model stress-strain curve for PC to variations in μ_R.

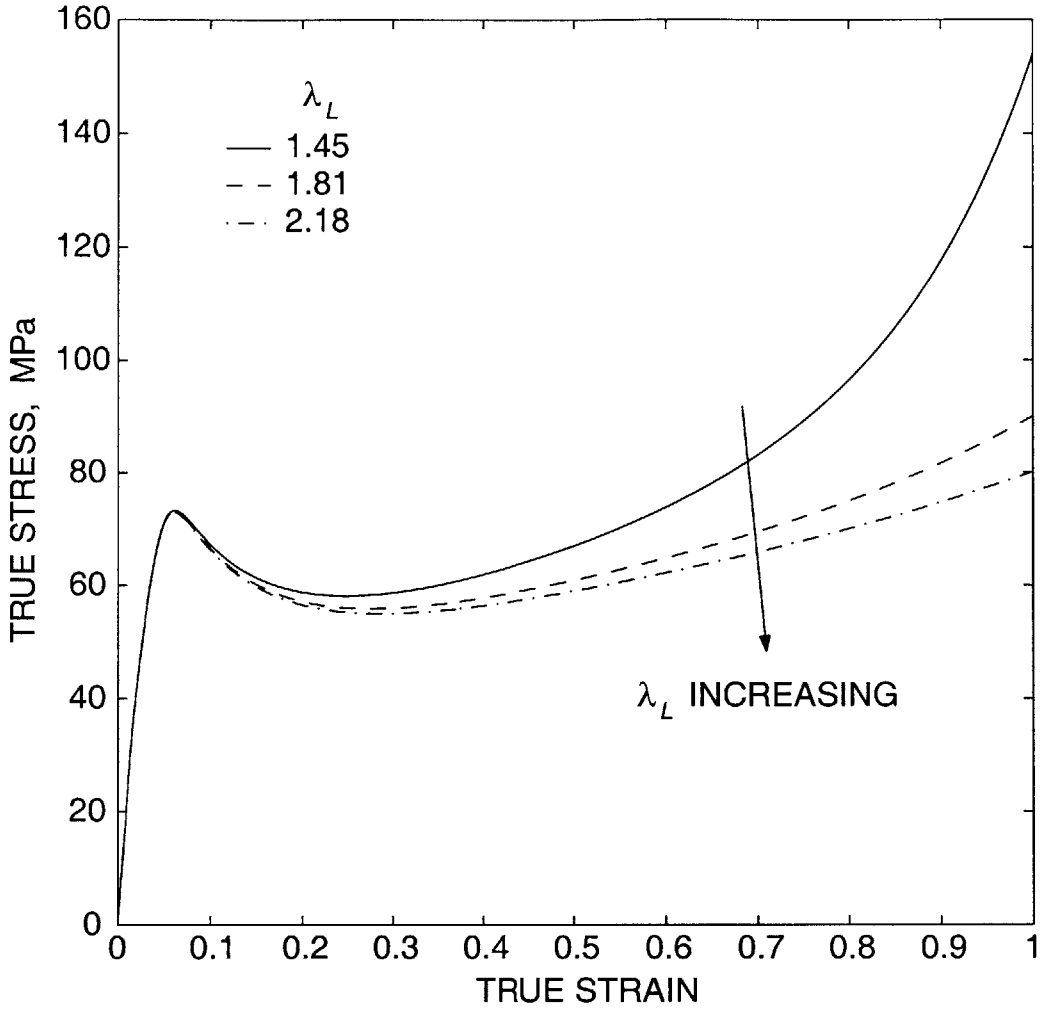

Figure F-89: Sensitivity of the model stress-strain curve for PC to variations in λ_L.

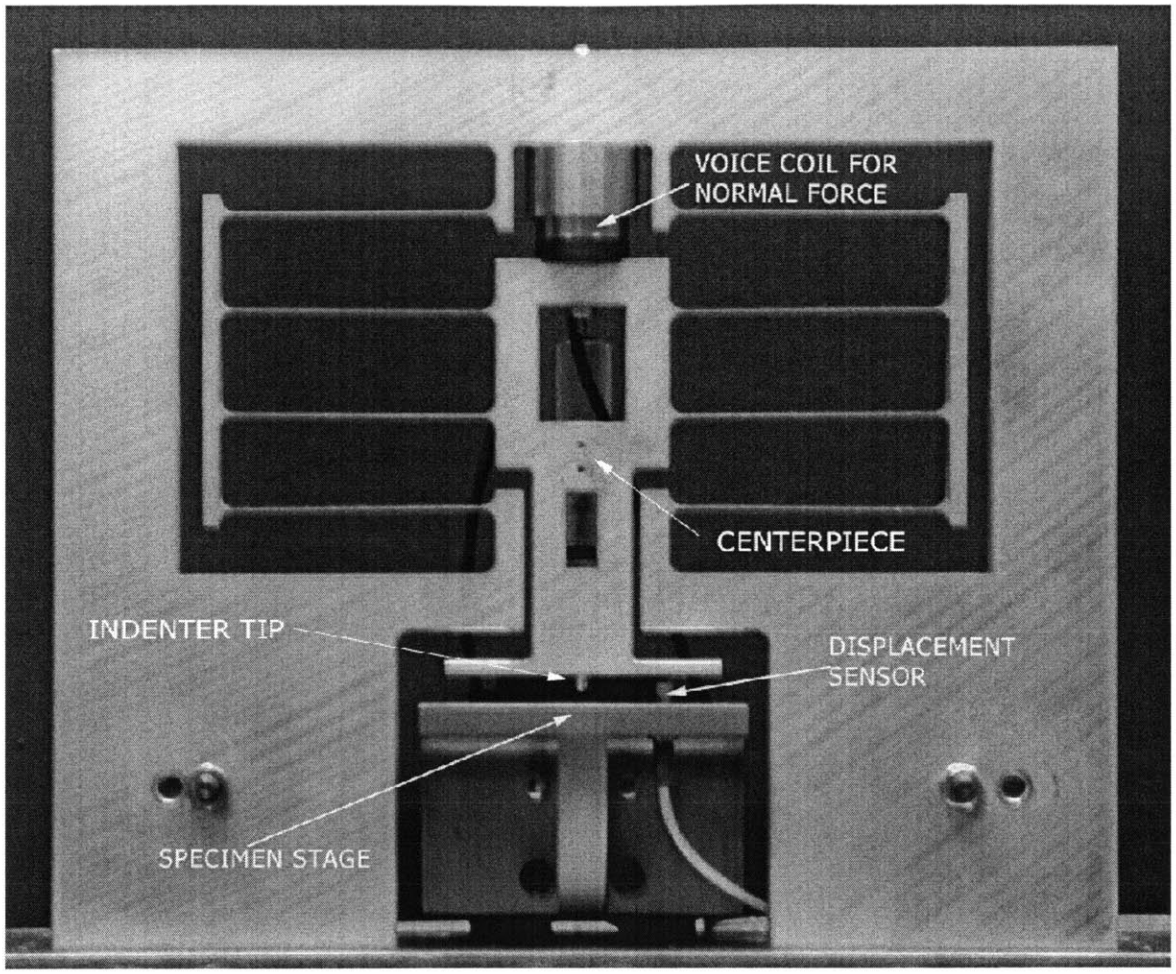

Figure F-90: Instrumented microindentation apparatus. The "centerpiece" transmits the load from the voice coil to the sample to be indented.

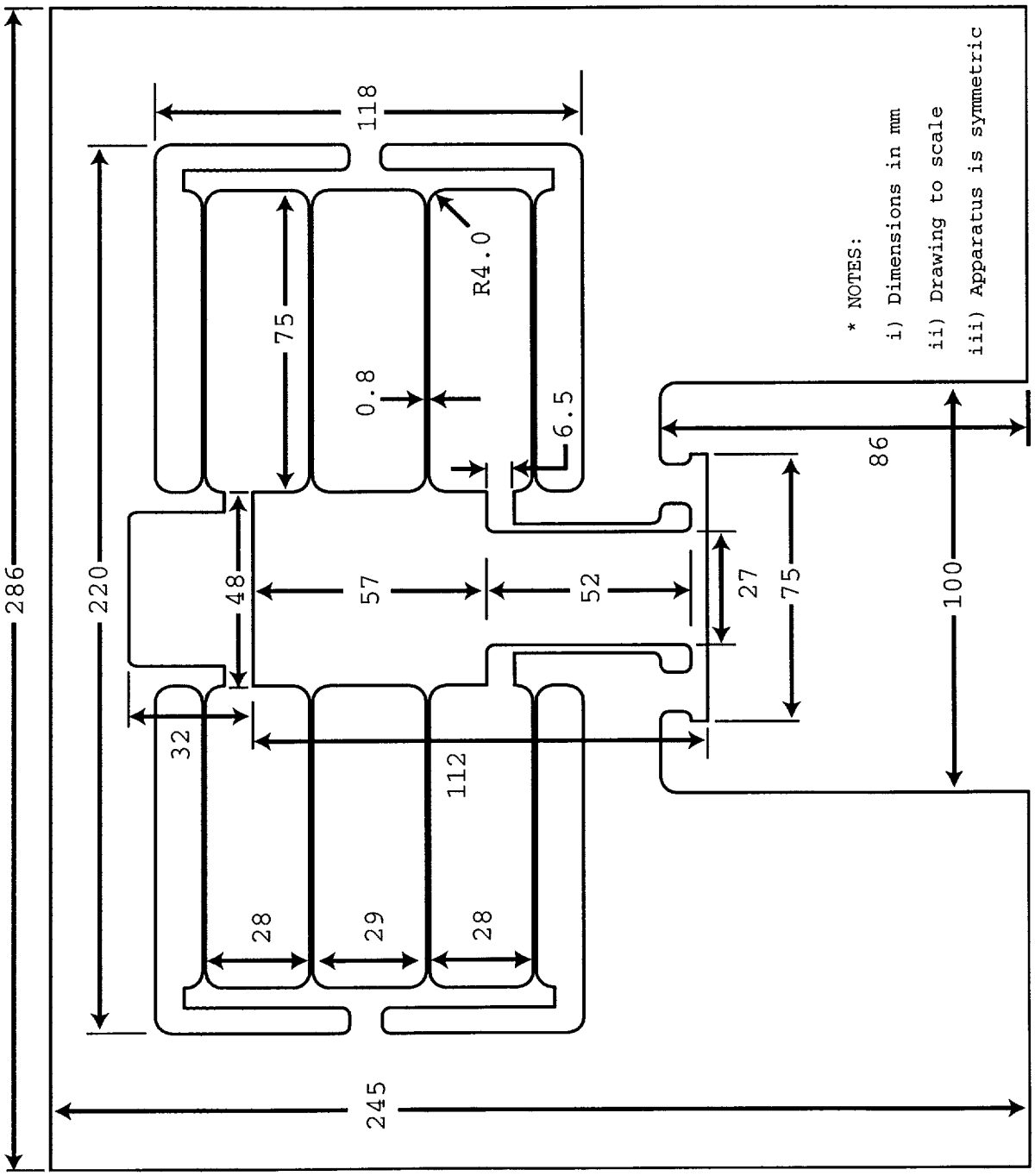

Figure F-91: Key dimensions of the microindenter. All radii are 4 mm.

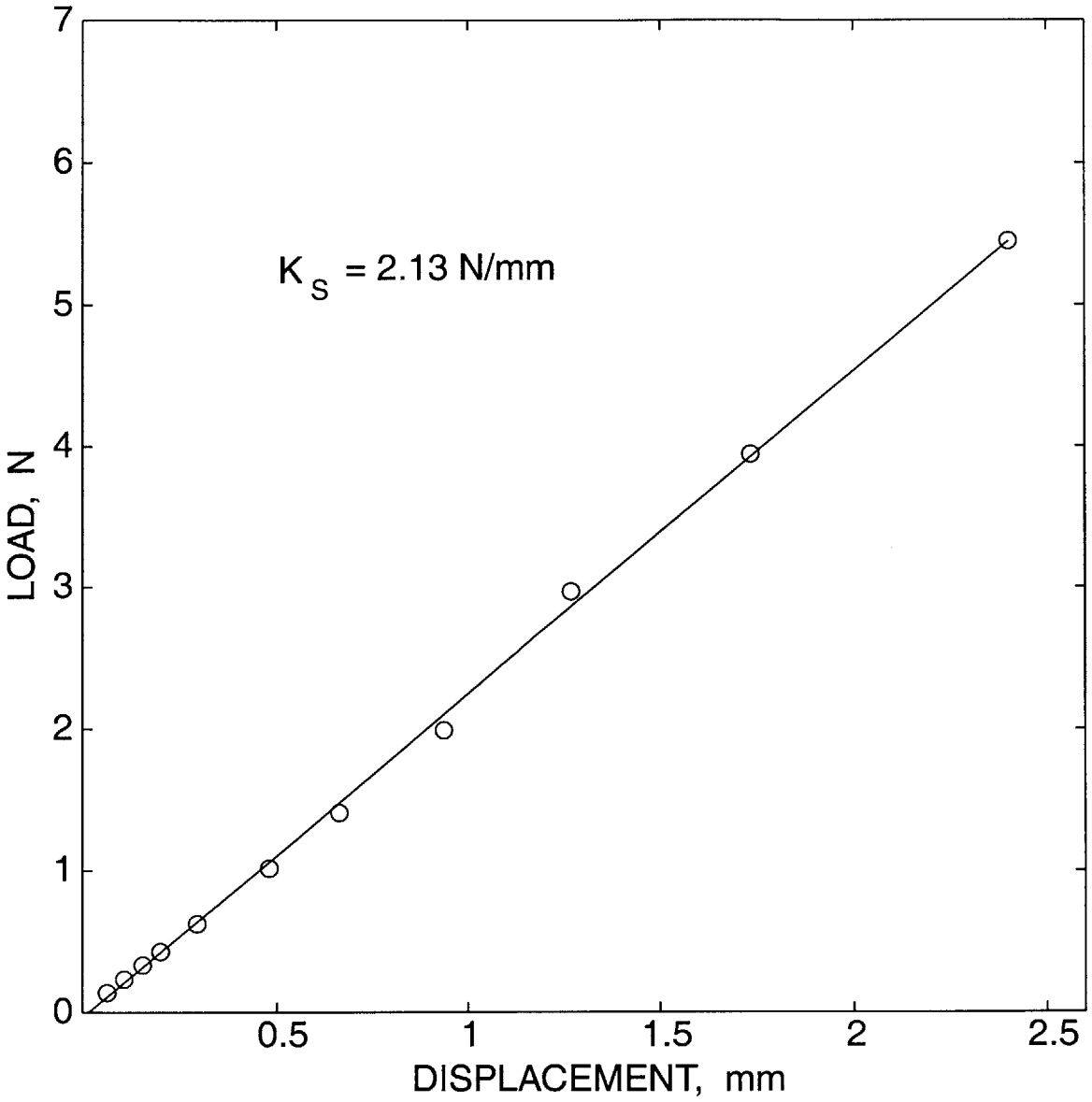

Figure F-92: Calibration curve for the system spring stiffness of the microindenter.

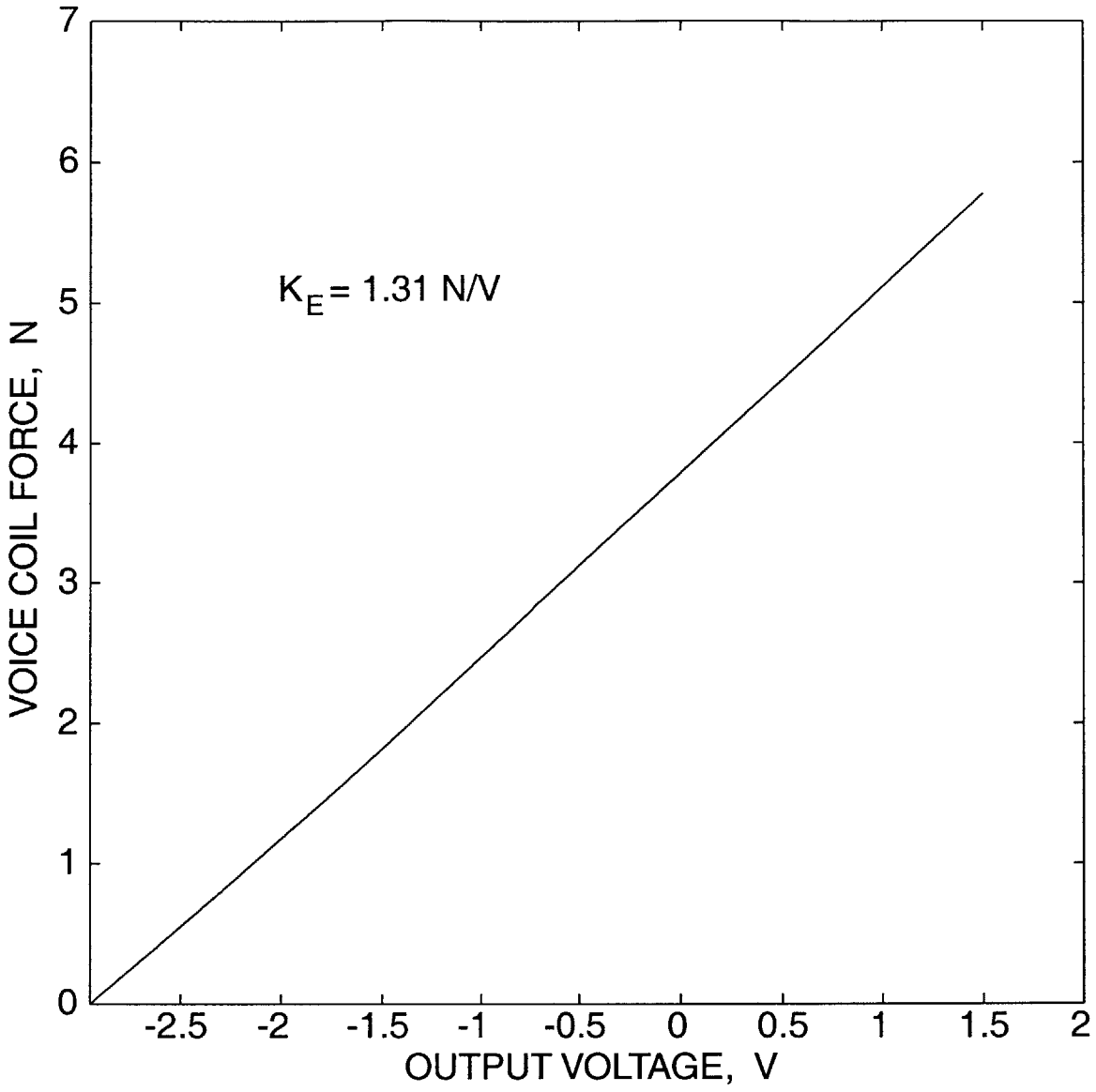

Figure F-93: Calibration curve for the driving electronics of the microindenter.

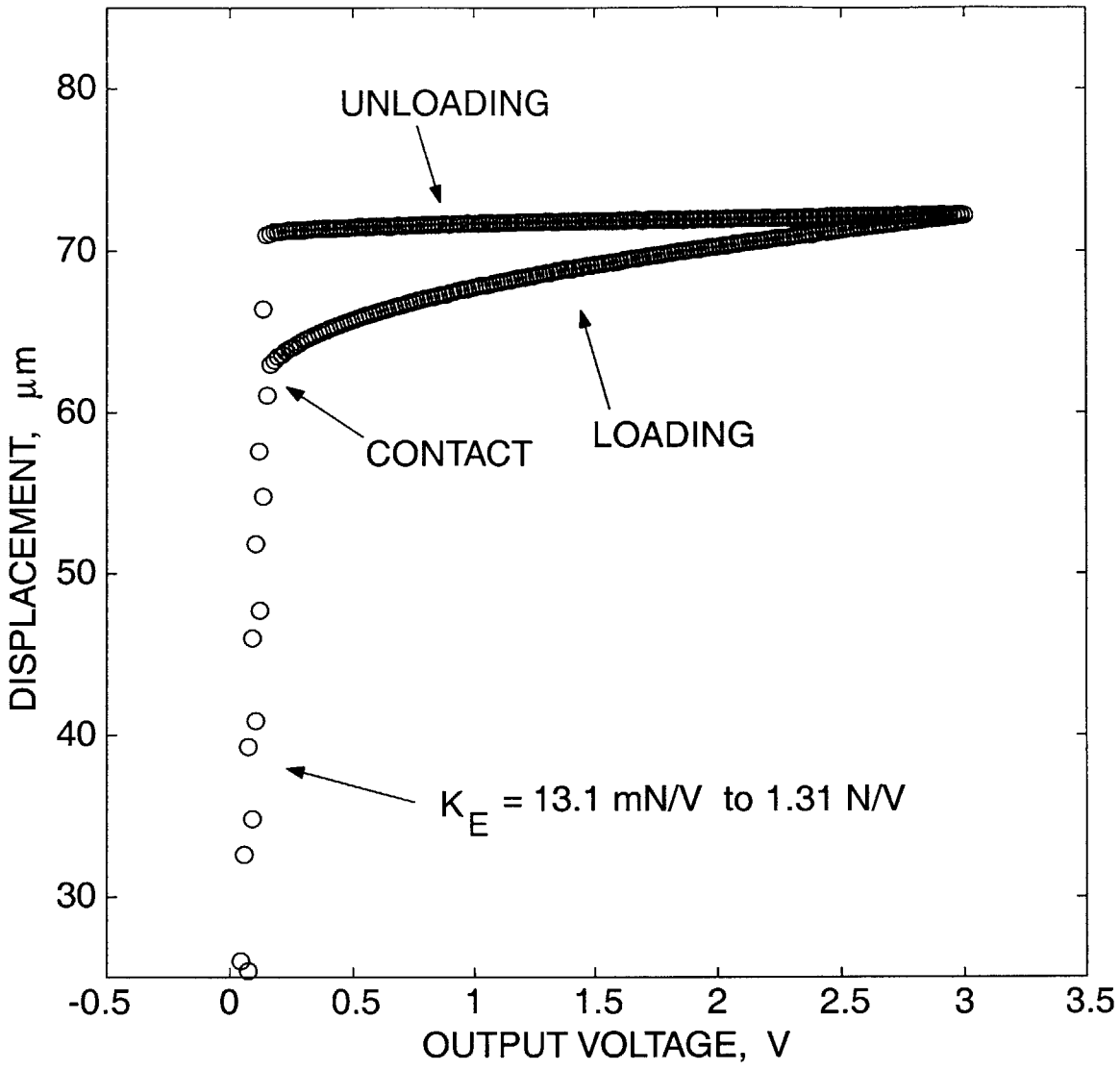

Figure F-94: Acquired displacement vs. output voltage during an indentation test.

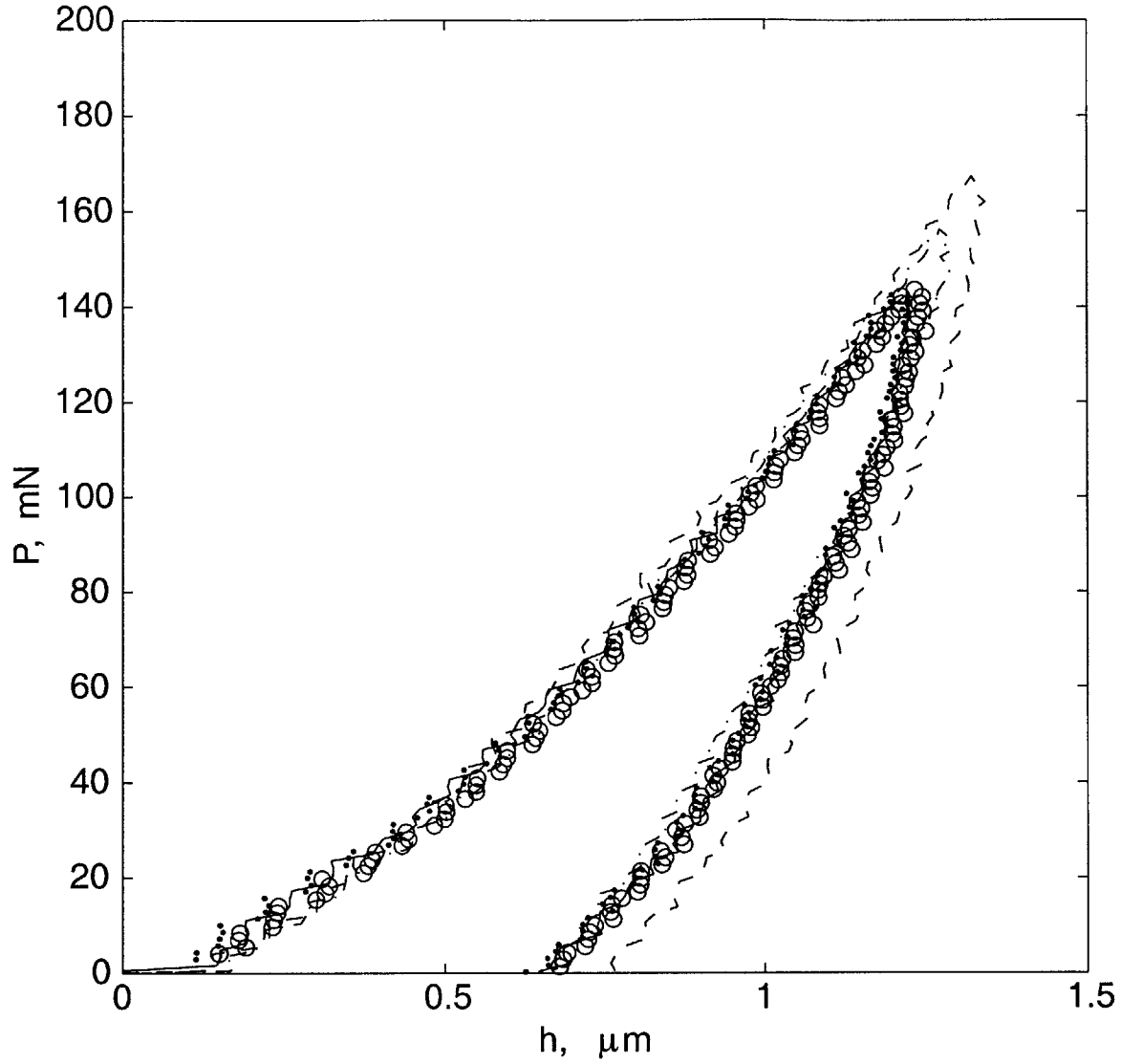

Figure F-95: P-h curves for indentation of fused silica at 5 mN/s.

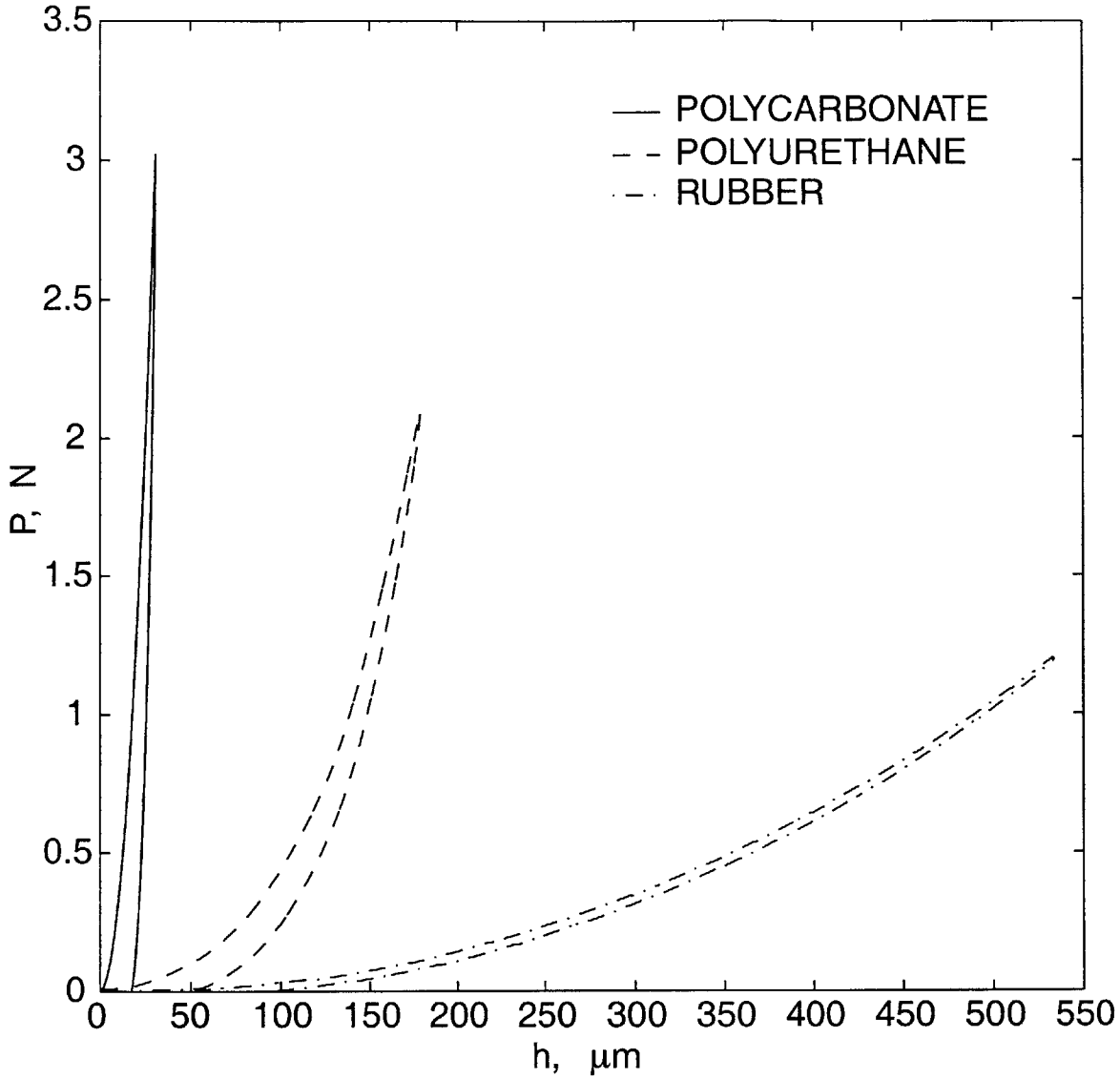

Figure F-96: Exemplary P-h curves for indentation of a variety of materials loaded at 50 mN/s.

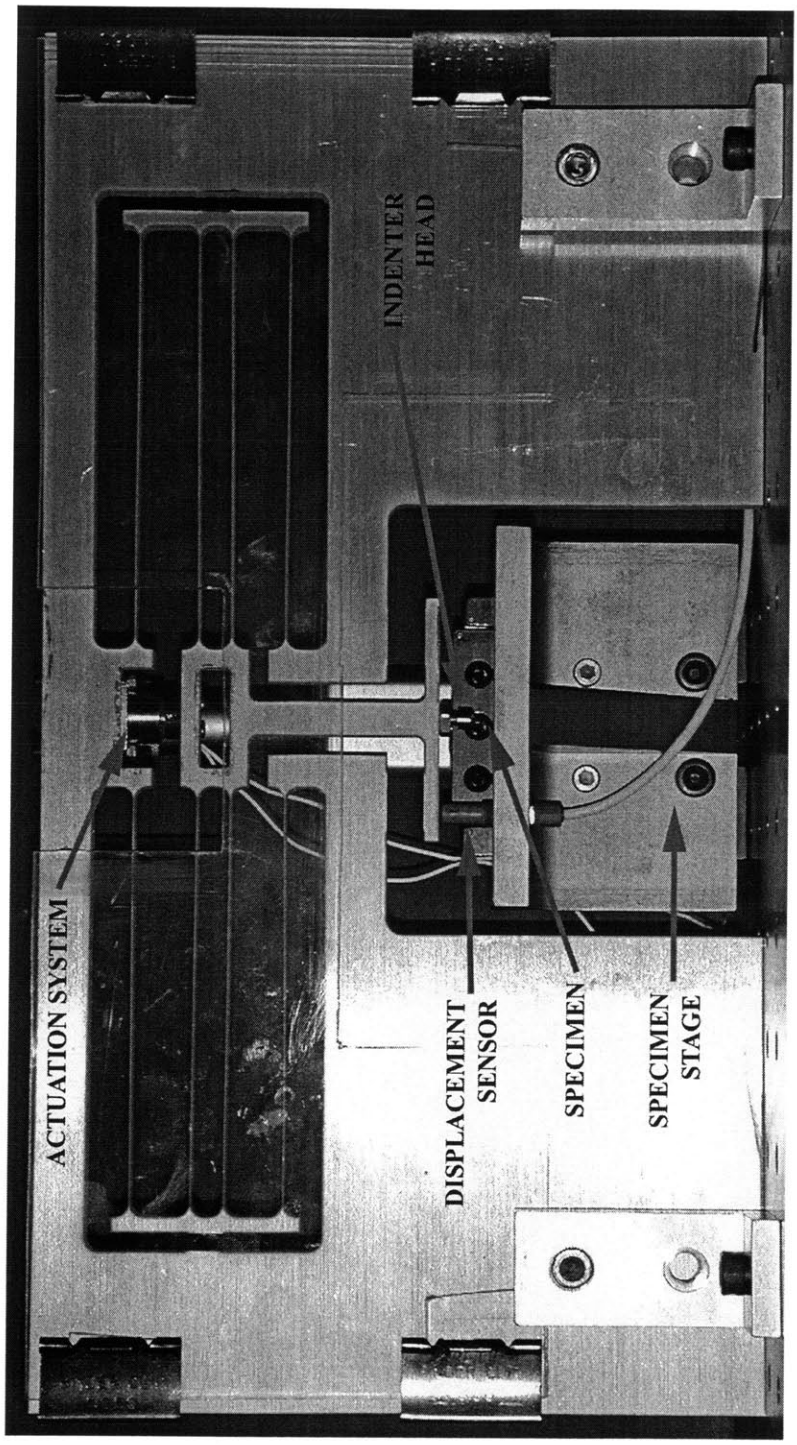

Figure F-97: Instrumented nanoindentation apparatus.

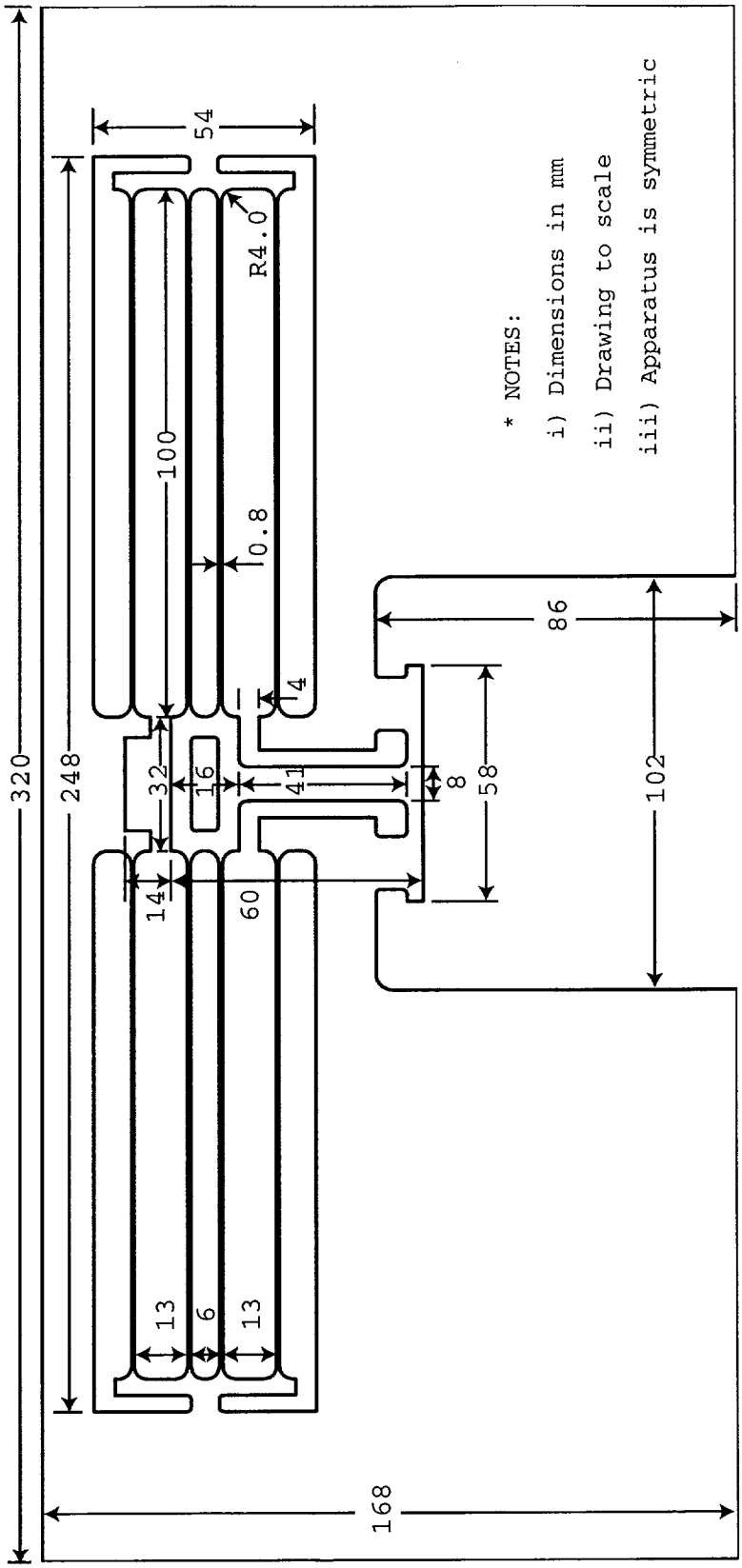

Figure F-98: Key dimensions of the nanoindenter. All radii are 4 mm.

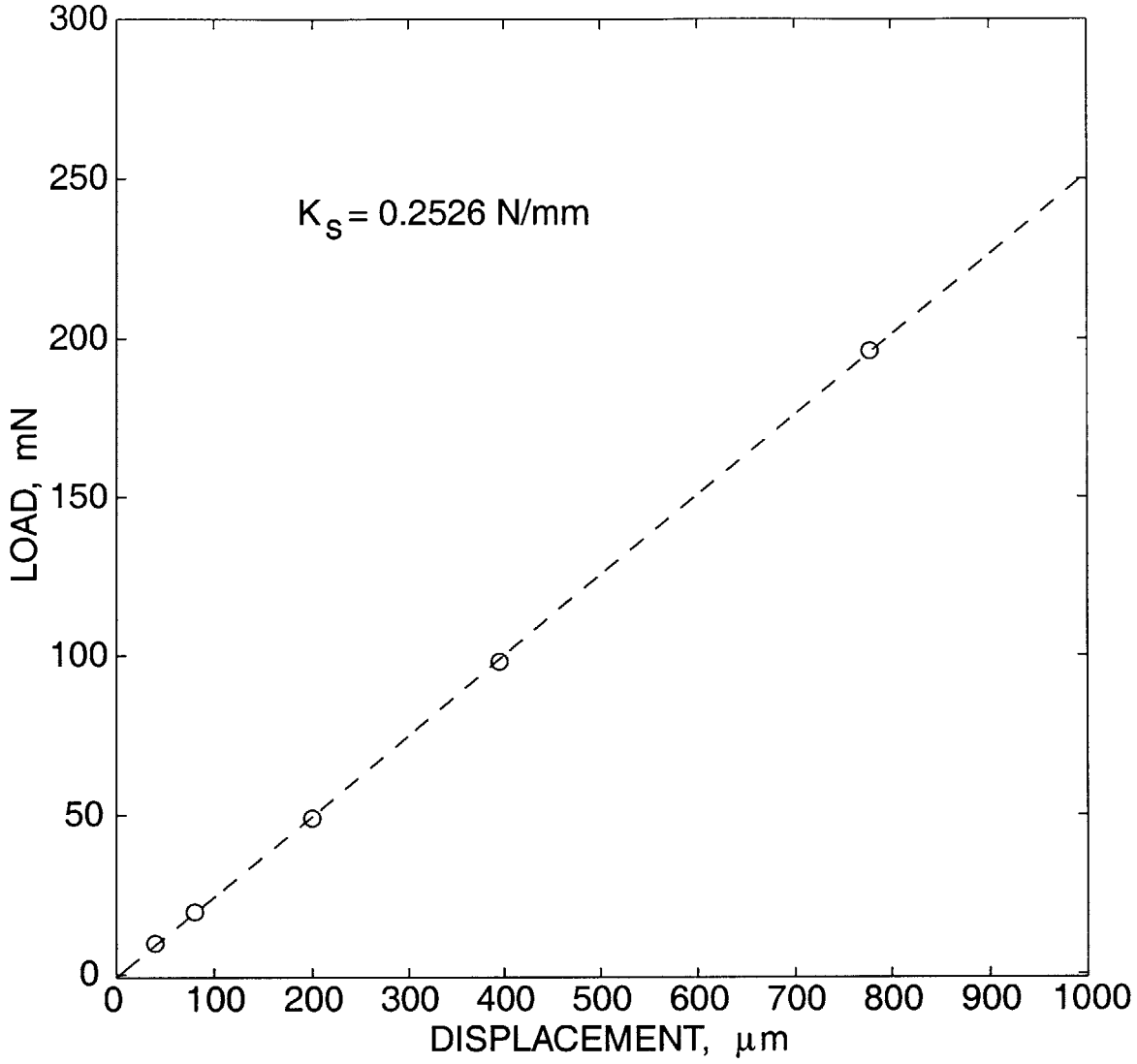

Figure F-99: Calibration curve for the system spring stiffness of the nanoindenter.

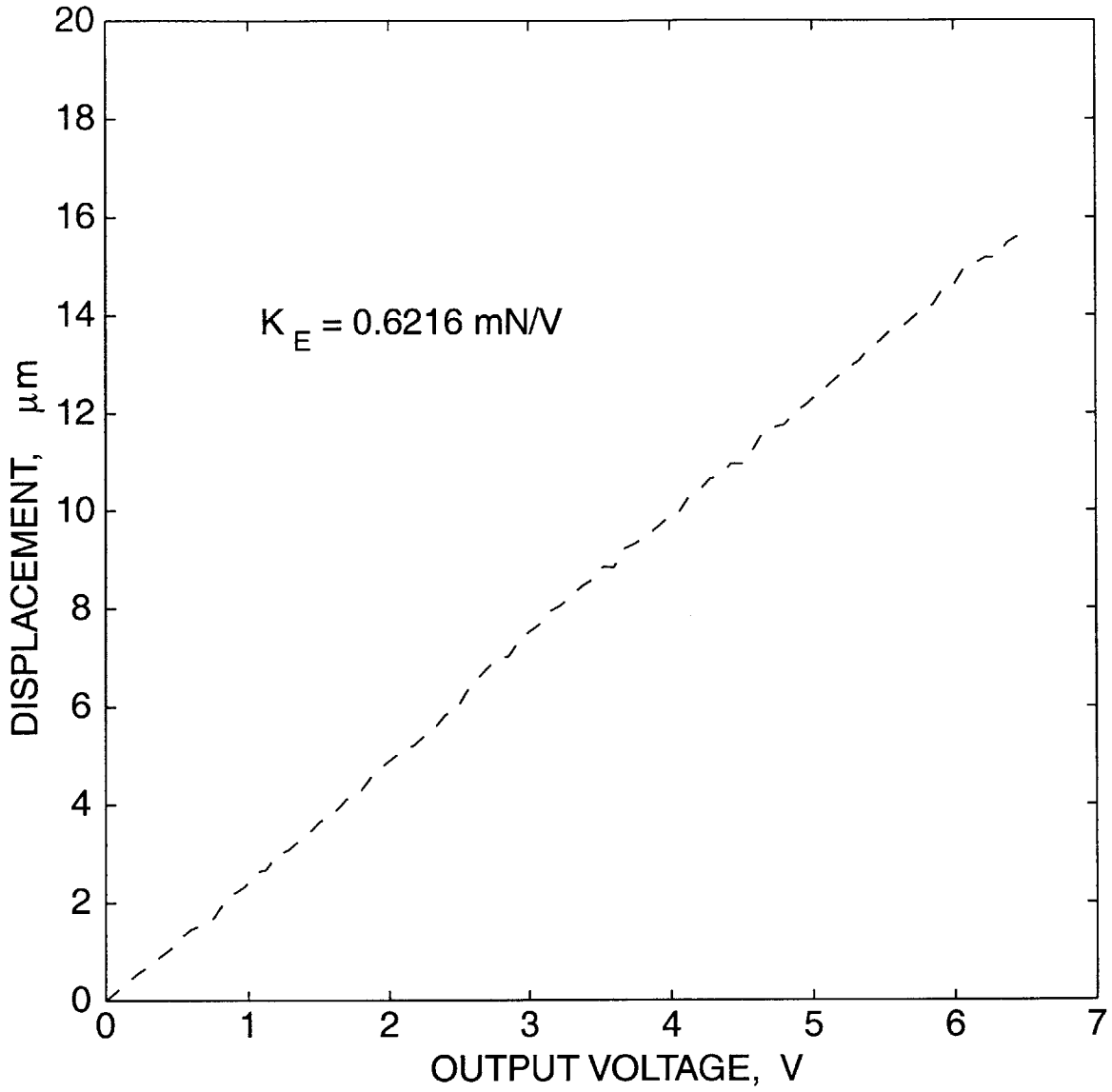

Figure F-100: Calibration curve for the driving electronics of the nanoindenter.

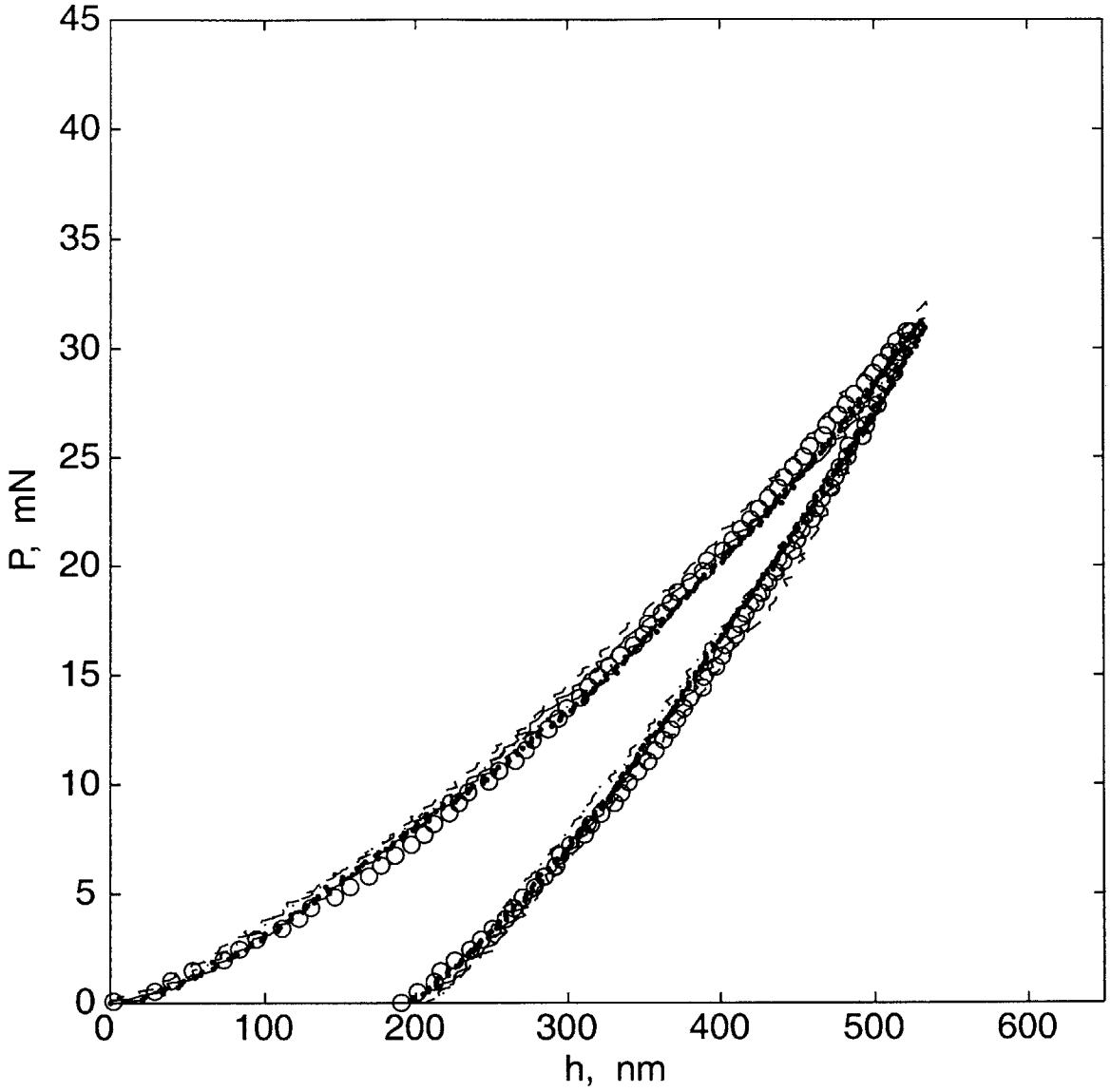

Figure F-101: Berkovich indentation of fused silica; P-h curves obtained with the nanoindentation apparatus.

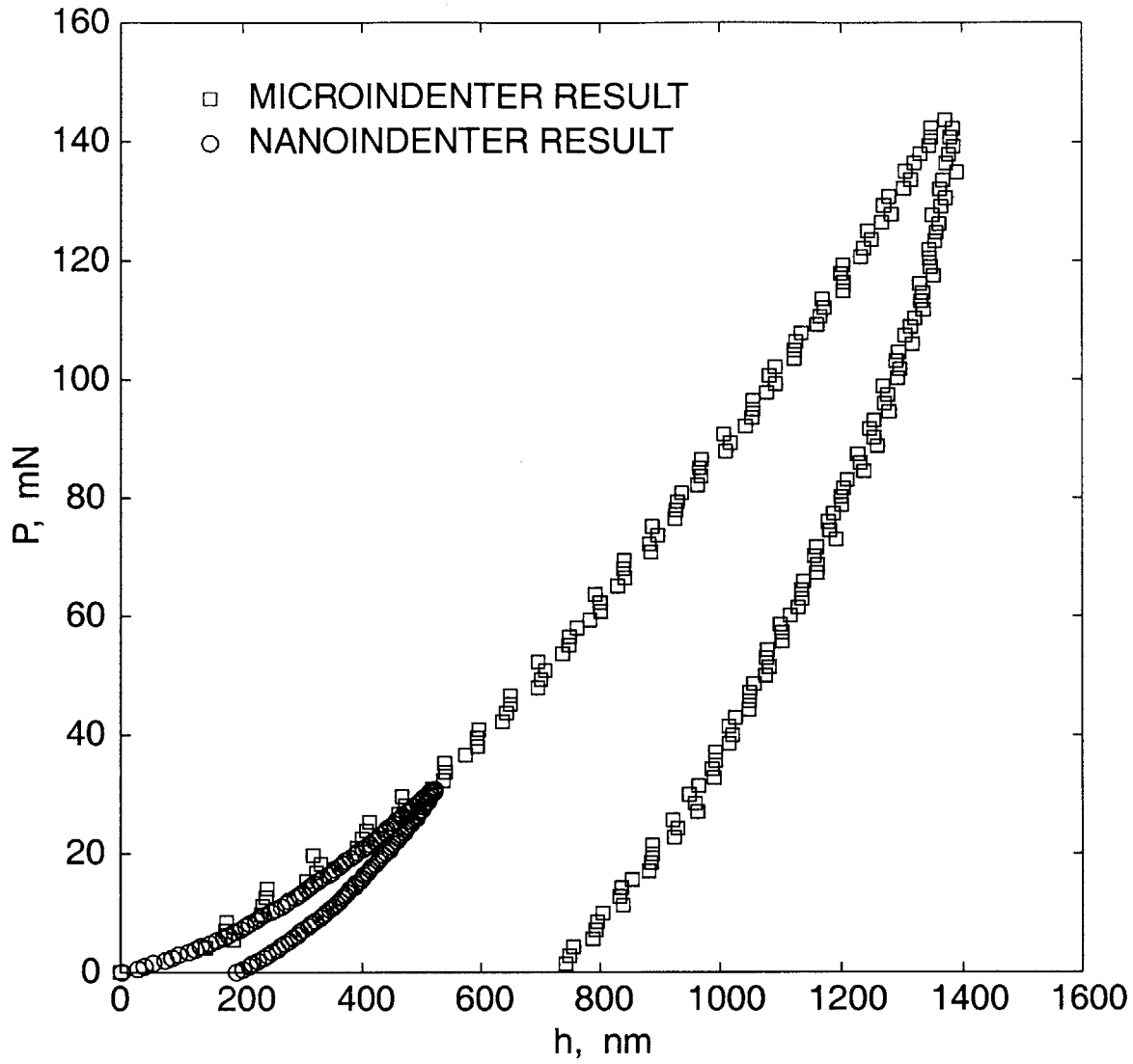

Figure F-102: Berkovich indentation of fused silica; comparison of P-h curves for the microindentation and nanoindentation apparatuses.

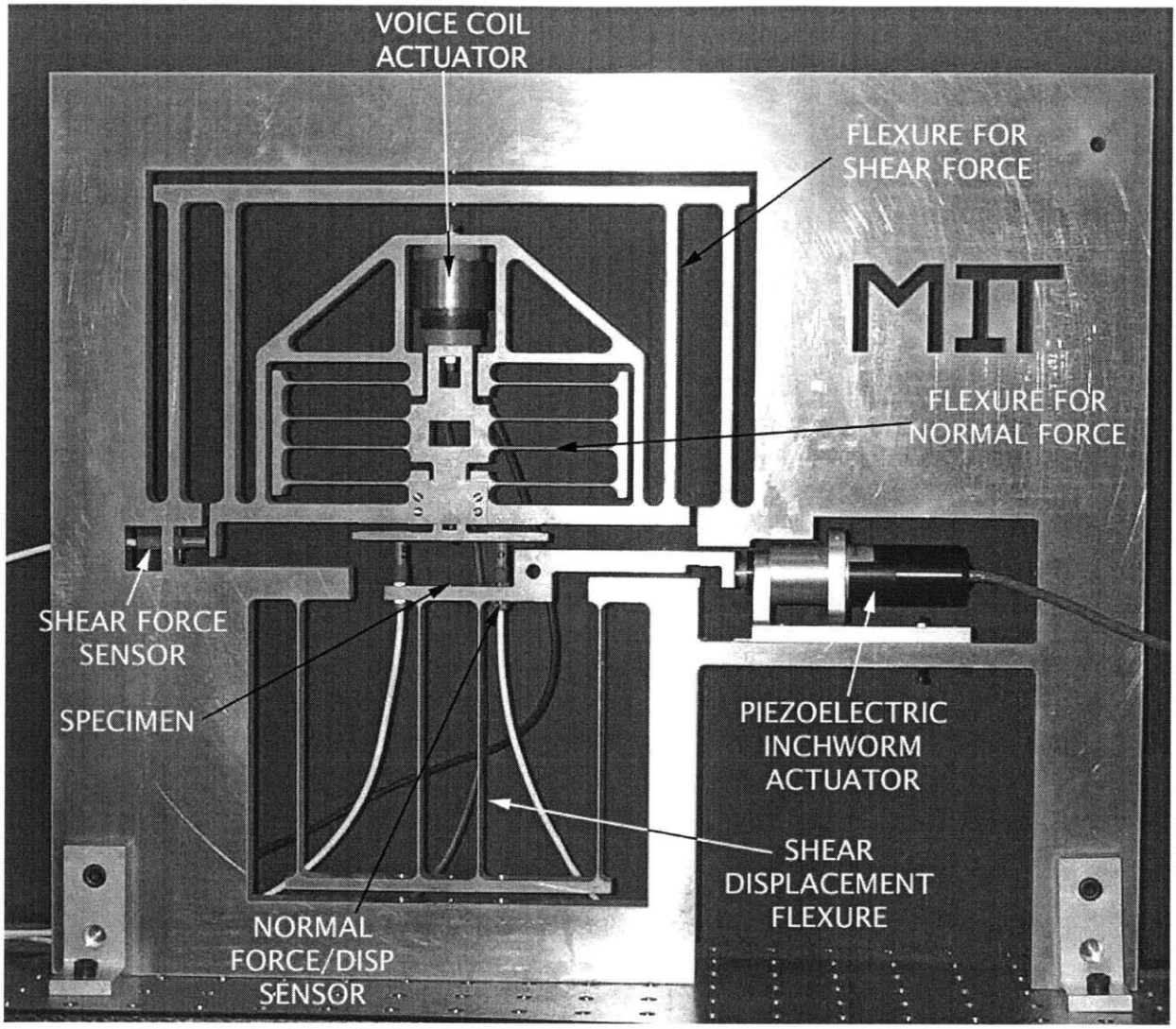

Figure F-103: Biaxial compression/shear apparatus.

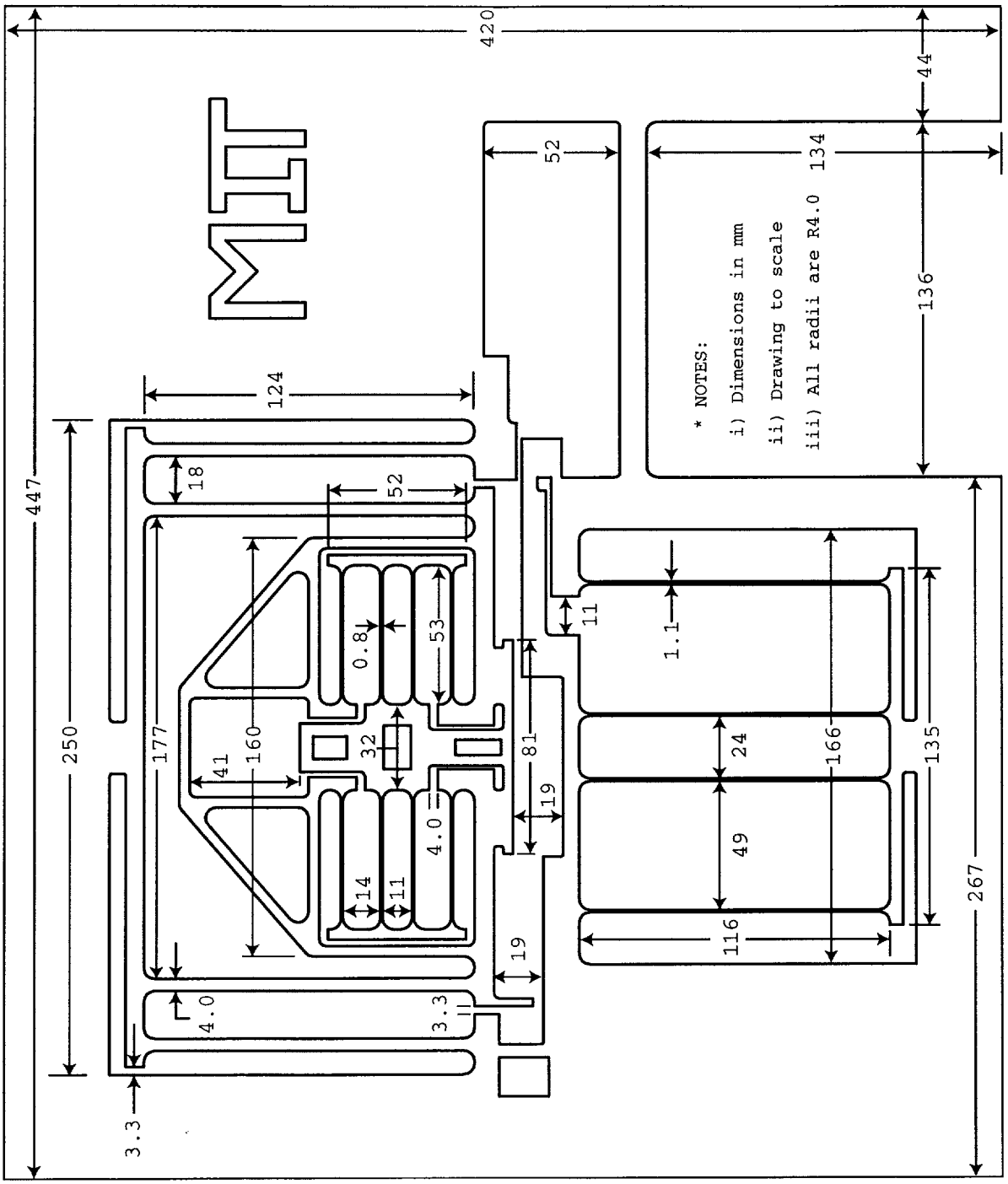

Figure F-104: Key dimensions of the biaxial compression/shear apparatus.

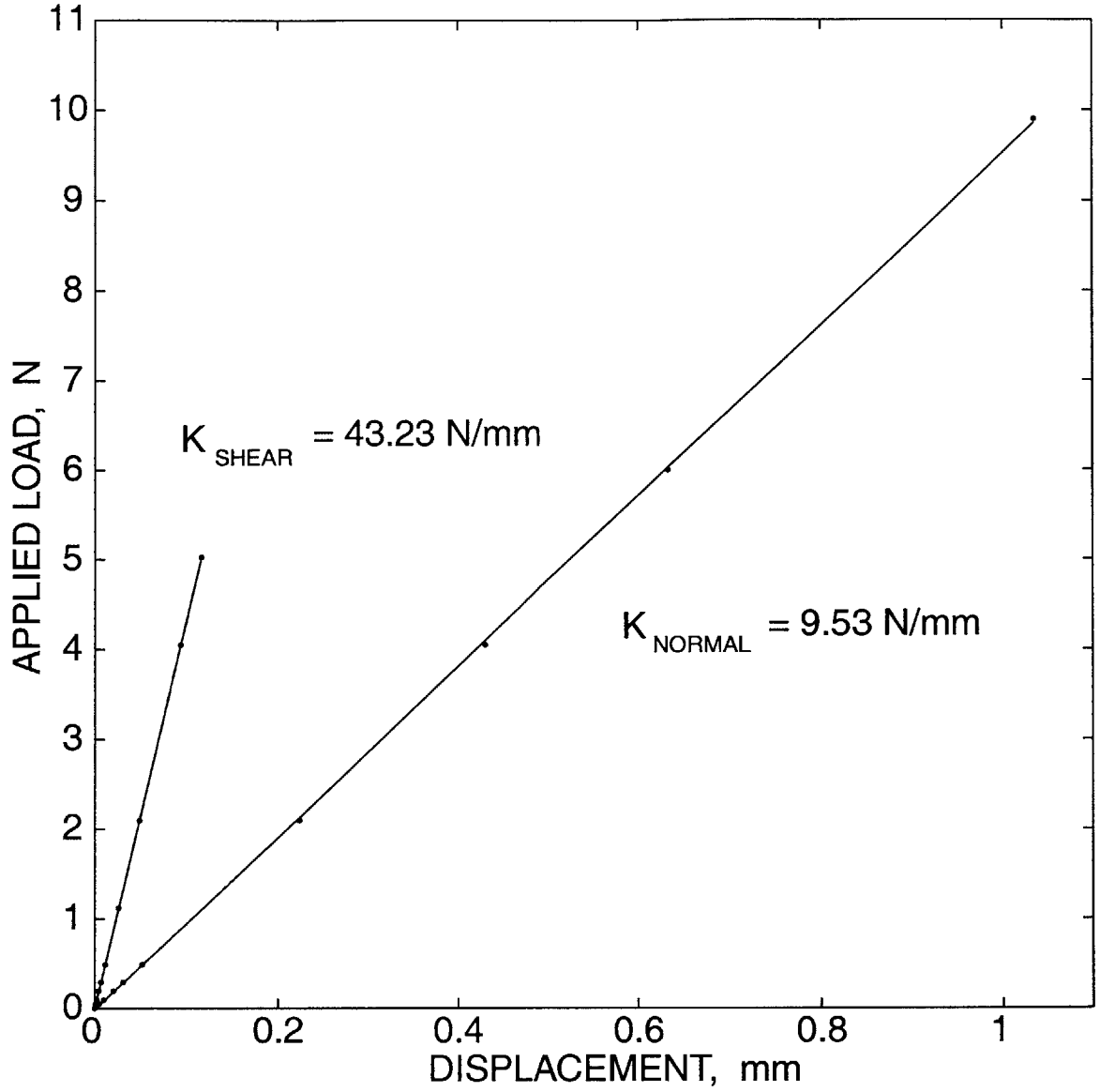

Figure F-105: Calibration curves for the spring stiffnesses of the normal and shear axes of the biaxial compression/shear apparatus.

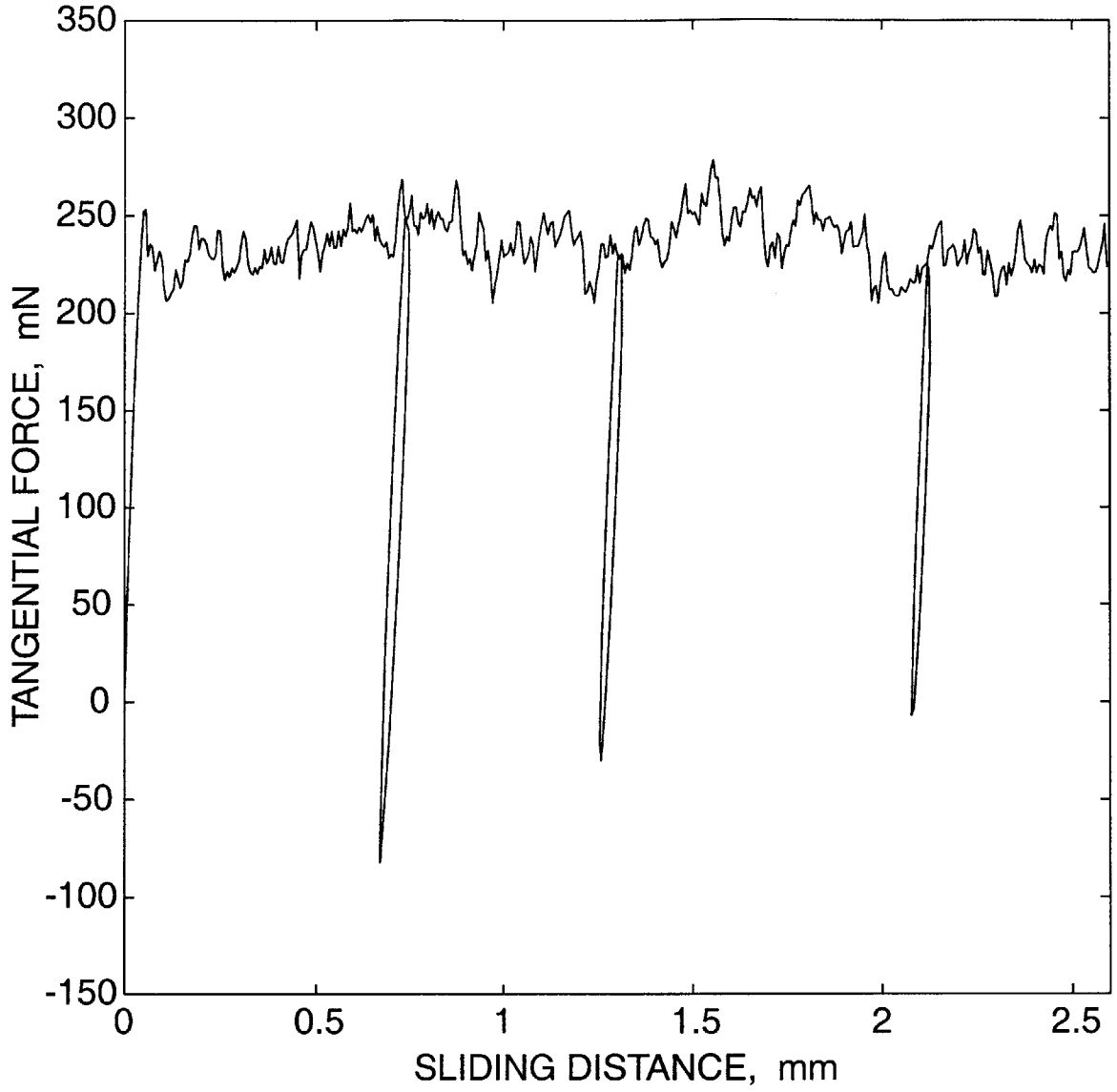

Figure F-106: Frictional response of an Al6111/tool steel interface at a normal force of 1 N.

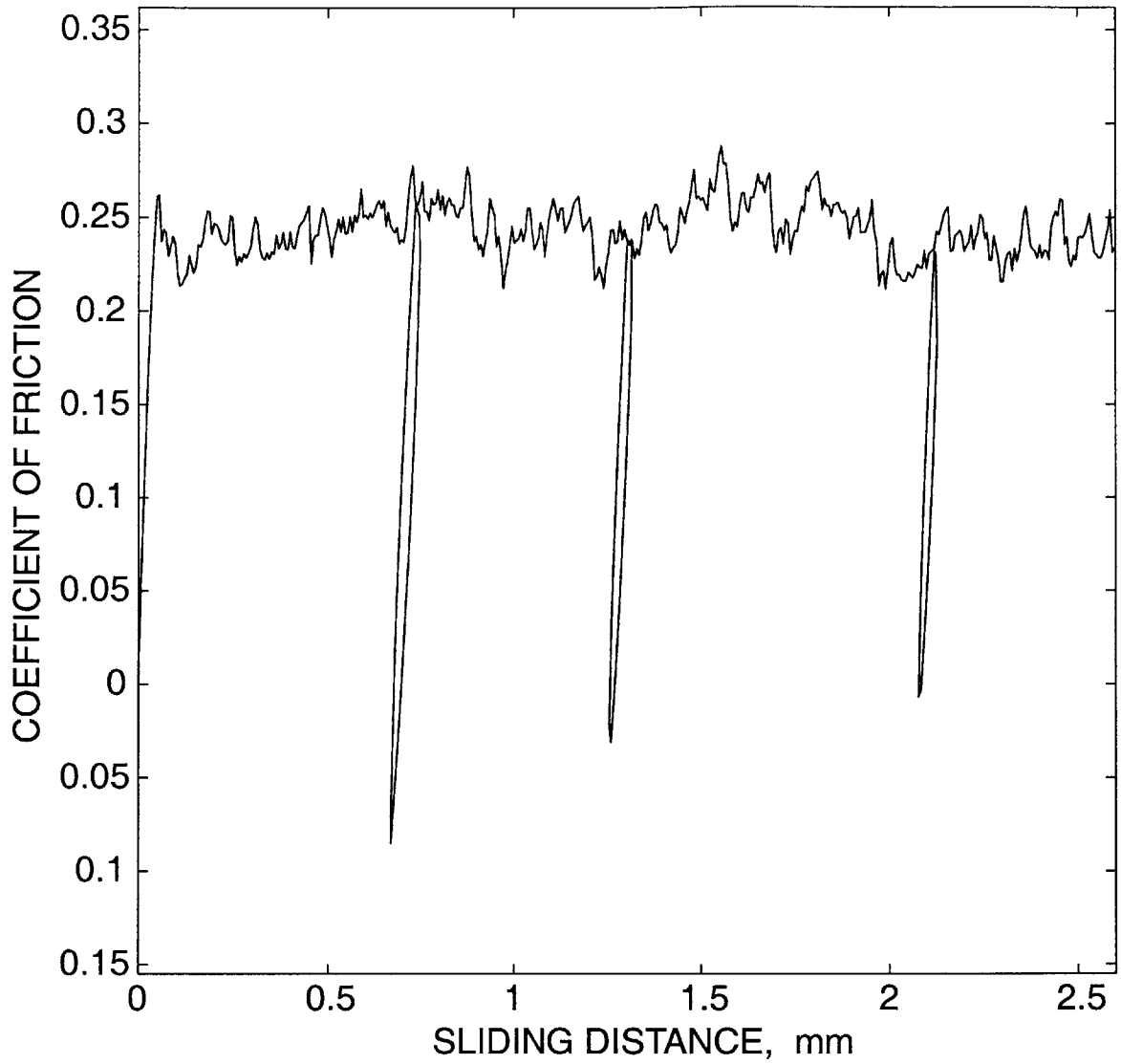

Figure F-107: Coefficient of friction for an Al6111/tool steel interface at a normal force of 1 N.

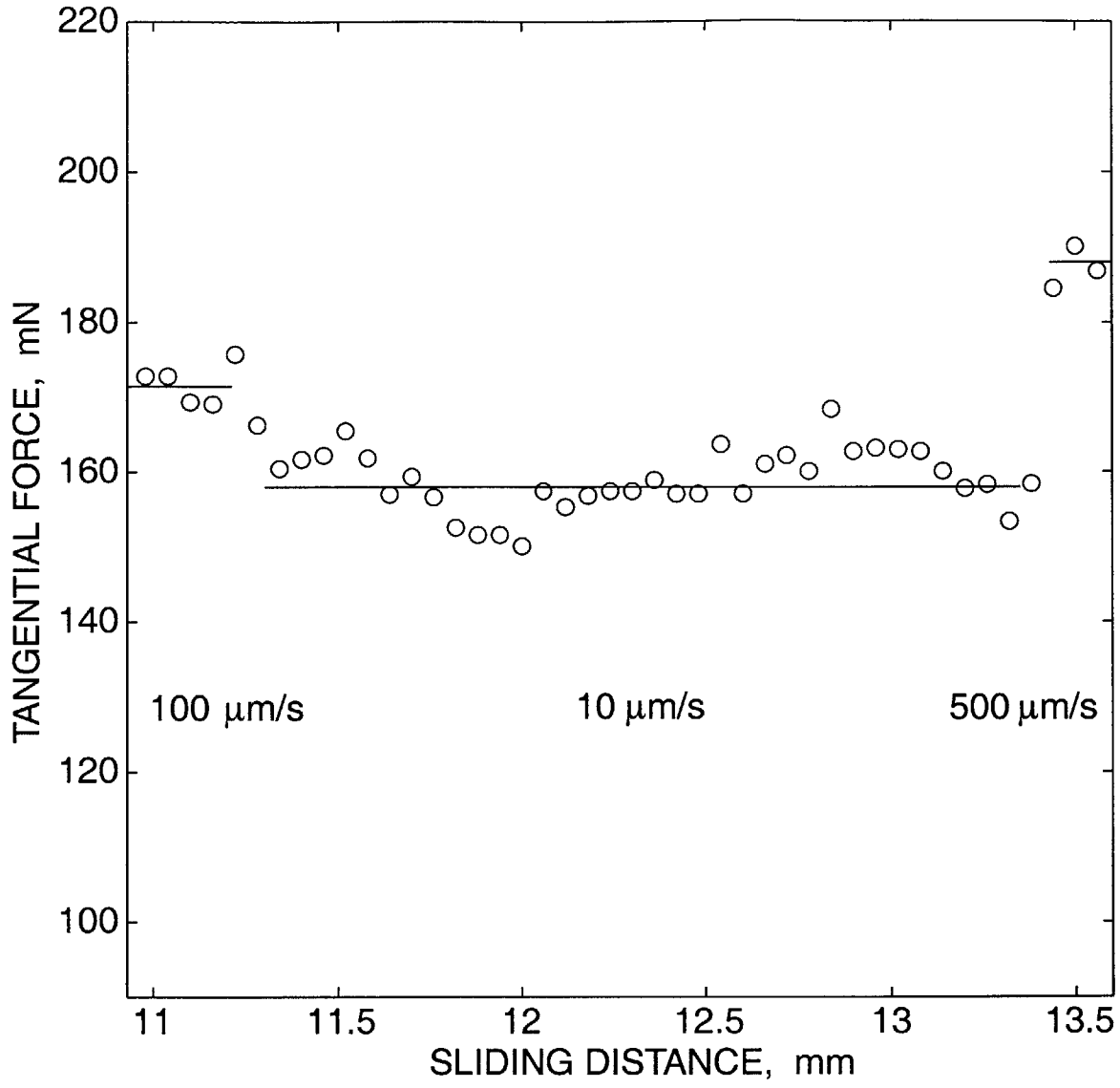

Figure F-108: Rate sensitivity of a dry PC/tool steel interface at a normal force of 750 mN.

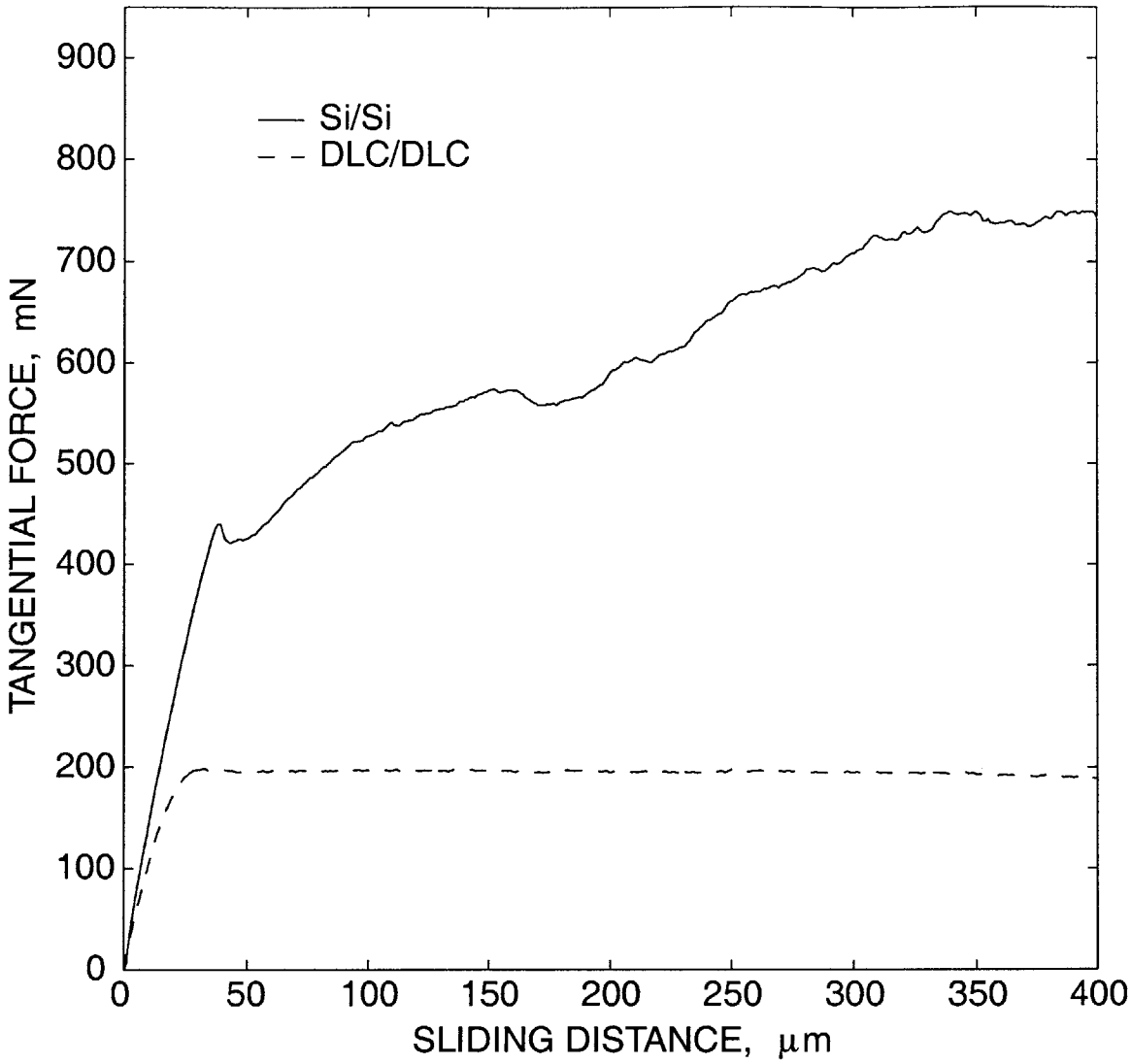

Figure F-109: Frictional response of MEMS interfaces at a normal force of 2 N.

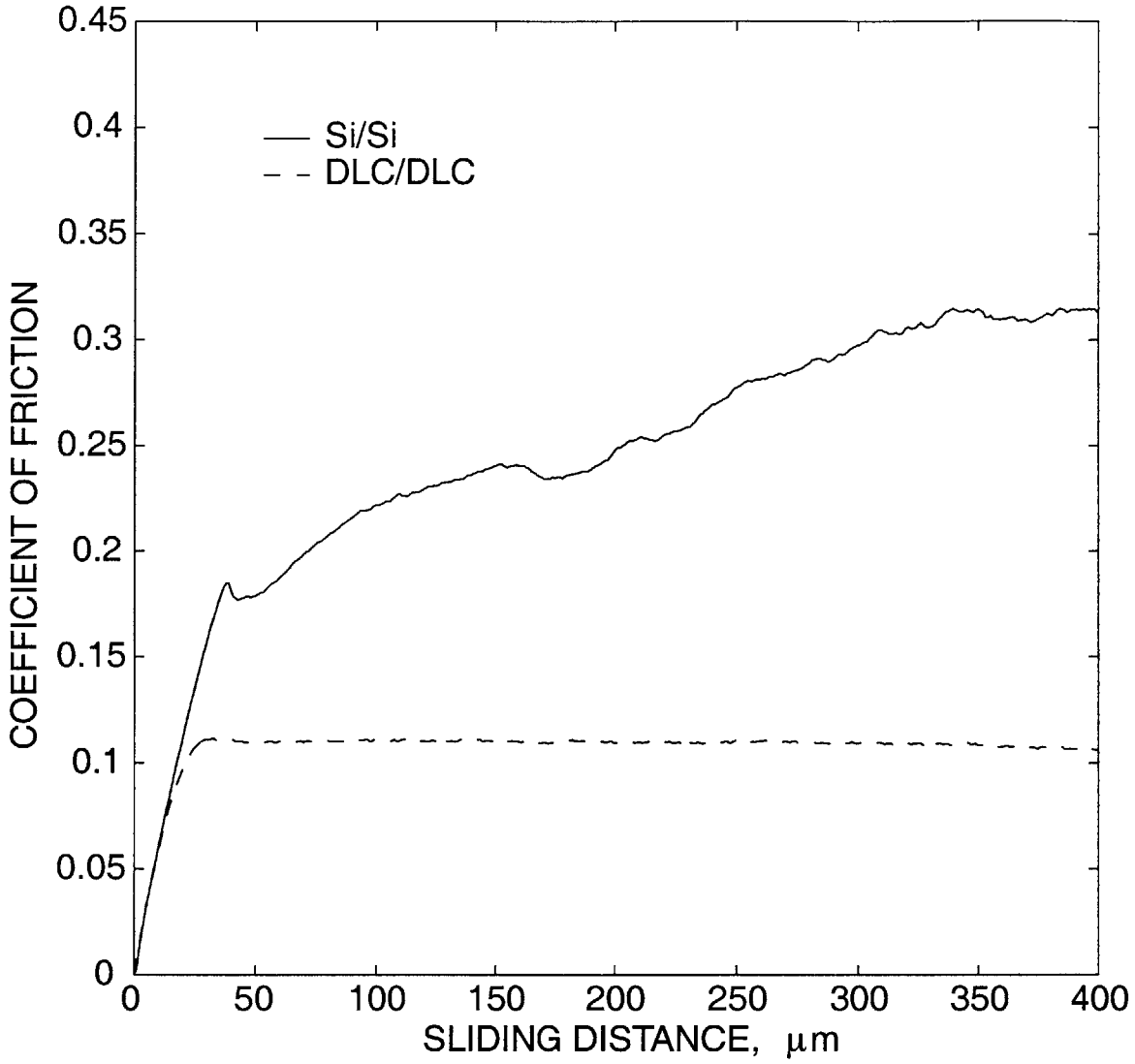

Figure F-110: Coefficient of friction for MEMS interfaces at a normal force of 2 N.

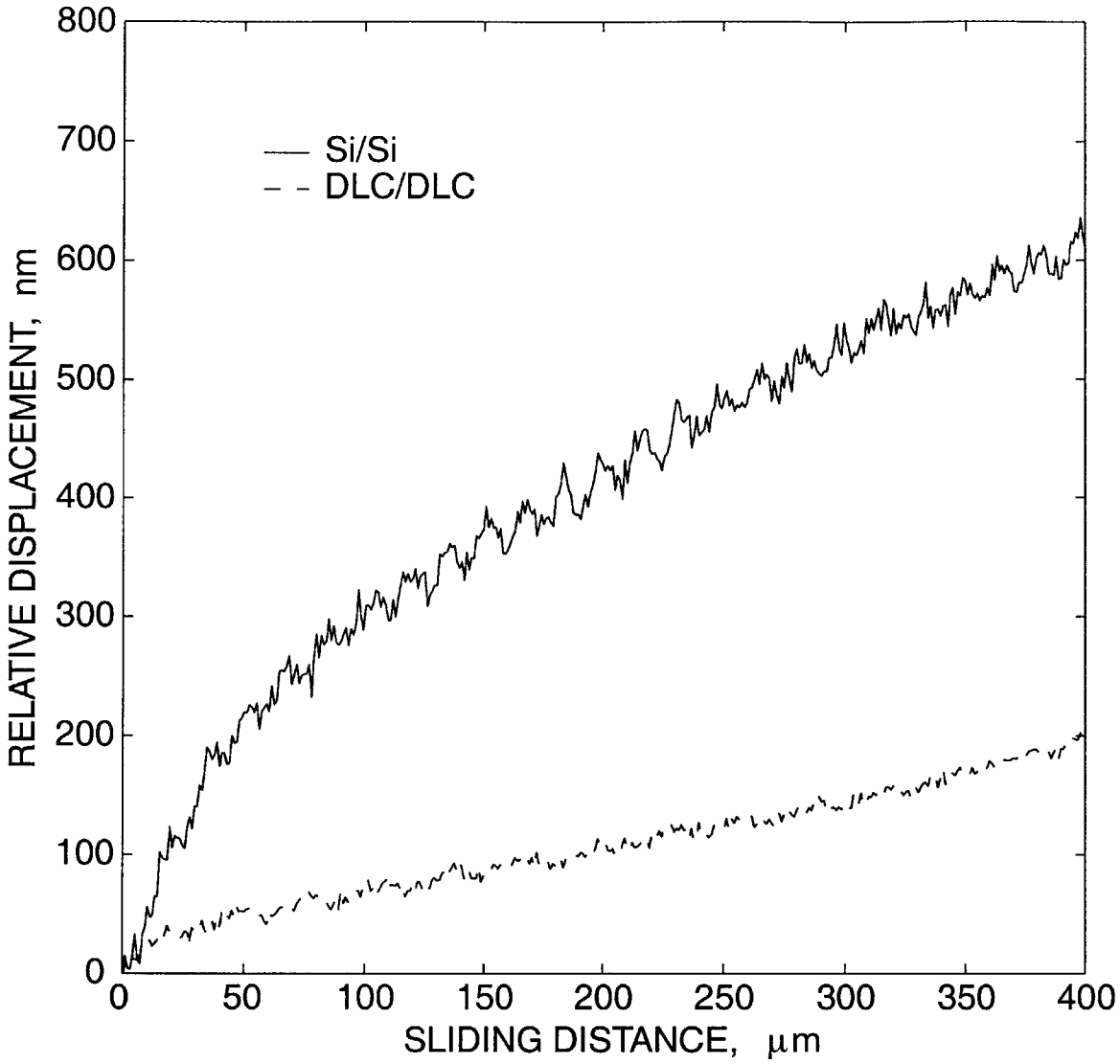

Figure F-111: Relative displacement for MEMS interfaces at a normal force of 2 N.

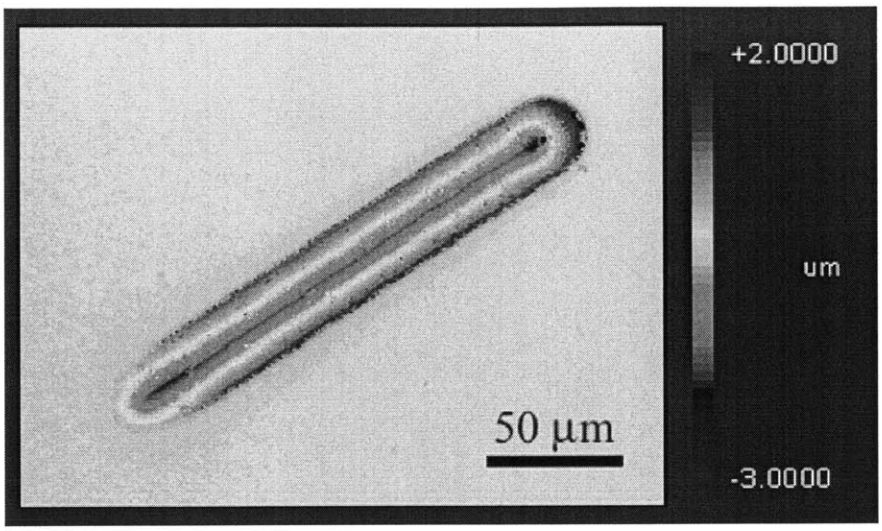

(a)

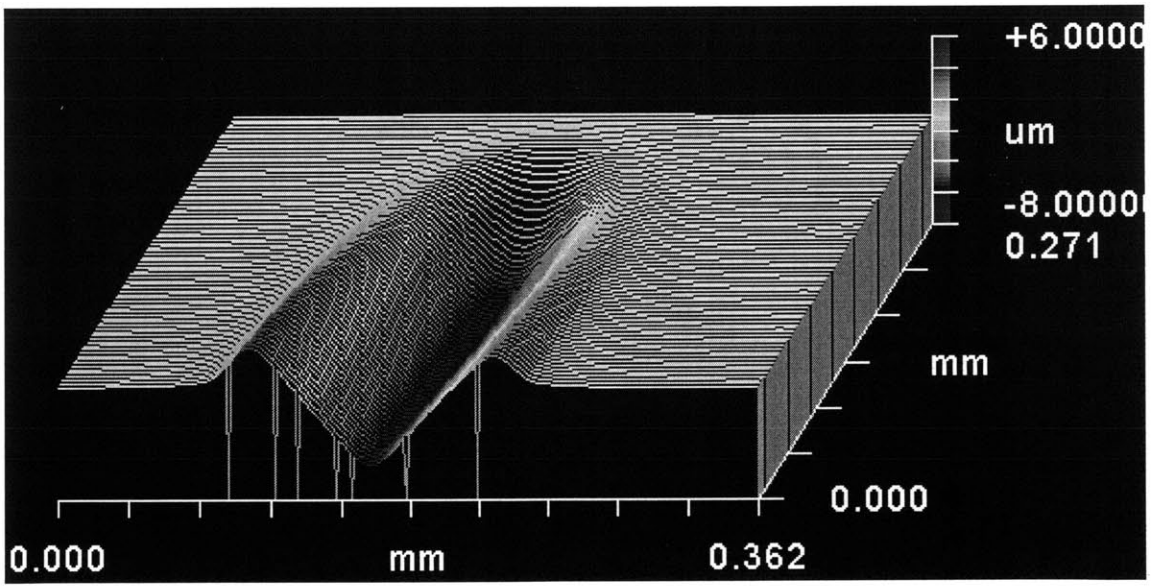

(b)

Figure F-112: Scratch testing of PC using a conical indenter tip at 10 μm/s: (a) scratch morphology for a test conducted at a fixed normal force of 174 mN; (b) cross-section of the scratch.

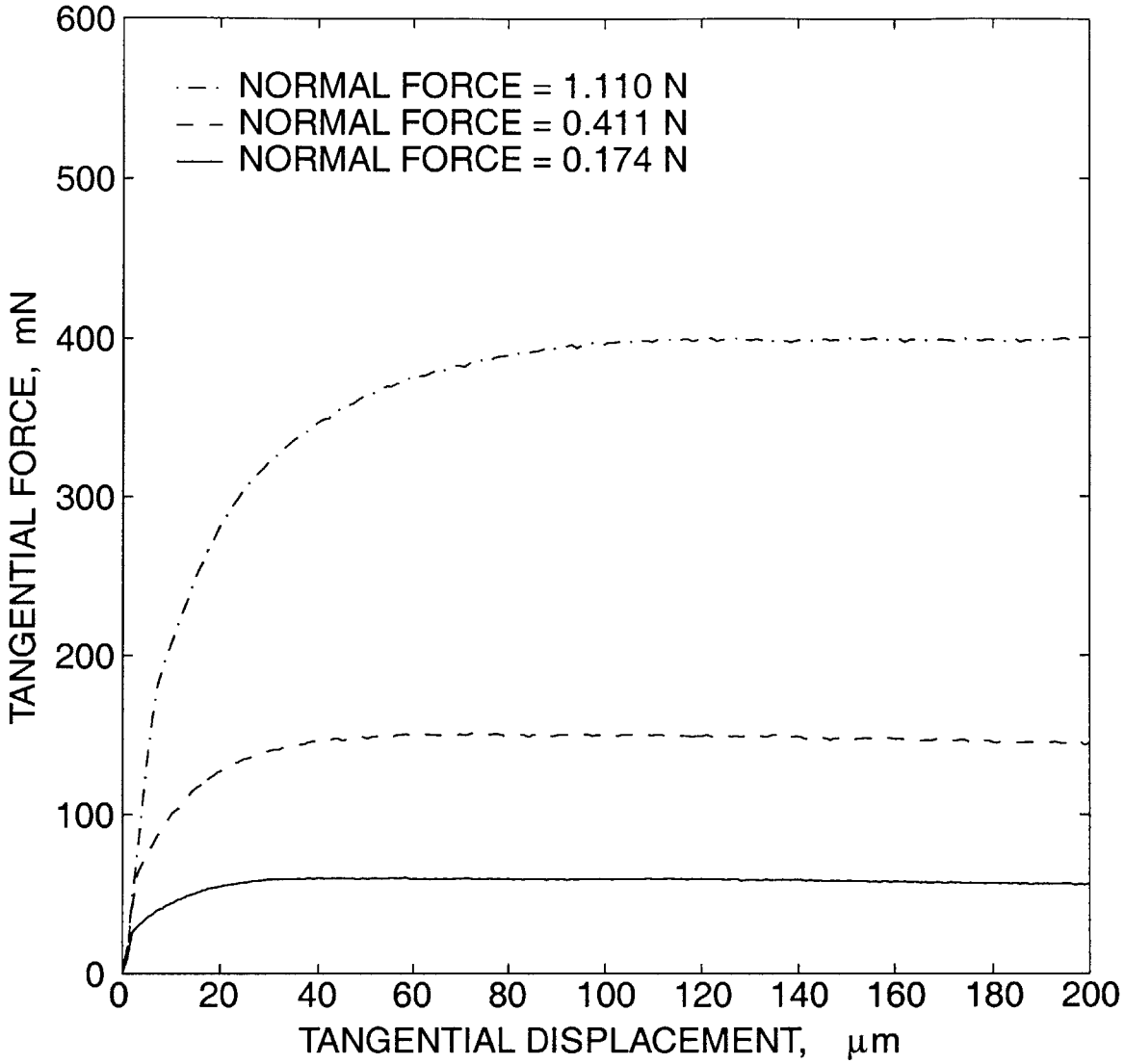

Figure F-113: Scratch testing of PC using a conical indenter tip at 10 μm/s; tangential force-displacement curves.

Appendix G

Tables

$\dot{P}_l$ (mN/s)	$\dot{P}_u$ (mN/s)	P_m (N)	h_m (μm)	S_m (N/μm)	h_c (μm)	A_c (μm^2)	f	E (GPa)	Error (%)
25	25	0.205	8.63	0.251	8.02	1574.4	0.989	4.57	47.1
25	50	0.207	8.64	0.196	7.84	1507.6	0.989	3.65	17.4
25	250	0.207	8.61	0.186	7.78	1481.9	0.989	3.49	12.3
25	25	2.85	27.6	1.32	26.0	16530	0.846	6.33	104
25	25	0.92	18.9	0.499	17.6	7546.9	0.950	3.99	28.3
250	250	2.82	28.1	1.54	26.7	17435	0.848	7.24	133
1020	1020	2.85	27.3	2.29	26.4	17032	0.846	10.9	249

Table G.1: Experimental values used for the calculation of E from the P-h curves shown in Fig. F-76. The "Error" is calculated relative to the reference value of E = 3.11 GPa.